frontiers | Research Topics

Women in nanotechnology, volume I

Edited by
Sonu Gandhi, Neha Kaushik, Beatriz Noheda,
Estela Blaisten-Barojas and Theresa Schoetz

Published in
Frontiers in Nanotechnology

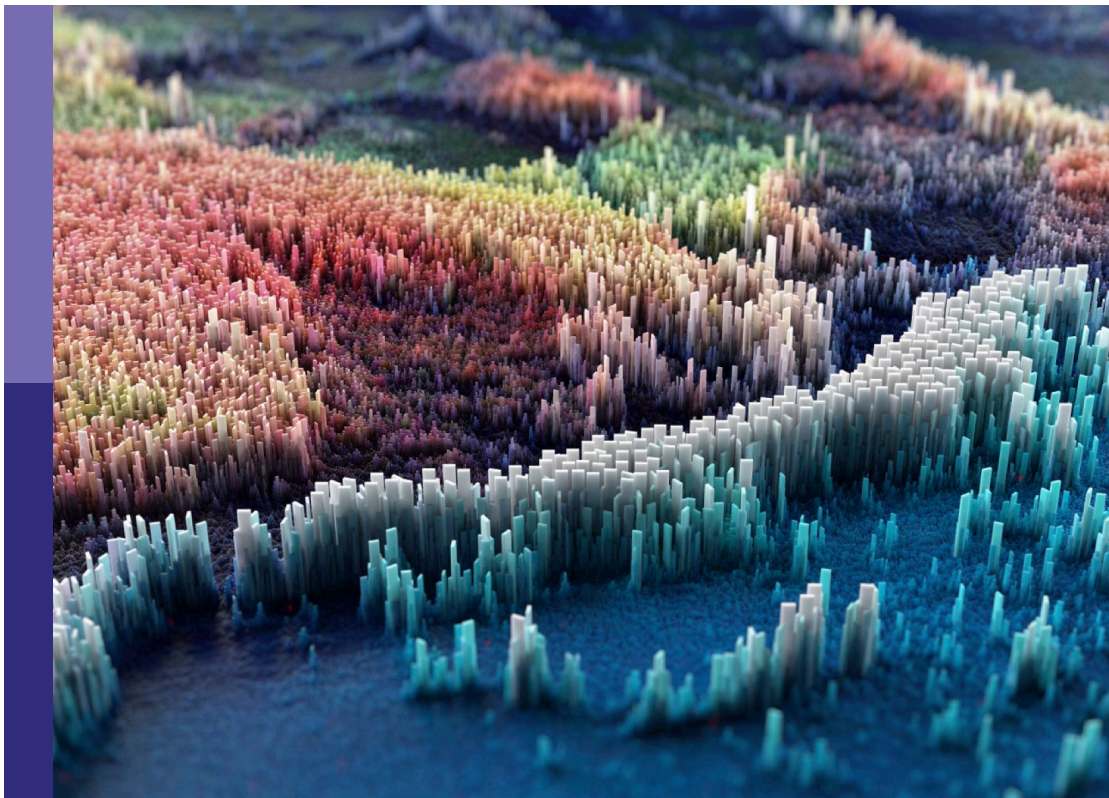

ISSN 1664-8714
ISBN 978-2-8325-5155-4
DOI 10.3389/978-2-8325-5155-4

About Frontiers

Frontiers is more than just an open access publisher of scholarly articles: it is a pioneering approach to the world of academia, radically improving the way scholarly research is managed. The grand vision of Frontiers is a world where all people have an equal opportunity to seek, share and generate knowledge. Frontiers provides immediate and permanent online open access to all its publications, but this alone is not enough to realize our grand goals.

Frontiers journal series

The Frontiers journal series is a multi-tier and interdisciplinary set of open-access, online journals, promising a paradigm shift from the current review, selection and dissemination processes in academic publishing. All Frontiers journals are driven by researchers for researchers; therefore, they constitute a service to the scholarly community. At the same time, the *Frontiers journal series* operates on a revolutionary invention, the tiered publishing system, initially addressing specific communities of scholars, and gradually climbing up to broader public understanding, thus serving the interests of the lay society, too.

Dedication to quality

Each Frontiers article is a landmark of the highest quality, thanks to genuinely collaborative interactions between authors and review editors, who include some of the world's best academicians. Research must be certified by peers before entering a stream of knowledge that may eventually reach the public - and shape society; therefore, Frontiers only applies the most rigorous and unbiased reviews. Frontiers revolutionizes research publishing by freely delivering the most outstanding research, evaluated with no bias from both the academic and social point of view. By applying the most advanced information technologies, Frontiers is catapulting scholarly publishing into a new generation.

What are Frontiers Research Topics?

Frontiers Research Topics are very popular trademarks of the *Frontiers journals series*: they are collections of at least ten articles, all centered on a particular subject. With their unique mix of varied contributions from Original Research to Review Articles, Frontiers Research Topics unify the most influential researchers, the latest key findings and historical advances in a hot research area.

Find out more on how to host your own Frontiers Research Topic or contribute to one as an author by contacting the Frontiers editorial office: frontiersin.org/about/contact

Women in nanotechnology, volume I

Topic editors

Sonu Gandhi — National Institute of Animal Biotechnology (NIAB), India
Neha Kaushik — University of Suwon, Republic of Korea
Beatriz Noheda — University of Groningen, Netherlands
Estela Blaisten-Barojas — George Mason University, United States
Theresa Schoetz — University of Illinois at Urbana-Champaign, United States

Citation

Gandhi, S., Kaushik, N., Noheda, B., Blaisten-Barojas, E., Schoetz, T., eds. (2024). *Women in nanotechnology, volume I*. Lausanne: Frontiers Media SA.
doi: 10.3389/978-2-8325-5155-4

Table of contents

frontiers | Frontiers in Nanotechnology

TYPE Editorial
PUBLISHED 01 July 2024
DOI 10.3389/fnano.2024.1443473

OPEN ACCESS

EDITED AND REVIEWED BY
Themis Prodromakis,
University of Edinburgh, United Kingdom

*CORRESPONDENCE
Neha Kaushik,
neha.bioplasma@gmail.com

RECEIVED 04 June 2024
ACCEPTED 18 June 2024
PUBLISHED 01 July 2024

CITATION
Kaushik N (2024), Editorial: Women in nanotechnology: Vol. I.
Front. Nanotechnol. 6:1443473.
doi: 10.3389/fnano.2024.1443473

Editorial: Women in nanotechnology: Vol. I

Neha Kaushik*

[1]Department of Biotechnology, College of Engineering, The University of Suwon, Hwaseong, Republic of Korea

KEYWORDS

nanoparticle synthesis, graphene synthesis, biomedical applications, nanotechnology, electric devices

Editorial on the Research Topic
Women in nanotechnology: Vol. I

Introduction

This Research Topic in Frontiers in Nanotechnology was honored to provide this platform to encourage the work of women scientists in all nanotechnology-related fields. We believe that the studies displayed here highlight the variety of research executed within the entire scale of the nanotechnology areas and portray innovations in hypothesis, experimentation, and methodology with applications to lean on problems.

This unique volume features nine articles authored by 43 researchers, indicating high attention and engagement in the field. The research volume includes diverse studies at the forefront of nanotechnology, each offering unique insights and contributions to the field in various domains (Figure 1).

Eco-friendly synthesis of nanoparticles

The volume opens up with a novel investigation by Sergievskaya et al. on the environmental-friendly synthesis of stable colloidal gold nanoparticles utilizing magnetron sputter deposition onto castor oil through varying parameters, for instance, sputter power, deposition time, gas pressure, and plasma type. This innovative method underlines the merit of sustainable nanotechnology systems and vegetable oils' ability to fabricate nanoparticles.

In other work, Campaña et al. also emphasize the benefit of a green, economical, and nature-friendly process with promises of microorganism-facilitated production of metal nanoparticles (MNPs). Their broad review examines the complex mechanisms bacteria use to uptake and moderate metal ions, featuring the ability of microbial synthesis to generate high-end MNPs appropriate for distinct purposes. In contrast, challenges, such as polydispersity and modest yield, endure, and enhancing growth environments and purification practices propose possibilities for development. Most importantly, this work highlights the extensive industrial promise and features the significance of continuing research in comprehensive microbial redox action and metal transport for remote advancements in this field.

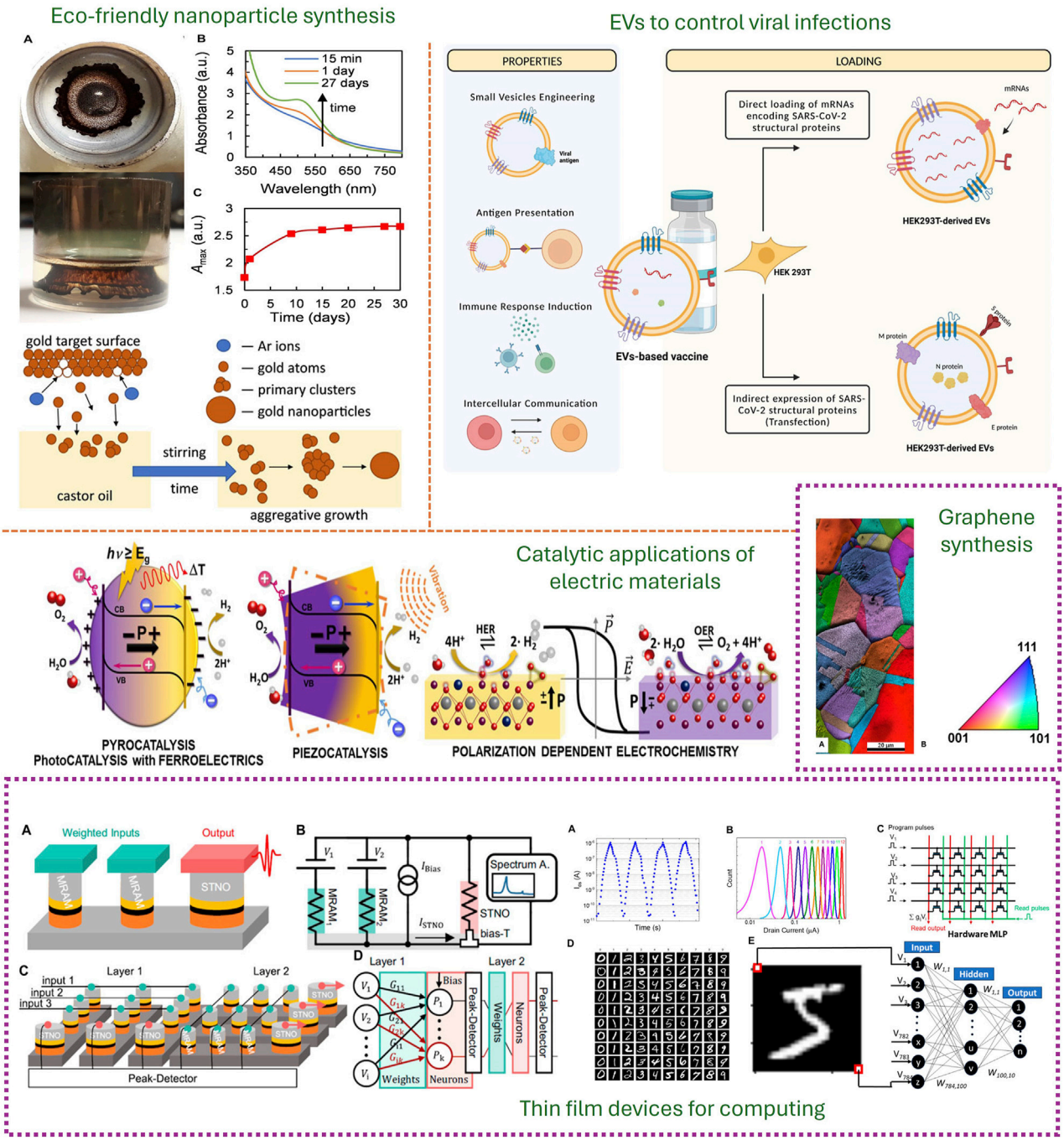

FIGURE 1
Glances of some studies published in this research volume.

Role of extracellular vesicles to combat viral infections

Regarding the past pandemic, the fundamental function of extracellular vesicles (EVs) in intercellular communication, especially in the settings of coronavirus infections, has been explored by Sbarigia et al. In this detailed review, their in-depth assessment glances at EVs' capability as SARS-CoV-2 diagnostic and therapeutic tools alongside observing EVs' functions in immune escape, virus entry, and duplication. Their effort explains the fabrication of EVs, their structural resemblance to viruses, and their competence to persuade immune functions. On the other hand, EV heterogeneity's obstacles and their suggested purposes in therapies and diagnostics emphasize the requirement for additional consideration to improve our understanding and clinical expenditures of EVs.

Advanced relevance of thermoresponsive polymers

Hopkins et al. studied the thermoresponsive characteristics of polymers, for example, poly (N, N-diethylacrylamide) (PDEA) and poly (N-isopropylacrylamide) (PNIPAM), identifying their implications in biomedical as well as industrial domains. Their work delves into the coil-to-globule modification of these polymers in diverse solvents, revealing glycerol's capability to reach elevated minimal critical solution temperatures, sustaining the potential for industrial products. Employing simulations, this research supplies worthy perceptions into polymer performance, placing the grounds for forthcoming biosensing, water treatment, drug delivery, etc.

Catalytic applications of electric materials

Domingo researched the developing application of ferroelectric and piezoelectric materials in catalytic perspectives. Pointing out the impact of identifying process time range, this work supports developing innovative characterization equipment to drive piezo catalyst design forward. Although existing concentrations predominantly aim for pollutant refinement, this study emphasizes the requirement for additional studies to improve the decrease of CO_2 and water-splitting productivity. These advancements hold promise for catalyzing progress in energy harvesting and biomedical applications.

Graphene synthesis

Grubišić-Čabo et al. discovered the influence of calcium intercalation in quasi-freestanding bilayer graphene on silicon carbide (SiC). Their outcomes expose that calcium intercalation shifts hydrogen at the graphene-SiC interface, ensuing in considerable n-doping and varying AB-stacked bilayer graphene into AA-stacked bilayer graphene. Adjusting the electronic form enhances carrier strength by barely marginally affecting Fermi velocity. This groundbreaking study opens up new possibilities for inspecting the typical traits of homogeneous quasi-freestanding AA-stacked graphene.

In another way, Zehra and colleagues portrayed a novel attempt established on photo-polymerized 1,1′-biphenyl-4-thiol self-assembled monolayers (SAMs) on copper substrates for graphene synthesis. Throughout light-induced polymerization and annealing, single-layer graphene was constructed using this system. They encountered that, in contrast to electropolished substrates, graphene on oxidized copper produces higher-value graphene. Importantly, this procedure makes it feasible to synthesize graphene on insulating substrates, which opens up opportunities for forming doped graphene in succeeding studies.

Laser-synthesized nanodiamonds for immunomodulation

The immunomodulatory influences of laser-synthesized nanodiamonds (LNDs) in numerous preparations—unconjugated, PEGylated, and antibody-conjugated—on peripheral blood mononuclear cells investigated by Alexander et al. According to their research, PEGylated and raw LNDs at extreme concentrations trigger minimal cytotoxicity. However, antibody-conjugated LNDs initiate immunological responses at elevated concentrations. These findings focus on the possible advantage of LNDs in biomedical applications and foster more experiments to expand their therapeutic design.

Thin film devices for computing

For post-von Neumann computing, Majumdar et al. explores the prospects of recently increasing nanoelectronic devices with ferroic ordering. They discover spintronic and ferroelectric devices in detail, underlining their exploits in neuromorphic routines and analog memory, exceptionally in critical environments. Their work emphasizes the implication of interdisciplinary assistance and the necessity to lay out neuromorphic hardware for future generations. It also investigates the consequence of ferroelectric effects and photo-induced magnetoresistance in emerging photonic memory and neuromorphic circuits, which are critical for the evolution of space and quantum computing machinery.

Numerous works on the manufacture of nanoparticles and their uses are explored in this research volume. It integrates cutting-edge performances for creating stable gold nanoparticles, such as magnetron sputter deposition onto castor oil. Likewise, investigations on the tasks of EVs in viral infections, the microbial synthesis of metal nanoparticles, and the performance of thermoresponsive polymers support information for industrial and biological applications. Nanotechnology is advanced in other areas like calcium intercalation in graphene, immunomodulatory effects of nanodiamonds, graphene synthesis from self-assembled monolayers, and piezoelectric materials for catalysis. Concerns on ferroic ordering in thin film devices pave the way for next-generation computer systems. When shown as an entirety, these works show the diverse prospects and exciting outlook of nanotechnology exploration.

Author contributions

NK: Writing–original draft, Writing–review and editing.

Funding

The author(s) declare that no financial support was received for the research, authorship, and/or publication of this article.

Acknowledgments

NK acknowledges all her co-topic editors Estela Blaisten-Barojas, Beatriz Noheda, Sonu Gandhi, and Theresa Schoetz, for their significant contributions to the successful management of this research volume.

Conflict of interest

The author declares that the research was conducted in the absence of any commercial or financial relationships that could be construed as a potential conflict of interest.

The author(s) declared that they were an editorial board member of Frontiers, at the time of submission. This had no impact on the peer review process and the final decision.

Publisher's note

frontiers in Nanotechnology

ORIGINAL RESEARCH
published: 09 August 2021
doi: 10.3389/fnano.2021.710612

Insights on the Formation of Nanoparticles Prepared by Magnetron Sputtering Onto Liquids: Gold Sputtered Onto Castor Oil as a Case Study

Anastasiya Sergievskaya[1], Amy O'Reilly[1], Halima Alem[2], Julien De Winter[3], David Cornil[4], Jérôme Cornil[4] and Stephanos Konstantinidis[1]**

[1]Plasma-Surface Interaction Chemistry (ChIPS), University of Mons, Mons, Belgium, [2]Université de Lorraine, CNRS, Nancy, France, [3]Organic Synthesis and Mass Spectrometry Laboratory (S[2]MOs), University of Mons, Mons, Belgium, [4]Laboratory for Chemistry of Novel Materials (CMN), University of Mons, Mons, Belgium

OPEN ACCESS

Edited by:
Zheng Han,
Shanxi University, China

Reviewed by:
Xiao Xi Li,
Institute of Metals Research, Chinese Academy of Sciences (CAS), China
Simone Dal Zilio,
Consiglio Nazionale delle Ricerche (CNR), Italy

***Correspondence:**
Anastasiya Sergievskaya
anastasiya.sergievskaya@umons.ac.be
Stephanos Konstantinidis
stephanos.konstantinidis@umons.ac.be

Specialty section:
This article was submitted to Nanofabrication, a section of the journal Frontiers in Nanotechnology

Received: 16 May 2021
Accepted: 07 July 2021
Published: 09 August 2021

Citation:
Sergievskaya A, O'Reilly A, Alem H, De Winter J, Cornil D, Cornil J and Konstantinidis S (2021) Insights on the Formation of Nanoparticles Prepared by Magnetron Sputtering Onto Liquids: Gold Sputtered Onto Castor Oil as a Case Study. Front. Nanotechnol. 3:710612. doi: 10.3389/fnano.2021.710612

Magnetron sputter deposition of metal targets over liquids allows producing colloidal solutions of small metal nanoparticles (NPs) without any additional reducing or stabilizing reagents. Despite that this synthetic approach is known for almost 15 years, the detailed mechanism of NP formation is still unclear. Detailed investigations must be carried out to better understand the growth mechanism and, ultimately, control the properties of the NPs. Here, the combination of the gold (Au) target and castor oil, a highly available green solvent, was chosen as a model system to investigate how different experimental parameters affect the growth of NPs. The effect of deposition time, applied sputter power, working gas pressure, and type of sputter plasma (direct current magnetron sputtering (DC-MS) vs. high-power impulse magnetron sputtering (HiPIMS)) on properties of Au NPs has been studied by UV-vis spectroscopy and transmission electron microscopy (TEM), and further supported by quantum-chemistry calculations and mass-spectrometry analysis. The mechanism of the Au NP formation includes the production of primary NPs and their subsequent aggregative growth limited by diffusion in the viscous castor oil medium. Final Au NPs have a narrow size distribution and a medium diameter of 2.4–3.2 nm when produced in DC-MS mode. The NP size can be increased up to 5.2 ± 0.8 nm by depositing in HiPIMS mode which, therefore, mimics energy and time-consuming post synthesis annealing.

Keywords: Sputtering onto liquid, castor oil, gold nanoparticles, aggregative growth, HiPIMS

INTRODUCTION

The synthesis of nanomaterials has been intensely studied during the last few decades (Liz-Marzán, 2020). Thousands of experimental protocols have been reported for the production of colloidal dispersions of nanoparticles (NPs) and supercrystals having different sizes, shapes, and compositions (Boles et al., 2016; García-Lojo et al., 2019). These dispersions can be used for fabricating new materials with properties that are not available in traditional bulk component systems (Talapin et al., 2010; Kovalenko et al., 2015; Kagan et al., 2016). Typical recipe for the synthesis of metal NPs

includes reduction of the precursor (usually the metal salt) in certain solvent in the presence of capping molecules. The resulting colloidal solution contains metal NPs and other reaction products as well as the excess of the reducing reagents, so that the post-synthetic purification of NPs might be required for certain applications (Sebastian et al., 2014). In this respect, physical vapor deposition (PVD) onto liquid substrates is an alternative green approach allowing obtaining pure colloidal dispersions of metallic NPs containing only two components: the NP-forming atoms and the low-vapor pressure liquid that acts as a dispersion medium preventing fast agglomeration of NPs because of the high viscosity or/and the presence of stabilizing functional groups (Wender et al., 2013; Torimoto et al., 2016; Nguyen and Yonezawa, 2018). Although magnetron sputtering onto liquids is studied since 1996 with the work of Wagener et al. who produced silver NPs in silicone oil (Wagener et al., 1996), the mechanism of NP formation is not yet fully understood, although more than 100 papers dedicated to depositions on different liquids have been published. There are still open questions such as where does the nucleation process take place—on the liquid surface or in the bulk solution, what is the particle growth mechanism, why are the secondary growth processes more typical for certain NPs and host liquids, and how does the liquid affect the properties of the final NPs? These questions need to be answered to control better the NPs production and scale up the synthetic procedure for real-life applications. The way to go is to collect more quantitative information about NP synthesized via magnetron sputtering onto liquids under a wide range of controlled experimental conditions and analyze which factor(s) affect(s) the particle properties. The difficulty of today is also to compare the results obtained by different research groups due to the variety of sputter devices used and due to the absence of the full set of experimental conditions in the published papers (like deposition rates) which are mandatory information to reproduce completely NPs synthesis in different vacuum chambers or small sputter devices.

In this work we present new data on the formation of small, stable Au NPs in a castor oil. This vegetable oil is an unexpensive, highly available, nontoxic, green solvent that mainly consists of triglyceride of ricinoleic acid (~87%, see composition in **Supplementary Figure 1**) (Patel et al., 2016). Here, we discuss the systematic study of Au NP formation within a broad range of sputtering conditions. The effect of sputter time, applied power, argon pressure (from 0.07 to 2 Pa), and the type of sputtering plasma (Direct Current-Magnetron Sputtering (DC-MS) vs. High Power Impulse Magnetron Sputtering (HiPIMS)) on the behavior of colloidal solutions of Au NPs in castor oil has been studied by UV-vis spectroscopy during several months. The size and shape of the obtained NPs were characterized by TEM and the stability of colloidal solutions of Au NPs in castor oil was discussed in light of quantum-chemistry calculations and mass-spectrometry analysis. We believe that this massive new set of experimental data will open the way for the development of universal reproducible protocols of metal NP dispersions by magnetron sputter depositions onto liquids.

MATERIALS AND METHODS

Materials

Castor oil (CAS number 8001-79-4) was purchased from Alfa Aesar and used as received. Gold target (99.99%; 5.08 cm (2") in diameter; 1.59 mm (0.0625") in thickness; elastomer bonded to copper backing plate) was purchased from Kurt J. Lesker Company Ltd. and used as received.

Preparation of Colloidal Solutions of Au NPs

The sputtering procedure was similar to the previously reported in detail by our group (Sergievskaya et al., 2021). The schematic image of the vacuum chamber can be found in **Supplementary Figure 2**. The main deposition chamber, i.e., where sputtering takes place, was permanently pumped down to the pressure of 10^{-6} Pa. In a typical experiment, 4.0 g of castor oil placed into a cylindrical plastic beaker (3 cm in height; 2.8 cm in diameter) were degassed inside the load-lock chamber until the pressure of 10^{-5} Pa was reached. After this, the sample was transferred into the deposition chamber. The argon pressure was precisely controlled by a throttle valve placed in front of the turbomolecular pump. The working distance between the target and liquid surfaces was equal to 20 cm. Depositions lasted 10 min for all cases except when studying the effect of the sputter time. The magnetron was cooled by water line, hence allowing stable deposition conditions. Depositions in DC-MS regime were done with commercial power supply (Advanced Energy MDX 500), while for HiPIMS experiments a prototype constructed in MATERIA NOVA R&D center (Britun et al., 2018)) was used. In this case magnetron sputtering was carried out at an argon pressure of 0.7 Pa, at a time-averaged sputter power of 80 W (current 92 mA; voltage 867 V), and with the following pulse parameters (pulse repetition frequency 800 Hz, pulse duration 20 μs; peak target current density 0.3 A/cm^2). Typical current and voltage waveforms can be found in Britun et al. (2018).

All the samples were photographed after venting the load-lock chamber and immediately stirred at the magnetic stirrer for 5 min. A detailed set of experimental conditions for each deposition can be found in **Supplementary Table 1** in the Supplementary material. The concentration of deposited gold atoms in colloidal solutions was estimated based on gold flux measurement (experimental procedure and obtained values can be found in the Supplementary material in **Supplementary Table 2** and in **Supplementary Figure 3**).

Characterization Methods

Colloidal dispersion of Au NPs obtained via magnetron sputtering of gold target onto castor oil was regularly characterized by means of UV-vis spectroscopy with Agilent Cary 5000 UV-vis-NIR spectrometer. The shape, size, and size distributions of particles were determined by transmission electron microscopy (TEM) with Philips CM200 microscope. The castor oil composition before and after exposure to the argon-based plasma was analyzed by Positive-ion Matrix assisted LASER Desorption/Ionization-Mass Spectrometry (MALDI-MS) with Waters QToF Premier mass spectrometer.

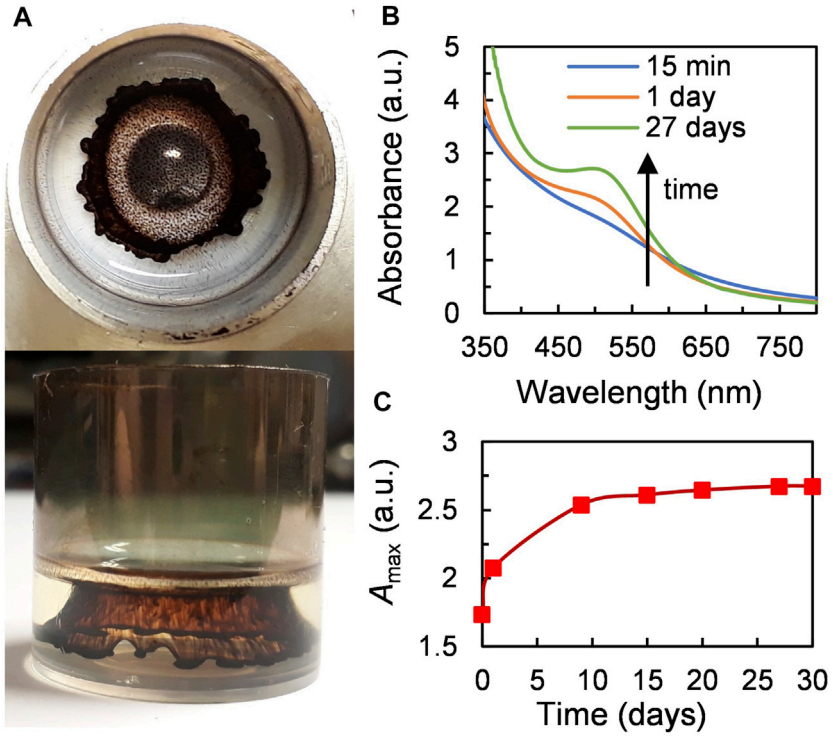

FIGURE 1 | A typical sample produced by magnetron sputtering of gold onto castor oil. **(A)** Photographs of the sample just after venting the vacuum chamber (experimental conditions: Ar pressure–0.07 Pa, applied power–80 W (488 V, 162 mA), sputter time–5 min). **(B)** UV-vis spectra of the solution obtained after stirring the sample (time marks indicate the time after finishing sputtering). **(C)** Increase in absorbance at the maximum of SPR of Au NPs (505 nm) with time.

Additional information about characterization methods can be found in the Supplementary material.

Density Functional Theory Calculations

To better understand the chemical interactions between the castor oil components and Au NPs, quantum-chemical calculations were carried out at the density functional theory (DFT) and density functional tight-binding (DFTB) levels in two steps, as done in our previous paper (Sergievskaya et al., 2021). A detailed protocol leading to the interaction energy values is placed in the Supplementary material.

RESULTS AND DISCUSSION

Reproducibility of the Synthesis and Stability of the Products

Formation of Au NPs after magnetron sputtering of gold target onto castor oil was first observed with the naked eye. As can be seen in **Figure 1A**, a jellyfish-like brownish cloud of particles was formed under the oil surface. The size and color intensity of this cloud is proportional to the amount of gold deposited during the experiment. Transparent colloidal dispersions were obtained after stirring the samples. The color of the solutions changed from brown to red with storage time. As depicted in the UV-vis spectra in **Figure 1B** no surface plasmon resonance (SPR) band was observed 15 min after sputter deposition. However, the formation of well-developed SPR band with maximum at 505 nm started 1 day after stirring the sample. The absorbance reached its maximum located at 505 nm 3 weeks after the synthesis (see **Figure 1C**). An increase in absorbance might be explained by secondary growth processes taking place in the solution after sputter deposition is over. Such a behavior of Au NPs has been mentioned by other research groups performing magnetron sputtering onto ionic liquids (Vanecht et al., 2011, 2012; Hamm et al., 2014), PEEL (Shishino et al., 2011), PEGs (Slepička et al., 2015), and oleic acid (Nguyen et al., 2020).

To check the reproducibility of sputter experiments, several depositions were made on different days but under similar experimental conditions. At first, the samples look similar with the naked (see **Supplementary Figure 5A**) but to analyze the reproducibility in a more rigorous way the UV-vis spectra of two samples 3.1 and 3.2 were recorded 15 min after venting the vacuum chamber and stirring and compared. The two absorbance curves are superimposed (**Supplementary Figure 5B**). On the same graph, we also verified the UV-vis spectra of the solutions recorded 24 h after stirring. The curves have the same shape but sample 3.1 has an absorbance at 505 nm 3.8% higher than the one of sample 3.2. However, this is not a significative variation for colloidal systems with secondary growth processes. Nevertheless, even though there is a marginal variation in the UV-vis spectra after sputtering, all the experiments were performed under time-controlled conditions. TEM characterization was done after all the samples reached the maximum absorbance.

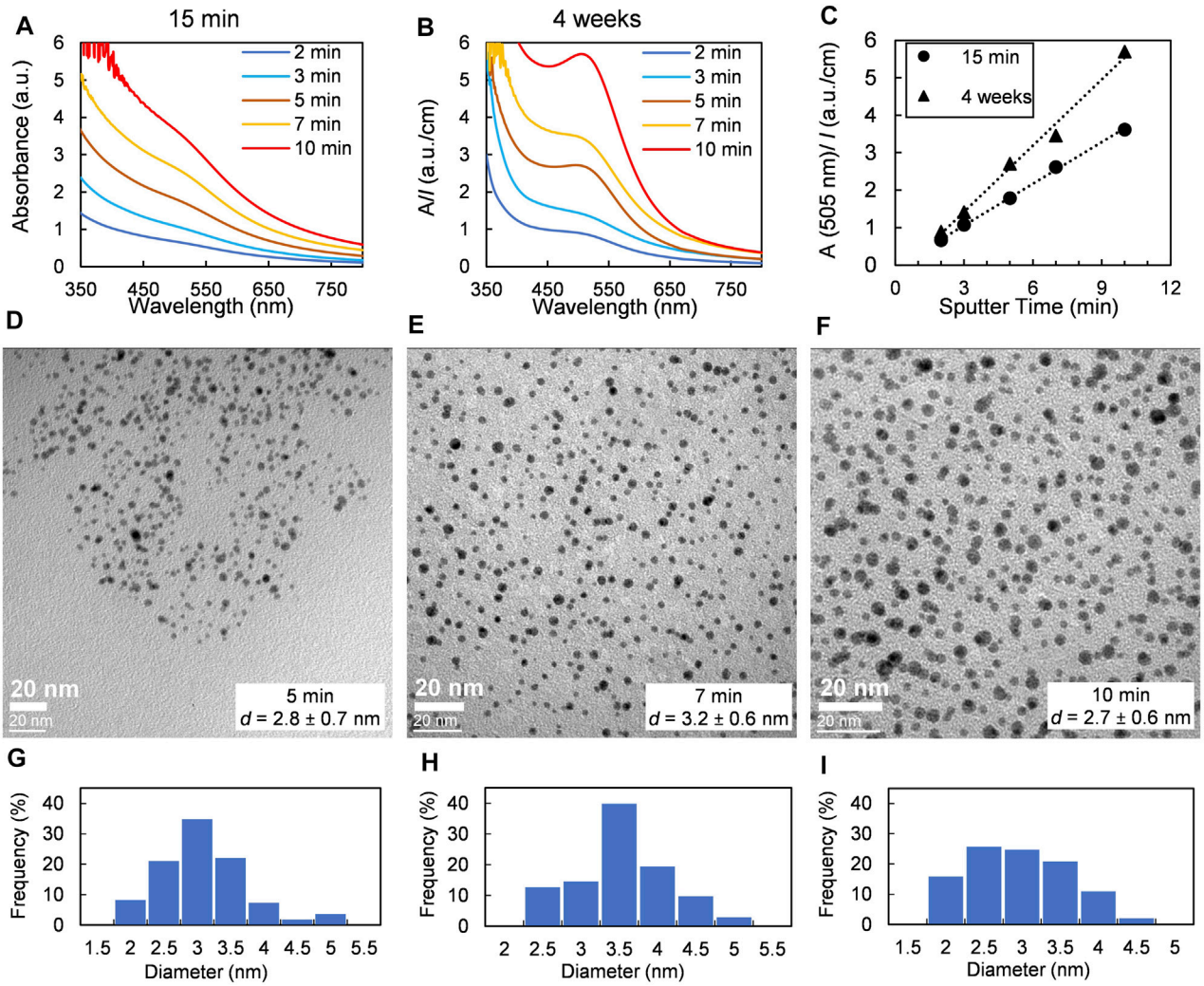

FIGURE 2 | Effect of sputter time: samples were obtained at a fixed argon pressure of 0.07 Pa and an applied power of 80 W. **(A)** and **(B)** UV-vis spectra of dispersions of Au NPs in castor oil recorded 15 min and 4 weeks later after deposition, respectively. **(C)** Changes in absorbance at the maximum of SPR band of Au NPs. **(D–F)** TEM images and **(G–I)** size distributions of Au NPs obtained at sputter time of 5, 7, and 10 min, respectively.

Dispersions of Au NPs obtained via magnetron sputtering onto castor oil have a good colloidal stability. 25 depositions were made and no decrease in the absorbance at maximum SPR band or precipitation was noticed during at least one year for 23 of them, the energetic position of SPR stayed also constant during this period. Heating of the samples to 100 C for 2 h does not cause any significant changes in UV-vis spectra (**Supplementary Figure 6**) and does not provoke aggregation.

MALDI-mass spectrometry analyses of castor oil before and after plasma treatment have been done. As presented in **Supplementary Figure 7**, beside a slight oxidation, there is no significant modification of the chemical composition of the substrate (the host liquid) during the deposition with the DC-MS procedure. According to the results of quantum-chemical calculations performed at the DFT and DFTB levels, the chemical interactions between the triglyceride of ricinoleic acid, i.e., the main castor oil component, and the surfaces of Au NPs are favorable. As a matter of fact, the interaction energy between the model molecule, 1/3 part of triglyceride of ricinoleic acid, and the Au 111) surface is negative (−0.14 eV) (see **Supplementary Figure 4**). In our previous work, the interaction energy between the same model module molecule and the Ag 111) surface was positive, and colloidal solutions of Ag NPs in castor oil produced by magnetron sputtering were indeed not stable (Sergievskaya et al., 2021). These new data imply that castor oil is a good capping agent for Au NPs.

All the data reported above prove that magnetron sputter deposition of a gold target onto castor oil allows producing stable colloidal solutions of Au NPs.

Effect of Sputter Time

Under fixed sputter conditions the gold flux is constant so that an increase in sputter time leads to an increase in the number of gold atoms deposited onto the liquid surface. The size and

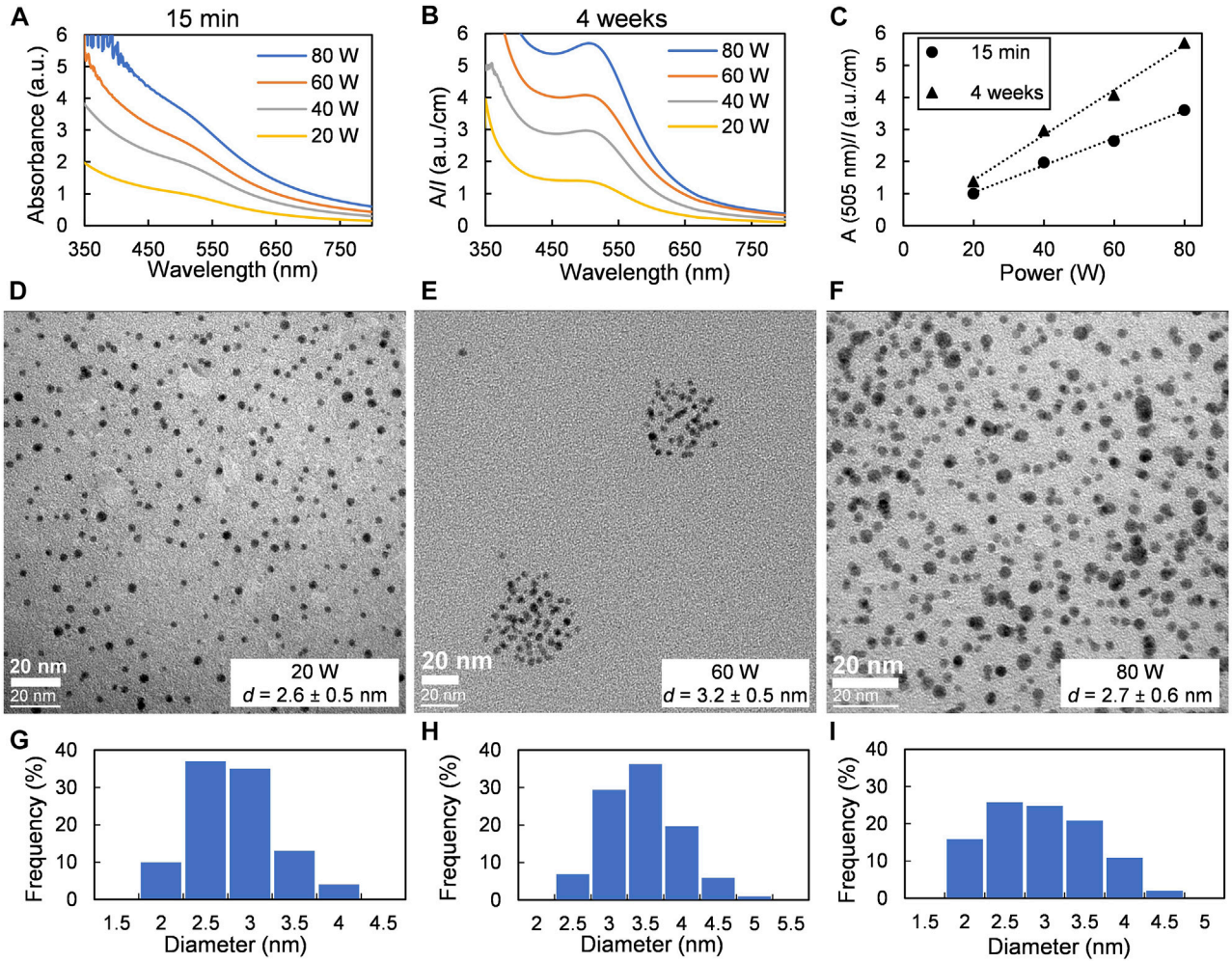

FIGURE 3 | Effect of applied power: samples were obtained at a fixed argon pressure of 0.07 Pa and a sputter time of 10 min. **(A)** and **(B)** UV-vis spectra of dispersions of Au NPs in castor oil recorded 15 min and 4 weeks after deposition, respectively. **(C)** Changes in absorbance at the maximum of SPR band of Au NPs. **(D–F)** TEM images and **(G–I)** size distributions of Au NPs obtained at sputter power of 20, 60, and 80 W, respectively.

the color intensity of the Au NPs cloud under the castor oil surface significantly increases with sputter time (**Supplementary Figure 8**). As seen in **Figures 2A,B**, the absorbance of colloidal solutions obtained after stirring of the samples increases linearly with sputter time. The fact that this dependence stays linear 4 weeks after sample preparation means that the aging of Au NPs goes synchronically. Different research groups have already shown that sputter time does not affect the size of metal NPs but increases their concentration inside the host liquid solution (Torimoto et al., 2006; Suzuki et al., 2009; Shishino et al., 2010; Tsuda et al., 2010; Hatakeyama et al., 2011; Slepička et al., 2015; Sumi et al., 2015; Lee et al., 2018; Sergievskaya et al., 2021). According to TEM images (see **Figures 2D–F**), obtained Au NPs have spherical shape and narrow size distribution (**Figures 2G–I**); the mean diameter of Au NPs in castor oil is independent of sputter time or gold concentration.

Effect of Sputter Power

An increase in sputter power leads to an increase in gold deposition flux (see **Supplementary Figure 3A**). The size of the NP cloud under the oil surface increased with sputter power as well as the color intensity of obtained colloidal dispersions (**Supplementary Figure 9**). One can see a linear increase in absorbance of the colloidal solutions when changing the sputter power from 20 to 80 W, i.e., for power densities equal to 1 and 4W/cm^2 (**Figures 3A,B**). The dependence of absorbance at 505 nm (the maximum of SPR band of Au NPs) vs power stays linear both 15 min and 1 month after sample preparation (**Figure 3C**). The size of the obtained NPs does not depend on sputter power and is approximately 2.6–3.2 nm (see **Figures 3D–I**). The fact that discharge current or power, or more straightforwardly, the deposition flux, does not affect the size of metal NPs obtained via sputtering onto liquids has been noticed before by us (Sergievskaya et al., 2021) and other research groups (Hatakeyama et al., 2011; Sumi et al., 2015; Qadir et al., 2019).

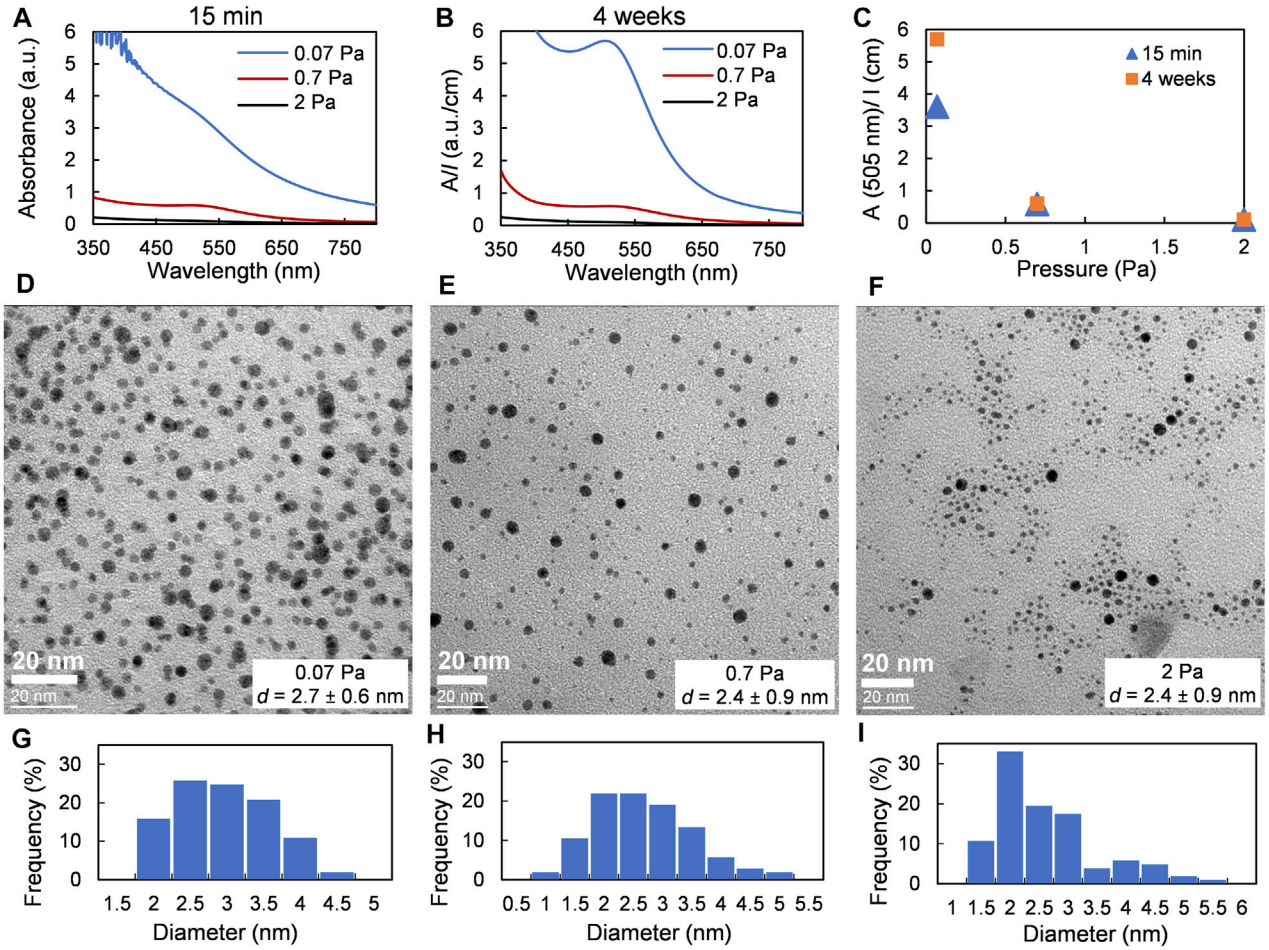

FIGURE 4 | | Effect of argon pressure. Samples were obtained at a fixed applied power of 80 W and a sputter time of 10 min. **(A)** and **(B)** UV-vis spectra of dispersions of Au NPs in castor oil recorded 15 min and 4 weeks after deposition, respectively **(C)** Changes in absorbance at the maximum of SPR band of Au NPs. **(D–F)** TEM images and **(G–I)** size distributions of Au NPs obtained at argon pressure of 0.07, 0.7, and 2 Pa, respectively.

Therefore, it can be reasonably assumed that the variation of the sputter power does not provoke any significant alteration of the nucleation and growth conditions of the gold NPs, in our experimental conditions. However, some scientists reported an increase in the NP size with discharge voltage (Suzuki et al., 2009; Wender et al., 2010, 2011; Sugioka et al., 2015). This behavior might be explained by the heating of the host liquid by plasma-born species and sputtered metal atoms and the IR radiations emitted by the target during the deposition (Orozco-Montes et al., 2021). For example, it has been recently shown that the temperature of 4 ml of glycerol was increased by 17°C during 20 min platinum deposition with 12 cm of working distance (100 W; 5 W/cm^2) and by 40°C with 5 cm of working distance at the same DC power density (Orozco-Montes et al., 2021). An increase in liquid temperature leads to a decrease in both the viscosity and surface tension of the host liquid, so that the sputter atoms more easily penetrate under the liquid surface and the number of collisions between freshly solvated sputtered atoms and primary clusters formed under the liquid surface increases. As a result, NPs of larger size might form.

Effect of Argon Pressure

An increase in pressure leads to a significant decrease in gold flux (see **Supplementary Figure 3B**) but also in the kinetic energy of the sputtered atoms reaching the liquid surface because of increased gas phase scattering. It was seen with the naked eye that the area of deposited material drastically decreased with pressure at a fixed sputter time of 10 min (**Supplementary Figure 10A**). Consequently, the color of the colloidal solution obtained after stirring the sample produced at 2 Pa was almost yellow. No strong SPR resonance band was observed in UV-vis spectra of initial or aged solutions in this condition (2 Pa–**Figure 4A**); however, the SPR peak appeared with time for samples prepared at a pressure of 0.07 and 0.7 Pa (**Figure 4B**). The UV-vis spectrum of 2 Pa sample did not change significantly even one month after the preparation of the solution; the increase in absorbance at 505 nm was about 5% (**Figure 4C**). The size of NPs was measured by TEM 10 months after the sputtering procedure; it was found that the mean diameter of the final Au NPs does not depend on gas pressure (see **Figures 4D–I**). The effect of argon pressure on metal NP size obtained by sputtering

onto liquids has been already studied in three works (Wagener et al., 1996; Orozco-Montes et al., 2021; Sergievskaya et al., 2021), showing in all the cases that the size of NPs increased with argon pressure. The fact that NPs produced in this work was in a range of 2.4–2.7 nm might be explained by the difference in concentrations of the deposited gold atoms. A large number of small gold clusters form initially at a pressure of 0.07 Pa and their size increased because of the collisions during the storage time, as can be seen by UV-vis spectroscopy (**Figures 4A–C**). In contrast, at 0.7 and 2 Pa pressure, since the total concentration of deposited gold is lower at a higher pressure, a smaller number of larger particles form. These particles will collide less frequently in a viscous oil medium.

The sample obtained at a pressure of 2 Pa allows us to compare Au NPs obtained in the frame of this work with the results provided in Wender et al. (2010) (see the list of experimental parameters in **Supplementary Table 3**). In both the cases, Au NPs have a spherical shape with a mean diameter of 2.4 ± 0.9 nm (this work) vs. 3.8 ± 1.1 nm (Wender et al., 2010). The larger size of Au NPs produced by Wender might be explained by the fact that the deposition rate was higher so that more primary gold clusters were formed in smaller volume of castor oil and led to the formation of larger NPs. The difference in the deposition conditions might also lead to different liquid heating rates. Indeed, the modeling of the metal flux reaching the liquid surface with the SIMTRA Monte Carlo-based simulation package (Van Aeken et al., 2008; Depla and Leroy, 2012) has shown that obtained energy flux is dramatically increased in case of work (Wender et al., 2010). Considering that the thickness of the oil layer was 3 times less in case of Wender's research, it might be assumed that in that case the liquid substrate was heated much more efficiently than in case of the present work after the same treatment duration of 10 min. Decreasing in viscosity with the increase in oil temperature made diffusion faster, hence promoting collisions inside the liquid and allowing the formation of larger Au NPs. According to Wender et al. (2011), solutions of Au NPs in castor oil were stable about 8 months while our samples demonstrated a similar UV-vis spectrum for 14 months after the solutions reached the maximum of absorption.

Effect of Plasma Type: DC-MS vs. HiPIMS

Changing the power supply from DC-MS to HiPIMS allows us to deposit metal ions instead of metal neutrals. During DC-MS deposition, the film-forming species, i.e., metal neutrals, have kinetic energy typically in the range of several eV (Depla, 2013), but in the case of HiPIMS discharges, metal ions have kinetic energy of several tens of eV (Sarakinos et al., 2010). Such species might cause the heating up of the top liquid layer and penetrate deeper in the bulk solution, and hence affect the properties of NPs (Sergievskaya et al., 2021). HiPIMS power supplies were used only twice for sputtering onto liquids: during the deposition of Cr-Mn-Fe-Co-Ni alloy onto BMIM-TFSI ionic liquid (Garzón-Manjón et al., 2018) and by us for depositing silver onto castor oil (Sergievskaya et al., 2021). In both cases, the size of particles obtained with HiPIMS plasmas was larger than with DC-MS ones.

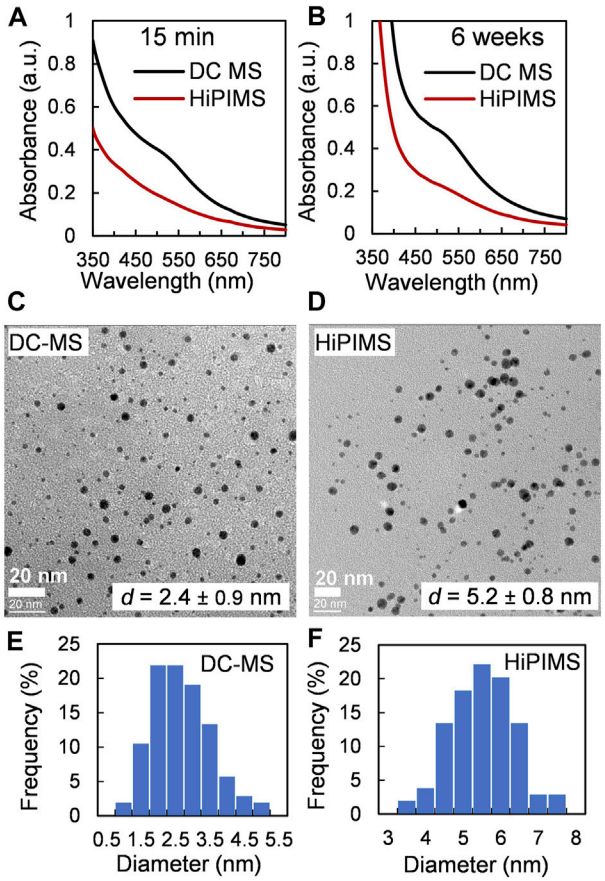

FIGURE 5 | Effect of plasma type: samples were obtained at a fixed argon pressure of 0.7 Pa and a sputter time of 10 min. **(A)** and **(B)** UV-vis spectra of dispersions of Au NPs in castor oil recorded 15 min and 6 weeks after deposition, respectively. **(C, D)** TEM images and **(E, F)** size distributions of Au NPs obtained with DC-MS and HiPIMS power supplies, respectively.

The photographs of the samples produced with DC-MS and HIPIMS power supplies can be found in **Supplementary Figure 11A**. One can see with the naked eye that the size of the NP cloud is smaller in case of the HiPIMS mode. This might be explained by the lower gold flux (see **Supplementary Table 2**). All colloidal solutions obtained after stirring of the HiPIMS samples were transparent and had brownish color (**Supplementary Figure 11B**). No strong SPR band appeared in the UV-vis spectra of HiPIMS samples even after one-month storage time (**Figures 5A,B**). Even though in case of the HiPIMS regime the concentration of gold in the solution was almost twice lower than in the DC-MS regime, the size of final gold NPs was larger: 5.2 ± 0.8 nm (HiPIMS) vs. 2.4 ± 0.9 nm (DC-MS), **Figures 5C–F**. This increase in NP size might be explained once again by the heating up of the host liquid by the HiPIMS plasma as discussed previously in Sergievskaya et al. (2021). Thus, the number of collisions between forming primary gold clusters increases and larger NPs are expected to form. Because the high-kinetic energy ions present in HiPIMS plasma might affect the host liquid components, the characterization of castor oil before and after exposure to the

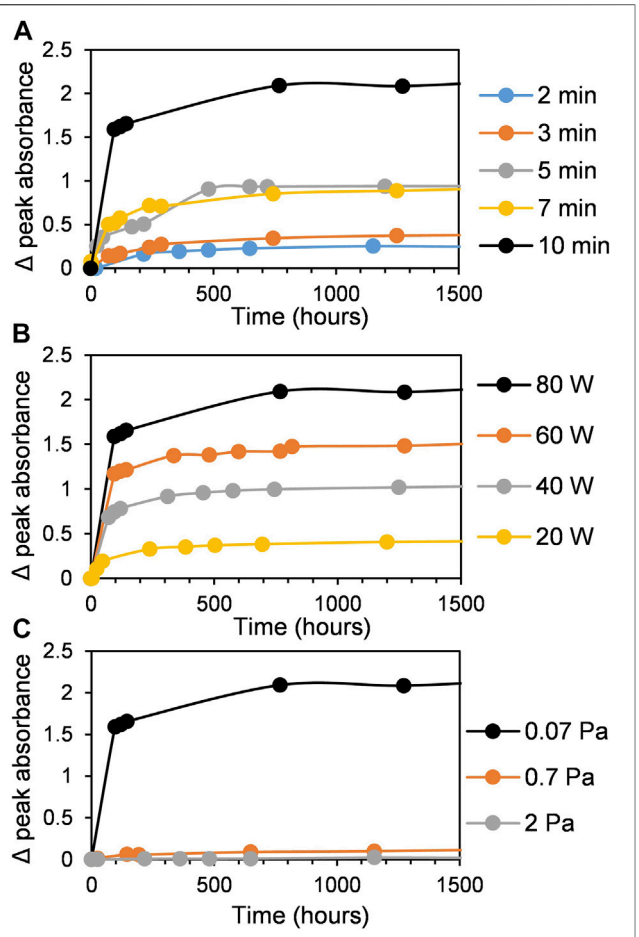

FIGURE 6 | The evolution of the absorbance at the maximum of SPR band (505 nm) as a function of time. **(A)** Effect of sputter time, **(B)** effect of sputter power, and **(C)** effect of argon pressure.

plasma was done by MALDI-mass spectrometry. Owing to a more aggressive treatment, some changes in oil structure were observed (**Supplementary Figure 7**). Even if an additional detailed future research is needed to explain the mechanism of oil degradation process, it is more probably due to successive oxidation reactions that could correspond to the 16 mass units difference observed in the mass spectrum. The here-provided data show once again that 1-step deposition with HiPIMS power supply might be used as an alternative to the 2-step process when primed metal NPs produced in the DC-MS regime were annealed with the aim of increasing their size (Meischein et al., 2019; Chauvin et al., 2020).

Mechanism of Nanoparticle Formation

The growth of metal NPs produced by reduction of metal ions in solution is much more studied than the formation of NPs during the magnetron sputtering process due to the absence of *in situ* observations inside the vacuum chamber. For the wet-chemistry synthesis, the kinetic curves representing the growth of metal NPs have a sigmoidal shape with an induction period corresponding to the nucleation step (Watzky and Finke, 1997; Finney and Finke, 2008). According to works reported in Ref. (Watzky and Finke, 1997, 2018; Finney and Finke, 2008; Sergievskaya et al., 2015), an autocatalytic growth step follows the nucleation process which leads to the formation of primary metal NPs. Secondary growth processes such as aggregation, coalescence, or Ostwald ripening might also take place in the solution (Finney et al., 2012; Thanh et al., 2014; Wang et al., 2014). In contrast to the classical colloidal synthesis, the concentration of metal in the solution is not constant in the case of sputtering onto liquid processes; it increases with sputtering time. Moreover, in case of sputtering onto still host liquid (without stirring), the obtained solutions are not homogeneous (see **Figure 1A**). Because of the rather high kinetic energy of the gold atoms (which depends on the working conditions), these species might reach the liquid subsurface and the nucleation and growth processes would then occur in the bulk solution. Small primary gold clusters with size less than 2 nm form during this time. There is no induction period on the typical kinetic curve shown in **Figure 1C** since the sample characterization was done after venting of the vacuum chamber. In view of the absence of a strong SPR band in the UV-vis spectra of colloidal solutions of AuNPs obtained after the sample stirring, we believe that the concentration of small gold clusters (<2 nm) stays high. We cannot exclude the presence of small amount of Au atoms stabilized by castor oil in the mixture. As the peak absorption of the SPR band increases with time (see **Figure 6**), one can see that, during the first week, the concentration of larger Au NPs is growing faster in case of more concentrated solutions. This process gets significantly slower with time. These findings lead to the hypothesis that the growth process is limited by the diffusion of the primary clusters in the castor oil (**Figure 7**). The clusters and atoms remaining after the nucleation processes aggregate and form larger Au NPs. Moreover, this aggregation process might have an autocatalytic nature (Finney et al., 2012; Wang et al., 2014). Finally, we stress that the growth of Au NPs after the end of the magnetron sputter deposition process has already been considered in previous works in the frame of aggregative models (Shishino et al., 2011; Vanecht et al., 2011, 2012; Hamm et al., 2014; Slepička et al., 2015).

To estimate the growth process rate, we plotted graphs in the coordinates ln (a/(1-a)) *vs.* t, where a is A_t/A_{max} (normalized absorbance) and t is the time after the end of the deposition process. The observed rate constants, k_{obs}, were determined from

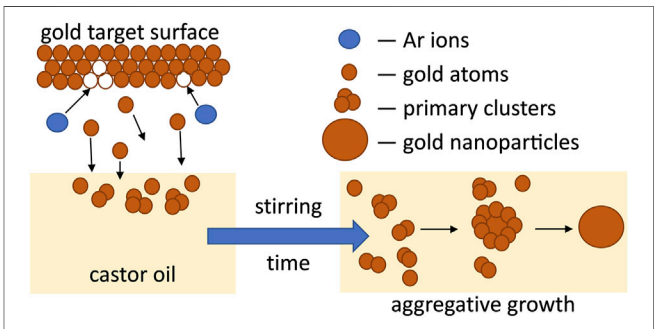

FIGURE 7 | Scheme of the formation of Au NPs after magnetron sputtering of gold target onto castor oil.

the slope of the curves (see **Supplementary Figure 12**) as it was done before in other works (Esumi et al., 2000; Harada and Inada, 2009; Mohamed et al., 2011). Such an approach describes only approximately 50% of the kinetic curves (Watzky and Finke, 2018) from **Figure 6**, i.e., the part of aggregative growth of Au NPs. As expected for an aggregation process in such a viscous medium such as castor oil (0.650 Pas (Patel et al., 2016)), k_{obs} are in the range of $(1–10)\cdot10^{-7}$ s^{-1} (see **Supplementary Table 1**) and slightly increase with gold concentration (**Supplementary Figure 13**). The values of k_{obs} estimated in less viscous aqueous solutions are usually much higher (approximately 10^{-3} s^{-1} or more (Esumi et al., 2000)) due to fast diffusion of reactive species and high concentrations of reducing reagents. However, in the case of sputtering onto the liquid procedure, there are no reducers; thus, the process rate is limited by the diffusion and coalescence between primary particles inside the vegetable oil. For a more precise analysis, a larger set of kinetic data, including the nucleation period, is needed.

CONCLUSION

1Magnetron sputtering of a gold target onto low-cost, nontoxic, vegetable castor oil allows us to obtain stable colloidal solutions of small spherical Au NPs. It was clearly shown that a brownish cloud forms underneath the oil surface during the deposition process onto still liquids. Stirring of the obtained systems leads to the formation of transparent colloidal solutions containing the primary gold clusters with diameter less than 2 nm according to their UV-vis spectra. The Au NPs grow with time due to aggregation of primary clusters and sputtered atoms; the process is limited by diffusion in the viscous oil medium. The size of the final Au NPs does not depend on sputter time, sputter power, or argon pressure, and the mean diameter stays in a range of 2.4–3.2 nm for the DC-MS mode, while deposition with HiPIMS power supply allows us to produce Au NPs with size of 5.2 ± 0.8 nm. The HiPIMS-related data set and the comparison with previously published work for which the plasma parameters were different provide insight on the influence of the heating of the host liquid during the plasma process, and the subsequent formation of larger NPs. Our results show that magnetron sputter deposition onto vegetable oils is an effective green technique to produce stable colloidal solutions of small NPs. These dispersions might be used in further (environmentally friendly plasma-based) polymerization processes for the production of composite polymers.

DATA AVAILABILITY STATEMENT

The original contributions presented in the study are included in the article/**Supplementary Material**, further inquiries can be directed to the corresponding authors.

AUTHOR CONTRIBUTIONS

AS and AO performed the synthesis of nanoparticles, its characterization by UV-vis spectroscopy and the analysis of experimental data. HA performed the characterization of the products by TEM. JW was responsible for MALDI analysis. AS, DC, and JC were responsible for the DFT calculations. SK was responsible for the work conceptualization, SIMTRA simulations and project supervision. AS wrote the original draft of the manuscript, all the authors were actively involved in the manuscript editing.

FUNDING

SK and JC are senior research associate and research director of the National Fund for Scientific Research (F.R.S.-FNRS, Belgium), respectively. SK and AS thank the FNRS for the financial support through the "SOLUTIoN" project No T.0134.19. The DFT calculations were supported by the Consortium des Équipements de Calcul Intensif (CÉCI), funded by the Fonds National de la Recherche Scientifique (F.R.S.-FNRS) under Grant No. 2.5020.11. The S^2MOs lab is grateful to the Fonds National de la Recherche Scientifique (F. R. S.-FNRS) for financial support for the acquisition of the Waters QTof Premier mass spectrometer.

ACKNOWLEDGMENTS

Authors would like to thank Dany Cornelissen for the excellent vacuum chamber maintenance.

SUPPLEMENTARY MATERIAL

The Supplementary Material for this article can be found online at: https://www.frontiersin.org/articles/10.3389/fnano.2021.710612/full#supplementary-material.

REFERENCES

Boles, M. A., Engel, M., and Talapin, D. V. (2016). Self-Assembly of Colloidal Nanocrystals: From Intricate Structures to Functional Materials. *Chem. Rev.* 116, 11220–11289. doi:10.1021/acs.chemrev.6b00196

Britun, N., Michiels, M., Godfroid, T., and Snyders, R. (2018). Ion Density Evolution in a High-Power Sputtering Discharge With Bipolar Pulsing. *Appl. Phys. Lett.* 112, 234103. doi:10.1063/1.5030697

Chauvin, A., Sergievskaya, A., El Mel, A.-A., Fucikova, A., Antunes Corrêa, C., Vesely, J., et al. (2020). Co-Sputtering of Gold and Copper onto Liquids: A Route towards the Production of Porous Gold Nanoparticles. *Nanotechnology* 31, 455303. doi:10.1088/1361-6528/abaa75

Depla, D., and Leroy, W. P. (2012). Magnetron Sputter Deposition as Visualized by Monte Carlo Modeling. *Thin Solid Films* 520, 6337–6354. doi:10.1016/j.tsf.2012.06.032

Depla, D. (2013). Magnetrons, Reactive Gases and Sputtering. Diederik Depla Available at: https://biblio.ugent.be/publication/4239033 (Accessed February 08, 2021).

Esumi, K., Hosoya, T., Suzuki, A., and Torigoe, K. (2000). Formation of Gold and Silver Nanoparticles in Aqueous Solution of Sugar-Persubstituted Poly(Amidoamine) Dendrimers. *J. Colloid Interf. Sci.* 226, 346–352. doi:10.1006/jcis.2000.6849

Finney, E. E., and Finke, R. G. (2008). Nanocluster Nucleation and Growth Kinetic and Mechanistic Studies: A Review Emphasizing Transition-Metal Nanoclusters. *J. Colloid Interf. Sci.* 317, 351–374. doi:10.1016/j.jcis.2007.05.092

Finney, E. E., Shields, S. P., Buhro, W. E., and Finke, R. G. (2012). Gold Nanocluster Agglomeration Kinetic Studies: Evidence for Parallel Bimolecular Plus Autocatalytic Agglomeration Pathways as a Mechanism-Based Alternative to an Avrami-Based Analysis. *Chem. Mater.* 24, 1718–1725. doi:10.1021/cm203186y

García-Lojo, D., Núñez-Sánchez, S., Gómez-Graña, S., Grzelczak, M., Pastoriza-Santos, I., Pérez-Juste, J., et al. (2019). Plasmonic Supercrystals. *Acc. Chem. Res.* 52, 1855–1864. doi:10.1021/acs.accounts.9b00213

Garzón-Manjón, A., Meyer, H., Grochla, D., Löffler, T., Schuhmann, W., Ludwig, A., et al. (2018). Controlling the Amorphous and Crystalline State of Multinary Alloy Nanoparticles in an Ionic Liquid. *Nanomaterials* 8, 903. doi:10.3390/nano8110903

Hamm, S. C., Basuray, S., Mukherjee, S., Sengupta, S., Mathai, J. C., Baker, G. A., et al. (2014). Ionic Conductivity Enhancement of Sputtered Gold Nanoparticle-In-Ionic Liquid Electrolytes. *J. Mater. Chem. A.* 2, 792–803. doi:10.1039/C3TA13431H

Harada, M., and Inada, Y. (2009). *In Situ* Time-Resolved XAFS Studies of Metal Particle Formation by Photoreduction in Polymer Solutions. *Langmuir* 25, 6049–6061. doi:10.1021/la900550t

Hatakeyama, Y., Onishi, K., and Nishikawa, K. (2011). Effects of Sputtering Conditions on Formation of Gold Nanoparticles in Sputter Deposition Technique. *RSC Adv.* 1, 1815–1821. doi:10.1039/c1ra00688f

Kagan, C. R., Lifshitz, E., Sargent, E. H., and Talapin, D. V. (2016). Building Devices from Colloidal Quantum Dots. *Science* 353, aac5523. doi:10.1126/science.aac5523

Kovalenko, M. V., Manna, L., Cabot, A., Hens, Z., Talapin, D. V., Kagan, C. R., et al. (2015). Prospects of Nanoscience with Nanocrystals. *ACS Nano* 9, 1012–1057. doi:10.1021/nn506223h

Lee, S. H., Jung, H. K., Kim, T. C., Kim, C. H., Shin, C. H., Yoon, T.-S., et al. (2018). Facile Method for the Synthesis of Gold Nanoparticles Using an Ion Coater. *Appl. Surf. Sci.* 434, 1001–1006. doi:10.1016/j.apsusc.2017.11.008

L. Liz-Marzán (Editors) (2020). *Colloidal Synthesis of Plasmonic Nanometals* (New York: Jenny Stanford Publishing). doi:10.1201/9780429295188

Meischein, M., Garzón-Manjón, A., Frohn, T., Meyer, H., Salomon, S., Scheu, C., et al. (2019). Combinatorial Synthesis of Binary Nanoparticles in Ionic Liquids by Cosputtering and Mixing of Elemental Nanoparticles. *ACS Comb. Sci.* 21, 743–752. doi:10.1021/acscombsci.9b00140

Mohamed, H. H., Dillert, R., and Bahnemann, D. W. (2011). Growth and Reactivity of Silver Nanoparticles on the Surface of TiO2: A Stopped-Flow Study. *J. Phys. Chem. C* 115, 12163–12172. doi:10.1021/jp2031576

Nguyen, M. T., and Yonezawa, T. (2018). Sputtering Onto a Liquid: Interesting Physical Preparation Method for Multi-Metallic Nanoparticles. *Sci. Technol. Adv. Mater.* 19, 883–898. doi:10.1080/14686996.2018.1542926

Nguyen, M. T., Wongrujipairoj, K., Tsukamoto, H., Kheawhom, S., Mei, S., Aupama, V., et al. (2020). Synergistic Effect of the Oleic Acid and Oleylamine Mixed-Liquid Matrix on Particle Size and Stability of Sputtered Metal Nanoparticles. *ACS Sustainable Chem. Eng.* 8, 18167–18176. doi:10.1021/acssuschemeng.0c06549

Orozco-Montes, V., Caillard, A., Brault, P., Chamorro-Coral, W., Bigarre, J., Sauldubois, A., et al. (2021). Synthesis of Platinum Nanoparticles by Plasma Sputtering onto Glycerol: Effect of Argon Pressure on Their Physicochemical Properties. *J. Phys. Chem. C* 125, 3169–3179. doi:10.1021/acs.jpcc.0c09746

Patel, V. R., Dumancas, G. G., Viswanath, L. C. K., Maples, R., and Subong, B. J. J. (2016). Castor Oil: Properties, Uses, and Optimization of Processing Parameters in Commercial Production. *Lipid Insights* 9, 1–12. doi:10.4137/LPI.S40233

Qadir, M. I., Kauling, A., Ebeling, G., Fartmann, M., Grehl, T., and Dupont, J. (2019). Functionalized Ionic Liquids Sputter Decorated With Pd Nanoparticles. *Aust. J. Chem.* 72, 49. doi:10.1071/CH18183

Sarakinos, K., Alami, J., and Konstantinidis, S. (2010). High Power Pulsed Magnetron Sputtering: A Review on Scientific and Engineering State of the Art. *Surf. Coat. Technol.* 204, 1661–1684. doi:10.1016/j.surfcoat.2009.11.013

Sebastian, V., Arruebo, M., and Santamaria, J. (2014). Reaction Engineering Strategies for the Production of Inorganic Nanomaterials. *Small* 10, 835–853. doi:10.1002/smll.201301641

Sergievskaya, A. P., Tatarchuk, V. V., Makotchenko, E. V., and Mironov, I. V. (2015). Formation of Gold Nanoparticles during the Reduction of HAuBr4 in Reverse Micelles of Oxyethylated Surfactant: Influence of Gold Precursor on the Growth Kinetics and Properties of the Particles. *J. Mater. Res.* 30, 1925–1933. doi:10.1557/jmr.2015.121

Sergievskaya, A., O'Reilly, A., Chauvin, A., Veselý, J., Panepinto, A., De Winter, J., et al. (2021). Magnetron Sputter Deposition of Silver onto castor Oil: The Effect of Plasma Parameters on Nanoparticle Properties. *Colloids Surf. A: Physicochem. Eng. Aspects* 615, 126286. doi:10.1016/j.colsurfa.2021.126286

Shishino, Y., Yonezawa, T., Kawai, K., and Nishihara, H. (2010). Molten Matrix Sputtering Synthesis of Water-Soluble Luminescent Au Nanoparticles with a Large Stokes Shift. *Chem. Commun.* 46, 7211. doi:10.1039/c0cc01702g

Shishino, Y., Yonezawa, T., Udagawa, S., Hase, K., and Nishihara, H. (2011). Preparation of Optical Resins Containing Dispersed Gold Nanoparticles by the Matrix Sputtering Method. *Angew. Chem.* 123, 729–731. doi:10.1002/ange.201005723

Slepička, P., Elashnikov, R., Ulbrich, P., Staszek, M., Kolská, Z., and Švorčík, V. (2015). Stabilization of Sputtered Gold and Silver Nanoparticles in PEG Colloid Solutions. *J. Nanopart. Res.* 17. doi:10.1007/s11051-014-2850-z

Sugioka, D., Kameyama, T., Kuwabata, S., and Torimoto, T. (2015). Single-step Preparation of Two-Dimensionally Organized Gold Particles via Ionic Liquid/Metal Sputter Deposition. *Phys. Chem. Chem. Phys.* 17, 13150–13159. doi:10.1039/c5cp01602a

Sumi, T., Motono, S., Ishida, Y., Shirahata, N., and Yonezawa, T. (2015). Formation and Optical Properties of Fluorescent Gold Nanoparticles Obtained by Matrix Sputtering Method with Volatile Mercaptan Molecules in the Vacuum Chamber and Consideration of Their Structures. *Langmuir* 31, 4323–4329. doi:10.1021/acs.langmuir.5b00294

Suzuki, T., Okazaki, K.-i., Kiyama, T., Kuwabata, S., and Torimoto, T. (2009). A Facile Synthesis of AuAg Alloy Nanoparticles Using a Chemical Reaction Induced by Sputter Deposition of Metal onto Ionic Liquids. *Electrochemistry* 77, 636–638. doi:10.5796/electrochemistry.77.636

Talapin, D. V., Lee, J.-S., Kovalenko, M. V., and Shevchenko, E. V. (2010). Prospects of Colloidal Nanocrystals for Electronic and Optoelectronic Applications. *Chem. Rev.* 110, 389–458. doi:10.1021/cr900137k

Thanh, N. T. K., Maclean, N., and Mahiddine, S. (2014). Mechanisms of Nucleation and Growth of Nanoparticles in Solution. *Chem. Rev.* 114, 7610–7630. doi:10.1021/cr400544s

Torimoto, T., Okazaki, K.-i., Kiyama, T., Hirahara, K., Tanaka, N., and Kuwabata, S. (2006). Sputter Deposition onto Ionic Liquids: Simple and Clean Synthesis of Highly Dispersed Ultrafine Metal Nanoparticles. *Appl. Phys. Lett.* 89, 243117. doi:10.1063/1.2404975

Torimoto, T., Kameyama, T., and Kuwabata, S. (2016). "Top-Down Synthesis Methods for Nanoscale Catalysts," in *Nanocatalysis In Ionic Liquids*. Weinheim, Germany: Wiley-VCH Verlag GmbH & Co. KGaA, 171–205. doi:10.1002/9783527693283.ch9

Tsuda, T., Yoshii, K., Torimoto, T., and Kuwabata, S. (2010). Oxygen Reduction Catalytic Ability of Platinum Nanoparticles Prepared by Room-Temperature Ionic Liquid-Sputtering Method. *J. Power Sourc.* 195, 5980–5985. doi:10.1016/j.jpowsour.2009.11.027

Van Aeken, K., Mahieu, S., and Depla, D. (2008). The Metal Flux from a Rotating Cylindrical Magnetron: A Monte Carlo Simulation. *J. Phys. D: Appl. Phys.* 41, 205307. doi:10.1088/0022-3727/41/20/205307

Vanecht, E., Binnemans, K., Seo, J. W., Stappers, L., and Fransaer, J. (2011). Growth of Sputter-Deposited Gold Nanoparticles in Ionic Liquids. *Phys. Chem. Chem. Phys.* 13, 13565–13571. doi:10.1039/c1cp20552h

Vanecht, E., Binnemans, K., Patskovsky, S., Meunier, M., Seo, J. W., Stappers, L., et al. (2012). Stability of Sputter-Deposited Gold Nanoparticles in Imidazolium Ionic Liquids. *Phys. Chem. Chem. Phys.* 14, 5662. doi:10.1039/c2cp23677j

Wagener, M., Murty, B. S., and Günther, B. (1996). Preparation of Metal Nanosuspensions by High-Pressure DC-Sputtering on Running Liquids. *MRS Proc.* 457, 149. doi:10.1557/PROC-457-149

Wang, F., Richards, V. N., Shields, S. P., and Buhro, W. E. (2014). Kinetics and Mechanisms of Aggregative Nanocrystal Growth. *Chem. Mater.* 26, 5–21. doi:10.1021/cm402139r

Watzky, M. A., and Finke, R. G. (1997). Transition Metal Nanocluster Formation Kinetic and Mechanistic Studies. A New Mechanism When Hydrogen is the Reductant: Slow, Continuous Nucleation and Fast Autocatalytic

Surface Growth. *J. Am. Chem. Soc.* 119, 10382–10400. doi:10.1021/ja9705102

Watzky, M. A., and Finke, R. G. (2018). Gold Nanoparticle Formation Kinetics and Mechanism: A Critical Analysis of the "Redox Crystallization" Mechanism. *ACS Omega* 3, 1555–1563. doi:10.1021/acsomega.7b01772

Wender, H., De Oliveira, L. F., Feil, A. F., Lissner, E., Migowski, P., Meneghetti, M. R., et al. (2010). Synthesis of Gold Nanoparticles in a Biocompatible Fluid from Sputtering Deposition Onto Castor Oil. *Chem. Commun.* 46, 7019–7021. doi:10.1039/c0cc01353f

Wender, H., Gonçalves, R. V., Feil, A. F., Migowski, P., Poletto, F. S., Pohlmann, A. R., et al. (2011). Sputtering onto Liquids: From Thin Films to Nanoparticles. *J. Phys. Chem. C* 115, 16362–16367. doi:10.1021/jp205390d

Wender, H., Migowski, P., Feil, A. F., Teixeira, S. R., and Dupont, J. (2013). Sputtering Deposition of Nanoparticles onto Liquid Substrates: Recent Advances and Future Trends. *Coord. Chem. Rev.* 257, 2468–2483. doi:10.1016/j.ccr.2013.01.013

Conflict of Interest: The authors declare that the research was conducted in the absence of any commercial or financial relationships that could be construed as a potential conflict of interest.

Publisher's Note: All claims expressed in this article are solely those of the authors and do not necessarily represent those of their affiliated organizations, or those of the publisher, the editors and the reviewers. Any product that may be evaluated in this article, or claim that may be made by its manufacturer, is not guaranteed or endorsed by the publisher.

frontiers | Frontiers in Nanotechnology

TYPE Review
PUBLISHED 31 August 2022
DOI 10.3389/fnano.2022.987034

OPEN ACCESS

EDITED BY
Sima Umrao,
Indian Institute of Science (IISc), India

REVIEWED BY
Shahnaz Majid Qadri,
Texas A&M University, United States
Abhishesh Kumar Mehata,
Indian Institute of Technology (BHU), India

*CORRESPONDENCE
L. Dini,
luciana.dini@uniroma1.it

†These authors share first authorship

SPECIALTY SECTION
This article was submitted to Biomedical Nanotechnology, a section of the journal Frontiers in Nanotechnology

RECEIVED 05 July 2022
ACCEPTED 11 August 2022
PUBLISHED 31 August 2022

CITATION
Sbarigia C, Vardanyan D, Buccini L, Tacconi S and Dini L (2022), SARS-CoV-2 and extracellular vesicles: An intricate interplay in pathogenesis, diagnosis and treatment.
Front. Nanotechnol. 4:987034.
doi: 10.3389/fnano.2022.987034

SARS-CoV-2 and extracellular vesicles: An intricate interplay in pathogenesis, diagnosis and treatment

C. Sbarigia[1†], D. Vardanyan[2†], L. Buccini[1], S. Tacconi[1] and L. Dini[1,3,4*]

[1]Department of Biology and Biotechnology "C. Darwin", University of Rome Sapienza, Rome, Italy, [2]Department of Biological and Environmental Sciences and Technologies (Di. S. Te. B. A.), University of Salento, Lecce, Italy, [3]Research Center for Nanotechnology for Engineering of Sapienza (CNIS), University of Rome Sapienza, Rome, Italy, [4]CNR Nanotec, Lecce, Italy

Extracellular vesicles (EVs) are widely recognized as intercellular communication mediators. Among the different biological processes, EVs play a role in viral infections, supporting virus entrance and spread into host cells and immune response evasion. Severe acute respiratory syndrome coronavirus 2 (SARS-CoV-2) infection became an urgent public health issue with significant morbidity and mortality worldwide, being responsible for the current COVID-19 pandemic. Since EVs are implicated in SARS-CoV-2 infection in a morphological and functional level, they have gained growing interest for a better understanding of SARS-CoV-2 pathogenesis and represent possible diagnostic tools to track the disease progression. Furthermore, thanks to their biocompatibility and efficient immune activation, the use of EVs may also represent a promising strategy for the development of new therapeutic strategies against COVID-19. In this review, we explore the role of EVs in viral infections with a focus on SARS-CoV-2 biology and pathogenesis, considering recent morphometric studies. The common biogenesis aspects and structural similarities between EVs and SARS-CoV-2 will be examined, offering a panoramic of their multifaceted interplay and presenting EVs as a machinery supporting the viral cycle. On the other hand, EVs may be exploited as early diagnostic biomarkers and efficient carriers for drug delivery and vaccination, and ongoing studies will be reviewed to highlight EVs as potential alternative therapeutic strategies against SARS-CoV-2 infection.

KEYWORDS

extracellular vesicles, SARS–CoV–2, COVID-19, EVs-based vaccines, COVID-19 vaccination, drug delivery

Introduction

Severe acute respiratory syndrome coronavirus 2 (SARS-CoV-2) is a novel strain of coronavirus emerged first in China in 2019 and etiological agent of the current coronavirus disease 2019 (COVID-19) outbreak (Kulkarni et al., 2022). Due to its ease of spread, SARS-CoV-2 represents a serious threat to global health, also having a strong socio-economic impact. To date, on 27 June 2022, there have been 540,923,532 confirmed cases of COVID-19, including 6,325,785 deaths, reported to WHO (https://covid19.who.int). The vaccination campaign helped to counteract severe clinical outcomes, but the ability of SARS-CoV-2 to mutate and evade immune responses still implies the need to find new intervention strategies, requiring in turn a deeper understanding of SARS-CoV-2 biology (Boni et al., 2020). Several morphometric studies are ongoing to elucidate SARS-CoV-2 infection mechanisms, especially egress events and cell-to-cell spreading that are still poorly characterized (Klein et al., 2020; Eymieux et al., 2021b; Kumar et al., 2021; Laue et al., 2021; Mendonça et al., 2021). According to these, extracellular vesicles (EVs) trafficking seems to be a deeply involved pathway in SARS-CoV-2 infection, contributing to viral replication, immune evasion, egression from infected cells, and spread to other cell targets, through the so-called "replicative organelles" (Pleet et al., 2018; Bello-Morales et al., 2020). Several hypotheses further support a role of EVs in SARS-CoV-2 infection, like the existence of "quasi-enveloped viruses" (Feng et al., 2014), the "Trojan exosome" hypothesis (Hildreth, 2017), and the "secretory autophagy" model (Bunz et al., 2022), but none of these has been confirmed as the prevalent and further investigations are needed. EVs are well known as membrane-enveloped, nano- and micro-sized particles secreted by different cell types, distinct in their size, composition and function according to their biogenesis, delivering different cargoes to distant targets and thus affecting intercellular signaling (Kalluri and LeBleu, 2020). Thanks to their intrinsic properties, EVs display an important role in a physiological level, as well as in several pathological conditions, being mediators of host-pathogen interactions. Depending on their cargo, EVs may also functionally support or counteract viral infection. Next to supplying a replication machinery, EVs may also transport and present antigens, modulating the host immune responses against the virus (Babaei et al., 2022). The intricate morpho-functional interplay between SARS-CoV-2 and EVs gained particular interest among the scientific community and defining EVs dynamics and cargo may be pivotal to get not only a better comprehension of the viral cycle, but also to take advantage of it, to find new clues for biomarker tracing, disease treatment, and vaccine development. To date, EVs have been exploited to deliver immunomodulatory cargoes, acting prevalently on the cytokine storm occurring in COVID-19, in combination with antiviral drugs (Romagnoli et al., 2015; Somiya et al., 2017). Some clinical trials are currently underway to test the efficacy and safety of EVs formulations, but the results are still fragmentary and incomplete (Karn et al., 2021). Despite the use of EVs for therapeutic purposes seems promising, further investigations are needed to find effective strategies with minimal side effects. In this paper, multiple aspects of the SARS-CoV-2 and EVs network are reviewed, from the role of EVs in SARS-CoV-2 viral cycle and COVID-19 pathogenesis, to their potential as diagnostic biomarkers and tools for treatment, drug delivery and vaccine design.

Extracellular vesicles and viral infections

Biogenesis, classification, and function of extracellular vesicles

Historically, EVs have been considered as cellular "junk bags", assigned to remove unwanted material. To date, EVs have great importance in different biological systems as carriers of biomolecules, such as proteins, lipids, and nucleic acids, playing a crucial role in cell-to-cell communication. Furthermore, EVs have been used as therapeutic drug carriers and as diagnostic tools for several diseases (Dini et al., 2020). EVs are small membrane-enclosed nano- and micro-structures released by different cells and can be found in several human biofluids (i.e., blood, urine, cerebrospinal fluid, saliva, breast milk, bronchoalveolar lavage fluid) (Doyle and Wang, 2019). Due to their heterogeneity, EVs are difficult to categorize. However, according to their biogenesis pathways, EVs are generally distinguished in three main subtypes: exosomes (small EVs, 30–100 nm in size), microvesicles (large EVs, 100–1,000 nm in size), and apoptotic bodies (bigger than 1,000 nm) (Rai et al., 2021). Exosomes, also referred as small EVs, are derived from multivesicular bodies (MVBs) (Yue et al., 2020) and formed by the inward budding of the late endosomal membrane, which encapsulates biomolecules and generates intraluminal vesicles (ILVs) within the MVBs. Then, MVBs fuse with the plasma membrane and release ILVs into the extracellular space in the form of exosomes via exocytosis (Vella et al., 2008). Several peripheral membrane protein complexes, necessary for the formation of ILVs in MVBs and the budding of microvesicles from the plasma membrane, are known as "endosomal sorting complexes required for transport". In the ESCRT system, there are four complexes known as ESCRT-0, ESCRT-I, ESCRT-II, and ESCRT-III with associated proteins (Tsg101, ALIX, and VPS4) and, during biogenesis, each complex has its own role. To initiate the pathway, ESCRT-0 forms a protein network on endosomal membranes that captures ubiquitinated cargo proteins and allows their sorting based on the MVBs pathway (Raiborg et al., 2001; Mayers et al., 2011). ESCRT-I binds to ubiquitinated cargo proteins on the endosomes

and activates ESCRT-II, which plays a direct role in cargo sorting at multivesicular endosomes (MVEs). In turn, ESCRT III, with the charged multivesicular body proteins, performs membrane remodeling, including fission, protein dissociation and recycling of the endosomal sorting machinery, which depends on the participation of the Vps4 AAA-ATPase (Obita et al., 2007). Besides these processes, ESCRT-III and its accessory proteins, like Vps4, Vta1, Vsp60 and ALIX, are also involved in virus budding, cytokinesis and nuclear envelope remodeling (Hurley, 2015). Another pathway for exosome biogenesis involves the syndecan/syntenin complex, which requires the activity of phospholipase D 2 (PLD2) and ADP-ribosylation factor 6 (Arf6) (Tricarico et al., 2016). Despite the central role of the ESCRT-dependent pathway for EVs formation, the SMase2/ceramide pathway, independent from the canonical ESCRT pathway, has been also characterized (Kosaka et al., 2010). For EVs transport and release, distinct effectors are implicated, such as RAB GTPases (Rocha et al., 2009). RAB GTPases regulate trafficking in both the endocytic and secretory pathways, by recruiting specific effector proteins onto membrane surfaces to either facilitate cargo collection, organelle movement, or vesicle docking. There is growing evidence linking RAB GTPases to the secretion of exosomes, mainly RAB5 and RAB7 (Hutagalung & Novick, 2011). Further studies have also demonstrated that RAB27A and RAB27B participate in MVEs transport, while RAB11 and RAB35 proteins regulate MVEs fusion with the plasma membrane and secretion directly or indirectly (van Niel et al., 2018). Furthermore, RAB22A has been found to colocalize with budding microvesicles, participating in cargo sorting in hypoxic breast cancer cells (Wang et al., 2014).

Microvesicles (MVs), also referred as large EVs, are instead formed by the direct plasma membrane budding and fission. Several proteins are involved in MVs biogenesis, such as Ca^{2+} dependent aminophospholipid translocases, scramblases, and calpains, driving the rearrangement of membrane phospholipids and the reconstitution of the actin cytoskeleton, and finally determining the plasma membrane curvature and MVs release in the extracellular space (Lynch and Ludlam, 2007). Despite the apparent distinct biogenesis modality, exosomes and microvesicles may share common sorting machinery and intracellular mechanisms, often displaying an overlapping size and similar composition that hamper discriminating different subpopulations. Indeed, there is still a need to uncover the exact dynamics of EVs biogenesis (van Niel et al., 2018). Here, we adhere to the nomenclature guidelines published by the International Society of Extracellular Vesicles (ISEV), that suggests the use of the general term “EVs”, as there is still no definitive distinctive marker of each EVs subpopulation (Théry et al., 2018; Witwer et al., 2021).

Apoptotic bodies, or apoptosomes, are formed only during apoptosis, characterized by the condensation of nuclear chromatin and involving nuclear chromatin condensation followed by membrane blebbing (Kerr et al., 1972). As well as ESCRT proteins, tetraspanins (CD81, CD82, CD63, CD9), and proteins responsible for cargo transport and membrane fusion (annexins, RABs), EVs may be enriched in proteins involved in many processes including cell adhesion (integrins), antigen presentation (MHC-I, MHC-II), stress regulation (HSP70, HSP90), cell migration (actin, myosin, tubulin) and metabolic enzymes (Lakkaraju and Rodriguez-Boulan, 2008; Colombo et al., 2014). EVs may also contain several types of nucleic acids, such as messenger RNAs (mRNAs), micro-RNAs (miRNAs), transfer RNAs (tRNA) and long non-coding RNAs (lncRNAs) (Valadi et al., 2007; Gusachenko et al., 2013). The ability of EVs to carry cargo, budding, shedding, and being reacquired by neighboring cells, may contribute to the spread of infections, progression of diseases, as well as the modulation of immune-related processes. In particular, the role of EVs in the pathogenesis of infectious diseases suggests that EVs may serve as potential biomarkers to track mild bacterial infection and chronic viral diseases, with the possibility of harnessing EVs to prevent infection or spread (Jones et al., 2018; Pérez et al., 2019).

EVs and viral infections: A multifaceted interplay

Viruses are intracellular pathogens exploiting the cellular compartments to carry out their life cycle. Given the role of EVs in intercellular communication and in pathological disorders, the interplay between viruses and EVs gained a lot of attention, especially for their similarities in structure and biogenesis (Bello-Morales et al., 2020). Indeed, EVs display a multifaceted role in viral infections, contributing in first place to viral replication, dissemination, and immune evasion modulating the host immune system activation. Furthermore, EVs may block (Ipinmoroti and Matthews, 2020) or otherwise trigger the antiviral response, exacerbating the damage and causing several detrimental effects, such as oncogenesis (Zheng et al., 2019), inflammation (Sadri Nahand et al., 2020) or autoimmune responses (Gunasekaran et al., 2020). Several viruses exploit intracellular membrane rearrangements, creating peculiar double-membrane structures known as “replicative organelles”, to complete their replication facilitating new virions formation and budding from the host cell (Wolff et al., 2020). Viral infection seems to have influence on lipid metabolism and processing, driving the formation of protective structures representing the main strategy for a successful viral cycle (Müller et al., 2018). Lipid rafts and myelin and lymphocyte protein (MAL), an integral membrane protein found in cholesterol and glycolipids-enriched membrane, are believed to be implicated in virion uptake, constituting platforms for viral particle assembly (Kulkarni et al., 2022). Besides the formation of replication organelles, viruses must exit the infected cell and disseminate, evading at the same time the host immune system, to ensure their biological success. To

accomplish this, both enveloped and non-enveloped viruses exploit EVs as a strategy to maximize their tropism without being recognized by the host immune cells (Schorey et al., 2015). Indeed, EVs may mediate and enhance viral propagation creating the so-called "collective infectious units", consisting in multiple virions within a single vesicle or multiple viral genomes in a single virion. Through this dispersal strategy, viruses increase their multiplicity of infection (MOI) (Leeks et al., 2019; Andreu-Moreno and Sanjuán, 2020). Whether these vesicles are EVs containing viral molecules or defective viral particles is still under debate but, since EVs and viruses share similar size, density, and composition, it is difficult to isolate and analyze distinct fractions and improved strategies of isolation are needed (van der Grein et al., 2018). An overlap between viral particles release and EVs biogenesis pathway is represented by the "quasi-enveloped" viruses, non-enveloped viruses generally promoting cell lysis for their release and not surrounded by host membrane, which have been found to be enclosed inside vesicles during their propagation. In this phenomenon, viruses take advantage of the host ESCRT machinery to acquire a protective membrane and exit the infected cell without lysis, avoiding then the recognition by the host immune system (Feng et al., 2014). This behavior, first reported in hepatitis A virus (HAV) (Feng et al., 2013; Jiang et al., 2020), was found also in hepatitis E virus (HEV) (Nagashima et al., 2014), Coxsackie B virus (CBV) (Sin et al., 2017), but also in enveloped viruses, like hepatitis C virus (HCV) (Bunz et al., 2022) and others. Furthermore, the "Trojan exosome" hypothesis states that retroviruses, like human immunodeficiency virus (HIV), use EVs biogenesis pathways for their egression, spread and uptake, enhancing their infectivity and modulating host gene expression and immune responses (Hildreth, 2017; Chen et al., 2021). Another model proposes the "secretory autophagy" for virus non-cytolytic egression from the infected cell through LC3-positive vesicles, originating from autophagosomes fusing with the plasma membrane instead of lysosomes (Altan-Bonnet, 2016; Bunz et al., 2022). According to this model, first described by Chen YH et al., multiple viral particles are selectively captured by LC3-positive "autophagosome-like" organelles, enriched in phosphatidylserine lipids, and released non-cytolitically from the infected cells (Chen et al., 2015). Indeed, several pathogens are able to perturbate the autophagic pathway by different mechanisms (Pleet et al., 2018; Zhao et al., 2021). Great evidence suggests that viral infection massively alters EVs composition causing multiple effects depending on the virus-host landscape, for instance supporting viral replication, transmission, and stability by transferring viral RNAs and proteins and by modulating interactions between membranes and receptors, making other cells more susceptible to infection (Bello-Morales and López-Guerrero, 2020; Dubrovsky et al., 2020; Hassanpour et al., 2020). However, EVs trafficking exploited by viruses may also imply differential immune responses helping the host to fight the infection, activating other cell targets (Velandia-Romero et al., 2020), inducing the production of pro-inflammatory molecules (Maemura et al., 2018) and promoting antiviral response (Yao et al., 2018). In conclusion, EVs can exacerbate or counteract viral infection, and sometimes both effects may be caused by the same virus. Since viruses and EVs are closely related in terms of biogenesis, dynamics and mechanisms of action, a deeper understanding of their interplay would be of great importance for translation in therapeutic approaches (Hoen et al., 2016).

SARS-CoV-2 and extracellular vesicles

SARS-CoV-2 biology and viral cycle

Severe acute respiratory syndrome coronavirus 2 (SARS-CoV-2) is an enveloped, positive-sense single-stranded RNA virus (family Coronaviridae, genus *betacoronavirus*) and causative agent of the running pandemic of coronavirus disease 19 (COVID-19) (V'kovski et al., 2021). Affecting mammals and birds and able to cross between the species, coronaviruses are generally associated with respiratory diseases, from the common cold to severe respiratory pathologies, such as Middle East respiratory syndrome (MERS), severe acute respiratory syndrome (SARS), and COVID-19. It is likely that SARS-CoV-2 has emerged during SARS-CoV evolution, by frequent recombination events occurred between severe acute respiratory syndrome-related coronaviruses coexisting in bats, being then transmitted to humans by an unknown intermediate host (Boni et al., 2020). Like SARS-CoV, SARS-CoV-2 is generally transmitted through respiratory droplets, but also by direct contact with contaminated surfaces and by oro-fecal transmission (Chan et al., 2020; Li et al., 2020). SARS-CoV-2 primarily affects the respiratory tract, causing fever, fatigue, and dry cough as common symptoms. However, SARS-CoV-2 may disseminate into other organs, leading to systemic infection and finally resulting in multiorgan failure (Cao, 2020). For a successful viral cycle, including virus entry, replication, egress and diffusion, SARS-CoV-2 relies on its own structure and on molecular interaction with host factors (Knoops et al., 2010; V'kovski et al., 2019). SARS-CoV-2 virions are composed by structural proteins, namely spike (S), envelope (E), membrane (M), and nucleocapsid (N), ensuring the incorporation of the positive-sense, single-stranded RNA genome (+ssRNA) and thus the viral particle assembly. The SARS-CoV-2 entrance into the host cell requires a specific binding of the S protein to the angiotensin-converting enzyme 2 (ACE2), shared also by SARS-CoV, influencing its tropism and pathogenicity (Lu et al., 2020). The S protein and ACE2 binding affinity determines the severity of infection, and ACE2 is expressed in lungs, gut, kidney, heart, and adipose tissues (Adli et al., 2022).

ACE2 receptor is also expressed by platelets, which have been demonstrated to be hyperactivated in COVID-19 patients, being the main cause of the prothrombotic state occurring in SARS-CoV-2 infection (Zhang et al., 2020). Coronavirus S proteins are homotrimeric class I fusion glycoproteins, divided into two functionally distinct domains. The S1 domain, exposed to the surface, constitutes the receptor-binding domain, allowing the specific interaction with the host cell receptor, while the transmembrane S2 domain includes the fusion peptide, enabling the fusion between the viral and cell membranes by conformational rearrangements (Letko et al., 2020). Next to receptor binding, SARS-CoV-2 exploits cell-derived proteases, such as the cell-surface serine protease TMPRSS2, expressed in the human respiratory tract and mediating the S protein proteolytic cleavage, essential to permit the viral-host membrane fusion (Gierer et al., 2013; Hoffmann et al., 2020). The viral genome release into the host cell gives rise to the onset of a finely space and time-regulated gene expression program, which includes several non-structural proteins, involved in the formation of the viral replication and transcription complex, RNA synthesis, proofreading and modification, host cell factors interactions, intracellular membrane remodeling and host immune evasion (Snijder et al., 2016; Thoms et al., 2020). More importantly, non-structural proteins participate in the biogenesis of peculiar viral replication organelles, located at the perinuclear level and creating a protective microenvironment for genomic viral RNA replication, namely double-membrane vesicles (DMVs), convoluted membranes (CMs) and small open double membrane spherules (DMSs) (Knoops et al., 2008; Snijder et al., 2020). Conserved between coronaviruses, these characteristic structures are highly dynamic and, besides constituting a protective barrier to evade the cell cytosolic innate immune sensors, they contribute to the formation of new viral particles at the endoplasmic reticulum (ER)-to-Golgi intermediate compartment (ERGIC) and guide virus egression from the cell, supporting a role of the exocytic pathway in virus spread (Ghosh et al., 2020; Klein et al., 2020). Considering these observations, and since the cellular pathways involved in SARS-CoV-2 progression are still under investigation, vesicular trafficking gained a lot of attention as a mechanism implicated in COVID-19 pathogenesis. In the next paragraphs, the role of EVs in COVID-19 progression, treatment, and diagnosis will be reviewed.

Extracellular vesicles and COVID-19: The role in SARS-CoV-2 pathogenesis

As previously discussed in *Introduction* Section, EVs are nano- and micro-sized particles present in all body fluids and produced by all cell types, containing several biomolecules (such as proteins, lipids and nucleic acids) which are delivered to other cell targets, reprogramming their function and morphology and thus serving as modulators of intercellular communication (Van Niel et al., 2018; Kalluri and LeBleu, 2020). Given their vectorial properties, EVs are implicated in several pathological conditions (Robbins and Morelli, 2014; Dini et al., 2020; Xiao et al., 2021; Bao et al., 2022), including viral infections (Hassanpour et al., 2020). EVs and viruses share similarities in terms of size, structure, and biochemical composition, using similar biogenesis and membrane fusion pathways (Urciuoli and Peruzzi, 2020). As stated for several other viruses, vesicular structures seem to be first implicated in SARS-CoV-2 infection in a morphological level, participating in virus assembly, egression from infected cells, and dissemination to other cell targets. Similar mechanisms of replication, virion assembly and egression have been found to be shared between SARS-CoV and SARS-CoV-2, since both the coronaviruses may exploit the ERGIC or the Golgi apparatus, to exit from the cell probably through the exocytic pathway (Figure 1) (Knoops et al., 2010; Snijder et al., 2020; Saraste and Prydz, 2021). A recent study suggested that coronaviruses may use lysosomes rather than the secretory pathway, and this hypothesis is further supported by the fact that viral particles have been observed inside lysosomal compartments by Transmission Electron Microscopy (TEM) (Ghosh et al., 2020). However, the exact fusion mechanism between these organelles and the plasma membrane that would allow the virus release in the extracellular space remains unclear. Morphometric and ultrastructure analyses, although still in infancy, have been performed to fill the gap in the knowledge of the SARS-CoV-2 dynamics in its replicative cycle, especially regarding egress events (Klein et al., 2020; Eymieux et al., 2021b; Kumar et al., 2021; Laue et al., 2021; Mendonça et al., 2021). The presence of "exit tunnels", creating a link between viral particles-rich intracellular structures and the extracellular environment, has been proposed (Mendonça et al., 2021). On the other hand, another group highlighted the presence of morphologically distinct regions within infected cells from which SARS-CoV-2 could egress, including areas with a large cytoplasm invagination and plasma membrane microvilli, plasma membrane portions without prominent rearrangements, and intermediate situations. These regions were characterized by large or small intracellular vesicles, containing several viral particles or a single viral particle, respectively. According to this work, the prevalent egression route exploited by SARS-CoV-2 particles should be through small secretory vesicles crossing invaginated, microvilli-rich regions (Eymieux et al., 2021a; 2021b). Still, further investigations are needed in order to clarify the mechanism driving the exit of such viral particles-containing vesicles into the extracellular space. Vesicular pathways are involved in SARS-CoV-2 infection not only supporting morphologically the viral life cycle, but also in a functional way. It is well known that EVs are involved in several biological processes, maintaining tissue homeostasis, participating in disease progression, and mediating interactions between host and pathogens, including viral

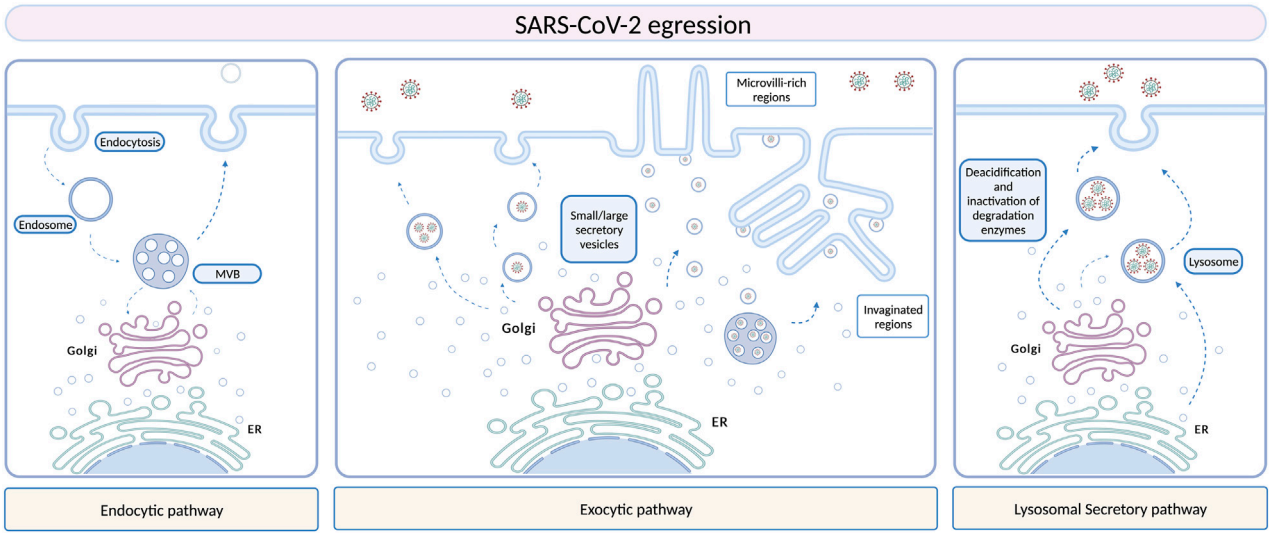

FIGURE 1
Different hypotheses have been stated and are still under investigation to define SARS-CoV-2 egression routes. Several morphological studies support a role of EVs in SARS-CoV-2 egression, especially the exocytic pathway, which involves membrane remodeling and formation of peculiar structures, as microvilli-rich or invaginated regions. Another hypothesis is the lysosomal pathway, but the fusion of these organelles with the plasma membrane is still unknown. Created with BioRender.com.

infections (Babaei et al., 2022). Viruses may exploit EVs for their entrance, packaging, spreading, and evading immune system responses. As well as for other viral infections, in which EVs play a role in promoting or counteracting viral spread depending on the virus-host landscape, EVs may act positively or negatively towards SARS-CoV-2 infection, according to their cargo. Virus-infected cells display an increase in EVs production, transferring viral nucleic acids, proteins, or entire virions, as well as viral entry receptors, to healthy cells, contributing not only to virus dissemination, but also to modulate target cell immune responses and susceptibility to infection. CD9 tetraspanin and ACE2 receptor are two examples of EVs-included elements contributing to SARS-CoV-2 infection, as CD9 tetraspanin, naturally enriched in EVs membranes, may be implicated in coronavirus fusion events, while the ACE2 receptor can be sorted in the EVs and transferred to target receptor-null cells, making them more permissive to viral infection (van Dongen et al., 2016; Wang et al., 2020). Furthermore, EVs from infected cells can also activate inflammatory responses and induce apoptosis and cytotoxicity, contributing to tissue damage (Urbanelli et al., 2019). On the other hand, the ability of EVs in transporting viral and self-antigens may represent a double-edged sword, allowing the host immune system to recognize the virus and modulate immune responses against the virus itself (Hassanpour et al., 2020). A few studies found an increased circulation of EVs containing lung-associated self-antigens, viral antigens, and 20S proteasome during coronavirus infection, further supporting the hypothesis of a potential implication of EVs also in SARS-CoV-2 dissemination, still under investigation as well as the intracellular vesicular structures supporting viral replication (Gunasekaran et al., 2020; Goodlet et al., 2021). Since EVs derived from infected cells display a distinct molecular signature than healthy cells, characterizing their cargo, as well as their dynamics, may result pivotal for a better understanding of COVID-19 pathogenesis, to add new clues to diagnostic and therapeutic strategies.

Extracellular vesicles and COVID-19: Finding early diagnostic biomarkers of the disease

As previously introduced, SARS-CoV-2 infection may lead to a differential clinical picture, from mild symptoms, as fever and cough, to severe, systemic disorders, as acute respiratory distress syndrome (ARDS), septic shock, coagulation disorders and multiorgan failure (Guan et al., 2020). Generally, the host responses to infection are driven by several factors, including disease progression and patients' genetic factors (Adli et al., 2022). Due to the heterogeneity of COVID-19 patients' responses, it is hard to detect individuals predisposed to a severe disease. However, the early identification of patients that will face up to serious outcomes results of great matter to improve therapeutic approaches for a reduced mortality (Fujita et al., 2021). In this context, multi-omic approaches are representing the first line strategy to evaluate EVs molecular

profiles (Lam et al., 2021). SARS-CoV-2 infection seems to influence EVs cargo, playing a role in inflammation, virus spreading and immunomodulation, and thus displaying a potential relationship with disease severity (Song et al., 2020; Barberis et al., 2021). Different types of extracellular RNAs (exRNAs), including mRNAs, miRNAs, tRNAs, lncRNAs and small nuclear RNAs (snRNAs), have been found to be released during antiviral responses, being incorporated into exosomes or lipoproteic complexes and protected from degradation once in circulation, and thus having effects in mediating host-virus interactions and modulating the host immune responses (Tenoever, 2013). Based on this evidence, a recent study analyzed EVs proteins and exRNAs profiles from a cohort of COVID-19 patients to find correlations between molecular profiles and disease trajectory, using a proteomic approach. Three distinct groups of components (liver damage-related exRNAs, antiviral response-related EVs proteins, and coagulation-related markers) have been revealed as potential early biomarkers for COVID-19, indicating that EVs proteins and exRNAs profiles in patients' sera may reflect specific host reactions to the infection, as well as disease progression (Fujita et al., 2021). Characterizing the patients' responses exploiting EVs molecular profile to find biomarkers of disease progression may result of great importance to find therapeutic targets to mitigate SARS-CoV-2 infection effects. To date, no currently available EVs-associated biomarker has been detected for SARS-CoV-2, and, since studies in the diagnostic field are still in infancy, further studies are required.

Extracellular vesicles for COVID-19 treatment

Extracellular vesicles as a potential therapeutic tool for COVID-19

To date, SARS-CoV-2 infection has no specific antiviral treatment, but several clinical trials are ongoing to find new therapeutic approaches and vaccines exploiting the knowledge of the viral life cycle. The ability of EVs to communicate between cells and organs, protecting bioactive cargoes, being biocompatible, having small sizes and negatively charged surfaces, and crossing biological membranes including the blood-brain barrier (BBB), targeting at the same time specific cells, makes EVs promising therapeutic agents for COVID-19 (Nguyen et al., 2020). Small EVs, also referred as exosomes, have been proposed as a therapeutic option for SARS-CoV-2, being divided into three subtypes: natural exosomes, engineered small exosomes containing ACE2 receptor, and engineered exosomes containing antiviral drugs (Popowski et al., 2021). Recent advances in stem cell therapy are bringing out promising treatment approaches, mitigating inflammation and regenerating lung damage caused by the "cytokine storm syndrome" occurring during COVID-19 infection. Mesenchymal stem cells (MSCs) are widely used in regenerative medicine thanks to their ability to differentiate into several cell types, such as bone, nerve, skin, and muscle cells. MSCs, next to their ability to transdifferentiate into tissue cells, can also produce chemokines, cytokines, growth factors, and EVs (Satija et al., 2009; Zhao et al., 2019; Nikfarjam et al., 2020). In SARS-CoV-2 patients, MSCs present three distinct mechanisms of action, including immune response modulation, homeostasis maintenance and regeneration during lung-specific injuries, and inhibition of inflammation through EVs-mediated release of anti-inflammatory cytokines (Figure 2) (Morrison et al., 2017; Xu et al., 2019). SARS-CoV-2 infection is characterized by the so-called "cytokine storm syndrome", a massive release of pro-inflammatory cytokines and chemokines. For this reason, the main objective of SARS-CoV-2 treatment is to suppress the immune response induced by the virus, reducing the damage to both alveolar and capillary epithelial cells and allowing the recovery of lung tissue and function. Studies have demonstrated that, in experimental models of acute lung injury and sepsis, MSCs-derived EVs can modulate immune responses by increasing the secretion of anti-inflammatory cytokines (IL-4, IL-10 and TGF-β) and reducing pro-inflammatory factors (TNF-α, IFN-γ, IL-6, IL-17, and IL-1β), being effective against SARS-CoV-2 infection (Devaney et al., 2015; Monsel et al., 2015; Li et al., 2016; Noronha Nc et al., 2019). IL-17-producing T cells are inhibited by MSC-derived EVs by inducing the activation of IL-10-producing regulatory T cells, involved in the suppression of inflammation. Through the release of molecules like TGF-β, MSC-derived EVs suppress $CD4^+$ and $CD8^+$ T cell activation, reducing the inflammation (Álvarez et al., 2018). Treatment with MSCs-derived EVs also significantly reduced the activation and proliferation of NK cells, promoting the survival of alveolar macrophages and polarizing their phenotype from M1 pro-inflammatory to M2 anti-inflammatory by suppressing the NF-κB signaling pathway. MSCs-derived EVs immunomodulatory properties have also been associated with the anti-inflammatory activity of their cargo, such as IDO, HLA-G, PD-L1 and galectin-1 (Blazquez et al., 2014; Galland et al., 2017; Sicco et al., 2017). MSC-derived EVs miRNAs, for instance miR-124–3p, miR-21–5p, miR-146a and miR-145, have been shown to exert epigenetic effects, affecting cell receptor expression and the exchange of genetic material. Among these miRNAs, miR-124–3p binds to P2X ligand-gated ion channel 7 and suppresses oxidative stress and inflammation, miR-21–5p inhibits lung cell apoptosis, and miR-146a affects macrophages polarization. Lastly, by increasing macrophages phagocytosis, miR-145 facilitates a rapid clearance of infection-causing pathogens. These changes also prevent viruses, such as SARS-CoV-2, from invading cell systems (Wang et al., 2018; Hao et al., 2019; Xia et al., 2019). The results of the current studies are promising, but further research is needed to establish safety and

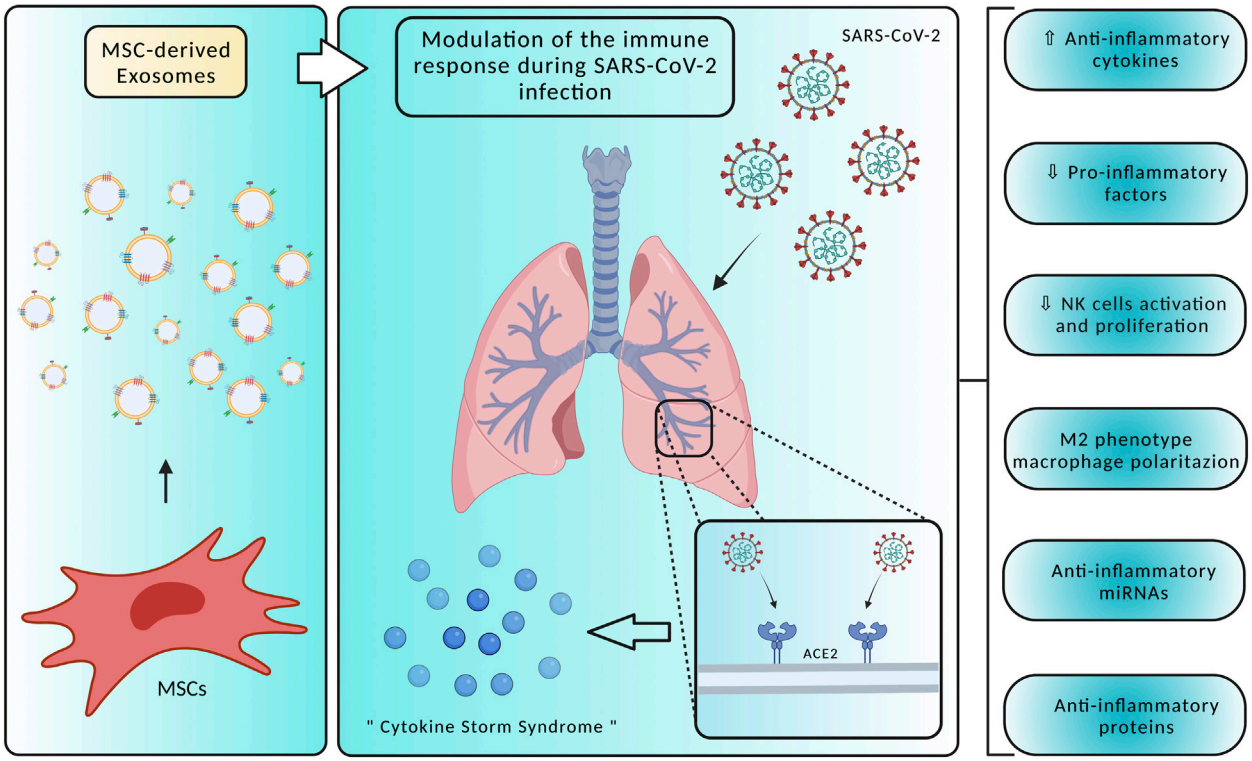

FIGURE 2
Mesenchymal Stem Cells (MSC)-derived exosomes display several mechanisms of action in counteracting SARS-CoV-2 infection, modulating the host immune responses and acting on the "cytokine storm syndrome". Specifically, treatment with MSC-derived exosomes may promote an anti-inflammatory environment by reducing pro-inflammatory factors and NK cells activation, producing anti-inflammatory factors, and polarizing macrophages towards an M2 phenotype. Created with BioRender.com.

efficacy of MSCs-derived EVs to treat and control symptoms associated with COVID-19.

Extracellular vesicles as carriers for drug delivery

A drug delivery system based on EVs has a great potential to maximize drug loading in the target cells and inhibit any off-target effects. To reduce viral spread and replication in recipient cells, drugs or biomodulators may be delivered *via* EVs. To stimulate antigen-specific immune responses, antiviral drugs loaded into EVs can be delivered directly to targeted sites, such as the nasal mucosa and lungs, to exert immunomodulatory effects. As a result of the encapsulation strategy, drugs are delivered to targeted organs more efficiently, and the toxicity associated with native drugs are minimized. To improve the efficiency and specificity of EVs-mediated delivery, there are two methodological approaches for drug loading into EVs, namely exogenous and endogenous (Romagnoli et al., 2015; Somiya et al., 2017). Depending on drug size, shape, and treatment needs, specific loading methods are selected for each drug of interest. Endogenous loading can be achieved by incubating drugs with disease-targeted cell lines, so drug internalization occurs by natural sorting. Then, cells can produce EVs containing the drug of interest, allowing to obtain large quantities of drug-loaded EVs (Vader et al., 2016). On the other hand, the exogenous approach consists in a therapeutic agent, mostly synthetic molecules, or small biomolecules, that can be included into EVs previously isolated from cells or plasma. EVs loading may be either passive or active. Passive loading occurs with the incubation of EVs with therapeutic molecules without further stimulation. Conversely, hydrophilic molecules, including nucleic acids and proteins, cannot spontaneously penetrate into EVs and, therefore, physically or chemically induced active loading is required. Physically induced loading utilizes sonication, electroporation, freeze-thaw, and extrusion methods. The membrane of EVs can also be permeated with chemicals, such as saponin and transfection reagents (Fuhrmann et al., 2015; Janas et al., 2015; Lener et al., 2015; Mantel et al., 2016). In the case of SARS-CoV-2, protease inhibitors (PIs), like anti-HIV PIs, or other antiviral drugs can be encapsulated by

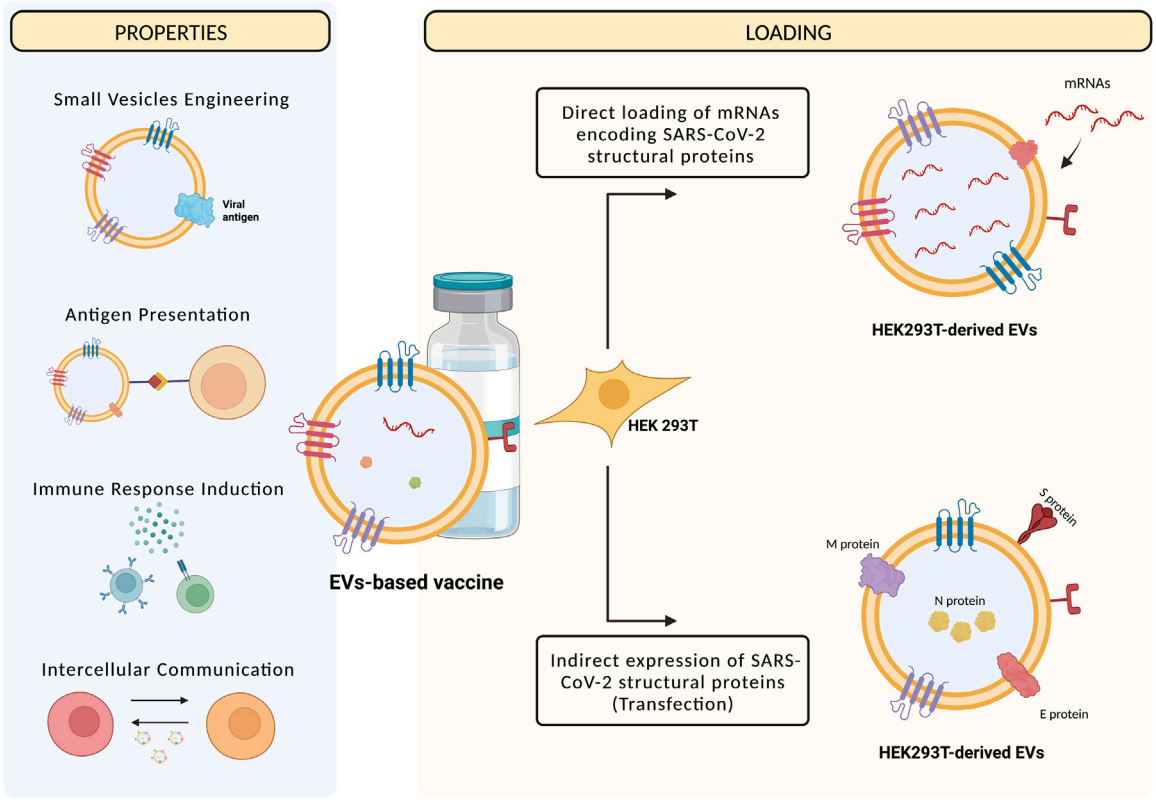

FIGURE 3
Next to being mediators of intercellular communication, EVs can present antigens and induce immune responses, and then being engineered to express viral proteins and used as vaccines. The methods currently used to realize EVs-based vaccines are the transfection of HEK293T cells with vectors expressing SARS-CoV-2 structural proteins, then expressed by EVs that are recognized by the host immune system, or the direct loading of mRNAs encoding for the SARS-CoV-2 proteins into EVs, that are then transferred to recipient cells that, in turn, are recognized by the host immune system. Created with BioRender.com.

endogenous loading technique in Vero CCL-81, Vero E6, and/or STAT1 knock-out cell lines, which can be infected by the virus. In addition, PIs can also be loaded exogenously into EVs isolated from patients' plasma for personalized therapy (Harcourt et al., 2020). Currently, only a few clinical trials are ongoing to test EVs formulations for therapeutic purposes towards COVID-19 (Karn et al., 2021). The Direct Biologics company, for instance, has promoted and tested in 24 COVID-19 patients an exosome-based drug derived from bone marrow MSCs (ExoFlo™). A single dose of this formulation came out to be safe and without severe side effects in all the patients, reducing inflammatory markers and rising oxygen levels (Sengupta et al., 2020). Despite the promising results of ExoFlo™, the biological activity, dose concentrations, and long-term effects should be also considered for therapeutic purposes, as well as for other EVs formulations. Furthermore, more EVs-based clinical trials on a larger number of COVID-19 patients must take place to assess their therapeutic relevance (Lim et al., 2020).

Potential use of extracellular vesicles for vaccination

Virus entry into cells is determined by the receptor-binding domain of SARS-CoV-2 spike protein that specifically binds to ACE2. For this reason, the main potential strategy for vaccine and small drug molecule development against COVID-19 is to block the receptor binding domain (RBD) and ACE2 association sites (Benítez-Cardoza and Vique-Sánchez, 2020; Tai et al., 2020). As stated before, next to their role in facilitating cell-to-cell communication, EVs can also induce an immune response due to their ability in presenting antigens. Therefore, EVs can be engineered to display viral antigens, evoking strong immune responses, and acting as a novel vaccine strategy. To date, several vaccines have been approved for SARS-CoV-2 treatment but, in the face of the emerging SARS-CoV-2 variants and the pandemic prosecution, there is still an urgent need to develop new, efficient vaccine strategies (Tregoning et al., 2021). As an alternative to viral attenuated and inactivated vaccines, viral Spike proteins

TABLE 1 Summary of the role of EVs in SARS-CoV-2 pathogenesis, diagnosis and treatment.

Pathogenesis	Assembly and packaging of viral particles
	Egression from infected cells
	Circulation/dissemination to other targets
	Inflammatory responses activation
	Immune response modulation
Diagnosis	EVs-incorporated exRNAs as potential early disease biomarkers
	Liver damage-related exRNAs
	Antiviral response-related EVs proteins
	Coagulation-related markers
Treatment	Therapeutic tools
	MSCs-derived EVs
	Drug delivery systems
	EVs-based vaccines

represent the main target for vaccines realized with different molecular approaches, such as viral-vector-based vaccines (particularly adenoviruses), mRNA vaccines, or vaccines with the full-length S protein or a RBD (Ghaebi et al., 2020). However, when a viral infection is present or when a vaccine against viral antigens is given, a phenomenon called "antibody-dependent enhancement" (ADE) may occur, resulting in an increased burden of the disease. In this context, the recognition and binding of viral particles by antibodies may promote the virus entry and replication in target cells, amplifying an infection rather than protecting from it. To avoid the possibility of side effects with an EVs-based vaccine, it is important to investigate the safety of EVs-producing cells employed for therapeutic purposes. Many studies have shown that human embryonic kidney HEK293T cells are a safe source for EVs production for therapeutic purposes, since they do not express disease markers (Arvin et al., 2020; van Doremalen et al., 2020; Greinacher et al., 2021; Kim et al., 2021). Two types of EVs-based vaccines have been developed to stimulate a long-term immune response to SARS-CoV-2 (Figure 3). The first type consists in HEK293T cells transfected with vectors encoding the four SARS-CoV-2 structural proteins (Spike, Nucleocapsid, Membrane, Envelope). Transfected cells, in turn, produce EVs enriched with viral proteins that may trigger immune responses. It has been shown that immunizing with multiple protein forms allows the modulation of the magnitude and nature of the immune response through cytokines production and Th1 or Th2 stimulation (Morel et al., 2004). The second HEK293T-derived EVs vaccine implies the direct loading of EVs with different mRNAs, encoding modified SARS-CoV-2 Nucleocapsid, Membrane, and Envelope proteins, and the full-length Spike of Wuhan-1 (SW1) isolate, all inserted in the extracellular domain of human Lysosomal Associated Membrane Protein 1 (LAMP1). This protein undergoes degradation into peptides for antigen presentation, inducing the immune response. The LSNME/SW1 vaccine induced a significant increase in both $CD4^+$ and $CD8^+$ T cell proliferation upon addition of N and S recombinant proteins to splenocyte culture medium, confirming the effectiveness of this formulation in triggering cellular immunity (Tsai et al., 2021). Additionally, an EVs-derived vaccine containing the antitumoral cytokine IL-12 from HEK293T cells has been tested in a Phase I trial (Lewis et al., 2021). To improve the immune responses generated by EVs-based vaccines, it might be worth to consider using modified mRNAs encoding for the prefusion conformation of the Spike protein, as has been done by Pfizer/BioNTech and Moderna. To fuse with the host cell membrane, Spike protein undergoes structural rearrangements, from an unstable pre-fusion conformation to a highly stable post-fusion conformation, and there has been indication that stabilizing prefusion-immunogens, preserving epitopes, offers a promising vaccine strategy for enveloped viruses. As part of the prefusion-stabilization process, Moderna substituted prolines in the SARS-CoV-2 S protein residues 986 and 987, and started the production of the mRNA-LNP for the SARS-CoV-2 S (2P) protein (mRNA-1273) (Corbett et al., 2020). Pfizer/BioNTech also developed vaccines using S protein mRNA (2P), although with further modifications. For instance, their vaccine consists of a lipid-nanoparticle containing a N-methyl-pseudouridine (m1Ψ) nucleoside-modified mRNA, encoding for an S protein (2P) that contains a native furin-cleavage site resulting in two fragments (Bansal et al., 2021; Dooley et al., 2021). The fact that this recombinant trimeric S (2P) protein can bind the human ACE2 receptor and human anti-RBD antibodies with high affinity clearly demonstrates its structure and function (Vogel et al., 2020). Furthermore, EVs can be used at high concentrations without adverse effects on cells or animals, so their future use in dosing regimens that require ongoing repeated injections is promising.

Conclusions and future perspectives

EVs are nano- and micro-sized particles released by several cell types and capable of trespassing biological membranes, protecting and delivering their cargo to other targets. For this reason, EVs have been recognized as intercellular signaling mediators in both physiological and pathological conditions, including in virus-host interactions (Kalluri and LeBleu, 2020). Viruses and EVs share some similarities in terms of morphology and biogenesis, so EVs trafficking is now gaining growing emphasis in the study of viral infections, such as COVID-19 (V'kovski et al., 2021). Several morphological studies highlighted the involvement of EVs during SARS-CoV-2 infection, in which the virus exploits intracellular membranes forming the so-called "replicative organelles". SARS-CoV-2 would take advantage of these structures to

enhance its replication within the infected cell, but also to maximize its multiplicity of infection, and thus its diffusion, to other cells, creating "collective infectious units" as previously described (Bello-Morales et al., 2020; Eymieux et al., 2021b). However, concerning the mechanisms through which SARS-CoV-2 virions inside vesicular structures egress from infected cells and spread towards other cell targets, several hypotheses have been proposed, but there are still discrepancies and further investigations are needed (Klein et al., 2020; Eymieux et al., 2021b; Kumar et al., 2021; Laue et al., 2021; Mendonça et al., 2021). The contribute of EVs in SARS-CoV-2 infection occurs not only at a morphological level, but also functionally. Indeed, in relationship with their cargo, EVs may exert beneficial or detrimental effects towards SARS-CoV-2 infection, promoting viral spread (Wang et al., 2020) or stimulating host immune responses towards the virus (Hassanpour et al., 2020), respectively. Further studies to elucidate the morphological and functional role of EVs in SARS-CoV-2 infection, especially in terms of EVs dynamics that can be characterized by microscopy methods, and definition of their molecular profiles that can be achieved by multi-omics approaches, are needed for a better understanding of SARS-CoV-2 infection process and a potential exploiting EVs pathway as a target for COVID-19 in diagnosis and treatment applications. Indeed, EVs intrinsic properties and their potential to maximize drug delivery, reducing at the same time the risks of off-targets, make them appealing as tools for therapeutic applications, such as drug delivery and vaccine development. However, there are some limitations that must be considered. The heterogeneity of EVs populations and the lack of standardized protocols for their isolation and downstream processing make it challenging to predict their effects for therapeutic applications. For this reason, it is pivotal to set up proper experimental conditions in pre-clinical models, recapitulating in the best way the physiopathological state of interest, and to consider that the isolation of a heterogeneous population of EVs may provide a more precise overview of their synergic effects respect to the purification of single subpopulations, which may offer instead unreliable information. Concerning clinical trials, MSCs-derived EVs displayed positive effects in reducing the cytokine storm characterizing SARS-CoV-2 infection (Devaney et al., 2015; Monsel et al., 2015; Li et al., 2016; Noronha Nc et al., 2019). Despite the encouraging potential of EVs-based treatment for COVID-19 and the fact that several companies are developing new EVs-based formulations (Karn et al., 2021), there is still a paucity of data and clinical trials need to be improved, assessing next to the effectiveness of the system also the safety and long-term effects. Since EVs display several benefits, such as reduced off-targets, minimal immunogenicity, the ability to transport drugs and high biocompatibility, they still represent a valid alternative to offer new perspectives in the diagnostic and therapeutic field. In conclusion, EVs display an intricate role in SARS-CoV-2 pathogenesis, diagnosis, and treatment (summarized in Table 1). In light of these observations, a deeper understanding of the role of EVs in SARS-CoV-2 pathogenesis, next to improved pre-clinical and clinical studies for an improvement of their use in the diagnostic and therapeutic field, may offer a new weapon to face the emerging SARS-CoV-2 variants that are contributing to an unceasing pandemic.

Author contributions

Conceptualization, CS, DV, and LD; writing-original draft preparation, CS and DV; graphics, LB; writing-review and editing final draft, ST and LD.

Conflict of interest

The authors declare that the research was conducted in the absence of any commercial or financial relationships that could be construed as a potential conflict of interest.

Publisher's note

All claims expressed in this article are solely those of the authors and do not necessarily represent those of their affiliated organizations, or those of the publisher, the editors and the reviewers. Any product that may be evaluated in this article, or claim that may be made by its manufacturer, is not guaranteed or endorsed by the publisher.

References

Adli, A., Rahimi, M., Khodaie, R., Hashemzaei, N., and Hosseini, S. M. (2022). Role of genetic variants and host polymorphisms on COVID-19: From viral entrance mechanisms to immunological reactions. *J. Med. Virol.* 94, 1846–1865. doi:10.1002/JMV.27615

Altan-Bonnet, N. (2016). Extracellular vesicles are the Trojan horses of viral infection. *Curr. Opin. Microbiol.* 32, 77–81. doi:10.1016/J.MIB.2016.05.004

Álvarez, V., Sánchez-Margallo, F. M., Macías-García, B., Gómez-Serrano, M., Jorge, I., Vázquez, J., et al. (2018). The immunomodulatory activity of extracellular vesicles derived from endometrial mesenchymal stem cells on CD4+ T cells is partially mediated by TGFbeta. *J. Tissue Eng. Regen. Med.* 12, 2088–2098. doi:10.1002/TERM.2743

Andreu-Moreno, I., and Sanjuán, R. (2020). Collective viral spread mediated by virion aggregates promotes the evolution of defective interfering particles. *MBio* 11, e02156-19. doi:10.1128/MBIO.02156-19

Arvin, A. M., Fink, K., Schmid, M. A., Cathcart, A., Spreafico, R., Havenar-Daughton, C., et al. (2020). A perspective on potential antibody-dependent

enhancement of SARS-CoV-2. *Nature* 584, 353–363. doi:10.1038/s41586-020-2538-8

Babaei, G., Zare, N., Mihanfar, A., and Ansari, M. H. K. (2022). Exosomes and COVID-19: Challenges and opportunities. *Comp. Clin. Path.* 31, 347–354. doi:10.1007/S00580-021-03311-3

Bansal, S., Perincheri, S., Fleming, T., Poulson, C., Tiffany, B., Bremner, R. M., et al. (2021). Cutting edge: Circulating exosomes with covid spike protein are induced by BNT162b2 (Pfizer–BioNTech) vaccination prior to development of antibodies: A novel mechanism for immune activation by mRNA vaccines. *J. I.* 207, 2405–2410. doi:10.4049/JIMMUNOL.2100637

Bao, Q., Huang, Q., Chen, Y., Wang, Q., Sang, R., Wang, L., et al. (2022). Tumor-derived extracellular vesicles regulate cancer progression in the tumor microenvironment. *Front. Mol. Biosci.* 8, 796385. doi:10.3389/FMOLB.2021.796385

Barberis, E., Vanella, V. V., Falasca, M., Caneapero, V., Cappellano, G., Raineri, D., et al. (2021). Circulating exosomes are strongly involved in SARS-CoV-2 infection. *Front. Mol. Biosci.* 8, 632290. doi:10.3389/FMOLB.2021.632290

Bello-Morales, R., and López-Guerrero, J. A. (2020). Isolation/Analysis of extracellular microvesicles from HSV-1-Infected cells. *Methods Mol. Biol.* 2060, 305–317. doi:10.1007/978-1-4939-9814-2_17

Bello-Morales, R., Ripa, I., and López-Guerrero, J. A. (2020). Extracellular vesicles in viral spread and antiviral response. *Viruses* 12, 623. doi:10.3390/V12060623

Benítez-Cardoza, C. G., and Vique-Sánchez, J. L. (2020). Potential inhibitors of the interaction between ACE2 and SARS-CoV-2 (RBD), to develop a drug. *Life Sci.* 256, 117970. doi:10.1016/J.LFS.2020.117970

Blazquez, R., Sanchez-Margallo, F. M., de la Rosa, O., Dalemans, W., Álvarez, V., Tarazona, R., et al. (2014). Immunomodulatory potential of human adipose mesenchymal stem cells derived exosomes on *in vitro* stimulated T cells. *Front. Immunol.* 5, 556. doi:10.3389/FIMMU.2014.00556

Boni, M. F., Lemey, P., Jiang, X., Lam, T. T. Y., Perry, B. W., Castoe, T. A., et al. (2020). Evolutionary origins of the SARS-CoV-2 sarbecovirus lineage responsible for the COVID-19 pandemic. *Nat. Microbiol.* 511 (5), 1408–1417. doi:10.1038/s41564-020-0771-4

Bunz, M., Ritter, M., and Schindler, M. (2022). HCV egress - unconventional secretion of assembled viral particles. *Trends Microbiol.* 30, 364–378. doi:10.1016/J.TIM.2021.08.005

Cao, X. (2020). COVID-19: Immunopathology and its implications for therapy. *Nat. Rev. Immunol.* 20, 269–270. doi:10.1038/s41577-020-0308-3

Chan, J. F. W., Yuan, S., Kok, K. H., To, K. K. W., Chu, H., Yang, J., et al. (2020). A familial cluster of pneumonia associated with the 2019 novel coronavirus indicating person-to-person transmission: A study of a family cluster. *Lancet* 395, 514–523. doi:10.1016/S0140-6736(20)30154-9

Chen, J., Li, C., Li, R., Chen, H., Chen, D., and Li, W. (2021). Exosomes in HIV infection. *Curr. Opin. HIV AIDS* 16, 262–270. doi:10.1097/COH.0000000000000694

Chen, Y. H., Du, W., Hagemeijer, M. C., Takvorian, P. M., Pau, C., Cali, A., et al. (2015). Phosphatidylserine vesicles enable efficient *en bloc* transmission of enteroviruses. *Cell* 160 (4), 619–630. doi:10.1016/j.cell.2015.01.032

Colombo, M., Raposo, G., and Théry, C. (2014). Biogenesis, secretion, and intercellular interactions of exosomes and other extracellular vesicles. *Annu. Rev. Cell Dev. Biol.* 30, 255–289. doi:10.1146/ANNUREV-CELLBIO-101512-122326

Corbett, K. S., Edwards, D. K., Leist, S. R., Abiona, O. M., Boyoglu-Barnum, S., Gillespie, R. A., et al. (2020). SARS-CoV-2 mRNA vaccine design enabled by prototype pathogen preparedness. *Nature* 586, 567–571. doi:10.1038/s41586-020-2622-0

Devaney, J., Horie, S., Masterson, C., Elliman, S., Barry, F., O'Brien, T., et al. (2015). Human mesenchymal stromal cells decrease the severity of acute lung injury induced by *E. coli* in the rat. *Thorax* 70, 625–635. doi:10.1136/THORAXJNL-2015-206813

Dini, L., Tacconi, S., Carata, E., Tata, A. M., Vergallo, C., and Panzarini, E. (2020). Microvesicles and exosomes in metabolic diseases and inflammation. *Cytokine Growth Factor Rev.* 51, 27–39. doi:10.1016/J.CYTOGFR.2019.12.008

Dooley, K., McConnell, R. E., Xu, K., Lewis, N. D., Haupt, S., Youniss, M. R., et al. (2021). A versatile platform for generating engineered extracellular vesicles with defined therapeutic properties. *Mol. Ther.* 29, 1729–1743. doi:10.1016/J.YMTHE.2021.01.020

Doyle, L. M., and Wang, M. Z. (2019). Overview of extracellular vesicles, their origin, composition, purpose, and methods for exosome isolation and analysis. *Cells* 8, 727. doi:10.3390/CELLS8070727

Dubrovsky, L., Ward, A., Choi, S. H., Pushkarsky, T., Brichacek, B., Vanpouille, C., et al. (2020). Inhibition of HIV replication by apolipoprotein A-I binding protein targeting the lipid rafts. *MBio* 11, e02956. doi:10.1128/MBIO.02956-19

Eymieux, S., Rouillé, Y., Terrier, O., Seron, K., Blanchard, E., Rosa-Calatrava, M., et al. (2021a). Ultrastructural modifications induced by SARS-CoV-2 in Vero cells: A kinetic analysis of viral factory formation, viral particle morphogenesis and virion release. *Cell. Mol. Life Sci.* 78, 3565–3576. doi:10.1007/S00018-020-03745-Y

Eymieux, S., Uzbekov, R., Rouillé, Y., Blanchard, E., Hourioux, C., Dubuisson, J., et al. (2021b). Secretory vesicles are the principal means of SARS-CoV-2 egress. *Cells* 10, 2047. doi:10.3390/CELLS10082047

Feng, Z., Hensley, L., McKnight, K. L., Hu, F., Madden, V., Ping, L., et al. (2013). A pathogenic picornavirus acquires an envelope by hijacking cellular membranes. *Nature* 496, 367–371. doi:10.1038/nature12029

Feng, Z., Hirai-Yuki, A., McKnight, K. L., and Lemon, S. M. (2014). Naked viruses that aren't always naked: Quasi-enveloped agents of acute hepatitis. *Annu. Rev. Virol.* 1, 539–560. doi:10.1146/annurev-virology-031413-08535910.1146/ANNUREV-VIROLOGY-031413-085359

Fuhrmann, G., Serio, A., Mazo, M., Nair, R., and Stevens, M. M. (2015). Active loading into extracellular vesicles significantly improves the cellular uptake and photodynamic effect of porphyrins. *J. Control. Release* 205, 35–44. doi:10.1016/J.JCONREL.2014.11.029

Fujita, Y., Hoshina, T., Matsuzaki, J., Yoshioka, Y., Kadota, T., Hosaka, Y., et al. (2021). Early prediction of COVID-19 severity using extracellular vesicle COPB2. *J. Extracell. Vesicles* 10, e12092. doi:10.1002/JEV2.12092

Galland, S., Vuille, J., Martin, P., Letovanec, I., Caignard, A., Fregni, G., et al. (2017). Tumor-derived mesenchymal stem cells use distinct mechanisms to block the activity of natural killer cell subsets. *Cell Rep.* 20, 2891–2905. doi:10.1016/J.CELREP.2017.08.089

Ghaebi, M., Osali, A., Valizadeh, H., Roshangar, L., and Ahmadi, M. (2020). Vaccine development and therapeutic design for 2019-nCoV/SARS-CoV-2: Challenges and chances. *J. Cell. Physiol.* 235, 9098–9109. doi:10.1002/JCP.29771

Ghosh, S., Dellibovi-Ragheb, T. A., Kerviel, A., Pak, E., Qiu, Q., Fisher, M., et al. (2020). β-Coronaviruses use lysosomes for egress instead of the biosynthetic secretory pathway. *Cell* 183, 1520–1535.e14. doi:10.1016/J.CELL.2020.10.039

Gierer, S., Bertram, S., Kaup, F., Wrensch, F., Heurich, A., Krämer-Kühl, A., et al. (2013). The spike protein of the emerging betacoronavirus EMC uses a novel coronavirus receptor for entry, can Be activated by TMPRSS2, and is targeted by neutralizing antibodies. *J. Virol.* 87, 5502–5511. doi:10.1128/JVI.00128-13

Goodlet, K. J., Bansal, S., Arjuna, A., Nailor, M. D., Buddhdev, B., Abdelrazek, H., et al. (2021). COVID-19 in a lung transplant recipient: Exploring the diagnostic role of circulating exosomes and the clinical impact of advanced immunosuppression. *Transpl. Infect. Dis.* 23, e13480. doi:10.1111/TID.13480

Greinacher, A., Thiele, T., Warkentin, T. E., Weisser, K., Kyrle, P. A., and Eichinger, S. (2021). Thrombotic thrombocytopenia after ChAdOx1 nCov-19 vaccination. *N. Engl. J. Med.* 384, 2092–2101. doi:10.1056/NEJMOA2104840

Guan, W., Ni, Z., Hu, Y., Liang, W., Ou, C., He, J., et al. (2020). Clinical characteristics of coronavirus disease 2019 in China. *N. Engl. J. Med.* 382, 1708–1720. doi:10.1056/NEJMOA2002032

Gunasekaran, M., Bansal, S., Ravichandran, R., Sharma, M., Perincheri, S., Rodriguez, F., et al. (2020). Respiratory viral infection in lung transplantation induces exosomes that trigger chronic rejection. *J. Heart Lung Transpl.* 39, 379–388. doi:10.1016/J.HEALUN.2019.12.009

Gusachenko, O. N., Zenkova, M. A., and Vlassov, V. V. (2013). Nucleic acids in exosomes: Disease markers and intercellular communication molecules. *Biochem. Mosc.* 78, 1–7. doi:10.1134/S000629791301001X

Hao, Q., Gudapati, V., Monsel, A., Park, J. H., Hu, S., Kato, H., et al. (2019). Mesenchymal stem cell–derived extracellular vesicles decrease lung injury in mice. *J. I.* 203, 1961–1972. doi:10.4049/JIMMUNOL.1801534

Harcourt, J., Tamin, A., Lu, X., Kamili, S., Kumar Sakthivel, S., Murray, J., et al. (2020). Isolation and characterization of SARS-CoV-2 from the first US COVID-19 patient. *bioRxiv.* 2020, 2020.03.02.972935. doi:10.1101/2020.03.02.972935

Hassanpour, M., Rezaie, J., Nouri, M., and Panahi, Y. (2020). The role of extracellular vesicles in COVID-19 virus infection. *Infect. Genet. Evol.* 85, 104422. doi:10.1016/J.MEEGID.2020.104422

Hildreth, J. E. K. (2017). HIV as trojan exosome: Immunological paradox explained? *Front. Immunol.* 8, 1715. doi:10.3389/FIMMU.2017.01715

Hoen, E. N., Cremer, T., Gallo, R. C., and Margolis, L. B. (2016). Extracellular vesicles and viruses: Are they close relatives? *Proc. Natl. Acad. Sci. U. S. A.* 113, 9155–9161. doi:10.1073/PNAS.1605146113

Hoffmann, M., Kleine-Weber, H., Schroeder, S., Krüger, N., Herrler, T., Erichsen, S., et al. (2020). SARS-CoV-2 cell entry depends on ACE2 and TMPRSS2 and is blocked by a clinically proven protease inhibitor. *Cell* 181, 271–280.e8. doi:10.1016/j.cell.2020.02.052

Hurley, J. H. (2015). ESCRTs are everywhere. *EMBO J.* 34, 2398–2407. doi:10.15252/EMBJ.201592484

Hutagalung, A. H., and Novick, P. J. (2011). Role of Rab GTPases in membrane traffic and cell physiology. *Physiol. Rev.* 91 (1), 119–149. doi:10.1152/physrev.00059.2009

Ipinmoroti, A. O., and Matthews, Q. L. (2020). Extracellular vesicles: Roles in human viral infections, immune-diagnostic, and therapeutic applications. *Pathogens* 20209, 1056. doi:10.3390/PATHOGENS9121056

Janas, T., Janas, M. M., Sapoń, K., and Janas, T. (2015). Mechanisms of RNA loading into exosomes. *FEBS Lett.* 589, 1391–1398. doi:10.1016/J.FEBSLET.2015.04.036

Jiang, W., Ma, P., Deng, L., Liu, Z., Wang, X., Liu, X., et al. (2020). Hepatitis A virus structural protein pX interacts with ALIX and promotes the secretion of virions and foreign proteins through exosome-like vesicles. *J. Extracell. Vesicles* 9, 1716513. doi:10.1080/20013078.2020.1716513

Jones, L. B., Bell, C. R., Bibb, K. E., Gu, L., Coats, M. T., and Matthews, Q. L. (2018). Pathogens and their effect on exosome biogenesis and composition. *Biomedicines* 6, 79. doi:10.3390/BIOMEDICINES6030079

Kalluri, R., and LeBleu, V. S. (2020). The biology, function, and biomedical applications of exosomes. *Science* 80, eaau6977. doi:10.1126/SCIENCE.AAU6977

Karn, V., Ahmed, S., Tsai, L. W., Dubey, R., Ojha, S., Singh, H. N., et al. (2021). Extracellular vesicle-based therapy for COVID-19: Promises, challenges and future prospects. *Biomedicines* 9 (10), 1373. doi:10.3390/biomedicines9101373

Kerr, J. F. R., Wyllie, A. H., and Currie, A. R. (1972). Apoptosis: A basic biological phenomenon with wideranging implications in tissue kinetics. *Br. J. Cancer* 26, 239–257. doi:10.1038/bjc.1972.33

Kim, J., Song, Y., Park, C. H., and Choi, C. (2021). Platform technologies and human cell lines for the production of therapeutic exosomes. *Extracell. Vesicles Circ. Nucl. Acids* 2, 3–17. doi:10.20517/EVCNA.2020.01

Klein, S., Cortese, M., Winter, S. L., Wachsmuth-Melm, M., Neufeldt, C. J., Cerikan, B., et al. (2020). SARS-CoV-2 structure and replication characterized by *in situ* cryo-electron tomography. *Nat. Commun.* 11, 5885–5910. doi:10.1038/s41467-020-19619-7

Knoops, K., Kikkert, M., Van Den Worm, S. H. E., Zevenhoven-Dobbe, J. C., Van Der Meer, Y., Koster, A. J., et al. (2008). SARS-coronavirus replication is supported by a reticulovesicular network of modified endoplasmic reticulum. *PLoS Biol.* 6, e226. doi:10.1371/JOURNAL.PBIO.0060226

Knoops, K., Swett-Tapia, C., van den Worm, S. H. E., te Velthuis, A. J. W., Koster, A. J., Mommaas, A. M., et al. (2010). Integrity of the early secretory pathway promotes, but is not required for, severe acute respiratory syndrome coronavirus RNA synthesis and virus-induced remodeling of endoplasmic reticulum membranes. *J. Virol.* 84, 833–846. doi:10.1128/JVI.01826-09

Kosaka, N., Iguchi, H., Yoshioka, Y., Takeshita, F., Matsuki, Y., and Ochiya, T. (2010). Secretory mechanisms and intercellular transfer of microRNAs in living cells. *J. Biol. Chem.* 285, 17442–17452. doi:10.1074/JBC.M110.107821

Kulkarni, R., Wiemer, E. A. C., and Chang, W. (2022). Role of lipid rafts in pathogen-host interaction - a mini review. *Front. Immunol.* 12, 815020. doi:10.3389/FIMMU.2021.815020

Kumar, B., Hawkins, G. M., Kicmal, T., Qing, E., Timm, E., and Gallagher, T. (2021). Assembly and entry of severe acute respiratory syndrome coronavirus 2 (SARS-CoV2): Evaluation using virus-like particles. *Cells* 10, 853. doi:10.3390/cells10040853

Lakkaraju, A., and Rodriguez-Boulan, E. (2008). Itinerant exosomes: Emerging roles in cell and tissue polarity. *Trends Cell Biol.* 18, 199–209. doi:10.1016/J.TCB.2008.03.002

Lam, S. M., Zhang, C., Wang, Z., Ni, Z., Zhang, S., Yang, S., et al. (2021). A multi-omics investigation of the composition and function of extracellular vesicles along the temporal trajectory of COVID-19. *Nat. Metab.* 3 (7), 909–922. doi:10.1038/s42255-021-00425-4

Laue, M., Kauter, A., Hoffmann, T., Möller, L., Michel, J., and Nitsche, A. (2021). Morphometry of SARS-CoV and SARS-CoV-2 particles in ultrathin plastic sections of infected Vero cell cultures. *Sci. Rep.* 11, 3515–3611. doi:10.1038/s41598-021-82852-7

Leeks, A., Sanjuán, R., and West, S. A. (2019). The evolution of collective infectious units in viruses. *Virus Res.* 265, 94–101. doi:10.1016/J.VIRUSRES.2019.03.013

Lener, T., Gimona, M., Aigner, L., Börger, V., Buzas, E., Camussi, G., et al. (2015). Applying extracellular vesicles based therapeutics in clinical trials – An ISEV position paper. *J. Extracell. Vesicles* 4, 30087. doi:10.3402/JEV.V4.30087

Letko, M., Marzi, A., and Munster, V. (2020). Functional assessment of cell entry and receptor usage for SARS-CoV-2 and other lineage B betacoronaviruses. *Nat. Microbiol.* 54 (5), 562–569. doi:10.1038/s41564-020-0688-y

Lewis, N. D., Sia, C. L., Kirwin, K., Haupt, S., Mahimkar, G., Zi, T., et al. (2021). Exosome surface display of IL12 results in tumor-retained pharmacology with superior potency and limited systemic exposure compared with recombinant IL12. *Mol. Cancer Ther.* 20, 523–534. doi:10.1158/1535-7163.MCT-20-0484

Li, Q., Guan, X., Wu, P., Wang, X., Zhou, L., Tong, Y., et al. (2020). Early transmission dynamics in wuhan, China, of novel coronavirus–infected pneumonia. *N. Engl. J. Med.* 382, 1199–1207. doi:10.1056/NEJMOA2001316

Li, Y., Xu, J., Shi, W., Chen, C., Shao, Y., Zhu, L., et al. (2016). Mesenchymal stromal cell treatment prevents H9N2 avian influenza virus-induced acute lung injury in mice. *Stem Cell Res. Ther.* 7, 159–211. doi:10.1186/S13287-016-0395-Z

Lim, S. K., Giebel, B., Weiss, D. J., Witwer, K. W., and Rohde, E. (2020). Re: "Exosomes Derived from Bone Marrow Mesenchymal Stem Cells as Treatment for Severe COVID-19" by Sengupta et al. *Stem cells Dev.* 29 (14), 877–878. doi:10.1089/scd.2020.0089

Lu, R., Zhao, X., Li, J., Niu, P., Yang, B., Wu, H., et al. (2020). Genomic characterisation and epidemiology of 2019 novel coronavirus: Implications for virus origins and receptor binding. *Lancet* 395, 565–574. doi:10.1016/S0140-6736(20)30251-8

Lynch, S. F., and Ludlam, C. A. (2007). Plasma microparticles and vascular disorders. *Br. J. Haematol.* 137, 36–48. doi:10.1111/J.1365-2141.2007.06514.X

Maemura, T., Fukuyama, S., Sugita, Y., Lopes, T. J. S., Nakao, T., Noda, T., et al. (2018). Lung-derived exosomal miR-483-3p regulates the innate immune response to influenza virus infection. *J. Infect. Dis.* 217, 1372–1382. doi:10.1093/INFDIS/JIY035

Mantel, P. Y., Hjelmqvist, D., Walch, M., Kharoubi-Hess, S., Nilsson, S., Ravel, D., et al. (2016). Infected erythrocyte-derived extracellular vesicles alter vascular function via regulatory Ago2-miRNA complexes in malaria. *Nat. Commun.* 7, 12727–12815. doi:10.1038/ncomms12727

Mayers, J. R., Fyfe, I., Schuh, A. L., Chapman, E. R., Edwardson, J. M., and Audhya, A. (2011). ESCRT-0 assembles as a heterotetrameric complex on membranes and binds multiple ubiquitinylated cargoes simultaneously. *J. Biol. Chem.* 286, 9636–9645. doi:10.1074/JBC.M110.185363

Mendonça, L., Howe, A., Gilchrist, J. B., Sheng, Y., Sun, D., Knight, M. L., et al. (2021). Correlative multi-scale cryo-imaging unveils SARS-CoV-2 assembly and egress. *Nat. Commun.* 12, 4629. doi:10.1038/s41467-021-24887-y

Monsel, A., Zhu, Y. G., Gennai, S., Hao, Q., Hu, S., Rouby, J. J., et al. (2015). Therapeutic effects of human mesenchymal stem cell-derived microvesicles in severe pneumonia in mice. *Am. J. Respir. Crit. Care Med.* 192, 324–336. doi:10.1164/RCCM.201410-1765OC

Morel, P. A., Falkner, D., Plowey, J., Larregina, A. T., and Falo, L. D. (2004). DNA immunisation: Altering the cellular localisation of expressed protein and the immunisation route allows manipulation of the immune response. *Vaccine* 22, 447–456. doi:10.1016/J.VACCINE.2003.07.012

Morrison, T. J., Jackson, M. V., Cunningham, E. K., Kissenpfennig, A., McAuley, D. F., O'Kane, C. M., et al. (2017). Mesenchymal stromal cells modulate macrophages in clinically relevant lung injury models by extracellular vesicle mitochondrial transfer. *Am. J. Respir. Crit. Care Med.* 196, 1275–1286. doi:10.1164/RCCM.201701-0170OC

Müller, C., Hardt, M., Schwudke, D., Neuman, B. W., Pleschka, S., and Ziebuhr, J. (2018). Inhibition of cytosolic phospholipase A 2 α impairs an early step of coronavirus replication in cell culture. *J. Virol.* 92, e01463. doi:10.1128/JVI.01463-17

Nagashima, S., Jirintai, S., Takahashi, M., Kobayashi, T., Tanggis, Nishizawa, T., et al. (2014). Hepatitis E virus egress depends on the exosomal pathway, with secretory exosomes derived from multivesicular bodies. *J. Gen. Virol.* 95 (Pt 10), 2166–2175. doi:10.1099/VIR.0.066910-0

Nguyen, V. V. T., Witwer, K. W., Verhaar, M. C., Strunk, D., and van Balkom, B. W. M. (2020). Functional assays to assess the therapeutic potential of extracellular vesicles. *J. Extracell. Vesicles* 10, e12033. doi:10.1002/JEV2.12033

Nikfarjam, S., Rezaie, J., Zolbanin, N. M., and Jafari, R. (2020). Mesenchymal stem cell derived-exosomes: A modern approach in translational medicine. *J. Transl. Med.* 18, 449–521. doi:10.1186/S12967-020-02622-3

Noronha Nc, N. D. C., Mizukami, A., Caliári-Oliveira, C., Cominal, J. G., Rocha, J. L. M., Covas, D. T., et al. (2019). Priming approaches to improve the efficacy of mesenchymal stromal cell-based therapies. *Stem Cell Res. Ther.* 10, 131–221. doi:10.1186/S13287-019-1224-Y

Obita, T., Saksena, S., Ghazi-Tabatabai, S., Gill, D. J., Perisic, O., Emr, S. D., et al. (2007). Structural basis for selective recognition of ESCRT-III by the AAA ATPase Vps4. *Nature* 449, 735–739. doi:10.1038/nature06171

Pérez, P. S., Romaniuk, M. A., Duette, G. A., Zhao, Z., Huang, Y., Martin-Jaular, L., et al. (2019). Extracellular vesicles and chronic inflammation during HIV infection *J. Extracell. Vesicles* 8. 1687275. doi:10.1080/20013078.2019.1687275

Pleet, M. L., Branscome, H., DeMarino, C., Pinto, D. O., Zadeh, M. A., Rodriguez, M., et al. (2018). Autophagy, EVs, and infections: A perfect question for a perfect time. *Front. Cell. Infect. Microbiol.* 8, 362. doi:10.3389/FCIMB.2018.00362

Popowski, K. D., Dinh, P.-U. C., George, A., Lutz, H., and Cheng, K. (2021). Exosome therapeutics for COVID-19 and respiratory viruses. *View* 2, 20200186. doi:10.1002/VIW.20200186

Rai, A., Fang, H., Claridge, B., Simpson, R. J., and Greening, D. W. (2021). Proteomic dissection of large extracellular vesicle surfaceome unravels interactive surface platform. *J. Extracell. Vesicles* 10, e12164. doi:10.1002/JEV2.12164

Raiborg, C., Grønvold Bache, K., Mehlum, A., Stang, E., and Stenmark, H. (2001). Hrs recruits clathrin to early endosomes. *EMBO J.* 20, 5008–5021. doi:10.1093/EMBOJ/20.17.5008

Robbins, P. D., and Morelli, A. E. (2014). Regulation of immune responses by extracellular vesicles. *Nat. Rev. Immunol.* 14, 195–208. doi:10.1038/nri3622

Rocha, N., Kuijl, C., van der Kant, R., Janssen, L., Houben, D., Janssen, H., et al. (2009). Cholesterol sensor ORP1L contacts the ER protein VAP to control Rab7-RILP-p150 Glued and late endosome positioning. *J. Cell Biol.* 185 (7), 1209–1225. doi:10.1083/jcb.200811005

Romagnoli, G. G., Zelante, B. B., Toniolo, P. A., Migliori, I. K., and Barbuto, J. A. M. (2015). Dendritic cell-derived exosomes may be a tool for cancer immunotherapy by converting tumor cells into immunogenic targets. *Front. Immunol.* 6, 692. doi:10.3389/FIMMU.2014.00692

Sadri Nahand, J., Moghoofei, M., Salmaninejad, A., Bahmanpour, Z., Karimzadeh, M., Nasiri, M., et al. (2020). Pathogenic role of exosomes and microRNAs in HPV-mediated inflammation and cervical cancer: A review. *Int. J. Cancer* 146, 305–320. doi:10.1002/IJC.32688

Saraste, J., and Prydz, K. (2021). Assembly and cellular exit of coronaviruses: Hijacking an unconventional secretory pathway from the pre-golgi intermediate compartment via the Golgi ribbon to the extracellular space. *Cells* 10, 503. doi:10.3390/CELLS10030503

Satija, N. K., Singh, V. K., Verma, Y. K., Gupta, P., Sharma, S., Afrin, F., et al. (2009). Mesenchymal stem cell-based therapy: A new paradigm in regenerative medicine. *J. Cell. Mol. Med.* 13, 4385–4402. doi:10.1111/J.1582-4934.2009.00857.X

Schorey, J. S., Cheng, Y., Singh, P. P., and Smith, V. L. (2015). Exosomes and other extracellular vesicles in host–pathogen interactions. *EMBO Rep.* 16, 24–43. doi:10.15252/EMBR.201439363

Sengupta, V., Sengupta, S., Lazo, A., Woods, P., Nolan, A., and Bremer, N. (2020). Exosomes derived from bone marrow mesenchymal stem cells as treatment for severe COVID-19. *Stem cells Dev.* 29 (12), 747–754. doi:10.1089/scd.2020.0080

Sicco, C. L., Reverberi, D., Balbi, C., Ulivi, V., Principi, E., Pascucci, L., et al. (2017). Mesenchymal stem cell-derived extracellular vesicles as mediators of anti-inflammatory effects: Endorsement of macrophage polarization. *Stem Cells Transl. Med.* 6, 1018–1028. doi:10.1002/SCTM.16-0363

Sin, J., McIntyre, L., Stotland, A., Feuer, R., and Gottlieb, R. A. (2017). Coxsackievirus B escapes the infected cell in ejected mitophagosomes. *J. Virol.* 91, e01347-17. doi:10.1128/jvi.01347-17

Snijder, E. J., Decroly, E., and Ziebuhr, J. (2016). The nonstructural proteins directing coronavirus RNA synthesis and processing. *Adv. Virus Res.* 96, 59–126. doi:10.1016/BS.AIVIR.2016.08.008

Snijder, E. J., Limpens, R. W. A. L., de Wilde, A. H., de Jong, A. W. M., Zevenhoven-Dobbe, J. C., Maier, H. J., et al. (2020). A unifying structural and functional model of the coronavirus replication organelle: Tracking down RNA synthesis. *PLoS Biol.* 18, e3000715. doi:10.1371/JOURNAL.PBIO.3000715

Somiya, M., Yoshioka, Y., Ochiya, T., Somiya, M., Yoshioka, Y., and Ochiya, T. (2017). Drug delivery application of extracellular vesicles; insight into production, drug loading, targeting, and pharmacokinetics. *AIMS Bioeng.* 173 (4), 73–92. doi:10.3934/BIOENG.2017.1.73

Song, J. W., Lam, S. M., Fan, X., Cao, W. J., Wang, S. Y., Tian, H., et al. (2020). Omics-driven systems interrogation of metabolic dysregulation in COVID-19 pathogenesis. *Cell Metab.* 32, 188–202.e5. doi:10.1016/J.CMET.2020.06.016

Tai, W., He, L., Zhang, X., Pu, J., Voronin, D., Jiang, S., et al. (2020). Characterization of the receptor-binding domain (RBD) of 2019 novel coronavirus: Implication for development of RBD protein as a viral attachment inhibitor and vaccine. *Cell. Mol. Immunol.* 17, 613–620. doi:10.1038/s41423-020-0400-4

Tenoever, B. R. (2013). RNA viruses and the host microRNA machinery. *Nat. Rev. Microbiol.* 11, 169–180. doi:10.1038/nrmicro2971

Théry, C., Witwer, K. W., Aikawa, E., Alcaraz, M. J., Anderson, J. D., Andriantsitohaina, R., et al. (2018). Minimal information for studies of extracellular vesicles 2018 (MISEV2018): A position statement of the international society for extracellular vesicles and update of the MISEV2014 guidelines. *J. Extracell. vesicles* 7 (1), 1535750. doi:10.1080/20013078.2018.1535750

Thoms, M., Buschauer, R., Ameismeier, M., Koepke, L., Denk, T., Hirschenberger, M., et al. (2020). Structural basis for translational shutdown and immune evasion by the Nsp1 protein of SARS-CoV-2. *Science* 369, 1249–1255. doi:10.1126/SCIENCE.ABC8665

Tregoning, J. S., Flight, K. E., Higham, S. L., Wang, Z., and Pierce, B. F. (2021). Progress of the COVID-19 vaccine effort: Viruses, vaccines and variants versus efficacy, effectiveness and escape. *Nat. Rev. Immunol.* 21 (10), 626–636. doi:10.1038/s41577-021-00592-1

Tricarico, C., Clancy, J., and D'Souza-Schorey, C. (2016). Biology and biogenesis of shed microvesicles. *Small GTPases* 8, 220–232. doi:10.1080/21541248.2016.1215283

Tsai, S. J., Guo, C., Sedgwick, A., Kanagavelu, S., Nice, J., Shetty, S., et al. (2021). Exosome-mediated mRNA delivery for SARS-CoV-2 vaccination. *bioRxiv*, 2020.371419. doi:10.1101/2020.11.06.371419

Urbanelli, L., Buratta, S., Tancini, B., Sagini, K., Delo, F., Porcellati, S., et al. (2019). The role of extracellular vesicles in viral infection and transmission. *Vaccines* 7, 102. doi:10.3390/VACCINES7030102

Urciuoli, E., and Peruzzi, B. (2020). Inhibiting extracellular vesicle trafficking as antiviral approach to corona virus disease 2019 infection. *Front. Pharmacol.* 11, 580505. doi:10.3389/FPHAR.2020.580505

Vader, P., Mol, E. A., Pasterkamp, G., and Schiffelers, R. M. (2016). Extracellular vesicles for drug delivery. *Adv. Drug Deliv. Rev.* 106, 148–156. doi:10.1016/J.ADDR.2016.02.006

Valadi, H., Ekström, K., Bossios, A., Sjöstrand, M., Lee, J. J., and Lötvall, J. O. (2007). Exosome-mediated transfer of mRNAs and microRNAs is a novel mechanism of genetic exchange between cells. *Nat. Cell Biol.* 96 (9), 654–659. doi:10.1038/ncb1596

van der Grein, S. G., Defourny, K. A. Y., Slot, E. F. J., and Nolte-'t Hoen, E. N. M. (2018). Intricate relationships between naked viruses and extracellular vesicles in the crosstalk between pathogen and host. *Semin. Immunopathol.* 40, 491–504. doi:10.1007/S00281-018-0678-9

van Dongen, H. M., Masoumi, N., Witwer, K. W., and Pegtel, D. M. (2016). Extracellular vesicles exploit viral entry routes for cargo delivery. *Microbiol. Mol. Biol. Rev.* 80, 369–386. doi:10.1128/MMBR.00063-15

van Doremalen, N., Lambe, T., Spencer, A., Belij-Rammerstorfer, S., Purushotham, J. N., Port, J. R., et al. (2020). ChAdOx1 nCoV-19 vaccine prevents SARS-CoV-2 pneumonia in rhesus macaques. *Nature* 586, 578–582. doi:10.1038/s41586-020-2608-y

Van Niel, G., D'Angelo, G., and Raposo, G. (2018). Shedding light on the cell biology of extracellular vesicles. *Nat. Rev. Mol. Cell Biol.* 19, 213–228. doi:10.1038/nrm.2017.125

Velandia-Romero, M. L., Caldern-Pelaez, M. A., Balbas-Tepedino, A., Alejandro Marquez-Ortiz, R., Madroñero, L. J., Prieto, A. B., et al. (2020). Extracellular vesicles of U937 macrophage cell line infected with DENV-2 induce activation in endothelial cells EA.hy926. *PLoS One* 15, e0227030. doi:10.1371/JOURNAL.PONE.0227030

Vella, L. J., Sharples, R. A., Nisbet, R. M., Cappai, R., and Hill, A. F. (2008). The role of exosomes in the processing of proteins associated with neurodegenerative diseases. *Eur. Biophys. J.* 37, 323–332. doi:10.1007/S00249-007-0246-Z

V'kovski, P., Gerber, M., Kelly, J., Pfaender, S., Ebert, N., Lagache, S. B., et al. (2019). Determination of host proteins composing the microenvironment of coronavirus replicase complexes by proximity-labeling. *Elife* 8, e42037. doi:10.7554/ELIFE.42037

V'kovski, P., Kratzel, A., Steiner, S., Stalder, H., and Thiel, V. (2021). Coronavirus biology and replication: Implications for SARS-CoV-2. *Nat. Rev. Microbiol.* 19, 155–170. doi:10.1038/s41579-020-00468-6

Vogel, A. B., Kanevsky, I., Che, Y., Swanson, K. A., Muik, A., Vormehr, M., et al. (2020). A prefusion SARS-CoV-2 spike RNA vaccine is highly immunogenic and prevents lung infection in non-human primates. *bioRxiv*. 2020 doi:10.1101/2020.09.08.280818

Wang, J., Chen, S., and Bihl, J. (2020). Exosome-mediated transfer of ACE2 (Angiotensin-Converting enzyme 2) from endothelial progenitor cells promotes survival and function of endothelial cell. *Oxid. Med. Cell. Longev.*, 2020 1–11. doi:10.1155/2020/4213541

Wang, M., Yuan, Q., and Xie, L. (2018). Mesenchymal stem cell-based immunomodulation: Properties and clinical application. *Stem Cells Int.*, 2018 1–12. doi:10.1155/2018/3057624

Wang, T., Gilkes, D. M., Takano, N., Xiang, L., Luo, W., Bishop, C. J., et al. (2014). Hypoxia-inducible factors and RAB22A mediate formation of microvesicles that

stimulate breast cancer invasion and metastasis. *Proc. Natl. Acad. Sci. U. S. A.* 111 (31), E3234–E3242. doi:10.1073/pnas.1410041111

Witwer, K. W., Goberdhan, D. C., O'Driscoll, L., Théry, C., Welsh, J. A., Blenkiron, C., et al. (2021). Updating MISEV: Evolving the minimal requirements for studies of extracellular vesicles. *J. Extracell. Vesicles* 10 (14), e12182. doi:10.1002/jev2.12182

Wolff, G., Melia, C. E., Snijder, E. J., and Bárcena, M. (2020). Double-membrane vesicles as platforms for viral replication. *Trends Microbiol.* 28, 1022–1033. doi:10.1016/J.TIM.2020.05.009

Xia, X., Wang, Y., Huang, Y., Zhang, H., Lu, H., and Zheng, J. C. (2019). Exosomal miRNAs in central nervous system diseases: Biomarkers, pathological mediators, protective factors and therapeutic agents. *Prog. Neurobiol.* 183, 101694. doi:10.1016/J.PNEUROBIO.2019.101694

Xiao, Y., Wang, S. K., Zhang, Y., Rostami, A., Kenkare, A., Casella, G., et al. (2021). Role of extracellular vesicles in neurodegenerative diseases. *Prog. Neurobiol.* 201, 102022. doi:10.1016/J.PNEUROBIO.2021.102022

Xu, A. L., Rodriguez, L. A., Walker, K. P., Mohammadipoor, A., Kamucheka, R. M., Cancio, L. C., et al. (2019). Mesenchymal stem cells reconditioned in their own serum exhibit augmented therapeutic properties in the setting of acute respiratory distress syndrome. *Stem Cells Transl. Med.* 8, 1092–1106. doi:10.1002/SCTM.18-0236

Yao, Z., Qiao, Y., Li, X., Chen, J., Ding, J., Bai, L., et al. (2018). Exosomes exploit the virus entry machinery and pathway to transmit alpha interferon-induced antiviral activity. *J. Virol.* 92, e01578. doi:10.1128/JVI.01578-18

Yue, B., Yang, H., Wang, J., Ru, W., Wu, J., Huang, Y., et al. (2020). Exosome biogenesis, secretion and function of exosomal miRNAs in skeletal muscle myogenesis. *Cell Prolif.* 53, e12857. doi:10.1111/CPR.12857

Zhang, S., Liu, Y., Wang, X., Yang, L., Li, H., Wang, Y., et al. (2020). SARS-CoV-2 binds platelet ACE2 to enhance thrombosis in COVID-19. *J. Hematol. Oncol.* 13 (1), 120. doi:10.1186/s13045-020-00954-7

Zhao, T., Sun, F., Liu, J., Ding, T., She, J., Mao, F., et al. (2019). Emerging role of mesenchymal stem cell-derived exosomes in regenerative medicine. *Curr. Stem Cell Res. Ther.* 14, 482–494. doi:10.2174/1574888X14666190228103230

Zhao, Y. G., Codogno, P., and Zhang, H. (2021). Machinery, regulation and pathophysiological implications of autophagosome maturation. *Nat. Rev. Mol. Cell Biol.* 22 (11), 733–750. doi:10.1038/s41580-021-00392-4

Zheng, J., Shi, Y., Feng, Z., Zheng, Y., Li, Z., Zhao, Y., et al. (2019). Oncogenic effects of exosomes in γ-herpesvirus-associated neoplasms. *J. Cell. Physiol.* 234, 19167–19179. doi:10.1002/JCP.28573

frontiers | Frontiers in Nanotechnology

TYPE Review
PUBLISHED 10 August 2023
DOI 10.3389/fnano.2023.1216921

OPEN ACCESS

EDITED BY
Sonu Gandhi,
National Institute of Animal Biotechnology (NIAB), India

REVIEWED BY
Meghana Ramani,
Wayne State University, United States
Zijiao Zhang,
Microsoft, United States

*CORRESPONDENCE
Ana Lucía Campaña,
a.l.c.perilla@fys.uio.no
Dirk Linke,
dirk.linke@ibv.uio.no

RECEIVED 04 May 2023
ACCEPTED 02 August 2023
PUBLISHED 10 August 2023

CITATION
Campaña AL, Saragliadis A, Mikheenko P and Linke D (2023), Insights into the bacterial synthesis of metal nanoparticles. *Front. Nanotechnol.* 5:1216921. doi: 10.3389/fnano.2023.1216921

Insights into the bacterial synthesis of metal nanoparticles

Ana Lucía Campaña[1]*, Athanasios Saragliadis[2], Pavlo Mikheenko[1] and Dirk Linke[2]*

[1]Department of Physics, University of Oslo, Oslo, Norway, [2]Department of Biosciences, University of Oslo, Oslo, Norway

Metal nanoparticles have attracted considerable attention due to their astounding potential for a wide range of commercial applications. From targeted drug delivery and antimicrobial agents to electronics, metal nanoparticles seem to have immeasurable prospects in all areas of science. However, modern industrial production frequently involves complex procedures, large amounts of energy, utilizes strong chemical solvents, or produces hazardous waste. Biological synthesis has been proposed as an alternative for simpler, inexpensive, and more eco-friendly metal nanoparticle production. Microorganisms possess multiple mechanisms to transport, regulate and bind metal ions that may result in the biosynthesis of nanoparticles. They can synthesize even complex bimetallic nanoparticles, which are difficult to produce with normal chemical and physical processes. A better understanding of bacteria-metal interactions might thus pave the way for a wide array of industrial applications. This review will summarize the current methods for metal nanoparticle synthesis, with a focus on the microbial (bio) synthesis of nanoparticles. We will describe the general mechanisms of bacteria-metal ion interactions, including cellular uptake and the subsequent reduction into nanoparticles. Protocols for the production of metal-based nanoparticles of relevant elements with different bacterial strains are compiled and the current challenges in bacterial synthesis of metal nanoparticles in the industry are discussed.

KEYWORDS

bacteria, metal nanoparticles, biosynthesis, nanoparticles, bionanotechnology

1 Introduction

Nanoparticles (NPs) are defined as nano-structures with dimensions of 1–100 nm that can be comprised of a variety of materials such as carbon, metal, or organic substances. At the limits of this dimensions in the range of 1–10 nm, some literature may also referred to them as nanoclusters which are typically composed of up to 100 atoms and possess relevant physicochemical properties (Jimenez-Sandoval et al., 2023). Metal-based nanoparticles (MNPs) contain at least one metallic element and can display diverse shapes. Most of them have different properties compared to bulk metals due to their large surface-to-volume ratio, unique electromagnetic behavior, and high catalytic activity (Gao et al., 2021). In this review, a variety of MNPs is described, which not only comprise pure metals nanoparticles (e.g., Au, Ag, Pd, Pt, Fe), but also minerals or metal oxides NPs (e.g., Fe_2O_3, Co_3O_4, TiO_2), metal sulfides (e.g., Fe_3S_4, CdS), doped metal/metal compounds, and metal-organic complexes (Yaqoob et al., 2020).

The unique behavior of nanoparticles and other nanostructured materials is strictly size-dependent and can provide improved functional performance in a variety of technical

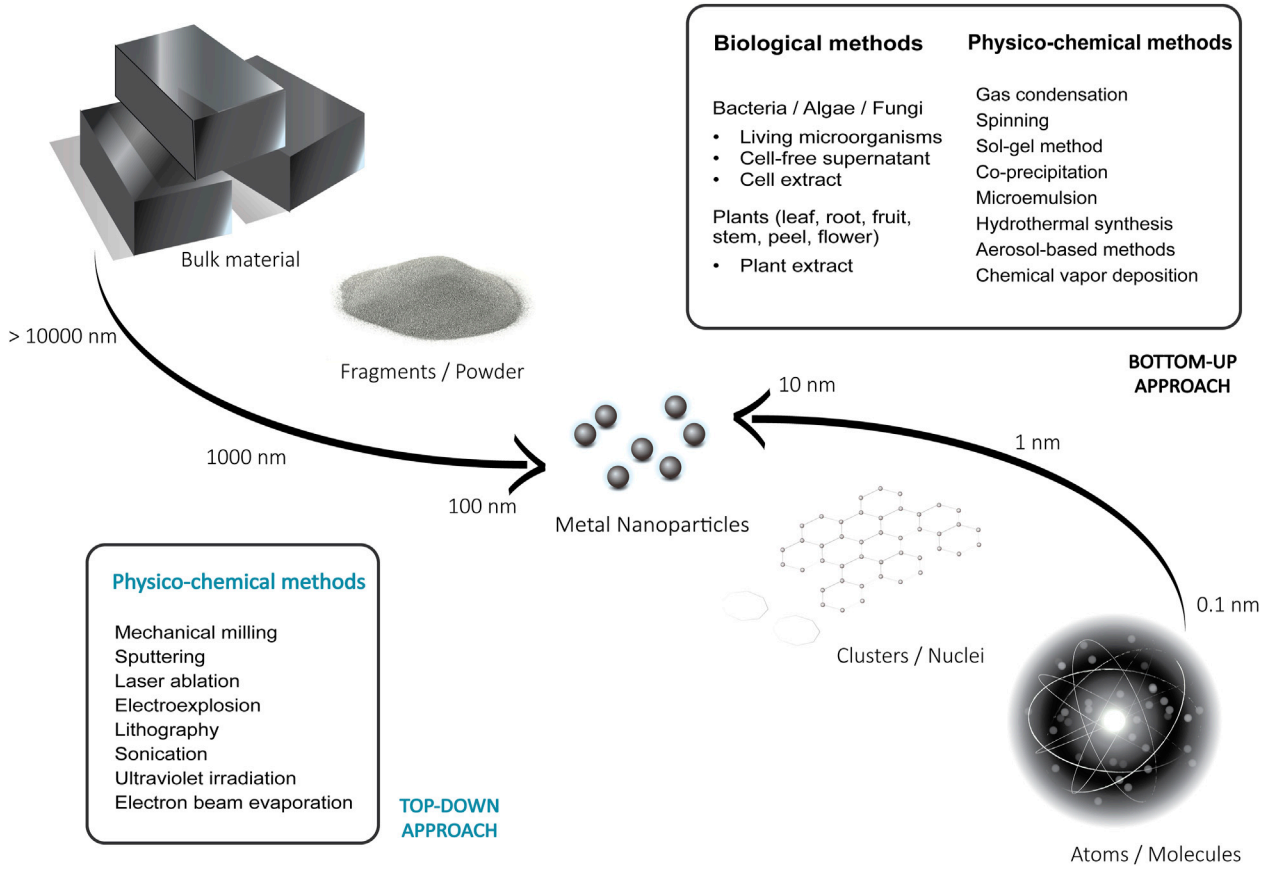

FIGURE 1
Illustration of the top-down and bottom-up approaches for the synthesis of metal nanoparticles.

applications. Examples of industrial applications of MNPs include their use in chemical catalysis, cosmetics, detergents, water remediation, and even medical applications. The particular electromagnetic properties of Fe-based nanoparticles have secured their place as one of the most frequently used contrast agents in medical imaging (Javed et al., 2017; Makela et al., 2022) while the antibacterial properties of Ag have been effectively enhanced when it is used in the nanoparticle form (Nanda and Saravanan, 2009; Jaidev and Narasimha, 2010; Oves et al., 2019; Das et al., 2020). The large active surface of MNPs makes them highly reactive, and therefore, nanoparticles based on Ag, Ni, Pt, Pd, and others, are distinctly effective in heterogeneous catalysis (Bogireddy et al., 2016; Weng et al., 2017; Stephen et al., 2019; Krebsz et al., 2021). Pd nanoparticles are an example of an efficient catalyst of Suzuki-Miyaura reactions, in which carbon-carbon single bonds are formed to produce a complex variety of molecules that are especially important for the pharmaceutical industry (Søbjerg et al., 2009). Other useful potential applications include the degradation of a variety of toxic Azo dyes present in the wastewater produced by the textile industries (Bogireddy et al., 2016; Narasaiah and Mandal, 2020; Krebsz et al., 2021), and their use in anticancer treatments (Patil et al., 2022).

The targeted production of nanoparticles with specific properties such as defined shapes or size distributions requires strict control of the experimental conditions. Small changes in the production process can have a strong effect on the size, crystallinity, porosity, roughness, and the shape of the produced nanoparticles (Vijayakumar et al., 2013; Jamkhande et al., 2019). Current methods for MNP synthesis are based on different chemical, physical, or biological methods, which can be classified into two major categories: (a) top-down and (b) bottom-up approaches (Figure 1). The preferred approach is dependent on the desired particles characteristics, the size of production, cost of operation, and the applications intended for the produced nanoparticles (de Jesus et al., 2021).

Top-down methods involve physical or chemical processes that aim to reduce or decompose large substrates or bulk materials. Preparation of MNPs by these methods allows the large-scale production of the high purity nanoparticles, which is crucial for many applications. It includes methods such as mechanical milling (Shojaei et al., 2021), sputtering (Orozco-Montes et al., 2021), chemical etching (Butterfield et al., 2020), laser ablation (Menazea, 2020), electroexplosion (Lozhkomoev et al., 2021), lithography (Fu et al., 2018), sonication (Tang et al., 2019), ultraviolet irradiation (Henglein, 1999), and electron beam evaporation (Nomoev and Bardakhanov, 2012). Traditional top-down methods can produce particles with well-controlled shapes and uniform sizes, however, they usually require specialized fabrication facilities, large amounts of energy, produce hazardous waste and entail high production costs (Fu et al., 2018). Additionally,

most of them are not suitable for the preparation of extremely small-sized nanoparticles (<10 nm) (Fu et al., 2018; Jamkhande et al., 2019).

In the bottom-up approaches, dissolved or evaporated substances are used as the basis for growth and synthesis of the particles. Using a variety of chemical reactions and physical processes, the building blocks are assembled by controlled precipitation, crystallization and condensation with a low energy input to result in the nanoparticles (Chan and Kwok, 2011). These bottom-up approaches are widely used, as they tend to be more accessible and cheaper compared to the top-down methods. Among them are gas condensation (Zheng and Branicio, 2020), spinning (Stoller and Ochando-Pulido, 2020), sol-gel method (Parashar et al., 2020), co-precipitation (Andrade Neto et al., 2020), microemulsion technique (Mangaiyarkarasi et al., 2020), hydrothermal synthesis (Vinay et al., 2020), aerosol-based methods (Quintanilla et al., 2010; Yang et al., 2020; Gautam et al., 2021), plasma arcing (Tavares et al., 2008), and chemical vapor deposition (Katsui and Goto, 2021). Frequently, they are referred to as wet methods since most of them involve solvents, stabilizers, reducing agents and other chemicals. Nanomaterials produced by these methods often must be capped to restrict the particle growth and to obtain homogeneous nanoparticle populations. Capping agents are stabilization molecules widely employed to control the material's particle size, agglomeration, and morphology. They attach to the surface of the nanoparticle and reduce the surface energy, which has a direct effect on the dispersion of the NPs in wet media. Examples include gums, cationic surfactants, polymers, and plant extracts (Restrepo and Villa, 2021). The toxicity of some of the capping agents and other chemicals involved in this process has proven to be an important disadvantage of the techniques, along with the lack of precise control of particle shape, size and dispersity (Fu et al., 2018). As an alternative, bio-based methods have received increasing attention, as they promise a more reliable, non-toxic and eco-friendly synthesis of MNPs (Iravani, 2014).

The production of metal nanoparticles using biological methods belongs to the bottom-up approaches. A great variety of organisms such as plants, bacteria, fungi, and algae have been explored for their potential to synthesize for example silver, gold, iron, palladium, selenium, zinc, and platinum-based nanoparticles (Iravani, 2014; Ahmad et al., 2019; Li et al., 2021; Li et al., 2022). In addition, not only living organisms, but also many chemical substances derived from the metabolism of microbes and plants, such as biopolymers and biological extracts have been proposed as agents for the biological synthesis of MNPs (de Jesus et al., 2021; Soni et al., 2021). The natural reduction and stabilization agents in these reactions result in a potentially more sustainable synthesis compared to current chemical and physical methods. In general, these biological methods are considered to be more inexpensive, non-toxic, and environmentally benign as most reactions occur at room temperature and with a low energy input (Prasad et al., 2021). However, it is pertinent to note that these bio-nanoparticles tend to be polydisperse and difficult to purify. Some of the most significant challenges of nanoparticle biosynthesis include the control of size distribution and dispersity. In addition, it is important to understand the pathways of reduction that may lead to efficient nanoparticle production, and to develop suitable purification protocols (Khalil et al., 2022).

Reports on the synthesis of nanoparticles with bacteria can be categorized into three main methodologies, where NP production is mediated by intact living cells, by bacterial cell-free supernatants, or by cell lysate supernatants (cell extracts). In contrast to NPs formed by intact bacterial cells, supernatant-based synthesis has the advantage of a simpler downstream purification, characterization, and easy visualization of the produced NPs. Most importantly, this biosynthesis is not directly mediated by the metabolic processes of the bacteria, but only by the functional groups of the bacterial proteins or other biomolecules present in the reaction mixture and can be more directly influenced by the experimental conditions. Nanoparticles produced by biological methods are usually capped with non-toxic biomolecule coatings. These bio-coatings can enhance bio-compatibility of the particles e.g., in medical applications, and can also work as stabilizers that promote the formation of homogeneous small-size nanoparticles by preventing their aggregation (Ahmad et al., 2019). An example is the reduced toxicity of iron oxide nanoparticles by the addition of a biocompatible coating of polysaccharides that enables targeted delivery of materials for cancer therapy (Kianpour et al., 2019). The biological synthesis of metal nanoparticles has many potential uses not only in biomedical applications, but also in bioremediation, bioleaching, and biocorrosion (Narayanan and Sakthivel, 2010).

This review provides a comprehensive description of the biological synthesis of metal nanoparticles by bacteria, both in nature and in technical processes. We focus not only on the general interaction of metal ions with bacteria, but also include the findings on the pathways that lead to their reduction and subsequent nanoparticle formation. Examples of recent advances in MNP synthesis using different bacterial strains are presented and their potential applications are reviewed. Finally, the current challenges of the industrial production of metal nanoparticles by bacteria are discussed.

2 Bacteria-metal interactions

Bacteria have ubiquitous interactions with metals. They can be classified into the homeostasis of essential metals, and (heavy) metal resistance to harmful metals. Some metals are important as micronutrients whereas other (heavy) metals (such as Al, Pd, Cd, Au, Hg, Ag) are toxic to living organisms and do not have specific biological roles (Igiri et al., 2018). The essential metals are nutrients and trace elements for key metabolic processes, such as metals in the bacterial respiratory chain. Therefore, microbes have developed a variety of often highly specific mechanisms for metal transport, oxidation/reduction, or detoxification. Nevertheless, the unintentional uptake of high concentrations of metal ions or toxic heavy metals can occur, and microorganisms have developed different strategies to cope with heavy metal stress. Microbial populations can survive in metal-polluted locations by, directly or indirectly, modifying the metal availability through physical or biochemical mechanisms to protect their integrity (Iravani, 2014). The complex mechanisms developed by different species and strains vary and depend both on the native environment and on the heavy metal content. The basic mechanisms of bacteria-metal interactions can be divided into the following four categories:

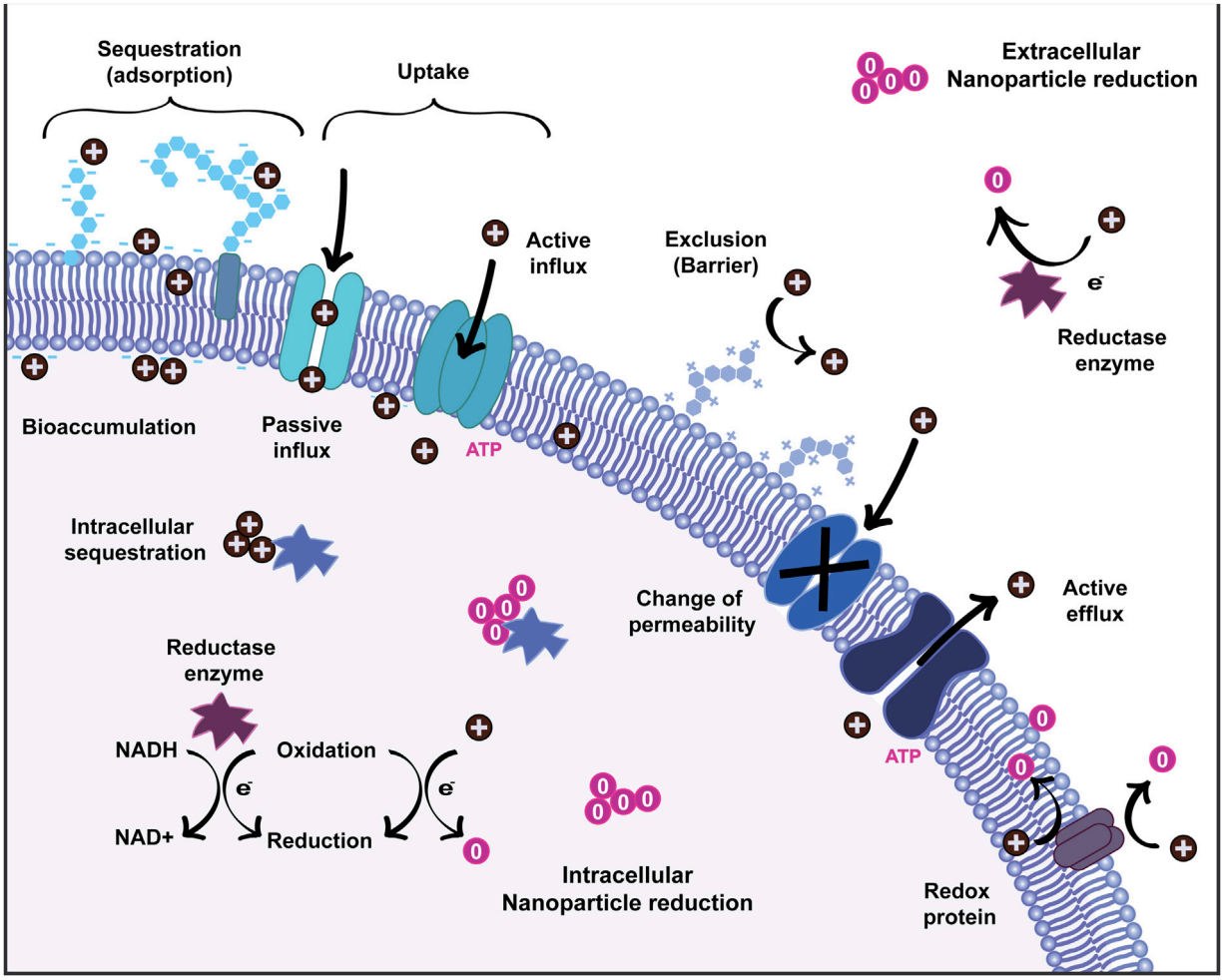

FIGURE 2
Schematics of bacteria interaction with heavy metals and mechanisms of nanoparticle formation.

2.1 Metal sequestration

Many essential biological processes involve metal ions, and in particular, redox active transition metals like manganese, iron, cobalt, copper and magnesium. For instance, divalent ions such as Mn^{2+} and Fe^{2+}, are indispensable for oxidative stress resistance or as cofactors for the respiratory chain in bacterial core metabolism (Palmer and Skaar, 2016). Hence, microorganisms have evolved pathways of metal sequestration to transport ions and to regulate ion availability. In the simplest case, the sequestration of metal ions occurs by adsorption. In Figure 2, metal ions are depicted as positively charged entities interacting with the bacterial membrane and other biomolecules. During adsorption, deprotonated functional groups (carboxyl, phosphonate, amine, and hydroxyl groups) on the cell surface result in a net negative charge which attracts metal cations and leads to non-specific binding of the metal to the cell surface (Saravanan et al., 2021). This process is independent of the cell metabolism, and it is mainly influenced by factors such as temperature, pH, ionic strength, concentration and by the complex composition of the microorganism's surface. As an example, Gram-positive bacteria expose a large amounts of carboxyl groups in their peptidoglycan-rich cell walls, making them efficient metal chelators (Pham et al., 2022). As a consequence of this sequestration, these metals are enriched on the cell surface and can be taken up by specific transport processes (discussed below).

However, the extracellular sequestration of heavy metals not only allows to accumulate relevant metabolic cofactors, it is also a defense mechanism against toxic metals, by reducing the availability of unwanted metal ions. Polymers secreted by bacteria such as the exopolysaccharide (EPS) coatings of some species, have the ability to adsorb and bind metals extracellularly, thus acting as a protective layer that prevents the uptake of toxic metals (Bruins et al., 2000). Bacteria are likely to sequester non-essential metal ions, such as Au and Pd, by adsorption mechanisms. Compared to other microorganisms, Gram-negative bacteria such as *Acinetobacter calcoaceticus*, *Erwinia herbicola*, *Pseudomonas maltophilia* and *Pseudomonas aeruginosa* have the highest ability to accumulate metals such as gold (Tsuruta, 2004). This is a result of the surface charge present on the Gram-negative bacterial membrane, which promotes the gold adsorption from aqueous solutions. In the same way, the biosorption of Pd is presumably a result of the

chemical affinity of metal complexes such as $[PdCl_4]^{2-}$ for protonated groups on the cell surface at an acidic pH (Deplanche et al., 2010).

Free metal ions passively or actively transported from outside of the membrane into the cytoplasm can pose a danger to the cell and must be immobilized or transformed. Bacteria can produce metabolites, like metallothioneins, phytochelatins and glutathione with high affinity for metals for the intracellular sequestration of metal ions. Metallothioneins are small, cysteine-rich proteins that are directly involved in the homeostasis of different metal ions, including Cu^{+} and Zn^{2+}. These proteins have been reported in bacteria such as *Bacillus altitudinis* MT422188 and *Mycobacterium tuberculosis* where they are expressed under Zn^{2+} and Cu^{+} induced stress, respectively (Johnstone and Nolan, 2015; Khan et al., 2022). The immobilization of the ions decreases the toxicity; however, the metal sequestration mechanisms are limited by the saturation of the binding sites in the extracellular and intracellular matrix (Bruins et al., 2000).

2.2 Metal uptake

The metal ions in proximity to the extracellular layers can be imported by passive or active influx through the different layers of the cell wall, using non-specific transporters, metal-specific channels or passive diffusion (Figure 2) (Bruins et al., 2000). The indispensable uptake of essential metals is highly regulated and typically mediated by specific, energy-dependent uptake systems. In *E. coli, Alcaligenes eutrophus* and many other enterobacteria, essential trace elements such as Ni^{2+}, Co^{2+}, and Zn^{2+} ions are transported into the cell by constitutive Mg^{2+} transport systems (Nies, 1992; Komeda et al., 1997). These relatively unspecific uptake systems allow the "cost-effective" accumulation of macronutrients such as Mg and of trace metal ions in environments with habitual metal concentrations. In extreme conditions, with deficits in trace metals, bacteria can upregulate genes related to specific, ATP-dependent uptake systems for these elements in order to transport the ions against the concentration gradient. The TonB-dependent transporter, OprC, is repressed in *P. aeruginosa* by high exogenous Cu ion concentrations and expressed in anaerobic conditions to bind and transport $Cu^{+/2+}$ (Bhamidimarri et al., 2021). In environments with low availability of essential metals, many bacteria also secrete metal-sequestering proteins or other chelators to bind the biologically relevant ions and to specifically import them (Palmer and Skaar, 2016). An example of this mechanism are iron siderophores, which are low molecular weight compounds known for their high affinity for Fe ions. Siderophores are frequently used by pathogenic bacteria to chelate Fe^{2+} and Fe^{3+} in host environments that are otherwise deprived of free Fe ions (Johnstone and Nolan, 2015). The siderophores with bound ions are then recognized by specific outer membrane receptors that guide the chelated ions through energy-dependent ATP-binding cassette (ABC) transporters (Krewulak and Vogel, 2008; Ma et al., 2009). Because of the different chemical properties of Fe^{3+} and Fe^{2+}, bacteria utilize different specific transport systems (and siderophores) for each ion (Lau et al., 2016; Crespo et al., 2017). Examples of different transport systems involved in bacterial Fe uptake, include MntH, ZupT, YfeABCD, FutABC, EfeUOB and Feo (Lau et al., 2016).

The uptake of precious metals like Au, Ag, Pt, and Pd ions into bacteria is not well understood, as cells do not possess inherent active, specific transport mechanisms to regulate non-essential ion uptake. The absorption of toxic heavy metals is presumably a process carried out by passive mechanisms such as diffusion. Therefore, at elevated concentrations, non-essential metals can interact with the cell, cross into the cytoplasm and accumulate there (Lusa et al., 2016). However, some authors suggest that heavy metals like Pd may also accidentally be absorbed and imported into living cells through systems specific for essential metallic metabolites, such as Fe, Ni, Cu or Zn (Omajali et al., 2015). Metal ions with comparable properties and ion radius, due to their similar conformations, can out-compete essential ions in binding to proteins. As an example, the high affinity of Hg and Cd ions to cysteine-rich sites in Zn-binding proteins results in translocation of these toxic metals. A similar effect is found in Cu-binding proteins with Au and Ag as competing metal ions (Waldron and Robinson, 2009). A special case of non-essential metal uptake is the homeostasis mechanism of specialized metal-resistant bacterial strains for some toxic heavy metal ions. In the case of *Cupriavidus metallidurans*, genes in the *gig* (gold-induced genes) operon are strongly upregulated after sequestration of Au ions in the membrane. The proteins encoded by this operon are suggested to be directly involved in the import of Au ions into the cytoplasm to prevent the harmful action of Au^{3+} in the periplasm. The reduced complexes there are later removed from the cytoplasm (Wiesemann et al., 2013; Zammit and Reith, 2013).

2.3 Metal detoxification

If not regulated, high concentrations of metals would have adverse effects in the metabolic processes of the cell. In metals such as Cu, their redox activity favors the formation of active oxygen species, which explains their toxicity. Excess of essential metals or toxic, non-essential heavy metals also leads to mismetallation of proteins which results in their inactivation (Andrei et al., 2020). The exposure to high concentrations of heavy metals activates a mechanism of defense called metal exclusion, in which the permeability of the cell membrane, the envelope, or the surface layer is modified to prevent or reduce the further influx of metal ions (Figure 2). Bacteria can alter the composition of the cell wall in an attempt to form a barrier for ions. A well-known example of this mechanism is the reduction of the expression of Porin channels in heavy-metal resistant mutants of *E. coli*. In this case, pore proteins such as OmpF are expressed at a reduced rate, leading to increased Cu and Ag resistance (Lutkenhaus, 1977; Rouch et al., 1995; Li et al., 1997). In a complementary mechanism, the active efflux of metal ions involves the use of highly specific membrane transport systems. This process to decrease the concentration of harmful metal ions inside the cell is wide-spread among bacteria. The transport of cations and anions from the cytoplasm against a concentration gradient requires energy. The involved efflux pumps can be broadly classified by their energy source into ATP-dependent and proton-gradient-based systems. Further classifications are based on sequence similarity, transport function and substrate specificity (Nies and Silver, 1995; Hynninen, 2010; Delmar et al., 2014).

TABLE 1 List of relevant standard reduction potential (E_0) in respect to the standard hydrogen electrode at 298.15 K (25°C), 101.325 kPa (1 atm). The list is in alphabetical order, according to the symbol of metal element. Taken from Haynes, (2014).

Reaction	E_0 (Volts)
$Ag^+ + e \rightleftharpoons Ag$	0.7996
$AuCl_4^- + 3\ e \rightleftharpoons Au + 4\ Cl^-$	1.0020
$Cd^{2+} + 2\ e \rightleftharpoons Cd$	−0.4030
$Co^{2+} + 2\ e \rightleftharpoons Co$	−0.2800
$Co^{3+} + e \rightleftharpoons Co^{2+}$	1.9200
$Cr^{2+} + 2\ e \rightleftharpoons Cr$	−0.9130
$Cr^{3+} + e \rightleftharpoons Cr^{2+}$	−0.4070
$Cr^{3+} + 3\ e \rightleftharpoons Cr$	−0.7440
$Cr_2O_7^{2-} + 14\ H^+ + 6\ e \rightleftharpoons 2\ Cr^{3+} + 7\ H_2O$	1.3600
$Fe^{2+} + 2\ e \rightleftharpoons Fe$	−0.4470
$Fe^{3+} + 3\ e \rightleftharpoons Fe$	−0.0370
$Fe^{3+} + e \rightleftharpoons Fe^{2+}$	0.7710
$2\ HFeO_4^- + 8\ H^+ + 6\ e \rightleftharpoons Fe_2O_3 + 5\ H_2O$	2.0900
$Mn^{2+} + 2\ e \rightleftharpoons Mn$	−1.1850
$Mn^{3+} + e \rightleftharpoons Mn^{2+}$	1.5415
$MnO_2 + 4H^+ + 2\ e \rightleftharpoons Mn^{2+} + 2\ H_2O$	1.224
$Ni^{2+} + 2\ e \rightleftharpoons Ni$	−0.2570
$[PdCl_4]^{2-} + 2\ e \rightleftharpoons Pd + 4\ Cl^-$	0.5910
$[PdCl_6]^{2-} + 2\ e \rightleftharpoons [PdCl_4]^{2-} + 2\ Cl^-$	1.2880
$[PtCl_4]^{2-} + 2\ e \rightleftharpoons Pt + 4\ Cl^-$	0.7550
$[PtCl_6]^{2-} + 2\ e \rightleftharpoons [PtCl_4]^{2-} + 2\ Cl^-$	0.6800
$TcO_4^- + 8\ H^+ + 7\ e \rightleftharpoons Tc + 4\ H_2O$	0.4720
$Ti^{2+} + 2\ e \rightleftharpoons Ti$	−1.6280
$UO_2^{2+} + 4\ H^+ + 6\ e \rightleftharpoons U + 2\ H_2O$	−1.4440
$Zn^{2+} + 2\ e \rightleftharpoons Zn$	−0.7618

Some examples of well-studied heavy metal efflux pumps are the P-type ATPase transport protein CopA, known to be involved in copper resistance (Rensing et al., 2000) and the resistance-nodulation-cell division (RND) family proteins, CzcA and CusA, which bind and export Cu^+ and Ag^+ in *E. coli* (Kim et al., 2011). In partly silver-resistant *E. coli* bacteria, the detoxification mechanism for silver is based on the expression of the CusCFBA copper/silver efflux systems that actively export the silver ions from the cytoplasm and bind it in the periplasm (Lin et al., 2014). In some bacteria, metal ions transported by efflux pumps may be retained in the periplasm even after the efflux process, along with the metal ions sequestered by EPSs and by other metal-binding proteins (Blindauer, 2011). The ions bioaccumulated in the cytoplasm, periplasm and in the extracellular matrix can later become sites for nucleation and formation of nanoparticles (Figure 2).

2.4 Metal transformation

Some microorganisms have a remarkable ability to transform heavy metal ions in their environment and to produce MNPs. Even when sequestered, the high reactivity of transition metal ions could disrupt metabolic processes or damage DNA molecules. Various metal ions have a high binding affinity for biological macromolecules such as nucleic acids, or thiol-containing proteins (Delmar et al., 2014; Boedicker et al., 2021), and therefore, they need to be transformed into inert or less toxic substances. This is mediated by redox-active metabolic pathways in order to change solubility and toxicity, and often leads to complexation or precipitation of metals extracellularly (Silver, 1996; Bruins et al., 2000; Hood and Skaar, 2012). Alternatively, biomethylation is a metabolic process in which methyl groups are transferred to the toxic metal ions or metalloids to create less toxic, sometimes volatile compounds. Hg, Sn, As, Se, Te, Au, Tl, and Pb have been reported as methyl group acceptors in primary and secondary metabolic processes (Kosolapov et al., 2004). The resulting products are more toxic than the inorganic compounds in many cases, so it is debatable whether methylation is, in fact, a detoxification mechanism. However, it is important to note that the volatility has an important effect on reducing the concentration of the metals in the surrounding environment. Extended descriptions of the general pathways for biomethylation can be found elsewhere (Ridley et al., 1977a; Ridley et al., 1977b; Fatoki, 1997).

Some bacteria can decrease the mobility of metal ions through enzymatically promoted redox reactions that reduce the metals irreversibly, leading to the assembly into metal clusters. An illustration of the general process of reduction of the metal ions to neutral ions by redox proteins intra- and extracellularly can be found in Figure 2. The electron-accepting potential of different metal ions known to be reduced by bacteria are shown in Table 1. The reduction potential is expressed as the E_0 value, ranging from very negative E_0 values for compounds that are easily oxidized, to large positive E_0 values for compounds that readily accept electrons (are easily reduced). "Precious" metals such as Au, Pd or Ag have cations species with very positive potentials and are frequently reduced into nanoparticles by bacteria.

The cornerstone of every living organism is energy conservation where chemical or light energy is ultimately converted into adenosine triphosphate (ATP). ATP production is facilitated by substrate-level phosphorylation, oxidative phosphorylation, or photophosphorylation. In order to achieve this, electrons need to be transferred in an oxidation-reduction coupled reaction. This electron movement within the cell is facilitated by electron carriers, such as nicotinamide adenine dinucleotide (NAD^+/NADH), which promotes a diversity of reduction-oxidation reactions as they allow a variety of electron partners to interact with each other (Muller, 2003; Herrmann et al., 2008; Schuchmann and Müller, 2012). It is these metabolic reactions and electron carriers that are diverted and used for metal ion reduction.

On an extracellular level, bacterial growth is heavily influenced by the oxidation-reduction (redox) potential of the environment, and in turn, bacteria can modify the redox potential of their environment. Surprisingly, this ability is highly species-specific and can be exploited to identify different species by using redox

electrodes (Reichart et al., 2007). A change in redox potential indicates the availability of electron acceptors and donors. Since bacteria can inhabit every niche that can support life, their diversity is also manifested in the type of electron acceptors that they can utilize intracellularly. Under aerobic respiration conditions, oxygen is the final electron acceptor while under anaerobic respiration conditions, a variety of electron acceptors can be utilized, such as nitrate (NO^{3-}), trimethylamine oxide/dimethyl sulfoxide (TMAO/DMSO), carbon dioxide (CO_2) or organic electron acceptors such as fumarate, depending on the bacterial species studied (Kröger et al., 1992; Vincent et al., 2021). Metal-based respiration is characterized by the utilization of manganic manganese (Mn^{4+}) or ferric iron (Fe^{3+}) as electron acceptors. Bacteria can reduce these metal compounds through mechanisms that involve redox-active proteins like reductases, cytochromes, and metallothioneins (Bloch et al., 2021).

Sulfate- and metal-reducing bacteria are frequently employed for the synthesis of metal nanoparticles, as these organisms are rich in membrane redox-active proteins and therefore easily enzymatically reduce different metal ions. These 'reducing' microorganisms can use the metal cations as terminal electron acceptors while performing anaerobic respiration, reducing Fe^{3+} to Fe^{2+} and Mn^{4+} to Mn^{2+} for energy conservation (Lloyd, 2003). These proteins however, are not necessarily highly specific and multiple enzymes are capable of reducing several redox-active metals ions (Barton and Fauque, 2009). The interaction of some bacteria with non-essential, toxic metal ions such as Au^{3+}, Ag^{+}, Pd^{2+} and Pt^{2+} also upregulates the expression of multiple redox-active enzymes located on the cell walls, in periplasmic space and intracellular contents, such as hydrogenases and NADH reductases, which can reduce ions to insoluble complexes that are subsequently transformed into MNPs (Omajali et al., 2015; Chen et al., 2019). One example is nitrate reductase known to be involved in the bioreduction of the bound Ag^{+} to Ag^{0} in *Bacillus licheniformis* as defense from heavy metals exposure (Kalimuthu et al., 2008; Rajora et al., 2016). As suggested by their negative reduction potential (Table 1), the NAD(P)H-dependent reduction of ions such as Cd^{2+}, Zn^{2+}, Co^{2+} or Ni^{2+} to metallic form may not be energetically favored, so the reduction of these ions is uncommon in bacteria and the particular cases of reduction must involve different mechanisms (Nies, 1992). In *Shewanella* strains, EPS-induced reduction and indirect electron transfer using electron shuttles such as flavins, L-cysteine, and quinones are possible alternative pathways that have been thoroughly described elsewhere (Yang et al., 2023). Metal NPs reduced and precipitated in the extracellular and intracellular space may possess different characteristics than their chemically produced counterparts. The biomolecules associated with them create a biological cap that stops nanoparticle growth, minimizes cytotoxicity, and may affect their chemical and physical properties (Bulgarini et al., 2021). The reduced metal particles accumulate without much effect on the cell population. Therefore, the formation of MNPs can be regarded as a by-product of microbial defense mechanisms, of bacterial metabolism, or as a biomineralization process intended to control, immobilize, or decrease the heavy metal bioavailability.

3 Bacterial synthesis of nanoparticles

During the microbial reduction of metals into MNPs, cations are transformed into ions with a lower valence. A special case is the precious metals, including Pd, Pt, Au, and Ag, that are easily reduced into elementary forms (Zhan et al., 2012). The challenge of producing nanoparticles using bacteria, is identifying the exact chemical components and mechanisms involved in nanoparticle formation. The pathways may result in nanoparticles formed only extracellularly, intracellularly, or both, and there is a debate about which method is the most efficient for production of NPs in industrial processes. The intracellular nanoparticles formed in living cells are attached to the biological material, making their purification difficult; however, capping of the nanoparticles provides better control of their size, generating more homogeneous populations of biocompatible nanoparticles with interesting novel physical and chemical properties. In contrast, nanoparticles produced externally are preferred in many cases due to their faster production, facile recovery, and simple purification. These extracellular nanoparticles can be produced using bacterial cell-free supernatants, cell lysate supernatants, and some living bacterial strains. In this section, examples of relevant metal-based nanoparticles produced by bacteria are described.

3.1 Bacterial metal nanoparticles in nature

Even though naturally occurring nanoparticles are widely found in living organisms, the intracellular accumulation of solid metals is usually not a favorable condition for the cells and can lead to cell death. A complete metal particle detoxification would require energy and elaborated mechanisms of particle excretion (Griffin et al., 2017). This is probably the reason why only few bacterial species produce metal-based nanoparticles as part of their normal metabolic processes. The most remarkable example are magnetotactic bacteria, an extraordinary group of Gram-negative organisms that rely on biosynthetic iron-based crystals to orient and migrate along the geomagnetic field lines in a behavior known as "magnetotaxis" (Yan et al., 2012). The highly specialized organelles made of nanometer-sized metal crystals wrapped in a membrane are called magnetosomes. They are composed of magnetic iron oxide magnetite (Fe_3O_4) or iron sulfide greigite (Fe_3S_4) of different shapes and sizes depending on the exact bacterial species. The magnetosomes are frequently aligned in chains across the motility axis of the cell. This imparts the bacteria with a permanent magnetic dipole moment, causing them to align passively in a parallel orientation with external magnetic fields (Monteil and Lefevre, 2020). The cells swim along the geomagnetic field lines of the Earth to the oxic-anoxic interface of the aquatic habitat where are the most favorable conditions for growth (Le Nagard et al., 2018).

Despite the abundance of magnetotactic bacteria in the environment, only a few strains have been isolated into pure culture due to their particular growth requirements. Strains from the proteobacterial genus *Magnetospirillum* are the most common isolates. However, recent publications report up to 16 different lineages that include *Proteobacteria*, *Nitrospirota*, and *Omnitrophota* (Gareev et al., 2021; Goswami et al., 2022). The

strains *Magnetospirillum gryphiswaldense* MSR-1 [first isolated in 1991 by Schleifer *et al.* (Schleifer et al., 1991)], *Magnetospirillum magnetotacticum* strain MS-1 and *Magnetospirillum magneticum* AMB-1, are currently the most studied bacteria for the understanding of magnetosome formation and its complex genetic regulation (Nudelman and Zarivach, 2014). In *M. gryphiswaldense* MSR-1, the magnetosome island (MAI) comprises most of the genes that control the magnetosome synthesis. These genes encode all the essential processes in the majors steps of the organelle formation and determine the morphology and chemical composition of the particles (Uzun et al., 2020; Dziuba et al., 2021). In the past, different models of magnetosome biomineralization have been proposed (Schuler, 2002; Yan et al., 2012; Nudelman and Zarivach, 2014). Currently, four major steps are considered necessary to achieve the biomineralization. The first step is i) the cytoplasmic membrane invagination into vesicles, followed by ii) the arrangement of specific magnetosome proteins into the organelle membrane. Then, iii) the internalization and accumulation of iron into the vesicles by energy-dependent transport proteins takes place. Here, the cell rapidly chemically transforms the Fe ions and combines them into metal crystals. Specific proteins guide this process in order to avoid the toxic effect of intracellular Fe. Finally, iv) the magnetosomes are assembled into a linear chain along cytoskeletal filaments (Dziuba et al., 2021).

The bacteria tightly controls the size and morphology of the magnetosomes. Magnetosome crystals typically fall in a size distribution of about 30–120 nm. However, some species can form particles up to 250 nm in length (Yan et al., 2012). The spirillum-shaped bacterium *M. magneticum* AMB-1, originally collected from fresh water sediments of a natural spring in Tokyo, presents magnetite magnetosomes with an average diameter of 50 nm, aligned in chains of around 15 particles per cell (Matsunaga et al., 1991). In contrast, the *M. gryphiswaldense* MSR-1 bacteria were found to produce chains of up to 60 homogeneous magnetosomes with particle sizes of around 42 nm (Schuler, 2002). Both strains, like other bacteria from the *Magnetospirillum genus*, produce cubo-octahedral crystalline magnetosomes. In general, three different morphologies of magnetosomes can be found in nature: i) cubic or cubo-octahedral, ii) elongated hexa- or octahedral and iii) even more elongated crystals with large, anisotropic faces, showing tooth, arrowhead, or bullet shapes (Cypriano et al., 2022). These crystal structures are consistently replicated in the magnetosomes of bacteria of the same strain and have a direct influence on the final magnetic behavior of the particles.

The magnetosomes, due to their narrow size distribution, low aggregation, and strong ferromagnetism, have many potential technical applications. The low toxicity of bacterial magnetosomes in comparison with synthetic magnetic nanoparticles makes them especially attractive for biomedical applications. Cytotoxicity of bacterial magnetosomes varies depending on various factors, including cell type, incubation time, and concentration. While many types of magnetite nanoparticles [such as Superparamagnetic iron oxide nanoparticles (SPION)] are considered cytotoxic at exposure levels above 70–100 μg/ml (AlphandÃ©ry, 2014; Singh et al., 2010; Toropova et al., 2017), a study by Alphandéry *et al.* in MDA-MB-231 cells suggested low cytotoxicity due to magnetosome exposure at concentrations below 1,000 μg/ml which can be further improved by removing bacterial endotoxins and using biocoatings (Alphandéry et al., 2011; Gareev et al., 2021). In a recent study, Gwisai *et al.* evaluated the use of the ferromagnetic properties of AMB-1 bacterial magnetosomes for targeted cancer therapy. Thanks to their susceptibility to external magnetic fields, magnetotactic bacterial cells were magnetically manipulated and studied as a vehicle for tumor infiltration and drug delivery (Gwisai et al., 2022). In a similar approach, Xing *et al.* successfully demonstrated the colonization and ablation of tumors in mice by means of *in vivo* magnetically manipulated *M. magneticum* AMB-1 bacteria, showing their enormous potential for an efficient cancer treatment (Xing et al., 2021). Other potential application of magnetosomes include their use as magnetic resonance contrast agents. *In vivo* experiments were conducted on mice to examine how magnetosomes were distributed and eliminated after injection as a contrast agent in magnetic resonance imaging (MRI). The researchers concluded that their use in MRI was adequate in terms of spatial resolution and sensitivity (Nan et al., 2021).

Microorganisms play an important role in the process of biomineralization and metal geochemistry. The metals transformation into nanoparticles is also a natural process observed in some astounding microorganisms known as dissimilatory metal-reducing bacteria. In anoxic environments with abundant metal species such as Fe^{3+}, $Mn^{3+/4+}$, U^{6+}, Cr^{6+}, Co^{3+} and Tc^{7+}, these metal cations are reduced into nanoparticles by the bacteria (Lovley, 1993; Shi et al., 2016). All these elements have in common that they are good electron acceptors due to their high reduction potential. Then, during anaerobic respiration, the bacteria can replace oxygen as the terminal electron acceptor with the available cations. Fe^{3+} is the most abundant possible electron acceptor in anoxic environments. Due to its comparatively high reactivity with oxygen, elemental Fe is not frequently found in nature, but instead, is commonly found in the form of iron oxides. In metal- and sulfur-reducing microorganisms like, *Geobacter sulfurreducens*, *Geobacter metallireducens* GS15 and *Shewanella oneidensis* MR1, specialized membrane proteins are suggested to be involved in the Fe^{3+} reduction. Their outer membranes are rich in c-type cytochromes that transfer electrons coupled to the oxidation of lactate and other carbon sources to soluble Fe^{3+} oxides resulting in iron oxide NPs (Lovley et al., 1993; Mehta et al., 2005; Shi et al., 2012). Many Fe-based NPs naturally synthesized by bacteria consist of diverse compositions of iron oxides. The metal-based anaerobic mechanism of respiration is considered part of the natural cycle of precipitation of many heavy metals into anoxic sediments (Lovley, 1993). Multiple processes of bioremediation of heavy metals from the environment and contaminated water streams have been engineered based on the reducing ability of these bacteria (Iravani and Varma, 2020). Other transition metals such as gold, silver, and copper have high positive reduction potentials and are exchanged with iron. Bacteria readily precipitate them during remediation, which can then be applied to the biogenic production of these metal nanoparticles.

TABLE 2 Bacteria-mediated metal-based nanoparticles reported in the literature.

Metal	Name of organism	NP	Size	Morphology	Localization	References
Au	*Bifidobacterium lactis*	Au	5–40 nm	Hexagonal	Intracellular	Chen et al. (2021)
	Bacillus cereus	Au	20–50 nm	Spherical/Hexagonal/ Octagonal	Extracellular	Pourali et al. (2017)
	Bacillus Licheniformis	Au	60–146 nm	Spherical	Intracellular	Tikariha et al. (2017)
	Caldicellulosiruptor changbaiensis CBS-Z	Au	1–20 nm	----	Membrane	Bing et al. (2018)
	Escherichia coli	Au	6–60 nm	Spherical	Extracellular	Chen et al. (2021)
	Lactobacillus casei	Au	7–56 nm	----	Membrane	Kikuchi et al. (2016)
	Marinobacter pelagius RS11	Au	2–10 nm	Spherical/Triangular	----	Sharma et al. (2012)
	Paracoccus haeundaensis BC74171	Au	15–35 nm	Spherical	Extracellular	Patil et al. (2019)
	Pseudomonas stutzeri KDP_M2	Au	10–20 nm	Spherical	----	Desai et al. (2021)
	Sporosarcina koreensis DC4	Au	92 nm	Spherical	Extracellular	Singh et al. (2016)
	Vibrio alginolyticus	Au	100–150 nm	Anisotropic	----	Shunmugam et al. (2021)
Ag	*Aeromonas* THG-FG1.2	Ag	8–16 nm	Spherical	Supernatant	Singh et al. (2017)
	Bacillus brevis	Ag	22–60 nm	Spherical	Supernatant	Saravanan et al. (2018)
	Bacillus cereus	Ag	5–7 nm	Spherical	----	Ibrahim et al. (2021)
	Bacillus clausii	Ag	30–80 nm	Spherical	Supernatant	Mukherjee et al. (2018)
	Bacillus Pumilus ROM6	Ag	20–70 nm	Spherical	Supernatant	Esmail et al. (2022)
	Escherichia coli 116AR	Ag	5–70 nm	----	Membrane	Lin et al. (2014)
	Escherichia coli Top 10	Ag	2–40 nm	----	Supernatant	Baltazar-Encarnación et al. (2019)
	Lactobacillus Acidophilus	Ag	10–20 nm	Spherical	Supernatant	Abishad et al. (2022)
	Lactobacillus brevis	Ag	30–100 nm	Spherical/Triangular/ Hexagonal	Supernatant	Riaz Rajoka et al. (2020)
	Paenarthrobacter nicotinovorans MAHUQ-43	Ag	13–27 nm	Spherical	Supernatant	Huq and Akter (2021)
	Pseudomonas aeruginosa	Ag	25 nm	Spherical	Supernatant	Quinteros et al. (2019)
	Pseudomonas putida MVP2	Ag	6–16 nm	Spherical	Membrane/ Supernatant	Gopinath et al. (2017)
	Pseudomonas stutzeri	Ag	22–46 nm	Spherical	Extracellular	Bachii et al. (2021)
	Pseudomonas stutzeri	Ag	10–50 nm	Anisotropic	----	Desai et al. (2020)
	Sporosarcina koreensis DC4	Ag	102 nm	Spherical	Extracellular	Singh et al. (2016)
	Stenotrophomonas maltophilia	Ag	93 nm	Cuboidal	Supernatant	Oves et al. (2013)
Pt	*Escherichia coli* MC4100	Pt	2.3–4.5 nm	Spherical	----	Attard et al. (2012)
	Pseudomonas kunmingensis ADR19	Pt	3.95 nm	Spherical	Supernatant	Eramabadi et al. (2020)
	Psychrobacter faecalis FZC6	Pt	2.49 nm	Spherical	Supernatant	Eramabadi et al. (2020)
	Vibrio fischeri NRRL B-11177	Pt	3.84 nm	Spherical	Supernatant	Eramabadi et al. (2020)
	Jeotgalicoccus coquinae ZC15	Pt	5.74 nm	Spherical	Supernatant	Eramabadi et al. (2020)
	Sporosarcina psychrophila KC19	Pt	4.24 nm	Spherical	Supernatant	Eramabadi et al. (2020)
	Kocuria rosea MN23	Pt	5.85 nm	Spherical	Supernatant	Eramabadi et al. (2020)
	Pseudomonas putida KT244	Pt	8.06 nm	Spherical	Supernatant	Eramabadi et al. (2020)

(Continued on following page)

TABLE 2 (*Continued*) Bacteria-mediated metal-based nanoparticles reported in the literature.

Metal	Name of organism	NP	Size	Morphology	Localization	References
	Acinetobacter calcoaceticus	Pt	2–3.5 nm	Cuboidal	Intracellular/ Membrane	Gaidhani et al. (2014)
Pd	*Bacillus benzeovorans*	Pd	1.7–5.8 nm	Anisotropic	Intracellular	Omajali et al. (2015)
	Bacillus megaterium Y-4	Pd	10–40 nm	Spherical	Intra/Extracellular	Chen et al. (2019)
	Bacillus wiedmannii MSM	Pd	10–36 nm	----	Membrane	Chen et al. (2018)
	Citrobacter sp.	Pd	11.3–15.6 nm	----	Membrane	Matsena et al. (2020)
	Citrobacter sp.	Pd	17.6–25.8 nm	Anisotropic	Membrane	Matsena and Chirwa (2021)
	Cupriavidus metallidurans	Pd	20–40 nm	Dendrite-Shaped	Intracellular	Tan et al. (2020)
	Desulfovibrio desulfuricans	Pd	3–13 nm	----	Intra/Extracellular	Mikheenko et al. (2022)
	Desulfovibrio desulfuricans	Pd	1.1–6.9 nm	Cubo-octahedron	Intracellular	Omajali et al. (2015)
	Escherichia coli BL21	Pd	2–3 nm	Spherical	Intracellular	Bachar et al. (2020)
	Escherichia coli MC4100	Pd	1–30 nm	Anisotropic	Intracellular/ Membrane	Gomez-Bolivar et al. (2019b)
	Shewanella loihica PV-4	Pd	4–10 nm	Spherical	Intra/Extracellular	Wang et al. (2018)
	Shewanella oneidensis MR-1	Pd	2–12 nm	Spherical	Extracellular	Zhang et al. (2022a)
	Shewanella oneidensis MR-1	Pd	2–25 nm	----	Supernatant	Zhang et al. (2022b)
Fe	*Bacillus cereus*	Fe_3O_4	18–29 nm	Spherical	Supernatant	Fatemi et al. (2018)
	Bacillus subtilis	Fe_3O_4	60–80 nm	Spherical	Supernatant	Khan et al. (2020)
	Escherichia coli	Fe_3O_4/ Fe_2O_3	18 nm	Spherical	Intra/Extracellular	Crespo et al. (2017)
	Proteus vulgaris	----	20–30 nm	Spherical	Supernatant	Majeed et al. (2021)
	Pseudomonas aeruginosa	Fe_3O_4/ Fe_2O_3	----	----	Extracellular	Crespo et al. (2017)
	Pseudomonas putida	Fe	1–4 nm	Spherical	Intra/Extracellular	Zaki et al. (2021)
Co	*Bacillus pasteurii*	Co_3O_4	10–31 nm	Anisotropic	----	Hsu et al. (2018)
	Bacillus subtilis	Co_3O_4	31.2 nm	Anisotropic	----	Mubraiz et al. (2021)
	Bacillus subtilis	Co_3O_4	2–5 nm	----	Membrane	Shim et al. (2011)
	Bacillus thuringiensis	Co	84.81 nm	Spherical	----	Marimuthu et al. (2013)
	Marinobacter hydrocarbonoclasticus	Co	8–22 nm	Spherical	Intracellular	Zaki et al. (2021)
	Microbacterium sp. MRS-1	Co_3O_4	10–100 nm	Spherical/pentagonal	Intra/Extracellular	Sundararaju et al. (2020)
	Micrococcus lylae	Co_3O_4	2–10 nm	----	Membrane	Shim et al. (2013)
	Proteus mirabilis 10B	Co_3O_4	22.1 nm	Quasi-spherical	Intracellular	Eltarahony et al. (2018)
Ni	*Bacillus subtilis*	$Ni_3(PO_4)_2$	40–90 nm	Anisotropic	----	Yu and Jiang (2019)
	Microbacterium sp. MRS-1	NiO	100–500 nm	Quasi-spherical	Extracellular	Sathyavathi et al. (2014)
	Pseudomonas alcaliphila	Ni	----	Anisotropic	Intra/Extracellular	Zhan et al. (2012)
Zn	*Alkalibacillus* sp. W7	ZnO	1–30 nm	Hexagonal/Quasi-spherical	Supernatant	Al-Kordy et al. (2021)
	Cyanobacterium Nostoc sp. EA03	ZnO	50–80 nm	Star shape	Supernatant	Ebadi et al. (2019)
	Bacillus sp PTCC 1538	ZnO	99 nm	Nano-rods	----	Mahdi et al. (2020)
	Halomonas elongata IBRC-M 10214	ZnO	18.11 nm	Anisotropic	Supernatant	Taran et al. (2017)
	Lactococcus lactis NCDO1281	ZnO	55 nm	Spherical	----	Mahdi et al. (2020)

(Continued on following page)

TABLE 2 (*Continued*) Bacteria-mediated metal-based nanoparticles reported in the literature.

Metal	Name of organism	NP	Size	Morphology	Localization	References
	Pseudomonas geniculata	Zn	4–13 nm	Spherical	Intracellular/ Membrane	Zaki et al. (2021)
	Shewanella oneidensis MR-1	ZnS	5.1 nm	Spherical	Extracellular/ Membrane	Xiao et al. (2015)
Cu	*Enterococcus thailandicus*	Cu	1–4 nm	Spherical	Intracellular	Zaki et al. (2021)
	Escherichia sp. SINT7	Cu	22.33–39.00 nm	Spherical	Extracellular	Noman et al. (2020)
	Pseudomonas fluorescens MAL2	Cu	20–80 nm	Spherical/hexagonal	----	El-Saadony et al. (2020)
Ti	*Halomonas elongata* IBRC-M 10214	TiO_2	104.63 nm	Spherical	Supernatant	Taran et al. (2017)
Cr	*Alishewanella* sp. WH16-1	Cr_2O_3	100–200 nm	Spherical	Intracellular	Xia et al. (2018)
	Bacillus cereus	Cr_2O_3	8–60 nm	Anisotropic/Spherical	Extracellular/ Membrane	Dong et al. (2013)
	Bacillus subtilis	Cr_2O_3	4–50 nm	Spherical	----	Kanakalakshmi et al. (2017)
Cd	*Bacillus badius*	CdS	20–80 nm	----	Supernatant	Sharma et al. (2021)
	Pedobacter sp. UYP1	CdS	2.8–4.9 nm	Anisotropic	Extracellular	Carrasco et al. (2021)
	Raoultella sp. X13	CdS	5–8 nm	----	----	Xu et al. (2021)

3.2 Biosynthetic nanoparticles

Bio-inspired NPs of different metals have been successfully synthesized using a large variety of bacterial strains. Under optimal conditions in temperature, pH and redox state, some bacterial species can reduce metal ions and form nanoparticles. Among the metals successfully recovered by bacteria in form of nanoparticles are iron, manganese, chromium, cobalt, palladium, gold, silver, arsenic, selenium, uranium, and polonium (Boedicker et al., 2021). Their resulting size-distribution, morphology and functional properties are highly dependent on the protocols used for the biosynthesis as well as on the type of bacteria and metal involved. In Table 2, details of recent, published protocols for metal nanoparticles fabrication using different bacterial strains are listed.

3.2.1 Gold nanoparticles

Metallic gold (Au) can be used in a wide range of applications due to its high stability, oxidation resistance, and biocompatibility. In nanoparticle form, gold displays an improved potential for chemical catalysis and has antimicrobial effects. Despite these antibacterial properties, some microorganisms have been successfully used to synthesize Au NPs. One of the first bacterial species studied for the reduction of Au was *Bacillus subtilis*. In their work, Beveridge and Murray exposed bacterial cells to solutions of Au^{3+} chloride at room temperature and observed the formation of Au NPs of octahedral morphology with sizes of approximately 5–25 nm (Beveridge and Murray, 1980; Iravani, 2014). Since then, many other species and strains have been examined for their capacity to synthesize Au NPs of diverse morphologies and dimensions. *Pseudomonas stutzeri* cells produce Au NPs in the size range of 10–20 nm with a spherical morphology when incubated at 80°C in a medium with chloroauric acid ($HAuCl_4$) as the precursor (Desai et al., 2021). *Escherichia coli* also biosynthesizes spherical Au NPs found primarily in the extracellular matrix with dimensions that vary with the pH of the medium from 6 to 60 nm in size. In similar conditions, Au NPs of sizes between 5 and 40 nm can be prepared with *Bifidobacterium lactis* bacteria, but with hexagonal morphologies and mostly intracellularly (Chen et al., 2021). Thus far, however, the complex mechanisms of Au NPs formation by bacteria are still not completely understood. For *Lactobacillus casei* bacteria, it was found that high cell numbers and high concentrations of Au salt solutions inhibit the particle formation. The same study suggested a direct participation of unsaturated fatty acids from di- and tri-glycosyldiacylglycerol glycolipids in the membrane in the formation of Au NPs (Kikuchi et al., 2016).

3.2.2 Silver nanoparticles

The production of Ag NPs is of special interest for their uses in the biotechnology industry. Drug delivery, diagnostics, cancer treatment and antibacterial agents are some of their most known applications (Jain et al., 2021). Several bacterial species have been exploited in the biogenic synthesis of intracellular and extracellular Ag NPs, including species from the *Pseudomonas* (Rajora et al., 2016; Quinteros et al., 2019), *Lactobacillus* (Riaz Rajoka et al., 2020; Abishad et al., 2022) and *Bacillus* (Mukherjee et al., 2018; Saravanan et al., 2018; Ibrahim et al., 2021; Esmail et al., 2022) genus. An example is *P. stutzeri* AG259, which was originally isolated from a silver mine and can bioaccumulate and synthesize silver crystalline nanoparticles when cultured in presence of high concentrations of silver salt ($AgNO_3$). These Ag and Ag_2S NPs are usually found in the bacteria plasma membrane and display triangular or hexagonal morphologies with a wide range of sizes from 35 to 200 nm (Klaus et al., 1999). Synthesis of Ag NPs with cell-free supernatants of *Stenotrophomonas maltophilia* bacteria results in cuboidal NPs of the average size of 93 nm (Oves et al., 2013), while *Pseudomonas aeruginosa* extracts can be used to synthesize spherical nanoparticles of 25 nm in size (Quinteros et al., 2019).

3.2.3 Platinum nanoparticles

Metals from the Platinum group of elements are notorious for their outstanding catalytic properties, in particular when used in nanoparticle form. However, limited studies have been conducted with bacteriogenic Pt nanoparticles, and their applications are rarely explored (Bloch et al., 2021). Zero-valent Pt NPs produced by the acidophilic Fe^{3+}-Reducing *Acidocella aromatica* PFBC and *Acidiphilium cryptum* SJH bacterial strains were tested in a Cr^{6+} reduction experiment for their catalytic activity. The experiment demonstrated comparable catalytic efficiency to a commercially purchased Pt/C catalyst (Matsumoto et al., 2021). Yet, the potential applications of Pt NPs also include their use in diagnostics (Dash et al., 2021), anticancer treatments (Baskaran et al., 2017), and as antibacterial agents (Hosny et al., 2022).

Live bacterial cells and bacterial lysate supernatants have been studied for Pt NP production. Typical synthesis of intracellular Pt NPs is performed under anaerobic conditions and starts with the incubation of bacteria such as *E. coli* or *Plectonema boryanum* in aqueous solutions of H_2PtCl_6 or Na_2PtCl_4 (Lengke et al., 2006; Attard et al., 2012; Gaidhani et al., 2014). The cells are then loaded with the metal ions and in some cases sodium formate solutions are added as an external electron donor for accelerating the metal reduction. For the extracellular biosynthesis of nanoparticles, the cells are utrasonicated and centrifuged. Then only the cell lysate supernatant is incubated with the Pt precursor solutions. Most of the Pt nanoparticles crystalize in spherical morphologies. *Pseudomonas kunmingensis* ADR19, *Psychrobacter faecalis* FZC6 and *Pseudomonas putida* KT244 synthesize spherical Pt NPs of the average sizes of 3.95, 2.49 and 8.06 nm (Eramabadi et al., 2020). Other species, such as *Acinetobacter calcoaceticus,* synthesize small cuboidal Pt NPs of 2–3.5 nm in size (Gaidhani et al., 2014).

3.2.4 Palladium nanoparticles

Palladium is a precious metal with outstanding catalytic properties. Currently it is extensively used in car converters and is crucial in a large variety of industrial-scale chemical reactions; in particular, it is an indispensable tool for modern organic synthesis (Chernyshev and Ananikov, 2022). In nanoparticle form, palladium is utilized for hydrogenation and as a carbon-carbon bond forming catalyst in Heck reactions and in Suzuki-Miyaura coupling. The synthesis of Pd NPs by bacteria has progressed rapidly, and a wide range of bacterial species and strains have been studied for the efficient production of nanoparticles. A recent study by Mikheenko *et al.* describes the formation of Pd NPs by sulfate-reducing bacteria, *Desulfovibrio desulfuricans*, and their application for the Heck reaction and hydrogenation. The cells were grown in anaerobic conditions, and a Na_2PdCl_4 solution in HNO_3 has been used with H_2 gas as supporting electron donor. The examination of the samples showed Pd NPs on the cell surface and in the different membrane layers with sizes in the range of 3–13 nm (Mikheenko et al., 2022). Some additional examples include the metal-reducing bacterium *Shewanella oneidensis* MR-1, which can synthesize extracellular 2–12 nm Pd NPs (Zhang et al., 2022a), the metal-resistant species *Cupriavidus metallidurans* (Tan et al., 2020), and the sulfate-reducing bacterium, *Desulfovibrio fructosivorans* (Mikheenko et al., 2008). Other strains studied for their capacity for Pd NP synthesis, which are not specialized in metal reduction for detoxification include *E. coli* (Bachar et al., 2020), *Bacillus megaterium* (Chen et al., 2019), and *Bacillus benzeovorans* (Omajali et al., 2015).

3.2.5 Iron-based nanoparticles

Iron is an indispensable element for all living organisms, known mainly as a co-factor in important biological redox reactions. The use of iron in nanoparticle form has attracted considerable interest in applications as contrast agents, as a drug carrier, and in cancer treatment (Samuel et al., 2021). It should be noted that not just the reduced metal but also some iron oxides possess remarkable magnetic properties that are attractive in countless applications, making the development of new methods for the synthesis of Fe nanoparticles an attractive field of research. Bio-production of iron-based nanoparticles is frequently described as a clean, simple, and economic way to obtain Fe NPs. Organisms such as bacteria can utilize various Fe sources to fulfill their nutritional requirements and have elaborate mechanisms to regulate the uptake of Fe ions. Some bacteria, including metal-reducing and magnetotactic bacteria (see above), also have the ability to reduce Fe ions and form crystals naturally.

For Fe-based NP biosynthesis, different sources of iron can be used, such as $FeSO_4$, $FeCl_3$, $FeCl_2$, and iron citrate. The NPs produced by *E. coli* living cells can be found intracellularly and extracellularly, depending on the iron precursor used, the pH and the metal concentration (Crespo et al., 2017). *E. coli* and *P. aeruginosa* cell extracts facilitate the synthesis of spherical magnetic Fe_3O_4 NPs when incubated on 1 mM $FeSO_4$ at pH 6.5 for 48 h and 37°C (Crespo et al., 2017). Fe_3O_4 NPs were also produced in cell-free *Enterococcus faecalis* supernatants incubated with $FeCl_3$ and $FeCl_2$ solutions. In this case, the reported nanoparticles were cubical, hexagonal, and irregular in shape of between 15 and 20 nm in size (Samuel et al., 2021). *Bacillus cereus* cell-free supernatant can also be used to reduce Fe into spherical magnetic Fe_3O_4 NPs in the size range of 18–29 nm (Fatemi et al., 2018).

3.2.6 Cobalt-based nanoparticles

Cobalt is a transition metal with interesting magnetic, catalytic, optical, and electrical properties. Cobalt oxide nanoparticles are considered promising in technologies for energy storage (Shim et al., 2011; Hsu et al., 2018), catalysis (Jang et al., 2015), and as antimicrobial agents (Hafeez et al., 2020; Mubraiz et al., 2021). The synthesis of pure Co NPs by microorganisms can be challenging due to the extreme toxicity of high concentrations of Co ions. Similar to Fe, Co is highly reactive in zero-valent state, and when in contact with aqueous solutions, it rapidly oxidizes. Therefore, the NPs produced by bacteria are typically composed of more stable, oxidized forms of cobalt such as Co_3O_4.

In *G. sulfurreducens,* the upregulation of c-cytocrome OmcC in Co-rich environments is an indication of Co competition with Fe for binding to the cytochromes, that ultimately promotes the reduction of Co^{2+} to Co^0 and its precipitation on the cell surface (Dulay et al., 2020). In other methods, Co_3O_4 NPs of 10–31 nm size are produced by chemical alteration in the media when the urealytic *Bacillus pasteurii* hydrolyzes urea in the presence of high concentrations of $Co(NO_3)_2$ (Hsu et al., 2018). *Brevibacterium casei* bacteria produce quasi-spherical 6-nm Co_3O_4 NPs when incubated in aqueous solution of cobalt acetate (Kumar et al., 2008). Other strains

TABLE 3 Bacteria-mediated bimetallic metal-based nanoparticles reported in the literature.

Name of organism	NPs	Size	Morphology	Localization	References
Bacillus benzeovorans	Pd-Ru	1–8 nm	Core-shell	Membrane	Omajali et al. (2019)
Cupriavidus necator	Pd-Au	10–50 nm	Spherical	Membrane	Hosseinkhani et al. (2012)
Deinococcus radiodurans	Au-Ag	60–400 nm	Spherical	Supernatant	Weng et al. (2020)
	Au-Ag	----	Spherical	Supernatant	Li et al. (2018)
Escherichia coli	Au-Pd	16 nm	Spherical	Intracellular/Membrane	Deplanche et al. (2012)
	Pd-Ru	1–3 nm	Core-shell	Intracellular/Membrane	Gomez-Bolivar et al. (2019a)
Lactobacillus	Au-Ag	100–500 nm	Irregular	Membrane	Nair and Pradeep (2002)
Paenibacillus polymyxa	FeO-MnO	11–54 nm	Spherical	Supernatant	de França Bettencourt et al. (2020)
Shewanella oneidensis	Pd-Fe_3O_4	5.5 nm	----	----	Tuo et al. (2015)
	Au-Fe_3O_4	15.4 nm	----	----	Tuo et al. (2015)
	PdAu-Fe_3O_4	8.3 nm	----	----	Tuo et al. (2015)
	Pd-Pt	3–40 nm	Spherical	Intracellular/Extracellular	Xu et al. (2019)
	Pd-Au	1–50 nm		Intracellular/Extracellular	De Corte et al. (2011)
	Pd-Ag	5–60 nm	Core-shell	Membrane	Kimber et al. (2021)
	Pd-Au	4–15 nm	Core-shell	Extracellular	Kimber et al. (2021)
Shewanella putrefaciens	Pd-Pt	4–60 nm	Flower-shaped	Membrane	Tuo et al. (2017)
Spirulina platensis	Au-Ag	17–25 nm	Core-Shell	Supernatant	Govindaraju et al. (2008)

studied for Co NP synthesis include *Micrococcus lylae*, *Bacilus subtilis*, *E. coli*, and *Haloarcula vallismortis* (Jang et al., 2015).

3.2.7 Nickel-based nanoparticles

In microorganisms, there are highly specific and efficient systems for the transport and regulation of nickel in the cell to avoid its accumulation and toxicity in the cytoplasm (Navarro et al., 1993). Taking into account that at high concentrations Ni is extremely toxic to bacteria, the interaction between Ni and the cells has to be carefully controlled. In addition, due to its low redox potential the reduction of Ni ions by bacteria is not energetically favorable for NP formation under standard growth conditions (Zhan et al., 2012). However, a recent study with metal-reducing bacteria *Pseudomonas alcaliphila* described the successful reduction of Ni^{2+} by incubation at 28°C under aerobic conditions in a solution with 2 mM $NiCl_2$ and sodium citrate as an electron donor. The formed Ni NPs were found intracellularly and in the bacterial periplasm, with irregular shapes (Zhan et al., 2012). Another example is the synthesis of NiO NPs by *Microbacterium sp.* MRS-1, as a result of the bioremediation of nickel electroplating industrial wastewater. The synthesized Ni NPs had spherical, flower-like structures and displayed particle sizes in the range of 100–500 nm (Sathyavathi et al., 2014).

3.2.8 Other elements, alloys, and bimetallic nanoparticles

Many other types of metal-based nanoparticles have been produced successfully using bacteria. These include nanoparticles composed of elements such as Zn, Cr, Cd, Ti, Cu, and different mixtures of metals. For example, antibacterial nanoparticles made of TiO_2 and ZnO can be bio-synthesized with bacteria. The Gram-negative bacterium *Halomonas elongata* can be used to produce spherical TiO_2 NPs and anisotropic ZnO NPs by incubating the cells with various concentrations of $TiO(OH)_2$ and $ZnCl_2$ solutions at different temperatures. The synthesized TiO_2 and ZnO NPs were on average of 104.63 ± 27.75 and 18.11 ± 8.93 nm in size, respectively (Taran et al., 2017). Other examples are the nanoparticles produced by the metal-reducing bacterium *Shewanella oneidensis* MR-1, known for its ability to live in heavy-metals polluted environments and studied for the synthesis of NPs of a wide range of metal ions, including ZnS (Taran et al., 2017), Pd (Zhang et al., 2022a; Zhang et al., 2022b), Cr (Wang et al., 2013) and U (Burgos et al., 2008). Synthesis of Te NPs has also been reported using a methanogenic microbial consortium in 270 ml continuous reactors as an alternative of Te recovery in wastewater treatments (Ramos-Ruiz et al., 2017).

Although microbial-mediated monometallic nanoparticles have been extensively studied, there is limited research on the production of bimetallic nanoparticles by bacteria. The synergistic effect of metal combinations can result in superior or novel catalytic, electronic, and optical properties. Therefore, bimetallic nanoparticles often exhibit improved performance that could be interesting for different applications (Xu et al., 2019). Exposing bacteria to high concentrations of various mixes of heavy metal ions can result in the formation of nanoparticles made of combinations of

these elements. Bimetallic nanoparticles can have structures such as core-shell, alloys, crown jewel, cluster-in-cluster, hollow, and porous NPs (Sasireka and Lalitha, 2021) and it is not surprising that the synthesis methodology has a direct effect on the final architecture of the formed bimetallic NP. An example is the synthesis of spherical bimetallic Pd-Pt NPs by S. *oneidensis* MR-1 prepared by incubation of the cell's biomass in a Pd^{2+} and Pt^{4+} mixed solution. Research showed that the synthesized polycrystalline Pd-Pt NPs possessed an improved catalytic performance in comparison with pure Pd or Pt NPs (Xu et al., 2019). Extracellular biosynthesis of bimetallic FeO-MnO NPs can be performed using *Paenibacillus polymyxa*. In this case, cell-free extracts were incubated with solutions of $FeCl_3$ and $MnSO_4$ at 45°C in the dark for 5 h and the formed spherical nanoparticles had sizes in the range of 11.28–543.59 nm. These particles are suitable as micronutrient additives to fertilizers for crop production (de França Bettencourt et al., 2020). For core-shell Pd-Ru bimetallic NP production, Gomez-Bolivar *et al.* incubated *E. coli* bacteria in a Pd^{2+} solution for an initial reduction of Pd under H_2 on the cell surface. The biomass with Pd^0 was then resuspended in Ru^{3+} solution for Pd-Ru NPs formation. Pd-Ru NPs synthesized mainly at the cell surface, although small MNPs were also present intracellularly. (Gomez-Bolivar et al., 2019a). Table 3 summarize examples of bimetallic nanoparticles produced by different bacteria.

4 Discussion—challenges for potential industrial-scale synthesis

There seems to be an enormous potential for a cost-effective and environmentally friendly synthesis of metal nanoparticles by bacteria. Yet, some special considerations must be assessed before the implementation of these approaches on a large scale and for commercial applications. The most common disadvantages of nanoparticle synthesis using microorganisms is the polydispersity of the particles, low yield and agglomeration (Narayanan and Sakthivel, 2010). Many bacterial strains that enable high yields of NPs are extremophilic organisms that require harsh environmental conditions in terms of temperature, radiation, pH and medium composition (metal concentration, oxygen, salinity, etc.,) in order to thrive (Atalah et al., 2022). The complicated culture conditions that are necessary for their isolation and cultivation, and the fact that small modifications of the environment can immediately result in the disruption of the metabolic routes that promote the metal ion reduction, make them challenging to use in large-scale processes. An example is the effect of dissolved oxygen concentration (DO) on the yield of magnetosomes produced by magnetotactic bacteria. It was suggested that *M. gryphiswaldense* MSR-1 bacteria form magnetosomes as a response to a low DO that is detrimental for their growth. Thus, only a strict control of the DO during production would guarantee higher yields of magnetosomes (Sun et al., 2008). This illustrates that optimized conditions for bacterial growth and nanoparticle formation must be determined in detail before any large-scale synthesis is considered, and that it is crucial to evaluate how controllable these parameters are on larger scales. Usually, large-scale cultivation requires further refinement of nutrients control and other culture conditions (Liu et al., 2010). In addition, the cost of specific culture media for microbial growth, instrumentation and facilities needs to be considered in potential commercial productions (Capuzzo, 2021).

By tuning the metal concentration and cell density, it is possible to obtain well-defined nanoparticles with narrow size distribution and homogeneous morphology using bacteria (Bing et al., 2018; Yu et al., 2020). The development of efficient mechanisms to supervise and adjust these parameters, in combination with choosing the ideal bacterial species and strains, would be important for an effective large-scale synthesis. Microbial MNP synthesis can occur intracellularly or extracellularly depending on the reduction mechanism used by the selected organism. Most studies favor the extracellular, cell lysate or cell-free production, as the resulting nanoparticles require less complex downstream processing. Intracellular synthesis tends to require a further purification processes to release nanoparticles from the cytosol, and ultrasound treatment to reduce agglomeration (Marooufpour et al., 2019). In addition, the biosynthesized NPs frequently use biological material as nucleation sites and scaffolding. Therefore, many of them feature biocappings that may have desired or undesired effects on the nanoparticle properties (Schröfel et al., 2014). Some of the capping agents ensure the production of small homogeneous nanoparticles by preventing the agglomeration and by decreasing their toxicity (Yahyaei et al., 2016). However, a removal process for these biocoatings from the nanoparticles is sometimes necessary depending on the targeted application. Excess proteins, ligands and impurities hinder the catalytic performance of MNPs like Ag NPs, and protocols such as dialysis, filtration, and sucrose density centrifugation have been introduced as purification methods (Khositanon et al., 2020; Ahmad et al., 2021). A study by Khositanon *et al.*, reported the removal of up to 73.3% of ligands by continuous-flow solvent extraction in a production of Ag NPs coated with surfactants (Khositanon et al., 2020). Yet, most of the methods to clean the bio-nanoparticles have proven to be time consuming, laborious, or not cost-effective, which may prevent the profitable use of the particles for their intended purposes.

Because of these technical hurdles, only few examples have been reported for the successful, large-scale production of NPs, showing that further research is necessary to develop sustainable production processes (Gahlawat and Choudhury, 2019). Successful examples include the productions of ZnS NPs by the thermophilic bacterium *Thermoanaerobacter* sp. X513 in 100-L and 900-L fermenters (Moon et al., 2016), and CdS NPs in cultures from 10 ml up to 24 L of volume (Moon et al., 2013). Magnetic, Fe-based NPs were synthesized by *Thermoanaerobacter* sp. TOR-39 in 35 L reactors (Moon et al., 2010).

The key parameters that have a significant effect on NP yield are time of incubation, biomass concentration, and type of precursor, aside from the choice of bacterial species. In principle, these parameters are relatively easy to control, and along with further understanding of the bacterial redox activity and the mechanism of metal transport would greatly benefit the development of strains that naturally have a high tolerance for heavy metals and remarkably produce large populations of nanoparticles. Then, the insights gained in numerous studies give hope that industrial-scale protocols can be implemented for commercial applications in the future (Narayanan and Sakthivel, 2010).

Author contributions

AC and DL contributed to conception of the manuscript. AC wrote the first draft and AS wrote sections of the manuscript. DL, AS, and PM conducted manuscript editing and proofreading. All authors contributed to the article and approved the submitted version.

Funding

This work is part of the Project "BEDPAN—Bio-Engineered Palladium Nanoparticles," funded by the Research Council of Norway, RCN294605.

Conflict of interest

The authors declare that the research was conducted in the absence of any commercial or financial relationships that could be construed as a potential conflict of interest.

Publisher's note

All claims expressed in this article are solely those of the authors and do not necessarily represent those of their affiliated organizations, or those of the publisher, the editors and the reviewers. Any product that may be evaluated in this article, or claim that may be made by its manufacturer, is not guaranteed or endorsed by the publisher.

References

Abishad, P., Vergis, J., Unni, V., Ram, V. P., Niveditha, P., Yasur, J., et al. (2022). Green synthesized silver nanoparticles using Lactobacillus acidophilus as an antioxidant, antimicrobial, and antibiofilm agent against multi-drug resistant enteroaggregative Escherichia coli. *Probiotics Antimicrob. Proteins* 14, 904–914. doi:10.1007/s12602-022-09961-1

Ahmad, B., Shireen, F., Rauf, A., Shariati, M. A., Bashir, S., Patel, S., et al. (2021). Phyto-fabrication, purification, characterisation, optimisation, and biological competence of nano-silver. *IET Nanobiotechnology* 15, 1–18. doi:10.1049/nbt2.12007

Ahmad, F., Ashraf, N., Ashraf, T., Zhou, R-B., and Yin, D-C. (2019). Biological synthesis of metallic nanoparticles (MNPs) by plants and microbes: Their cellular uptake, biocompatibility, and biomedical applications. *Appl. Microbiol. Biotechnol.* 103, 2913–2935. doi:10.1007/s00253-019-09675-5

Al-Kordy, H. M. H., Sabry, S. A., and Mabrouk, M. E. M. (2021). Statistical optimization of experimental parameters for extracellular synthesis of zinc oxide nanoparticles by a novel haloalaliphilic Alkalibacillus sp.W7. *Sci. Rep.* 11, 10924. doi:10.1038/s41598-021-90408-y

AlphandÃ©ry, E. (2014). Applications of magnetosomes synthesized by magnetotactic bacteria in medicine. *Front. Bioeng. Biotechnol.* 2, 5. doi:10.3389/fbioe.2014.00005

Alphandéry, E., Faure, S., Seksek, O., Guyot, F., and Chebbi, I. (2011). Chains of magnetosomes extracted from AMB-1 magnetotactic bacteria for application in alternative magnetic field cancer therapy. *ACS Nano* 5, 6279–6296. doi:10.1021/nn201290k

Andrade Neto, N. F., Nascimento, L. E., Correa, M., Bohn, F., Bomio, M. R. D., and Motta, F. V. (2020). Characterization and photocatalytic application of Ce4+, Co2+, Mn2+ and Ni2+ doped Fe3O4 magnetic nanoparticles obtained by the co-precipitation method. *Mater. Chem. Phys.* 242, 122489. doi:10.1016/j.matchemphys.2019.122489

Andrei, A., Öztürk, Y., Khalfaoui-Hassani, B., Rauch, J., Marckmann, D., Trasnea, P-I., et al. (2020). Cu homeostasis in bacteria: The ins and outs. *Membranes* 10, 242. doi:10.3390/membranes10090242

Atalah, J., Espina, G., Blamey, L., Muñoz-Ibacache, S. A., and Blamey, J. M. (2022). Advantages of using extremophilic bacteria for the biosynthesis of metallic nanoparticles and its potential for rare earth element recovery. *Front. Microbiol.* 13, 855077. doi:10.3389/fmicb.2022.855077

Attard, G., Casadesús, M., Macaskie, L. E., and Deplanche, K. (2012). Biosynthesis of platinum nanoparticles by *Escherichia coli* MC4100: Can such nanoparticles exhibit intrinsic surface enantioselectivity? *Langmuir* 28, 5267–5274. doi:10.1021/la204495z

Bachar, O., Meirovich, M. M., Kurzion, R., and Yehezkeli, O. (2020). *In vivo* and *in vitro* protein mediated synthesis of palladium nanoparticles for hydrogenation reactions. *Chem. Commun.* 56, 11211–11214. doi:10.1039/D0CC04812G

Bachii, S. A., Sahib, W. H. A-A., and Salah, A. A. R. (2021). Preparation and characterization of silver nanoparticles biosynthesis by Pseudomonas stutzeri environmental bacteria isolated from oil fields and their antimicrobial activity. *Sci. J. Med. Res.* 5.

Baltazar-Encarnación, E., Escárcega-González, C. E., Vasto-Anzaldo, X. G., Cantú-Cárdenas, M. E., and Morones-Ramírez, J. R. (2019). Silver nanoparticles synthesized through green methods using *Escherichia coli* top 10 (Ec-Ts) growth culture medium exhibit antimicrobial properties against nongrowing bacterial strains. *J. Nanomater.* 2019, 1–8. doi:10.1155/2019/4637325

Barton, L. L., and Fauque, G. D. (2009). "Chapter 2 biochemistry, physiology and biotechnology of sulfate-reducing bacteria," in *Advances in applied microbiology* (United States: Academic Press), 41–98. doi:10.1016/S0065-2164(09)01202-7

Baskaran, B., Muthukumarasamy, A., Chidambaram, S., Sugumaran, A., Ramachandran, K., and Rasu Manimuthu, T. (2017). Cytotoxic potentials of biologically fabricated platinum nanoparticles from Streptomyces sp. on MCF-7 breast cancer cells. *IET Nanobiotechnology* 11, 241–246. doi:10.1049/iet-nbt.2016.0040

Beveridge, T. J., and Murray, R. G. E. (1980). Sites of metal deposition in the cell wall of Bacillus subtilis. *J. Bacteriol.* 141, 876–887. doi:10.1128/jb.141.2.876-887.1980

Bhamidimarri, S. P., Young, T. R., Shanmugam, M., Soderholm, S., Baslé, A., Bumann, D., et al. (2021). Acquisition of ionic copper by the bacterial outer membrane protein OprC through a novel binding site. *Stock Am. PLOS Biol.* 19, e3001446. doi:10.1371/journal.pbio.3001446

Bing, W., Sun, H., Wang, F., Song, Y., and Ren, J. (2018). Hydrogen-producing hyperthermophilic bacteria synthesized size-controllable fine gold nanoparticles with excellence for eradicating biofilm and antibacterial applications. *J. Mater. Chem. B* 6, 4602–4609. doi:10.1039/C8TB00549D

Blindauer, C. A. (2011). Bacterial metallothioneins: Past, present, and questions for the future. *JBIC J. Biol. Inorg. Chem.* 16, 1011–1024. doi:10.1007/s00775-011-0790-y

Bloch, K., Pardesi, K., Satriano, C., and Ghosh, S. (2021). Bacteriogenic platinum nanoparticles for application in nanomedicine. *Front. Chem.* 9, 624344. doi:10.3389/fchem.2021.624344

Boedicker, J. Q., Gangan, M., Naughton, K., Zhao, F., Gralnick, J. A., and El-Naggar, M. Y. (2021). Engineering biological electron transfer and redox pathways for nanoparticle synthesis. *Bioelectricity* 3, 126–135. doi:10.1089/bioe.2021.0010

Bogireddy, N. K. R., Kiran Kumar, H. A., and Mandal, B. K. (2016). Biofabricated silver nanoparticles as green catalyst in the degradation of different textile dyes. *J. Environ. Chem. Eng.* 4, 56–64. doi:10.1016/j.jece.2015.11.004

Bruins, M. R., Kapil, S., and Oehme, F. W. (2000). Microbial resistance to metals in the environment. *Ecotoxicol. Environ. Saf.* 45, 198–207. doi:10.1006/eesa.1999.1860

Bulgarini, A., Lampis, S., Turner, R. J., and Vallini, G. (2021). Biomolecular composition of capping layer and stability of biogenic selenium nanoparticles synthesized by five bacterial species. *Microb. Biotechnol.* 14, 198–212. doi:10.1111/1751-7915.13666

Burgos, W. D., McDonough, J. T., Senko, J. M., Zhang, G., Dohnalkova, A. C., Kelly, S. D., et al. (2008). Characterization of uraninite nanoparticles produced by Shewanella oneidensis MR-1. *Geochimica Cosmochimica Acta* 72, 4901–4915. doi:10.1016/j.gca.2008.07.016

Butterfield, A. G., Steimle, B. C., and Schaak, R. E. (2020). Retrosynthetic design of morphologically complex metal sulfide nanoparticles using sequential partial cation exchange and chemical etching. *ACS Mater. Lett.* 2, 1106–1114. doi:10.1021/acsmaterialslett.0c00287

Capuzzo, A. M. (2021). Bacterial synthesis of nanoparticles: Current trends in biotechnology and biomedical fields. *Ann. Adv. Biomed. Sci.* 4. doi:10.23880/aabsc-16000161

Carrasco, V., Amarelle, V., Lagos-Moraga, S., Quezada, C. P., Espinoza-González, R., Faccio, R., et al. (2021). Production of cadmium sulfide quantum dots by the lithobiontic Antarctic strain Pedobacter sp. UYP1 and their application as photosensitizer in solar cells. *Microb. Cell Factories* 20, 41. doi:10.1186/s12934-021-01531-4

Chan, H-K., and Kwok, P. C. L. (2011). Production methods for nanodrug particles using the bottom-up approach. *Adv. Drug Deliv. Rev.* 63, 406–416. doi:10.1016/j.addr.2011.03.011

Chen, C-Y., Chang, Y-C., Tsai, T-H., Liu, M-H., and Chung, Y-C. (2021). Multifunctional activities of gold nanoparticles biosynthesized using bacteria isolated from mining areas. *Appl. Sci.* 11, 3670. doi:10.3390/app11083670

Chen, Y., Chen, Y., Wu, J., and Zhang, J. (2018). The effect of biotic and abiotic environmental factors on Pd(II) adsorption and reduction by Bacillus wiedmannii MSM. *Ecotoxicol. Environ. Saf.* 162, 546–553. doi:10.1016/j.ecoenv.2018.07.043

Chen, Y., Hu, K., and Chen, Y. (2019). The effect of biotic and abiotic environmental factors on Pd(II) adsorption and reduction by Bacillus megaterium Y-4. *Chemosphere* 220, 1058–1066. doi:10.1016/j.chemosphere.2019.01.011

Chernyshev, V. M., and Ananikov, V. P. (2022). Nickel and palladium catalysis: Stronger demand than ever. *ACS Catal.* 12, 1180–1200. doi:10.1021/acscatal.1c04705

Crespo, K. A., Baronetti, J. L., Quinteros, M. A., Páez, P. L., and Paraje, M. G. (2017). Intra- and extracellular biosynthesis and characterization of iron nanoparticles from prokaryotic microorganisms with anticoagulant activity. *Pharm. Res.* 34, 591–598. doi:10.1007/s11095-016-2084-0

Cypriano, J., Castro, J., Taveira, I., Correa, T., Acosta-Avalos, D., Abreu, F., et al. (2022). *Magnetosome biomineralization by magnetotactic bacteria*. Cham: Springer, 243–281. doi:10.1007/978-3-030-80807-5_7

Das, C. G. A., Kumar, V. G., Dhas, T. S., Karthick, V., Govindaraju, K., Joselin, J. M., et al. (2020). Antibacterial activity of silver nanoparticles (biosynthesis): A short review on recent advances. *Biocatal. Agric. Biotechnol.* 27, 101593. doi:10.1016/j.bcab.2020.101593

Dash, S. R., Bag, S. S., and Golder, A. K. (2021). Bio-inspired PtNPs/Graphene nanocomposite based electrocatalytic sensing of metabolites of dipyrone. *Anal. Chim. Acta* 1167, 338562. doi:10.1016/j.aca.2021.338562

De Corte, S., Hennebel, T., Fitts, J. P., Sabbe, T., Bliznuk, V., Verschuere, S., et al. (2011). Biosupported bimetallic Pd–Au nanocatalysts for dechlorination of environmental contaminants. *Environ. Sci. Technol.* 45, 8506–8513. doi:10.1021/es2019324

de França Bettencourt, G. M., Degenhardt, J., Zevallos Torres, L. A., de Andrade Tanobe, V. O., and Soccol, C. R. (2020). Green biosynthesis of single and bimetallic nanoparticles of iron and manganese using bacterial auxin complex to act as plant biofertilizer. *Biocatal. Agric. Biotechnol.* 30, 101822. doi:10.1016/j.bcab.2020.101822

de Jesus, R. A., de Assis, G. C., de Oliveira, R. J., Costa, J. A. S., da Silva, C. M. P., Bilal, M., et al. (2021). Environmental remediation potentialities of metal and metal oxide nanoparticles: Mechanistic biosynthesis, influencing factors, and application standpoint. *Environ. Technol. Innovation* 24, 101851. doi:10.1016/j.eti.2021.101851

Delmar, J. A., Su, C-C., and Yu, E. W. (2014). Bacterial multidrug efflux transporters. *Annu. Rev. Biophysics* 43, 93–117. doi:10.1146/annurev-biophys-051013-022855

Deplanche, K., Caldelari, I., Mikheenko, I. P., Sargent, F., and Macaskie, L. E. (2010). Involvement of hydrogenases in the formation of highly catalytic Pd(0) nanoparticles by bioreduction of Pd(II) using *Escherichia coli* mutant strains. *Microbiology* 156, 2630–2640. doi:10.1099/mic.0.036681-0

Deplanche, K., Merroun, M. L., Casadesus, M., Tran, D. T., Mikheenko, I. P., Bennett, J. A., et al. (2012). Microbial synthesis of core/shell gold/palladium nanoparticles for applications in green chemistry. *J. R. Soc. Interface* 9, 1705–1712. doi:10.1098/rsif.2012.0003

Desai, M. P., Patil, R. V., Harke, S. S., and Pawar, K. D. (2021). Bacterium mediated facile and green method for optimized biosynthesis of gold nanoparticles for simple and visual detection of two metal ions. *J. Clust. Sci.* 32, 341–350. doi:10.1007/s10876-020-01793-9

Desai, M. P., Patil, R. V., and Pawar, K. D. (2020). Selective and sensitive colorimetric detection of platinum using Pseudomonas stutzeri mediated optimally synthesized antibacterial silver nanoparticles. *Biotechnol. Rep.* 25, e00404. doi:10.1016/j.btre.2019.e00404

Dong, G., Wang, Y., Gong, L., Wang, M., Wang, H., He, N., et al. (2013). Formation of soluble Cr(III) end-products and nanoparticles during Cr(VI) reduction by Bacillus cereus strain XMCr-6. *Biochem. Eng. J.* 70, 166–172. doi:10.1016/j.bej.2012.11.002

Dulay, H., Tabares, M., Kashefi, K., and Reguera, G. (2020). Cobalt resistance via detoxification and mineralization in the iron-reducing bacterium geobacter sulfurreducens. *Front. Microbiol.* 11, 600463. doi:10.3389/fmicb.2020.600463

Dziuba, M., Riese, C. N., Borgert, L., Wittchen, M., Busche, T., Kalinowski, J., et al. (2021). The complex transcriptional landscape of magnetosome gene clusters in Magnetospirillum gryphiswaldense. *mSystems* 6, e0089321–e0089914. doi:10.1128/mSystems.00893-21

Ebadi, M., Zolfaghari, M. R., Aghaei, S. S., Zargar, M., Shafiei, M., Zahiri, H. S., et al. (2019). A bio-inspired strategy for the synthesis of zinc oxide nanoparticles (ZnO NPs) using the cell extract of cyanobacterium nostoc sp. EA03: From biological function to toxicity evaluation. *RSC Adv.* 9, 23508–23525. doi:10.1039/C9RA03962G

El-Saadony, M. T., Abd El-Hack, M. E., Taha, A. E., Fouda, M. M. G., Ajarem, J. S., Maodaa S, N., et al. (2020). Ecofriendly synthesis and insecticidal application of copper nanoparticles against the storage pest *Tribolium castaneum*. *Nanomaterials* 10, 587. doi:10.3390/nano10030587

Eltarahony, M., Zaki, S., ElKady, M., and Abd-El-Haleem, D. (2018). Biosynthesis, characterization of some combined nanoparticles, and its biocide potency against a broad spectrum of pathogens. *J. Nanomater.* 2018, 1–16. doi:10.1155/2018/5263814

Eramabadi, P., Masoudi, M., Makhdoumi, A., and Mashreghi, M. (2020). Microbial cell lysate supernatant (CLS) alteration impact on platinum nanoparticles fabrication, characterization, antioxidant and antibacterial activity. *Mater. Sci. Eng. C* 117, 111292. doi:10.1016/j.msec.2020.111292

Esmail, R., Afshar, A., Morteza, M., Abolfazl, A., and Akhondi, E. (2022). Synthesis of silver nanoparticles with high efficiency and stability by culture supernatant of Bacillus ROM6 isolated from Zarshouran gold mine and evaluating its antibacterial effects. *BMC Microbiol.* 22, 97. doi:10.1186/s12866-022-02490-5

Fatemi, M., Mollania, N., Momeni-Moghaddam, M., and Sadeghifar, F. (2018). Extracellular biosynthesis of magnetic iron oxide nanoparticles by Bacillus cereus strain HMH1: Characterization and *in vitro* cytotoxicity analysis on MCF-7 and 3T3 cell lines. *J. Biotechnol.* 270, 1–11. doi:10.1016/j.jbiotec.2018.01.021

Fatoki, O. S. (1997). Biomethylation in the natural environment: A review. *South Afr. J. Sci.* 1997, 366–370.

Fu, X., Cai, J., Zhang, X., Li, W-D. D., Ge, H., and Hu, Y. (2018). Top-down fabrication of shape-controlled, monodisperse nanoparticles for biomedical applications. *Adv. Drug Deliv. Rev.* 132, 169–187. doi:10.1016/j.addr.2018.07.006

Gahlawat, G., and Choudhury, A. R. (2019). A review on the biosynthesis of metal and metal salt nanoparticles by microbes. *RSC Adv.* 9, 12944–12967. doi:10.1039/C8RA10483B

Gaidhani, S. V., Yeshvekar, R. K., Shedbalkar, U. U., Bellare, J. H., and Chopade, B. A. (2014). Bio-reduction of hexachloroplatinic acid to platinum nanoparticles employing Acinetobacter calcoaceticus. *Process Biochem.* 49, 2313–2319. doi:10.1016/j.procbio.2014.10.002

Gao, C., Lyu, F., and Yin, Y. (2021). Encapsulated metal nanoparticles for catalysis. *Chem. Rev.* 121, 834–881. doi:10.1021/acs.chemrev.0c00237

Gareev, K. G., Grouzdev, D. S., Kharitonskii, P. V., Kosterov, A., Koziaeva, V. V., Sergienko, E. S., et al. (2021). Magnetotactic bacteria and magnetosomes: Basic properties and applications. *Magnetochemistry* 7, 86. doi:10.3390/magnetochemistry7060086

Gautam, M., Kim, J. O., and Yong, C. S. (2021). Fabrication of aerosol-based nanoparticles and their applications in biomedical fields. *J. Pharm. Investigation* 51, 361–375. doi:10.1007/s40005-021-00523-1

Gomez-Bolivar, J., Mikheenko, I. P., Macaskie, L. E., and Merroun, M. L. (2019). Characterization of palladium nanoparticles produced by healthy and microwave-injured cells of Desulfovibrio desulfuricans and *Escherichia coli*. *Nanomaterials* 9, 857. doi:10.3390/nano9060857

Gomez-Bolivar, J., Mikheenko, I. P., Orozco, R. L., Sharma, S., Banerjee, D., Walker, M., et al. (2019). Synthesis of Pd/Ru bimetallic nanoparticles by *Escherichia coli* and potential as a catalyst for upgrading 5-hydroxymethyl furfural into liquid fuel precursors. *Front. Microbiol.* 10, 1276–1317. doi:10.3389/fmicb.2019.01276

Gopinath, V., Priyadarshini, S., Loke, M. F., Arunkumar, J., Marsili, E., MubarakAli, D., et al. (2017). Biogenic synthesis, characterization of antibacterial silver nanoparticles and its cell cytotoxicity. *Arabian J. Chem.* 10, 1107–1117. doi:10.1016/j.arabjc.2015.11.011

Goswami, P., He, K., Li, J., Pan, Y., Roberts, A. P., and Lin, W. (2022). Magnetotactic bacteria and magnetofossils: Ecology, evolution and environmental implications. *npj Biofilms Microbiomes* 8, 43. doi:10.1038/s41522-022-00304-0

Govindaraju, K., Basha, S. K., Kumar, V. G., and Singaravelu, G. (2008). Silver, gold and bimetallic nanoparticles production using single-cell protein (Spirulina platensis) Geitler. *J. Mater. Sci.* 43, 5115–5122. doi:10.1007/s10853-008-2745-4

Griffin, S., Masood, M., Nasim, M., Sarfraz, M., Ebokaiwe, A., Schäfer, K-H., et al. (2017). Natural nanoparticles: A particular matter inspired by nature. *Antioxidants* 7, 3. doi:10.3390/antiox7010003

Gwisai, T., Mirkhani, N., Christiansen, M. G., Nguyen, T. T., Ling, V., and Schuerle, S. (2022). Magnetic torque–driven living microrobots for increased tumor infiltration. *Sci. Robotics* 7, eabo0665. doi:10.1126/scirobotics.abo0665

Hafeez, M., Shaheen, R., Akram, B., Zain-ul-AbdinHaq, S., Mahsud, S., et al. (2020). Green synthesis of cobalt oxide nanoparticles for potential biological applications. *Mater. Res. Express* 7, 025019. doi:10.1088/2053-1591/ab70dd

W. M. Haynes (Editor) (2014). *CRC handbook of chemistry and physics* (United States: CRC Press). doi:10.1201/b17118

Henglein, A. (1999). Radiolytic preparation of ultrafine colloidal gold particles in aqueous solution: Optical spectrum, controlled growth, and some chemical reactions. *Langmuir* 15, 6738–6744. doi:10.1021/la9901579

Herrmann, G., Jayamani, E., Mai, G., and Buckel, W. (2008). Energy conservation via electron-transferring flavoprotein in anaerobic bacteria. *J. Bacteriol.* 190, 784–791. doi:10.1128/JB.01422-07

Hood, M. I., and Skaar, E. P. (2012). Nutritional immunity: Transition metals at the pathogen–host interface. *Nat. Rev. Microbiol.* 10, 525–537. doi:10.1038/nrmicro2836

Hosny, M., Fawzy, M., El-Fakharany, E. M., Omer, A. M., El-Monaem, E. M. A., Khalifa, R. E., et al. (2022). Biogenic synthesis, characterization, antimicrobial, antioxidant, antidiabetic, and catalytic applications of platinum nanoparticles synthesized from Polygonum salicifolium leaves. *J. Environ. Chem. Eng.* 10, 106806. doi:10.1016/j.jece.2021.106806

Hosseinkhani, B., Søbjerg, L. S., Rotaru, A-E., Emtiazi, G., Skrydstrup, T., and Meyer, R. L. (2012). Microbially supported synthesis of catalytically active bimetallic Pd-Au nanoparticles. *Biotechnol. Bioeng.* 109, 45–52. doi:10.1002/bit.23293

Hsu, C-M., Huang, Y-H., Chen, H-J., Lee, W-C., Chiu, H-W., Maity, J. P., et al. (2018). Green synthesis of nano-Co3O4 by Microbial Induced Precipitation (MIP) process using Bacillus pasteurii and its application as supercapacitor. *Mater. Today Commun.* 14, 302–311. doi:10.1016/j.mtcomm.2018.02.005

Huq, M. A., and Akter, S. (2021). Bacterial mediated rapid and facile synthesis of silver nanoparticles and their antimicrobial efficacy against pathogenic microorganisms. *Materials* 14, 2615. doi:10.3390/ma14102615

Hynninen, A. (2010). *Zinc, cadmium and lead resistance mechanisms in bacteria and their contribution to biosensing*. Finland: University of Helsinki.

Ibrahim, S., Ahmad, Z., Manzoor, M. Z., Mujahid, M., Faheem, Z., and Adnan, A. (2021). Optimization for biogenic microbial synthesis of silver nanoparticles through response surface methodology, characterization, their antimicrobial, antioxidant, and catalytic potential. *Sci. Rep.* 11, 770. doi:10.1038/s41598-020-80805-0

Igiri, B. E., Okoduwa, S. I. R., Idoko, G. O., Akabuogu, E. P., Adeyi, A. O., and Ejiogu, I. K. (2018). Toxicity and bioremediation of heavy metals contaminated ecosystem from tannery wastewater: A review. *J. Toxicol.* 2018, 1–16. doi:10.1155/2018/2568038

Iravani, S. (2014). Bacteria in nanoparticle synthesis: Current status and future prospects. *Int. Sch. Res. Notices* 2014, 1–18. doi:10.1155/2014/359316

Iravani, S., and Varma, R. S. (2020). Bacteria in heavy metal remediation and nanoparticle biosynthesis. *ACS Sustain. Chem. Eng.* 8, 5395–5409. doi:10.1021/acssuschemeng.0c00292

Jaidev, L. R., and Narasimha, G. (2010). Fungal mediated biosynthesis of silver nanoparticles, characterization and antimicrobial activity. *Colloids Surfaces B Biointerfaces.* 81, 430–433. doi:10.1016/j.colsurfb.2010.07.033

Jain, A. S., Pawar, P. S., Sarkar, A., Junnuthula, V., and Dyawanapelly, S. (2021). Bionanofactories for green synthesis of silver nanoparticles: Toward antimicrobial applications. *Int. J. Mol. Sci.* 22, 11993. doi:10.3390/ijms222111993

Jamkhande, P. G., Ghule, N. W., Bamer, A. H., and Kalaskar, M. G. (2019). Metal nanoparticles synthesis: An overview on methods of preparation, advantages and disadvantages, and applications. *J. Drug Deliv. Sci. Technol.* 53, 101174. doi:10.1016/j.jddst.2019.101174

Jang, E., Shim, H-W., Ryu, B. H., An, D. R., Yoo, W. K., Kim, K. K., et al. (2015). Preparation of cobalt nanoparticles from polymorphic bacterial templates: A novel platform for biocatalysis. *Int. J. Biol. Macromol.* 81, 747–753. doi:10.1016/j.ijbiomac.2015.09.009

Javed, Y., Akhtar, K., Anwar, H., and Jamil, Y. (2017). MRI based on iron oxide nanoparticles contrast agents: Effect of oxidation state and architecture. *J. Nanoparticle Res.* 19:366. doi:10.1007/S11051-017-4045-X

Jimenez-Sandoval, R., Pedireddy, S., Katuri, K. P., and Saikaly, P. E. (2023). Facile biological-based synthesis of size-controlled palladium nanoclusters anchored on the surface of geobacter sulfurreducens and their application in electrocatalysis. *ACS Sustain. Chem. Eng.* 11, 1100–1109. doi:10.1021/acssuschemeng.2c06143

Johnstone, T. C., and Nolan, E. M. (2015). Beyond iron: Non-classical biological functions of bacterial siderophores. *Dalton Trans.* 44, 6320–6339. doi:10.1039/c4dt03559c

Kalimuthu, K., Suresh Babu, R., Venkataraman, D., Bilal, M., and Gurunathan, S. (2008). Biosynthesis of silver nanocrystals by Bacillus licheniformis. *Colloids Surfaces B Biointerfaces.* 65, 150–153. doi:10.1016/j.colsurfb.2008.02.018

Kanakalakshmi, A., Janaki, V., Shanthi, K., and Kamala-Kannan, S. (2017). Biosynthesis of Cr(III) nanoparticles from electroplating wastewater using chromium-resistant Bacillus subtilis and its cytotoxicity and antibacterial activity. *Artif. Cells, Nanomedicine, Biotechnol.* 45, 1304–1309. doi:10.1080/21691401.2016.1228660

Katsui, H., and Goto, T. (2021). *Chemical vapor deposition. Multi-Dimensional additive manufacturing*. Singapore: Springer Singapore, 75–95. doi:10.1007/978-981-15-7910-3_6

Khalil, A. T., Ovais, M., Iqbal, J., Ali, A., Ayaz, M., Abbas, M., et al. (2022). Microbes-mediated synthesis strategies of metal nanoparticles and their potential role in cancer therapeutics. *Seminars Cancer Biol.* 86, 693–705. doi:10.1016/j.semcancer.2021.06.006

Khan, M., Ijaz, M., Chotana, G. A., Murtaza, G., Malik, A., and Shamim, S. (2022). Bacillus altitudinis MT422188: A potential agent for zinc bioremediation. *Bioremediation J.* 26, 228–248. doi:10.1080/10889868.2021.1927973

Khan, S., Akhtar, N., Rehman, S. U., Shujah, S., Rha, E. S., and Jamil, M. (2020). Biosynthesized iron oxide nanoparticles (Fe3O4 NPs) mitigate arsenic toxicity in rice seedlings. *Toxics* 9, 2. doi:10.3390/toxics9010002

Khositanon, C., Adpakpang, K., Bureekaew, S., and Weeranoppanant, N. (2020). Continuous-flow purification of silver nanoparticles and its integration with flow synthesis. *J. Flow Chem.* 10, 353–362. doi:10.1007/s41981-020-00084-8

Kianpour, S., Ebrahiminezhad, A., Deyhimi, M., Negahdaripour, M., Raee, M. J., Mohkam, M., et al. (2019). Structural characterization of polysaccharide-coated iron oxide nanoparticles produced by Staphylococcus warneri, isolated from a thermal spring. *J. Basic Microbiol.* 59, 569–578. doi:10.1002/jobm.201800684

Kikuchi, F., Kato, Y., Furihata, K., Kogure, T., Imura, Y., Yoshimura, E., et al. (2016). Formation of gold nanoparticles by glycolipids of Lactobacillus casei. *Sci. Rep.* 6, 34626. doi:10.1038/srep34626

Kim, E-H., Nies, D. H., McEvoy, M. M., and Rensing, C. (2011). Switch or funnel: How RND-type transport systems control periplasmic metal homeostasis. *J. Bacteriol.* 193, 2381–2387. doi:10.1128/JB.01323-10

Kimber, R. L., Parmeggiani, F., Neill, T. S., Merroun, M. L., Goodlet, G., Powell, N. A., et al. (2021). Biotechnological synthesis of Pd/Ag and Pd/Au nanoparticles for enhanced Suzuki–Miyaura cross-coupling activity. *Microb. Biotechnol.* 14, 2435–2447. doi:10.1111/1751-7915.13762

Klaus, T., Joerger, R., Olsson, E., and Granqvist, C-G. (1999). Silver-based crystalline nanoparticles, microbially fabricated. *Proc. Natl. Acad. Sci.* 96, 13611–13614. doi:10.1073/pnas.96.24.13611

Komeda, H., Kobayashi, M., and Shimizu, S. (1997). A novel transporter involved in cobalt uptake. *Proc. Natl. Acad. Sci.* 94, 36–41. doi:10.1073/pnas.94.1.36

Kosolapov, D. B., Kuschk, P., Vainshtein, M. B., Vatsourina, A. V., Wießner, A., Kästner, M., et al. (2004). Microbial processes of heavy metal removal from carbon-deficient effluents in constructed wetlands. *Eng. Life Sci.* 4, 403–411. doi:10.1002/elsc.200420048

Krebsz, M., Kótai, L., Sajó, I. E., Váczi, T., and Pasinszki, T. (2021). Carbon microsphere-supported metallic nickel nanoparticles as novel heterogeneous catalysts and their application for the reduction of nitrophenol. *Molecules* 26, 5680. doi:10.3390/molecules26185680

Krewulak, K. D., and Vogel, H. J. (2008). Structural biology of bacterial iron uptake. *Biochimica Biophysica Acta (BBA) - Biomembr.* 1778, 1781–1804. doi:10.1016/j.bbamem.2007.07.026

Kröger, A., Geisler, V., Lemma, E., Theis, F., and Lenger, R. (1992). Bacterial fumarate respiration. *Archives Microbiol.* 158, 311–314. doi:10.1007/BF00245358

Kumar, U., Shete, A., Harle, A. S., Kasyutich, O., Schwarzacher, W., Pundle, A., et al. (2008). Extracellular bacterial synthesis of protein-functionalized ferromagnetic Co 3 O 4 nanocrystals and imaging of self-organization of bacterial cells under stress after exposure to metal ions. *Chem. Mater.* 20, 1484–1491. doi:10.1021/cm702727x

Lau, C. K. Y., Krewulak, K. D., and Vogel, H. J. (2016). Bacterial ferrous iron transport: The Feo system. *FEMS Microbiol. Rev.* 40, 273–298. doi:10.1093/femsre/fuv049

Le Nagard, L., Morillo-López, V., Fradin, C., and Bazylinski, D. A. (2018). Growing magnetotactic bacteria of the genus Magnetospirillum: Strains MSR-1, AMB-1 and MS-1. *J. Vis. Exp.* 2018, 58536. doi:10.3791/58536

Lengke, M. F., Fleet, M. E., and Southam, G. (2006). Synthesis of platinum nanoparticles by reaction of filamentous cyanobacteria with platinum(IV)−Chloride complex. *Langmuir* 22, 7318–7323. doi:10.1021/la060873s

Li, J., Tian, B., Li, T., Dai, S., Weng, Y., Lu, J., et al. (2018). Biosynthesis of Au, Ag and Au–Ag bimetallic nanoparticles using protein extracts of Deinococcus radiodurans and evaluation of their cytotoxicity. *Int. J. Nanomedicine* 13, 1411–1424. doi:10.2147/IJN.S149079

Li, Q., Liu, F., Li, M., Chen, C., and Gadd, G. M. (2022). Nanoparticle and nanomineral production by fungi. *Fungal Biol. Rev.* 41, 31–44. doi:10.1016/j.fbr.2021.07.003

Li, S-N., Wang, R., and Ho, S-H. (2021). Algae-mediated biosystems for metallic nanoparticle production: From synthetic mechanisms to aquatic environmental applications. *J. Hazard. Mater.* 420, 126625. doi:10.1016/j.jhazmat.2021.126625

Li, X. Z., Nikaido, H., and Williams, K. E. (1997). Silver-resistant mutants of *Escherichia coli* display active efflux of Ag+ and are deficient in porins. *J. Bacteriol.* 179, 6127–6132. doi:10.1128/jb.179.19.6127-6132.1997

Lin, I. W-S., Lok, C-N., and Che, C-M. (2014). Biosynthesis of silver nanoparticles from silver(i) reduction by the periplasmic nitrate reductase c-type cytochrome subunit NapC in a silver-resistant *E. coli*. *Chem. Sci.* 5, 3144–3150. doi:10.1039/C4SC00138A

Liu, Y., Li, G. R., Guo, F. F., Jiang, W., Li, Y., and Li, L. J. (2010). Large-scale production of magnetosomes by chemostat culture of Magnetospirillum gryphiswaldense at high cell density. *Microb. Cell Factories* 9, 99. doi:10.1186/1475-2859-9-99

Lloyd, J. R. (2003). Microbial reduction of metals and radionuclides. *FEMS Microbiol. Rev.* 27, 411–425. doi:10.1016/S0168-6445(03)00044-5

Lovley, D. R. (1993). Dissimilatory metal reduction. *Annu. Rev. Microbiol.* 47, 263–290. doi:10.1146/annurev.mi.47.100193.001403

Lovley, D. R., Giovannoni, S. J., White, D. C., Champine, J. E., Phillips, E. J. P., Gorby, Y. A., et al. (1993). Geobacter metallireducens gen. nov. sp. nov., a microorganism capable of coupling the complete oxidation of organic compounds to the reduction of iron and other metals. *Archives Microbiol.* 159, 336–344. doi:10.1007/BF00290916

Lozhkomoev, A. S., Pervikov, A. V., Kazantsev, S. O., Sharipova, A. F., Rodkevich, N. G., Toropkov, N. E., et al. (2021). Synthesis of Fe/Fe3O4 core-shell nanoparticles by electrical explosion of the iron wire in an oxygen-containing atmosphere. *J. Nanoparticle Res.* 23, 73. doi:10.1007/s11051-021-05180-x

Lusa, M., Lehto, J., and Bomberg, M. (2016). The uptake of Ni²⁺ and Ag⁺ by bacterial strains isolated from a boreal nutrient-poor bog. *AIMS Microbiol.* 2, 120–137. doi:10.3934/microbiol.2016.2.120

Lutkenhaus, J. F. (1977). Role of a major outer membrane protein in *Escherichia coli*. *J. Bacteriol.* 131, 631–637. doi:10.1128/jb.131.2.631-637.1977

Ma, Z., Jacobsen, F. E., and Giedroc, D. P. (2009). Coordination chemistry of bacterial metal transport and sensing. *Chem. Rev.* 109, 4644–4681. doi:10.1021/cr900077w

Mahdi, Z. S., Talebnia Roshan, F., Nikzad, M., and Ezoji, H. (2020). Biosynthesis of zinc oxide nanoparticles using bacteria: A study on the characterization and application for electrochemical determination of bisphenol A. *Inorg. Nano-Metal Chem.* 51, 1–9. doi:10.1080/24701556.2020.1835962

Majeed, S., Danish, M., Mohamad Ibrahim, M. N., Sekeri, S. H., Ansari, M. T., Nanda, A., et al. (2021). Bacteria mediated synthesis of iron oxide nanoparticles and their antibacterial, antioxidant, cytocompatibility properties. *J. Clust. Sci.* 32, 1083–1094. doi:10.1007/s10876-020-01876-7

Makela, A. V., Schott, M. A., Madsen, C. S., Greeson, E. M., and Contag, C. H. (2022). Magnetic particle imaging of magnetotactic bacteria as living contrast agents is improved by altering magnetosome arrangement. *Nano Lett.* 22, 4630–4639. doi:10.1021/acs.nanolett.1c05042

Mangaiyarkarasi, R., Priyanga, M., Santhiya, N., and Umadevi, S. (2020). *In situ* preparation of palladium nanoparticles in ionic liquid crystal microemulsion and their application in Heck reaction. *J. Mol. Liq.* 310, 113241. doi:10.1016/j.molliq.2020.113241

Marimuthu, S., Rahuman, A. A., Kirthi, A. V., Santhoshkumar, T., Jayaseelan, C., and Rajakumar, G. (2013). Eco-friendly microbial route to synthesize cobalt nanoparticles using Bacillus thuringiensis against malaria and dengue vectors. *Parasitol. Res.* 112, 4105–4112. doi:10.1007/s00436-013-3601-2

Marooufpour, N., Alizadeh, M., Hatami, M., and Asgari Lajayer, B. (2019). "Biological synthesis of nanoparticles by different groups of bacteria," in *Microbial nanobionics* (Berlin, Germany: Springer), 63–85. doi:10.1007/978-3-030-16383-9_3

Matsena, M. T., and Chirwa, E. M. N. (2021). Comparative analysis of biological versus chemical synthesis of palladium nanoparticles for catalysis of chromium (VI) reduction. *Sci. Rep.* 11, 16674. doi:10.1038/s41598-021-96024-0

Matsena, M. T., Tichapondwa, S. M., and Chirwa, E. M. N. (2020). Synthesis of biogenic palladium nanoparticles using Citrobacter sp. for application as anode electrocatalyst in a microbial fuel cell. *Catalysts* 10, 838. doi:10.3390/catal10080838

Matsumoto, T., Phann, I., and Okibe, N. (2021). Biogenic platinum nanoparticles' production by extremely acidophilic Fe(III)-Reducing bacteria. *Minerals* 11, 1175. doi:10.3390/min11111175

Matsunaga, T., Sakaguchi, T., and Tadakoro, F. (1991). Magnetite formation by a magnetic bacterium capable of growing aerobically. *Appl. Microbiol. Biotechnol.* 35, 651–655. doi:10.1007/BF00169632

Mehta, T., Coppi, M. V., Childers, S. E., and Lovley, D. R. (2005). Outer membrane c -type cytochromes required for Fe(III) and Mn(IV) oxide reduction in geobacter sulfurreducens. *Appl. Environ. Microbiol.* 71, 8634–8641. doi:10.1128/AEM.71.12.8634-8641.2005

Menazea, A. A. (2020). Femtosecond laser ablation-assisted synthesis of silver nanoparticles in organic and inorganic liquids medium and their antibacterial efficiency. *Radiat. Phys. Chem.* 168, 108616. doi:10.1016/j.radphyschem.2019.108616

Mikheenko, I. P., Bennett, J. A., Omajali, J. B., Walker, M., Johnson, D. B., Grail, B. M., et al. (2022). Selective hydrogenation catalyst made via heat-processing of biogenic Pd nanoparticles and novel 'green' catalyst for Heck coupling using waste sulfidogenic bacteria. *Appl. Catal. B Environ.* 306, 121059. doi:10.1016/j.apcatb.2021.121059

Mikheenko, I. P., Rousset, M., Dementin, S., and Macaskie, L. E. (2008). Bioaccumulation of palladium by Desulfovibrio fructosivorans wild-type and hydrogenase-deficient strains. *Appl. Environ. Microbiol.* 74, 6144–6146. doi:10.1128/AEM.02538-07

Monteil, C. L., and Lefevre, C. T. (2020). Magnetoreception in microorganisms. *Trends Microbiol.* 28, 266–275. doi:10.1016/j.tim.2019.10.012

Moon, J-W., Ivanov, I. N., Duty, C. E., Love, L. J., Rondinone, A. J., Wang, W., et al. (2013). Scalable economic extracellular synthesis of CdS nanostructured particles by a non-pathogenic thermophile. *J. Industrial Microbiol. Biotechnol.* 40, 1263–1271. doi:10.1007/s10295-013-1321-3

Moon, J-W., Phelps, T. J., Fitzgerald, C. L., Jr, Lind, R. F., Elkins, J. G., Jang, G. G., et al. (2016). Manufacturing demonstration of microbially mediated zinc sulfide nanoparticles in pilot-plant scale reactors. *Appl. Microbiol. Biotechnol.* 100, 7921–7931. doi:10.1007/s00253-016-7556-y

Moon, J-W., Rawn, C. J., Rondinone, A. J., Love, L. J., Roh, Y., Everett, S. M., et al. (2010). Large-scale production of magnetic nanoparticles using bacterial fermentation. *J. Industrial Microbiol. Biotechnol.* 37, 1023–1031. doi:10.1007/s10295-010-0749-y

Mubraiz, N., Bano, A., Mahmood, T., and Khan, N. (2021). Microbial and plant assisted synthesis of cobalt oxide nanoparticles and their antimicrobial activities. *Agronomy* 11, 1607. doi:10.3390/agronomy11081607

Mukherjee, K., Gupta, R., Kumar, G., Kumari, S., Biswas, S., and Padmanabhan, P. (2018). Synthesis of silver nanoparticles by Bacillus clausii and computational profiling of nitrate reductase enzyme involved in production. *J. Genet. Eng. Biotechnol.* 16, 527–536. doi:10.1016/j.jgeb.2018.04.004

Muller, V. (2003). Energy conservation in acetogenic bacteria. *Appl. Environ. Microbiol.* 69, 6345–6353. doi:10.1128/AEM.69.11.6345-6353.2003

Nair, B., and Pradeep, T. (2002). Coalescence of nanoclusters and formation of submicron crystallites assisted by Lactobacillus strains. *Cryst. Growth & Des.* 2, 293–298. doi:10.1021/cg0255164

Nan, X., Lai, W., Li, D., Tian, J., Hu, Z., and Fang, Q. (2021). Biocompatibility of bacterial magnetosomes as MRI contrast agent: A long-term *in vivo* follow-up study. *Nanomaterials* 11, 1235. doi:10.3390/nano11051235

Nanda, A., and Saravanan, M. (2009). Biosynthesis of silver nanoparticles from *Staphylococcus aureus* and its antimicrobial activity against MRSA and MRSE. *Nanomedicine Nanotechnol. Biol. Med.* 5, 452–456. doi:10.1016/j.nano.2009.01.012

Narasaiah, B. P., and Mandal, B. K. (2020). Remediation of azo-dyes based toxicity by agro-waste cotton boll peels mediated palladium nanoparticles. *J. Saudi Chem. Soc.* 24, 267–281. doi:10.1016/j.jscs.2019.11.003

Narayanan, K. B., and Sakthivel, N. (2010). Biological synthesis of metal nanoparticles by microbes. *Adv. Colloid Interface Sci.* 156, 1–13. doi:10.1016/j.cis.2010.02.001

Navarro, C., Wu, L-F., and Mandrand-Berthelot, M-A. (1993). The nik operon of *Escherichia coli* encodes a periplasmic binding-protein-dependent transport system for nickel. *Mol. Microbiol.* 9, 1181–1191. doi:10.1111/j.1365-2958.1993.tb01247.x

Nies, D. H. (1992). Resistance to cadmium, cobalt, zinc, and nickel in microbes. *Plasmid* 27, 17–28. doi:10.1016/0147-619X(92)90003-S

Nies, D. H., and Silver, S. (1995). Ion efflux systems involved in bacterial metal resistances. *J. Industrial Microbiol.* 14, 186–199. doi:10.1007/BF01569902

Noman, M., Shahid, M., Ahmed, T., Niazi, M. B. K., Hussain, S., Song, F., et al. (2020). Use of biogenic copper nanoparticles synthesized from a native Escherichia sp. as photocatalysts for azo dye degradation and treatment of textile effluents. *Environ. Pollut.* 257, 113514. doi:10.1016/j.envpol.2019.113514

Nomoev, A. V., and Bardakhanov, S. P. (2012). Synthesis and structure of Ag-Si nanoparticles obtained by the electron-beam evaporation/condensation method. *Tech. Phys. Lett.* 38, 375–378. doi:10.1134/S1063785012040268

Nudelman, H., and Zarivach, R. (2014). Structure prediction of magnetosome-associated proteins. *Front. Microbiol.* 5, 9. doi:10.3389/fmicb.2014.00009

Omajali, J. B., Gomez-Bolivar, J., Mikheenko, I. P., Sharma, S., Kayode, B., Al-Duri, B., et al. (2019). Novel catalytically active Pd/Ru bimetallic nanoparticles synthesized by Bacillus benzeovorans. *Sci. Rep.* 9, 4715. doi:10.1038/s41598-019-40312-3

Omajali, J. B., Mikheenko, I. P., Merroun, M. L., Wood, J., and Macaskie, L. E. (2015). Characterization of intracellular palladium nanoparticles synthesized by Desulfovibrio desulfuricans and Bacillus benzeovorans. *J. Nanoparticle Res.* 17, 264. doi:10.1007/s11051-015-3067-5

Orozco-Montes, V., Caillard, A., Brault, P., Chamorro-Coral, W., Bigarre, J., Sauldubois, A., et al. (2021). Synthesis of platinum nanoparticles by plasma sputtering onto glycerol: Effect of argon pressure on their physicochemical properties. *J. Phys. Chem. C* 125, 3169–3179. doi:10.1021/acs.jpcc.0c09746

Oves, M., Khan, M. S., Zaidi, A., Ahmed, A. S., Ahmed, F., Ahmad, E., et al. (2013). Antibacterial and cytotoxic efficacy of extracellular silver nanoparticles biofabricated from chromium reducing novel OS4 strain of Stenotrophomonas maltophilia. *PLoS ONE* 8, e59140. doi:10.1371/journal.pone.0059140

Oves, M., Rauf, M. A., Hussain, A., Qari, H. A., Khan, A. A. P., Muhammad, P., et al. (2019). Antibacterial silver nanomaterial synthesis from mesoflavibacter zeaxanthinifaciens and targeting biofilm formation. *Front. Pharmacol.* 10, 801. doi:10.3389/fphar.2019.00801

Palmer, L. D., and Skaar, E. P. (2016). Transition metals and virulence in bacteria. *Annu. Rev. Genet.* 50, 67–91. doi:10.1146/annurev-genet-120215-035146

Parashar, M., Shukla, V. K., and Singh, R. (2020). Metal oxides nanoparticles via sol–gel method: A review on synthesis, characterization and applications. *J. Mater. Sci. Mater. Electron.* 31, 3729–3749. doi:10.1007/s10854-020-02994-8

Patil, M. P., Kang, M., Niyonizigiye, I., Singh, A., Kim, J-O., Seo, Y. B., et al. (2019). Extracellular synthesis of gold nanoparticles using the marine bacterium Paracoccus haeundaensis BC74171T and evaluation of their antioxidant activity and antiproliferative effect on normal and cancer cell lines. *Colloids Surfaces B Biointerfaces.* 183, 110455. doi:10.1016/j.colsurfb.2019.110455

Patil, S., Sastry, M., and Bharde, A. (2022). Size and shape directed novel green synthesis of plasmonic nanoparticles using bacterial metabolites and their anticancer effects. *Front. Microbiol.* 13, 866849. doi:10.3389/fmicb.2022.866849

Pham, V. H. T., Kim, J., Chang, S., and Chung, W. (2022). Bacterial biosorbents, an efficient heavy metals green clean-up strategy: Prospects, challenges, and opportunities. *Microorganisms* 10, 610. doi:10.3390/microorganisms10030610

Pourali, P., Badiee, S. H., Manafi, S., Noorani, T., Rezaei, A., and Yahyaei, B. (2017). Biosynthesis of gold nanoparticles by two bacterial and fungal strains, Bacillus cereus and Fusarium oxysporum, and assessment and comparison of their nanotoxicity *in vitro* by direct and indirect assays. *Electron. J. Biotechnol.* 29, 86–93. doi:10.1016/j.ejbt.2017.07.005

Prasad, S. R., Teli, S. B., Ghosh, J., Prasad, N. R., Shaikh, V. S., Nazeruddin, G. M., et al. (2021). A review on bio-inspired synthesis of silver nanoparticles: Their antimicrobial efficacy and toxicity. *Eng. Sci.* 2021. doi:10.30919/es8d479

Quintanilla, A., Valvo, M., Lafont, U., Kelder, E. M., Kreutzer, M. T., and Kapteijn, F. (2010). Synthesis of anisotropic gold nanoparticles by electrospraying into a reductive-surfactant solution. *Chem. Mater.* 22, 1656–1663. doi:10.1021/cm903712y

Quinteros, M. A., Bonilla, J. O., Alborés, S. V., Villegas, L. B., and Páez, P. L. (2019). Biogenic nanoparticles: Synthesis, stability and biocompatibility mediated by proteins of *Pseudomonas aeruginosa*. *Colloids Surfaces B Biointerfaces* 184, 110517. doi:10.1016/j.colsurfb.2019.110517

Rajora, N., Kaushik, S., Jyoti, A., and Kothari, S. L. (2016). Rapid synthesis of silver nanoparticles by Pseudomonas stutzeri isolated from textile soil under optimised conditions and evaluation of their antimicrobial and cytotoxicity properties. *IET Nanobiotechnology* 10, 367–373. doi:10.1049/iet-nbt.2015.0107

Ramos-Ruiz, A., Sesma-Martin, J., Sierra-Alvarez, R., and Field, J. A. (2017). Continuous reduction of tellurite to recoverable tellurium nanoparticles using an upflow anaerobic sludge bed (UASB) reactor. *Water Res.* 108, 189–196. doi:10.1016/j.watres.2016.10.074

Reichart, O., Szakmár, K., Jozwiak, Á., Felföldi, J., and Baranyai, L. (2007). Redox potential measurement as a rapid method for microbiological testing and its validation for coliform determination. *Int. J. Food Microbiol.* 114, 143–148. doi:10.1016/j.ijfoodmicro.2006.08.016

Rensing, C., Fan, B., Sharma, R., Mitra, B., and Rosen, B. P. (2000). CopA: An *Escherichia coli* Cu(I)-translocating P-type ATPase. *Proc. Natl. Acad. Sci.* 97, 652–656. doi:10.1073/pnas.97.2.652

Restrepo, C. V., and Villa, C. C. (2021). Synthesis of silver nanoparticles, influence of capping agents, and dependence on size and shape: A review. *Environ. Nanotechnol. Monit. Manag.* 15, 100428. doi:10.1016/j.enmm.2021.100428

Riaz Rajoka, M. S., Mehwish, H. M., Zhang, H., Ashraf, M., Fang, H., Zeng, X., et al. (2020). Antibacterial and antioxidant activity of exopolysaccharide mediated silver nanoparticle synthesized by Lactobacillus brevis isolated from Chinese koumiss. *Colloids Surfaces B Biointerfaces*. 186, 110734. doi:10.1016/j.colsurfb.2019.110734

Ridley, W. P., Dizikes, L., Cheh, A., and Wood, J. M. (1977). Recent studies on biomethylation and demethylation of toxic elements. *Environ. Health Perspect.* 19, 43–46. doi:10.1289/ehp.771943

Ridley, W. P., Dizikes, L. J., and Wood, J. M. (1977). Biomethylation of toxic elements in the environment. *Science* 197, 329–332. doi:10.1126/science.877556

Rouch, D. A., Lee, B. T. O., and Morby, A. P. (1995). Understanding cellular responses to toxic agents: A model for mechanism-choice in bacterial metal resistance. *J. Industrial Microbiol.* 14, 132–141. doi:10.1007/BF01569895

Samuel, M. S., Datta, S., Chandrasekar, N., Balaji, R., Selvarajan, E., and Vuppala, S. (2021). Biogenic synthesis of iron oxide nanoparticles using *Enterococcus faecalis*: Adsorption of hexavalent chromium from aqueous solution and *in vitro* cytotoxicity analysis. *Nanomaterials* 11, 3290. doi:10.3390/nano11123290

Saravanan, A., Kumar, P. S., Karishma, S., Vo, D-V. N., Jeevanantham, S., Yaashikaa, P. R., et al. (2021). A review on biosynthesis of metal nanoparticles and its environmental applications. *Chemosphere* 264, 128580. doi:10.1016/j.chemosphere.2020.128580

Saravanan, M., Barik, S. K., MubarakAli, D., Prakash, P., and Pugazhendhi, A. (2018). Synthesis of silver nanoparticles from Bacillus brevis (NCIM 2533) and their antibacterial activity against pathogenic bacteria. *Microb. Pathog.* 116, 221–226. doi:10.1016/j.micpath.2018.01.038

Sasireka, K. S., and Lalitha, P. (2021). Biogenic synthesis of bimetallic nanoparticles and their applications. *Rev. Inorg. Chem.* 41, 223–244. doi:10.1515/revic-2020-0024

Sathyavathi, S., Manjula, A., Rajendhran, J., and Gunasekaran, P. (2014). Extracellular synthesis and characterization of nickel oxide nanoparticles from Microbacterium sp. MRS-1 towards bioremediation of nickel electroplating industrial effluent. *Bioresour. Technol.* 165, 270–273. doi:10.1016/j.biortech.2014.03.031

Schleifer, K. H., Schüler, D., Spring, S., Weizenegger, M., Amann, R., Ludwig, W., et al. (1991). The Genus Magnetospirillum gen. nov. Description of Magnetospirillum gryphiswaldense sp. nov. and Transfer of Aquaspirillum magnetotacticum to Magnetospirillum magnetotacticum comb. nov. *Syst. Appl. Microbiol.* 14, 379–385. doi:10.1016/S0723-2020(11)80313-9

Schröfel, A., Kratošová, G., Šafařík, I., Šafaříková, M., Raška, I., and Shor, L. M. (2014). Applications of biosynthesized metallic nanoparticles – a review. *Acta Biomater.* 10, 4023–4042. doi:10.1016/j.actbio.2014.05.022

Schuchmann, K., and Müller, V. (2012). A bacterial electron-bifurcating hydrogenase. *J. Biol. Chem.* 287, 31165–31171. doi:10.1074/jbc.M112.395038

Schuler, D. (2002). The biomineralization of magnetosomes in Magnetospirillum gryphiswaldense. *Int. Microbiol.* 5, 209–214. doi:10.1007/s10123-002-0086-8

Sharma, A., Chaturvedi, R., Islam, A., and Singh, P. K. (2021). Eco-friendly synthesis F Cadmium sulfide nanoparticles using supernatant of Bacillus badius and its characterization. *Mater. Today Proc.* 45, 3419–3421. doi:10.1016/j.matpr.2020.12.926

Sharma, N., Pinnaka, A. K., Raje, M., Fnu, A., Bhattacharyya, M. S., and Choudhury, A. R. (2012). Exploitation of marine bacteria for production of gold nanoparticles. *Microb. Cell Factories* 11, 86. doi:10.1186/1475-2859-11-86

Shi, L., Dong, H., Reguera, G., Beyenal, H., Lu, A., Liu, J., et al. (2016). Extracellular electron transfer mechanisms between microorganisms and minerals. *Nat. Rev. Microbiol.* 14, 651–662. doi:10.1038/nrmicro.2016.93

Shi, L., Rosso, K. M., Clarke, T. A., Richardson, D. J., Zachara, J. M., and Fredrickson, J. K. (2012). Molecular underpinnings of Fe(III) oxide reduction by Shewanella oneidensis MR-1. *Front. Microbiol.* 3, 50. doi:10.3389/fmicb.2012.00050

Shim, H-W., Jin, Y-H., Seo, S-D., Lee, S-H., and Kim, D-W. (2011). Highly reversible lithium storage in Bacillus subtilis-directed porous Co 3 O 4 nanostructures. *ACS Nano* 5, 443–449. doi:10.1021/nn1021605

Shim, H-W., Lim, A-H., Kim, J-C., Jang, E., Seo, S-D., Lee, G-H., et al. (2013). Scalable one-pot bacteria-templating synthesis route toward hierarchical, porous-Co3O4 superstructures for supercapacitor electrodes. *Sci. Rep.* 3, 2325. doi:10.1038/srep02325

Shojaei, M., Shokuhfar, A., and Zolriasatein, A. (2021). Synthesis and characterization of CuAlS2 nanoparticles by mechanical milling. *Mater. Today Commun.* 27, 102243. doi:10.1016/j.mtcomm.2021.102243

Shunmugam, R., Renukadevi Balusamy, S., Kumar, V., Menon, S., Lakshmi, T., and Perumalsamy, H. (2021). Biosynthesis of gold nanoparticles using marine microbe (Vibrio alginolyticus) and its anticancer and antioxidant analysis. *J. King Saud Univ. - Sci.* 33, 101260. doi:10.1016/j.jksus.2020.101260

Silver, S. (1996). Bacterial resistances to toxic metal ions - a review. *Gene* 179, 9–19. doi:10.1016/S0378-1119(96)00323-X

Singh, H., Du, J., and Yi, T-H. (2017). Biosynthesis of silver nanoparticles using Aeromonas sp. THG-FG1.2 and its antibacterial activity against pathogenic microbes. *Artif. Cells, Nanomedicine, Biotechnol.* 45, 584–590. doi:10.3109/21691401.2016.1163715

Singh, N., Jenkins, G. J. S., Asadi, R., and Doak, S. H. (2010). Potential toxicity of superparamagnetic iron oxide nanoparticles (SPION). *Nano Rev.* 1, 5358. doi:10.3402/nano.v1i0.5358

Singh, P., Singh, H., Kim, Y. J., Mathiyalagan, R., Wang, C., and Yang, D. C. (2016). Extracellular synthesis of silver and gold nanoparticles by Sporosarcina koreensis DC4 and their biological applications. *Enzyme Microb. Technol.* 86, 75–83. doi:10.1016/j.enzmictec.2016.02.005

Søbjerg, L. S., Gauthier, D., Lindhardt, A. T., Bunge, M., Finster, K., Meyer, R. L., et al. (2009). Bio-supported palladium nanoparticles as a catalyst for suzuki–miyaura and mizoroki–heck reactions. *Green Chem.* 11, 2041. doi:10.1039/b918351p

Soni, V., Raizada, P., Singh, P., Cuong, H. N., Rangabhashiyam, S., Saini, A., et al. (2021). Sustainable and green trends in using plant extracts for the synthesis of biogenic metal nanoparticles toward environmental and pharmaceutical advances: A review. *Environ. Res.* 202, 111622. doi:10.1016/j.envres.2021.111622

Stephen, A. J., Rees, N. V., Mikheenko, I., and Macaskie, L. E. (2019). Platinum and palladium bio-synthesized nanoparticles as sustainable fuel cell catalysts. *Front. Energy Res.* 7, 66. doi:10.3389/fenrg.2019.00066

Stoller, M., and Ochando-Pulido, J. M. (2020). ZnO nano-particles production intensification by means of a spinning disk reactor. *Nanomaterials* 10, 1321. doi:10.3390/nano10071321

Sun, J-B., Zhao, F., Tang, T., Jiang, W., Tian, J., Li, Y., et al. (2008). High-yield growth and magnetosome formation by Magnetospirillum gryphiswaldense MSR-1 in an oxygen-controlled fermentor supplied solely with air. *Appl. Microbiol. Biotechnol.* 79, 389. doi:10.1007/s00253-008-1453-y

Sundararaju, S., Arumugam, M., and Bhuyar, P. (2020). Microbacterium sp. MRS-1, a potential bacterium for cobalt reduction and synthesis of less/non-toxic cobalt oxide nanoparticles (Co3O4). *Beni-Suef Univ. J. Basic Appl. Sci.* 9, 44. doi:10.1186/s43088-020-00070-y

Tan, L., Ray Jones, T., Poitras, J., Xie, J., Liu, X., and Southam, G. (2020). Biochemical synthesis of palladium nanoparticles: The influence of chemical fixatives used in electron microscopy on nanoparticle formation and catalytic performance. *J. Hazard. Mater.* 398, 122945. doi:10.1016/j.jhazmat.2020.122945

Tang, S., Qiao, R., Lin, Y., Li, Y., Zhao, Q., Yuan, D., et al. (2019). Functional liquid metal nanoparticles produced by liquid-based nebulization. *Adv. Mater. Technol.* 4, 1800420. doi:10.1002/admt.201800420

Taran, M., Rad, M., and Alavi, M. (2017). Biosynthesis of TiO2 and ZnO nanoparticles by Halomonas elongata IBRC-M 10214 in different conditions of medium. *BioImpacts* 8, 81–89. doi:10.15171/bi.2018.10

Tavares, J., Swanson, E. J., and Coulombe, S. (2008). Plasma synthesis of coated metal nanoparticles with surface properties tailored for dispersion. *Plasma Process. Polym.* 5, 759–769. doi:10.1002/ppap.200800074

Tikariha, S., Banerjee, S., Dev, A., and Singh, S. (2017). *Growth phase-dependent synthesis of gold nanoparticles using Bacillus licheniformis. Applications of biotechnology for sustainable development*. Singapore: Springer Singapore, 121–128. doi:10.1007/978-981-10-5538-6_15

Toropova, Y., Golovkin, A., Malashicheva, A., Korolev, D., Gorshkov, A., Gareev, K., et al. (2017). *In vitro* toxicity of Fe_mO_n, Fe_mO_n-SiO₂ composite, and SiO₂-Fe_mO_n core-shell magnetic nanoparticles. *Int. J. Nanomedicine* 12, 593–603. doi:10.2147/IJN.S122580

Tsuruta, T. (2004). Biosorption and recycling of gold using various microorganisms. *J. General Appl. Microbiol.* 50, 221–228. doi:10.2323/jgam.50.221

Tuo, Y., Liu, G., Dong, B., Yu, H., Zhou, J., Wang, J., et al. (2017). Microbial synthesis of bimetallic PdPt nanoparticles for catalytic reduction of 4-nitrophenol. *Environ. Sci. Pollut. Res.* 24, 5249–5258. doi:10.1007/s11356-016-8276-7

Tuo, Y., Liu, G., Dong, B., Zhou, J., Wang, A., Wang, J., et al. (2015). Microbial synthesis of Pd/Fe3O4, Au/Fe3O4 and PdAu/Fe3O4 nanocomposites for catalytic reduction of nitroaromatic compounds. *Sci. Rep.* 5, 13515. doi:10.1038/srep13515

Uzun, M., Alekseeva, L., Krutkina, M., Koziaeva, V., and Grouzdev, D. (2020). Unravelling the diversity of magnetotactic bacteria through analysis of open genomic databases. *Sci. Data* 7, 252. doi:10.1038/s41597-020-00593-0

Vijayakumar, M., Priya, K., Nancy, F. T., Noorlidah, A., and Ahmed, A. B. A. (2013). Biosynthesis, characterisation and anti-bacterial effect of plant-mediated silver nanoparticles using Artemisia nilagirica. *Industrial Crops Prod.* 41, 235–240. doi:10.1016/j.indcrop.2012.04.017

Vinay, S. P., UdayabhanuNagaraju, G., Chandrappa, C. P., and Chandrasekhar, N. (2020). Hydrothermal synthesis of gold nanoparticles using spider cobweb as novel biomaterial: Application to photocatalytic. *Chem. Phys. Lett.* 748, 137402. doi:10.1016/j.cplett.2020.137402

Vincent, S. G. T., Jennerjahn, T., and Ramasamy, K. (2021). "Environmental variables and factors regulating microbial structure and functions," in *Microbial communities in coastal sediments* (Amsterdam, Netherlands: Elsevier), 79–117. doi:10.1016/B978-0-12-815165-5.00003-0

Waldron, K. J., and Robinson, N. J. (2009). How do bacterial cells ensure that metalloproteins get the correct metal? *Nat. Rev. Microbiol.* 7, 25–35. doi:10.1038/nrmicro2057

Wang, W., Zhang, B., Liu, Q., Du, P., Liu, W., and He, Z. (2018). Biosynthesis of palladium nanoparticles using Shewanella loihica PV-4 for excellent catalytic reduction of chromium(vi). *Environ. Sci. Nano.* 5, 730–739. doi:10.1039/C7EN01167A

Wang, Y., Sevinc, P. C., Belchik, S. M., Fredrickson, J., Shi, L., and Lu, H. P. (2013). Single-cell imaging and spectroscopic analyses of Cr(VI) reduction on the surface of bacterial cells. *Langmuir* 29, 950–956. doi:10.1021/la303779y

Weng, X., Guo, M., Luo, F., and Chen, Z. (2017). One-step green synthesis of bimetallic Fe/Ni nanoparticles by eucalyptus leaf extract: Biomolecules identification, characterization and catalytic activity. *Chem. Eng. J.* 308, 904–911. doi:10.1016/j.cej.2016.09.134

Weng, Y., Li, J., Ding, X., Wang, B., Dai, S., Zhou, Y., et al. (2020). <p> Functionalized gold and silver bimetallic nanoparticles using Deinococcus radiodurans protein extract mediate degradation of toxic dye malachite green</p>. *Int. J. Nanomedicine* 15, 1823–1835. doi:10.2147/IJN.S236683

Wiesemann, N., Mohr, J., Grosse, C., Herzberg, M., Hause, G., Reith, F., et al. (2013). Influence of copper resistance determinants on gold transformation by Cupriavidus metallidurans strain CH34. *J. Bacteriol.* 195, 2298–2308. doi:10.1128/JB.01951-12

Xia, X., Wu, S., Li, N., Wang, D., Zheng, S., and Wang, G. (2018). Novel bacterial selenite reductase CsrF responsible for Se(IV) and Cr(VI) reduction that produces nanoparticles in Alishewanella sp. WH16-1. *J. Hazard. Mater.* 342, 499–509. doi:10.1016/j.jhazmat.2017.08.051

Xiao, X., Ma, X-B., Yuan, H., Liu, P-C., Lei, Y-B., Xu, H., et al. (2015). Photocatalytic properties of zinc sulfide nanocrystals biofabricated by metal-reducing bacterium Shewanella oneidensis MR-1. *J. Hazard. Mater.* 288, 134–139. doi:10.1016/j.jhazmat.2015.02.009

Xing, J., Yin, T., Li, S., Xu, T., Ma, A., Chen, Z., et al. (2021). Sequential magneto-actuated and optics-triggered biomicrorobots for targeted cancer therapy. *Adv. Funct. Mater.* 31, 2008262. doi:10.1002/adfm.202008262

Xu, H., Xiao, Y., Xu, M., Cui, H., Tan, L., Feng, N., et al. (2019). Microbial synthesis of Pd–Pt alloy nanoparticles using Shewanella oneidensis MR-1 with enhanced catalytic activity for nitrophenol and azo dyes reduction. *Nanotechnology* 30, 065607. doi:10.1088/1361-6528/aaf2a6

Xu, S., Luo, X., Huang, Q., and Chen, W. (2021). Calcium-crosslinked alginate-encapsulated bacteria for remediating of cadmium-polluted water and production of CdS nanoparticles. *Appl. Microbiol. Biotechnol.* 105, 2171–2179. doi:10.1007/s00253-021-11155-8

Yahyaei, B., Peyvandi, N., Akbari, H., Arabzadeh, S., Afsharnezhad, S., Ajoudanifar, H., et al. (2016). Production, assessment, and impregnation of hyaluronic acid with silver nanoparticles that were produced by Streptococcus pyogenes for tissue engineering applications. *Appl. Biol. Chem.* 59, 227–237. doi:10.1007/s13765-016-0147-x

Yan, L., Zhang, S., Chen, P., Liu, H., Yin, H., and Li, H. (2012). Magnetotactic bacteria, magnetosomes and their application. *Microbiol. Res.* 167, 507–519. doi:10.1016/j.micres.2012.04.002

Yang, J., Ju, P., Dong, X., Duan, J., Xiao, H., Tang, X., et al. (2023). Green synthesis of functional metallic nanoparticles by dissimilatory metal-reducing bacteria "Shewanella": A comprehensive review. *J. Mater. Sci. Technol.* 158, 63–76. doi:10.1016/j.jmst.2023.01.041

Yang, Y., Song, B., Ke, X., Xu, F., Bozhilov, K. N., Hu, L., et al. (2020). Aerosol synthesis of high entropy alloy nanoparticles. *Langmuir* 36, 1985–1992. doi:10.1021/acs.langmuir.9b03392

Yaqoob, A. A., Ahmad, H., Parveen, T., Ahmad, A., Oves, M., Ismail, I. M. I., et al. (2020). Recent advances in metal decorated nanomaterials and their various biological applications: A review. *Front. Chem.* 8, 341. doi:10.3389/fchem.2020.00341

Yu, X., and Jiang, J. (2019). Phosphate microbial mineralization removes nickel ions from electroplating wastewater. *J. Environ. Manag.* 245, 447–453. doi:10.1016/j.jenvman.2019.05.091

Yu, Y-Y., Cheng, Q-W., Sha, C., Chen, Y-X., Naraginti, S., and Yong, Y-C. (2020). Size-controlled biosynthesis of FeS nanoparticles for efficient removal of aqueous Cr(VI). *Chem. Eng. J.* 379, 122404. doi:10.1016/j.cej.2019.122404

Zaki, S. A. E-F., Kamal, A., Ashmawy, N. A., and Shoeib, A. A. (2021). Nano-metals forming bacteria in Egypt. I. Synthesis, characterization and effect on some phytopathogenic bacteria *in vitro*. *Sci. Rep.* 11, 12876. doi:10.1038/s41598-021-92171-6

Zammit, C. M., and Reith, F. (2013). *Gold biomineralization in bacterium Cupriavidus metallidurans. Encyclopedia of metalloproteins*. New York, NY: Springer New York, 862–867. doi:10.1007/978-1-4614-1533-6_581

Zhan, G., Li, D., and Zhang, L. (2012). Aerobic bioreduction of nickel(II) to elemental nickel with concomitant biomineralization. *Appl. Microbiol. Biotechnol.* 96, 273–281. doi:10.1007/s00253-011-3827-9

Zhang, S., Zhou, H., Liao, H., Tan, P., Tian, W., and Pan, J. (2022). Microbial synthesis of efficient palladium electrocatalyst with high loadings for oxygen reduction reaction in acidic medium. *J. Colloid Interface Sci.* 611, 161–171. doi:10.1016/j.jcis.2021.12.080

Zhang, Y., Zhao, Q., and Chen, B. (2022). Reduction and removal of Cr(VI) in water using biosynthesized palladium nanoparticles loaded Shewanella oneidensis MR-1. *Sci. Total Environ.* 805, 150336. doi:10.1016/j.scitotenv.2021.150336

Zheng, K., and Branicio, P. S. (2020). Synthesis of metallic glass nanoparticles by inert gas condensation. *Phys. Rev. Mater.* 4, 076001. doi:10.1103/PhysRevMaterials.4.076001

frontiers | Frontiers in Nanotechnology

TYPE Original Research
PUBLISHED 16 October 2023
DOI 10.3389/fnano.2023.1292259

OPEN ACCESS

EDITED BY
Tomaz Urbic,
University of Ljubljana, Slovenia

REVIEWED BY
Animesh Pan,
University of Rhode Island, United States
Gokhan Kacar,
Trakya University, Türkiye

*CORRESPONDENCE
Estela Blaisten-Barojas,
blaisten@gmu.edu

RECEIVED 11 September 2023
ACCEPTED 03 October 2023
PUBLISHED 16 October 2023

CITATION
Hopkins SD and Blaisten-Barojas E (2023), Molecular dynamics simulations evidence the thermoresponsive behavior of PNIPAM and PDEA in glycerol solutions.
Front. Nanotechnol. 5:1292259.
doi: 10.3389/fnano.2023.1292259

Molecular dynamics simulations evidence the thermoresponsive behavior of PNIPAM and PDEA in glycerol solutions

Scott D. Hopkins[1,2] and Estela Blaisten-Barojas[1,2]*

[1]Center for Simulation and Modeling, George Mason University, Fairfax, VA, United States,
[2]Department of Computational and Data Sciences, George Mason University, Fairfax, VA, United States

Polymers exhibiting thermoresponsive behavior above a lower critical solution temperature (LCST) undergo a coil-to-globule phase transition that has many biomedical applications, including biosensing, the control of release devices, and gene or drug delivery systems. In addition, there has been sustained scientific interest in these polymers for their use in industrial applications, including water treatment and desalination. Since the coil-to-globule phase transition is greatly affected by the hydrophilic/hydrophobic balance of the polymer-solvent interactions, the LCST of a particular thermoresponsive polymer depends on the solvent environment and can be tuned through the modification of solution parameters such as co-solvent molar concentrations. While there have been numerous experimental and computational studies focused on the properties of these polymers in aqueous solutions, study of their behavior in more viscous solvents has been limited. In this article, the thermoresponsive behavior of poly (N-isopropylacrylamide) (PNIPAM) and poly (N,N-diethylacrylamide) (PDEA) has been evaluated when in solution with water, the highly viscous liquid glycerol, and both 50:50 and 90:10 glycerol:water mixtures. The adopted methodology includes molecular dynamics techniques and a modified OPLS all-atom force field, which is particularly challenging when the monomers of the targeted polymers have side-chains consisting of a hydrophobic isopropyl group and a hydrophilic amide group along the carbon backbone chain. Hence, our approach entailed simulations at the microsecond scale. The structural and energetic properties of the polymers were characterized, including radius of gyration, solvent accessible surface area, polymer-solvent hydrogen bonding, and interaction energies. Our predictions indicate that these polymers sustain a coil-to-globule phase transition in glycerol solvents at significantly higher LCSTs when compared to the LCST in less viscous aqueous solutions. These predictions highlight valuable insights that will prove advantageous for industrial and nano-scale applications requiring polymer phase behavior with elevated LCST well above ambient temperature.

KEYWORDS

thermoresponsive polymer, PNIPAM, PDEA, lower critical solution temperature (LCST), molecular dynamics, glycerol, coil-to-globule transition

1 Introduction

As part of a large family of thermoresponsive polymers, poly (N-isopropylacrylamide) (PNIPAM) and poly-(N,N-diethylacrylamide) (PDEA) exhibit a coil-to-globule phase transition above a lower critical solution temperature (LCST). The LCST of a particular polymer depends on the local solvent environment and can be tuned through solution parameters such as co-solvent molar concentrations or pH. There has been large scientific interest in these polymers regarding biomedical applications (Doberenz et al., 2020). In particular, PNIPAM and PDEA in water solutions have an experimental LCST of approximately 305 K, which is relatively close to body temperature and ideal for potential drug delivery systems (Idziak et al., 1999). As a result, numerous experimental and computational studies have been performed focusing on the properties of these polymers in aqueous solutions, including co-solvents of various salts, alcohols, and urea (Du et al., 2010; Pang and Cui, 2013; Kang et al., 2016; Micciulla et al., 2016; Dalgicdir and van der Vegt, 2019; Pérez-Ramirez et al., 2019; Bharadwaj et al., 2022; Concilio et al., 2022). In general, the addition of co-solvents has been shown to decrease the LCST of PNIPAM when compared to the LCST in a pure water system. There have also been a limited number of studies examining more viscous solvents or their mixture with water, such as experiments on the effect that various concentrations of either glycerol, erythritol, or xylitol mixed with water had on the LCST of PNIPAM (Narang and Venkatesu, 2018; Rosi et al., 2022). In the case of glycerol, it was shown that in aqueous solutions with up to 0.75 M of glycerol, the LCST of PNIPAM decreased from 305 K to 303 K (Narang and Venkatesu, 2018). However, such mixed solvent environments differ significantly from that of pure glycerol. Indeed, at 300 K the viscosity of pure glycerol is almost one thousand times higher than the viscosity of pure water (Gregory, 1963). There are recent experimental trends for employing high glycerol content solutions of 90:10 with polymers in micro channel experiments leading to biosensors novel architectures (Qin and Arratia, 2017).

In this research we predict the influence of high glycerol content in mixed aqueous solutions on the LCST of PNIPAM and PDEA 30-monomer oligomers. Indeed, the effect of glycerol dominated aqueous solutions on the LCST of PNIPAM and PDEA oligomers has yet to be unraveled. Currently, no experiments or simulations exist in the literature on the LCST of either polymer in pure glycerol or in high glycerol concentration of its mixed solutions with water. In a nutshell, the overall thermal behavior exhibited by these polymers in pure glycerol is unknown. In this article we report our Molecular Dynamics (MD) simulations of both oligomers in pure glycerol, in mixed glycerol:water solutions with relative concentration by mass of 90:10, 50:50, and in pure water. We do verify that for PNIPAM in pure water or in the 50:50 glycerol:water, the LCST remains in the range of 300–305 K and predict that PDEA in these solvents displays a similar LCST. Moreover, we predict the LCST of the PNIPAM and PDEA oligomers in pure glycerol and in the 90:10 glycerol:water mixture to be in the range of 380–390 K and 370–380 K, respectively.

This article is organized as follows. Section 2, Models and Methods, provides a description of how the various polymers in solution of pure and mixed liquids are built at the atomic scale providing extensive details on the all-atom MD large-scale simulation methodology. Section 3, Results and Discussion, provides analyses probing the fate that the PNIPAM and PDEA oligomers undergo when mixed in pure glycerol, 90:10 and 50:50 glycerol:water mixed liquids and in pure water at different temperatures until the LCST transition takes place and the oligomers at lower temperature in the coil structure collapse into the globule structure. The analytics is achieved following the oligomer radius of gyration, moments of inertia, interaction energy with the solvent, solvent accessible surface area (SASA), and an embedded structural approach through principal component analysis over the 280–400 K range of temperatures. An inspection into the hydrogen bonds formed between the oligomers and their liquid environments is also included. The Conclusions, Section 4, summarizes the observations and provides a critical discussion on the structural changes that the oligomers undergo when transitioning across the LCST. Quantitative details are provided in the Supplementary Material.

2 Model and methods

The chemical structure of the PNIPAM ($C_6H_{11}NO$) and PDEA ($C_{10}H_{15}NO_2$) monomers is provided in Figure 1. For the generation of a polymer chain with 30 monomers, a three-dimensional model of each polymer monomer was constructed using the chemical editor Avogadro (Hanwell et al., 2012). Meanwhile, the oligomers desired syndiotactic tacticity with alternating orientation of the side groups along the backbone chain, were created using a custom-built Python script. These polymeric chains have molecular weight less than 10 ku. Hence, we termed them *oligomers* (Litvinova, 2000). Specifically, the oligomers studied in this work are 30-PNIPAM (572 atoms, 3,396.819 u) and 30-PDEA (662 atoms, 3,817.629 u).

Concerning the modeling employed for all molecular systems, the all-atom OPLS-AA/M force field was used (Jorgensen et al., 1996; Robertson et al., 2015). As is described in previous work, custom atomic charges for the two oligomers were calculated within the restrained electrostatic potential (RESP) approach (Bayly et al., 1993; Frisch et al., 2013; Hopkins et al., 2020). In these oligomers the partial atomic charges of the head, middle, and tail monomers are redistributed to maintain the *sp*3 hybridization of the backbone carbon atoms. The latter was achieved using the utilities *Antechamber* and *prepgen* included in AmberTools 20 (Case et al., 2020). Our obtained atomic partial charges are reported in Supplementary Table S1 of the SM. The SPC/E force field was employed for water (Berendsen et al., 1987).

MD simulations were performed using GROMACS 20.4 (Lindahl et al., 2020). The required topology files containing parameters and oligomer geometry were generated with the aid of the *tppmktop* utility Erg Research Group: Laboratory of Theoretical (Erg Research Group, 2015). A similar process was used for establishing the topology file of the glycerol ($C_3H_8O_3$) liquid. The simulation strategy is an adaptation of our more general MD modeling process for macromolecular systems (Andrews and Blaisten-Barojas, 2022).

Since glycerol and water have similar polarity and form an homogeneous solution when mixed in all proportions, our simulations were initialized by placing the fully elongated

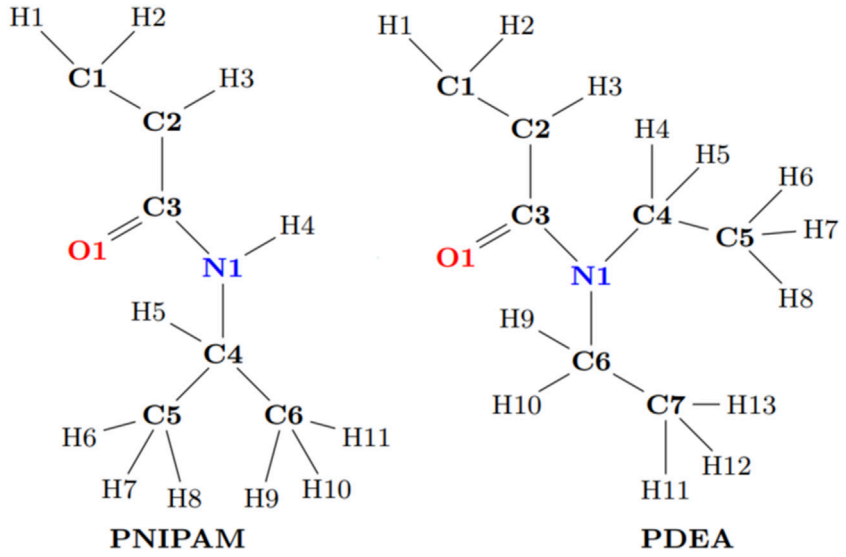

FIGURE 1
Chemical structure of the PNIPAM and the PDEA monomers.

oligomer inside a dodecahedral computational box and filling the box with randomly placed molecules of the surrounding liquid. For the systems with pure liquids, 2,383 glycerol molecules or 10,980 water molecules were added to the computational box. For the two mixed liquids systems, relative concentration by mass of glycerol:water to reach 50:50 and 90:10 required addition of 1,110:5,651 and 2,350:1,326 glycerol:water molecules to the computational box, respectively. Each system was initially minimized, followed by a series of NVT- and NPT-MD simulations to reach equilibration. A collection of temperatures was evaluated between 280 and 400 K, and the equilibration of the systems at each temperature was achieved though NPT-MD simulations over 40 ns, followed by NVT-MD simulations exceeding 1.0μs. While fully restraining the oligomer conformation, the system was equilibrated at 1.0 atm for all the temperatures using the Nosé-Hoover thermostat and the Parrinello-Rahman pressure coupling (Parrinello and Rahman, 1981; Nosé and Klein, 1983; Nosé, 1984; Hoover, 1985). In all cases, a 1.0 fs time step, periodic boundary conditions, and a 1.2 nm cutoff for the electrostatic and van der Waals interactions were used. The long-range electrostatic interactions were accounted for with the smooth particle-mesh Ewald method (PME) with a Fourier spacing of 0.12 nm (Essmann et al., 1995). For all bonded hydrogens, the linear constraint solver LINCS was applied (Hess et al., 1997). To ensure proper statistics of the oligomers fate, all production simulations were carried out for 1.0 μs. Reported values were averaged over the last 200 ns of each NPT MD run along which instantaneous configurations were saved every 20 ps yielding trajectory files with 10,000 time points. Supplementary Table S2 of the SM gives a summary on the relative concentration by mass of the oligomers in the various liquids and the equilibrated density of each system at two temperatures (below and above the LCST).

The data analyses employed several utilities embedded in the GROMACS package (Lindahl et al., 2020). The *sasa* utility enabled the computation of the oligomers SASA (Eisenhaber et al., 1995). The *hbond* utility was used for calculating the hydrogen bonds with donor-acceptor cutoff angle of 30°and cutoff distance of 0.35 nm. The interaction energy between the oligomer and the solvent, E_{int}, was determined via the *rerun* command that separates atoms according to groups and analyzes the Lennard-Jones and electrostatic energies between the oligomer atoms and the solvent molecules atoms via the following difference of potential energies:

$$E_{int} = E_{total} - E_{solvent} - E_{oligomer} \quad (1)$$

where E_{total} is the potential energy of the full system containing the oligomer plus the liquid environment, $E_{solvent}$ is the total potential energy of the pure or mixed liquids, and $E_{oligomer}$ is the potential energy of either the 30-PNIPAM, or the 30-PDEA.

Once the MD trajectories for each oligomer in its liquid environment was calculated, the *covar* and *anaeig* utilities were employed for performing a principal component analysis (PCA) (Jolliffe and Cadima, 2016). For each oligomer, the recorded instantaneous coordinates of its structure along the MD trajectory were first aligned to an arbitrary equilibrated configuration with the goal of eliminating the overall translation and rotation (Amadei et al., 1993). Next, a matrix $\boldsymbol{C}$ (nt, $3N$) was built containing $3N$ columns of mass-weighted coordinates of the N backbone atoms and nt rows with their instantaneous time values along the MD trajectory that were saved to file. The 30-PNIPAM and 30-PDEA oligomers have N_C = 60 carbon atoms in their backbones that give rise to 57 contiguous dihedral angles ϕ, ψ, where ϕ links C atoms of two contiguous monomers while ψ involves the C atoms of three contiguous monomers. The matrix was regularized by subtracting to each column its mean and dividing by the corresponding standard deviation. The covariance matrix was created, its eigenvalues and eigenvectors determined, followed by projection of the regularized original vectors onto the two most important principal components containing the largest portion of

the coordinates variance. Additionally, a similar analysis, termed dPCA, was performed creating the covariance matrix of the oligomer backbone ϕ, ψ cosines and sines collected over the MD trajectory (Mu et al., 2005).

3 Results

As a validation of the force field for pure glycerol, the NPT-MD equilibrated density as a function of temperature was compared to the experimental density (Gregory, 1963; Egorov et al., 2013). Supplementary Figure S1 of the SM depicts the excellent agreement of the MD density results with the experimental density. Altogether, eight systems were simulated in which one 30-PNIPAM or 30-PDEA was immersed in each of the four liquid environments considered: pure glycerol, 50:50 and 90:50 glycerol:water mixtures, and pure water. Each of these eight systems were MD simulated at a set of five temperatures between 280 and 350 K in the water and 50:50 systems, and between 330 and 400 K in the glycerol and 90:10 system. Hence, our results encompass over 40 μs of MD simulation, along which various properties of the oligomers were calculated. Of importance for this study is the analysis of the change in oligomer structure as a function of temperature and as a function of the liquid environment in which they are present.

A polymer *coil* is a flexible structure that undergoes continuous bending and twisting with an overall spatially elongated look, while under certain conditions the polymer structure may collapse into a *globule* structure that is not rigid, but is significantly more compact than the coil. Linear polymers tend to acquire the extended coil conformation when solvated in the residing liquid, while they collapse into a globular cluster if they do not solvate. In the latter case, most often, increasing the temperature of the mixture enhances the miscibility and the polymers extend into coils. In contrast to this general behavior, thermoreactive polymers solvate below their LCST, displaying elongated coil structures, and collapse into globular structures above their LCST, ending their miscibility with the liquid environment.

The oligomer radius of gyration R_g is a polymer structural property that permits a clear characterization of the size and compactness acquired by the polymer chain when acquiring the coil and the globule structures. Coil structural conformations are associated to a large R_g. Above the LCST, thermoresponsive polymers collapse into a globule-like structure with a significantly lower R_g. Hence the R_g as a function of time was calculated during the NVT-MD production runs for each temperature considered. The LCST of each system was determined by bracketing the R_g value between its high value at a lower temperature and its low value at the next higher temperature. Our reported values pertain to mass weighted, R_g, such that for an oligomer with N_o atoms at positions $\mathbf{r}_i$, center of mass position $\mathbf{r}_{cm}$, and masses m_i is given by

$$R_g = \sqrt{\sum_{i=1}^{N_o} m_i (\boldsymbol{r}_i - \boldsymbol{r}_{cm})^2 \Big/ \sum_{i=1}^{N_o} m_i} \qquad (2)$$

We determined that the LCST of 30-PNIPAM and 30-PDEA in water was in the range 292–300 K. This aligns with other computational studies and provides confidence in the developed polymer force field (Longhi et al., 2004; Kang et al., 2016; Moghadam and Larson, 2017; de Oliveira et al., 2018; Palivec et al., 2018; Dalgicdir and van der Vegt, 2019). Unexpectedly, the LCST of 30-PNIPAM in the 50:50, 90:10 glycerol:water mixtures, and in pure glycerol are predicted to occur within 312–320 K, 362–370 K, and 372–380 K, significantly higher than the phase transition in pure water. Additionally, the LCST of 30-PDEA in the mixed 50:50, 90:10, and pure glycerol systems are predicted to occur within 332–340 K, 362–370 K, and 372–380 K. These predictions have not been reported in the literature. Similarly, for 30-PDEA in pure glycerol, the LCST is predicted within 382–390 K while in water the transition occurs at the same temperature than for PNIPAM. Figure 2 illustrates the dramatic coil collapse of both oligomers in all four liquid environments when the temperature changes from below to above their LCST.

Hence, below the LCST both 30-PINPAM and 30-PDEA display the coil conformation as expected for thermoreactive polymers, and above the LCST the oligomers acquire the globule conformations. The MD simulations gave rise to abundant data that enabled relevant structural and energetic analyses on the polymers coil and globule phases. Compounding the LCST results, a phase diagram can be estimated as depicted in Figure 3, where the dashed lines joining the calculated points are a guide to the eye. Supplementary Figures S2, S3 of the SM show profiles of the R_g as a function of time along the NVT-MD trajectory for both oligomers in the vicinity of the LCST. Table 1 reports the R_g averages and standard deviations.

As summarized in Table 1, above the LCST temperature both 30-PNIPAM and 30-PDEA displayed an R_g depleted by 40%–50% from the coil phase, evidencing the existence of the phase transition in water and in glycerol solutions. Notably, in glycerol the globule R_g of 1.19 nm was approximately 16% higher than the 1.02 nm R_g in water. The oligomer more swollen structure in glycerol than in water is possibly due to the larger size of the glycerol molecules that hinder the compactness of the polymer chain while forming the globule phase. From a different perspective, the moments of inertia along the principal axis of the oligomers, I_a, I_b, I_c were also analyzed. The ratios I_b/I_a and I_c/I_a in the coil phase are approximately 5–6 times higher than those in the globule phase, emphasizing the appearance of the compact globule conformation above the LCST transition temperature, as reported in Table 1. The time profile of these properties is provided in Supplementary Figures S2, S3 of the SM.

Water, glycerol and their mixtures are liquids that form hydrogen bonds. The number of hydrogen bonds per monomer (HB) for each oligomer and in each liquid was calculated along the MD simulations, revealing that in water and glycerol HBs were formed between the oligomer monomers and the solvent, as well as between intra-oligomer monomers. For 30-PNIPAM and 30-PDEA, HBs occurred between the oligomer carbonyl oxygen and the solvent hydroxyl hydrogen, denoted as HB_{CO-HO}. For 30-PNIPAM, HBs also occurred between the oligomer amine hydrogen and the solvent hydroxyl oxygen, denoted as HB_{NH-OH}. Table 1 lists these values and Supplementary Figures S2, S3 of the SM display their time behavior. A small number of monomer-monomer HBs were also present

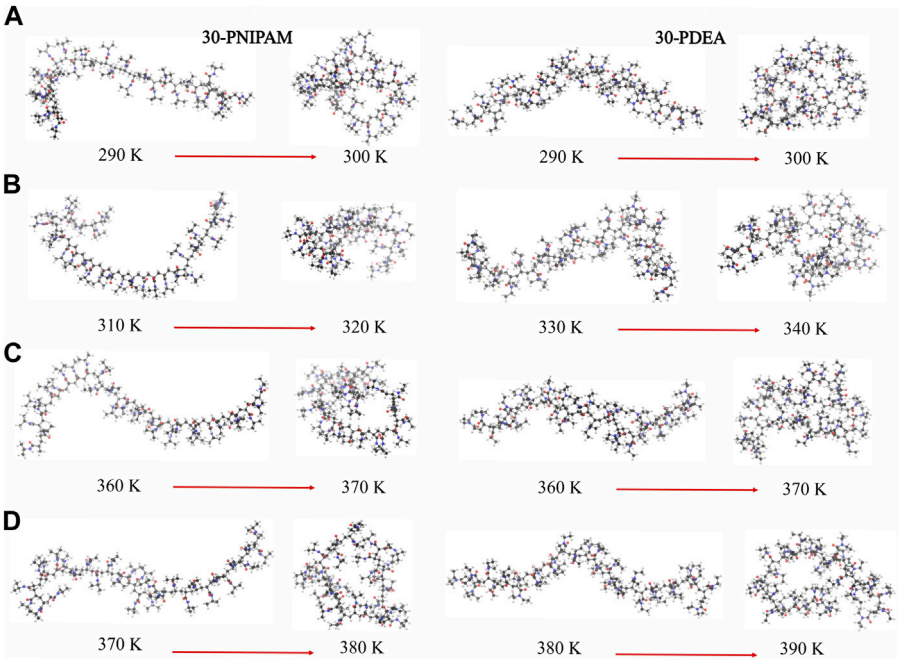

FIGURE 2
Instantaneous coil and globule configurations of 30-PNIPAM and 30-PDEA at temperatures below and above their LCST in **(A)** water **(B)** 50:50 and **(C)** 90:10 glycerol:water mixtures, and **(D)** glycerol. The atom color scheme is: carbon = gray, oxygen = red, hydrogen = white.

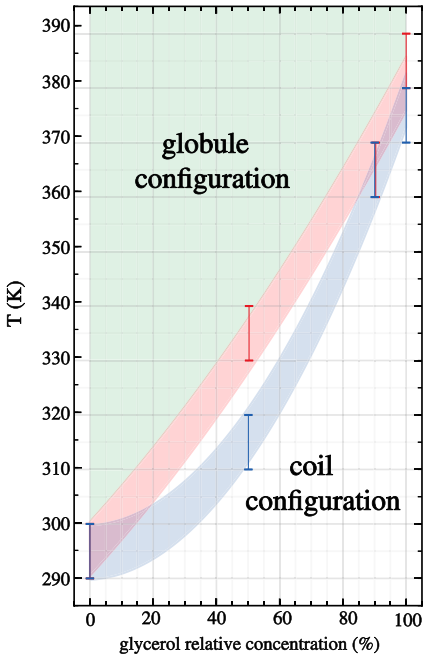

FIGURE 3
Phase diagram for 30-PNIPAM and 30-PDEA in glycerol:water mixed liquid environments as a function of the glycerol proportional concentration. The blue (PNIPAM) and orange (PDEA) shaded areas guide the eye identifying the predicted LCST regions where the transition occurs at different glycerol proportions in the liquid. Above these temperature regions (depicted green) the oligomers acquire the globule structures, while below them (depicted white) the oligomers are in the extended coil structure.

between the carbonyl oxygen and amine hydrogen. While the frequency of oligomer-solvent HBs decreased slightly above the LCST, the frequency of the intra-oligomer monomer-monomer HB increased slightly. Based on these observations, the number of HBs is not a distinctive characteristic for identifying the behavior of the oligomers either below and above the LCST in neither one of the four liquid environments studied in this work.

Another interesting property is E_{int}, the interaction energy per monomer between the oligomer and its liquid environment. Mean values of E_{int} are listed in Table 1 while their time profiles are provided in Supplementary Figures S2, S3 of the SM. For 30-PNIPAM and 30-PDEA in water the E_{int} increased approximately 10 kJ/mol when the system transitioned from below and above the LCST. This energy increase indicates a less favorable system state above the LCST due to the decrease in the oligomer solubility. In contrast, for both oligomers in pure glycerol, the E_{int} increased only 4 kJ/mol for 30-PNIPAM, and 7 kJ/mol for 30-PDEA, indicating a less prominent effect due to the solvent in the coil-to-globule structure transition of the two oligomers. In fact, the 50:50 and 90:10 glycerol:water mixtures display a progressive loss of solvent energy influence as the amount of glycerol becomes more dominant, indicating that the oligomer globule structure is less tightly bound the more glycerol is in the solution. Figure 4 contains a scatter plot showing the correlation between R_g and E_{int} occurring in all four studied liquid media for both oligomers, where the red color identifies a high number of occurrences along the 200 ns MD trajectory while blue indicates a small number. This plot gives a clear visual representation of the interaction energetics occurring in the four studied system for each oligomer.

TABLE 1 MD simulation summary. Values correspond to averages over the last 200 ns of the equilibrated 1.0 *μs* trajectory. Interaction energies and hydrogen bonds (HB) are per monomer.

Solvent	Oligomer	phase	R_g (nm)	SASA (nm^2)	I_b/I_a	I_c/I_a	$HB_{(CO-HO)}$	$HB_{(NH-OH)}$	E_{int} (kJ/mol)
PNIPAM	water	290	1.74 ± 0.16	41.5 ± 1.1	6.21 ± 2.77	6.69 ± 2.71	1.70 ± 0.09	0.55 ± 0.09	−97.88 ± 3.73
		300	1.02 ± 0.06	33.9 ± 1.9	1.70 ± 0.44	2.11 ± 0.47	1.56 ± 0.11	0.54 ± 0.09	−88.12 ± 5.12
	50:50	310	1.86 ± 0.13	41.7 ± 0.8	6.11 ± 4.74	6.77 ± 4.63	1.31 ± 0.11	0.53 ± 0.09	−101.16 ± 3.48
		320	1.14 ± 0.04	34.8 ± 1.8	3.05 ± 0.51	3.43 ± 0.47	1.17 ± 0.11	0.48 ± 0.09	−87.77 ± 5.72
	90:10	360	1.88 ± 0.07	41.9 ± 0.8	9.57 ± 3.08	10.01 ± 3.07	0.79 ± 0.09	0.49 ± 0.08	−96.16 ± 3.47
		370	1.19 ± 0.05	37.5 ± 1.5	2.45 ± 0.54	2.98 ± 0.53	0.76 ± 0.10	0.48 ± 0.09	−90.21 ± 4.34
	glycerol	370	1.92 ± 0.08	42.3 ± 0.9	11.04 ± 3.64	11.39 ± 3.60	0.59 ± 0.09	0.49 ± 0.08	−95.69 ± 3.60
		380	1.19 ± 0.05	39.5 ± 1.5	1.57 ± 0.39	2.15 ± 0.41	0.58 ± 0.09	0.49 ± 0.08	−91.32 ± 3.97
PDEA	water	290	1.74 ± 0.06	40.0 ± 0.7	14.25 ± 3.92	14.52 ± 3.82	1.50 ± 0.08	—	−86.83 ± 2.65
		300	1.02 ± 0.01	33.4 ± 0.8	1.79 ± 0.13	2.16 ± 0.19	1.36 ± 0.08	—	−76.49 ± 2.55
	50:50	330	1.65 ± 0.08	40.5 ± 0.9	8.51 ± 3.22	8.95 ± 3.11	1.14 ± 0.10	—	−85.52 ± 2.90
		340	1.17 ± 0.04	37.1 ± 1.4	2.29 ± 0.42	2.81 ± 0.41	1.11 ± 0.09	—	−81.04 ± 2.96
	90:10	360	1.68 ± 0.05	40.2 ± 0.7	7.01 ± 1.61	7.57 ± 1.53	0.76 ± 0.09	—	−85.90 ± 2.96
		370	1.15 ± 0.05	36.1 ± 1.4	2.38 ± 0.44	2.89 ± 0.46	0.71 ± 0.09	—	−79.03 ± 3.56
	glycerol	380	1.71 ± 0.07	40.8 ± 0.7	10.03 ± 2.49	10.35 ± 2.46	0.52 ± 0.09	—	−84.41 ± 3.48
		390	1.10 ± 0.03	36.4 ± 1.3	1.86 ± 0.38	2.36 ± 0.39	0.49 ± 0.08	—	−76.72 ± 3.24

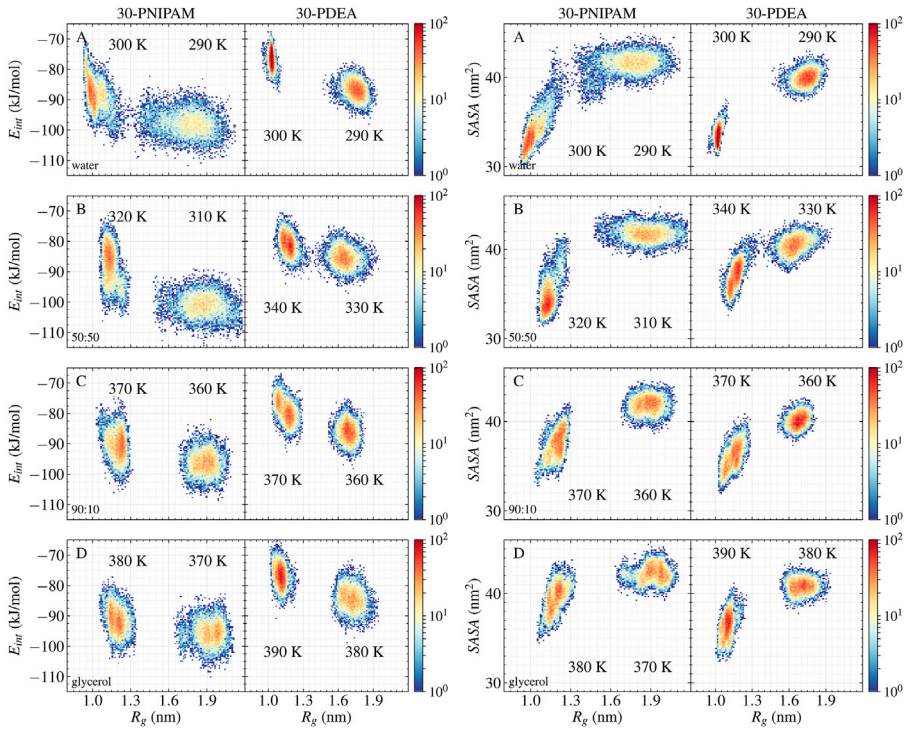

FIGURE 4
30-PNIPAM and 30-PDEA correlation plots between R_g and E_{int} per monomer (left), and between R_g and SASA (right) in **(A)** water **(B)** 50:50 **(C)** 90:10 glycerol:water mixtures, and **(D)** glycerol systems. For each temperature 200 ns of NPT MD trajectory times were spanned, with 10,000 instantaneous structures saved to file. Red and blue identify plot regions with large and small number of trajectory points.

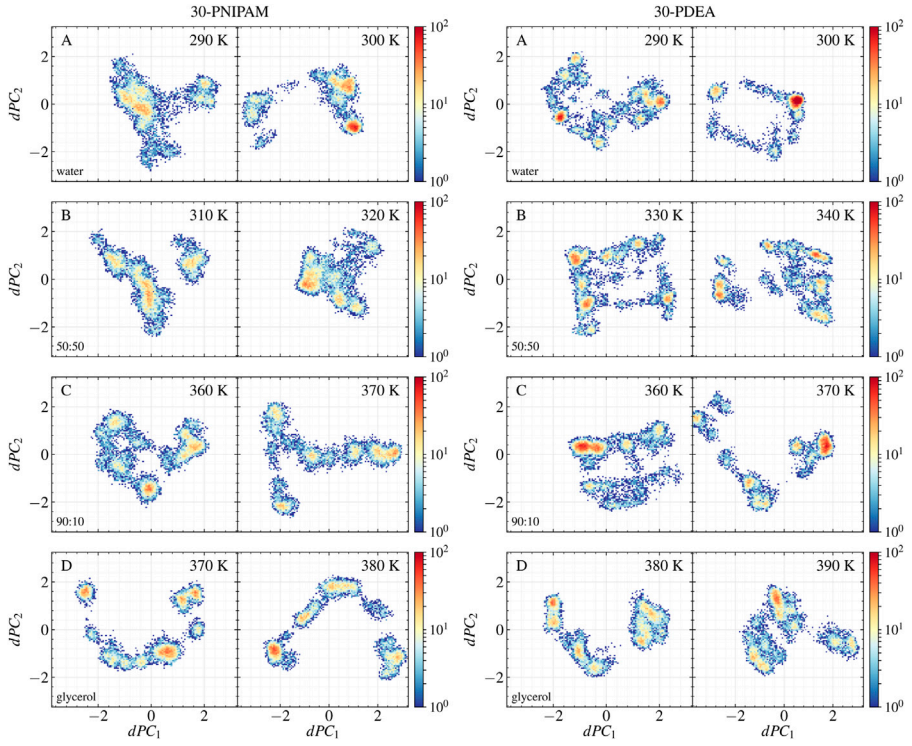

FIGURE 5
Scatter plots of the 30-PNIPAM and 30-PDEA dihedral angles data along the MD trajectories projected onto the dPC_1 and dPC_2 for the **(A)** water, **(B)** 50:50, **(C)** 90:10 glycerol:water mixtures, and **(D)** glycerol systems below the LCST (left) and above he LCST. (right) for each oligomer.

Supplementing the energetics of oligomer-solvent interactions, the SASA of the oligomers was determined along the MD trajectories, resulting in a visible characterization of the coil-to-globule transition. Table 1 lists the SASA mean values and standard deviations while Supplementary Figures S2, S3 of the SM provide the time evolution along the MD trajectory. For each oligomer in the coil phase, the SASA fluctuated between 39 and 45 nm^2 both in water and in glycerol solvents; whereas in the globule phase, the SASA fluctuations of 34 and 45 nm^2 in glycerol were comparatively larger than the 30 and 38 nm^2 fluctuations observed water, indicating of the spatial hindrance imposed by the size of glycerol molecules. By correlating the SASA with the R_g of the MD simulations, the coil and globule phases were well identified, as Figure 4 illustrates.

Two different principal component analyses were performed, yielding additional insight into which oligomer structures along the MD trajectories were coil or globular. One PCA analysis involved the pre-aligned oligomer backbone mass-weighted Cartesian coordinates as input features. This PCA was done at the two temperatures bracketing the LCST for each oligomer in each liquid system. The resulting PC_1 and PC_2 accounted for approximately 63% of the total variance in the analyses of the 30-PNIPAM and 30-PDEA. The input features of each oligomer along the MD trajectory are projected on these prominent principal components and their time profile is given in Supplementary Figures S4, S5 of the SM. The second PCA analysis (dPCA) involved the oligomer backbone dihedral angles (ϕ, ψ) along the trajectory. Again, the dPCA was performed with data from MD trajectories at the two temperatures bracketing the LCST for each oligomer in each liquid system. A similar total variance percentage was obtained in the dPCA analysis as in the previous case when only the dPC_1 and dPC_2 were considered. A projection of the original regularized data onto each of these two prominent principal components was achieved. Supplementary Figures S4, S5 of the SM provide the dPC_1 and dPC_2 time evolution along the MD trajectory. Meanwhile, the scatter plot of the projected original data onto dPC_1 and dPC_2 is shown in Figure 5 illustrating both, the 30-PNIPAM and 30-PDEA. Noticeable, the density of trajectory points in these scatter plots is not uniform. Indeed, the point density is associated to a probability distribution $\mathcal{P}$ spanning the plot plane, which was evaluated by assigning a color scale identifying highly dense regions of points in red low dense regions in blue as illustrated in Figure 5 while a similar analysis for the coordinates-based PCA is given in Supplementary Figures S6 of the SM. This $\mathcal{P}$ is an alternative tool for evaluating visually the fluctuations of the oligomer structure when it is in the coil or globule structures. As an example, for the dPCA analysis, Figure 6 provides a wireframe visualization of representative structures in the regions of high $\mathcal{P}$, clearly showing the difference between the elongated coil (left) and compact globule (right) configurations.

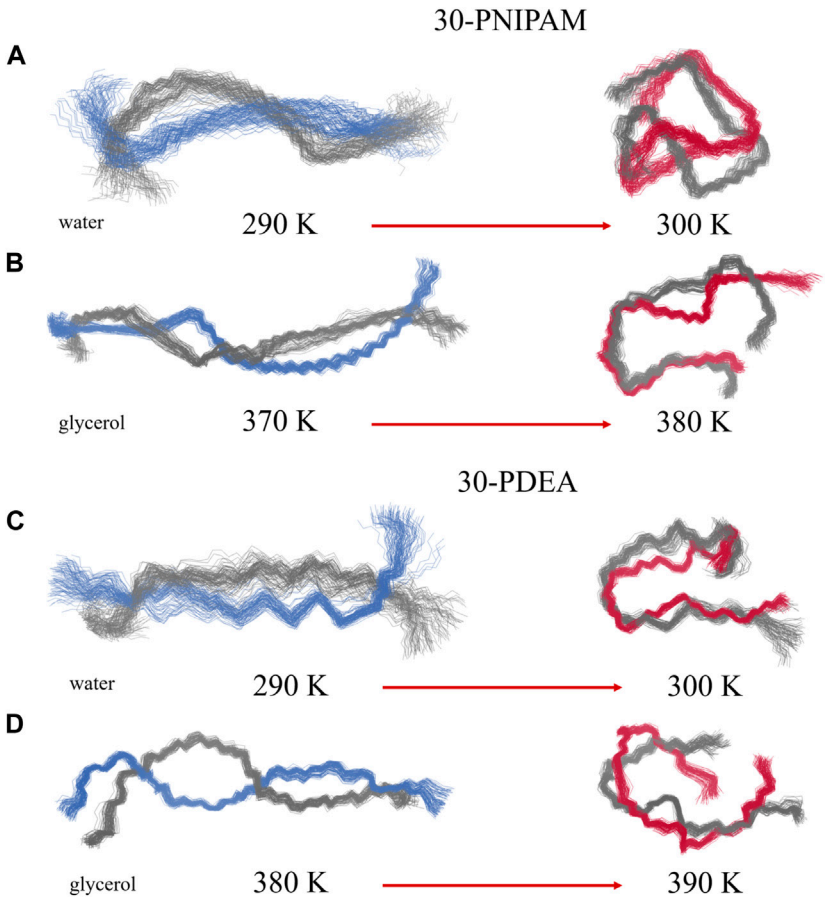

FIGURE 6
Collection of wireframe depiction of the 30-PNIPAM and the 30-PDEA backbones in water **(A, C)** and in glycerol **(B, D)** corresponding to the dPCA embedding of Figures 5A,D. Grey and blue/red wires identify the oligomers structure corresponding to two regions of high $\mathcal{P}$ (red) in Figures 5A,D at temperatures below and above the LCST.

4 Conclusion

This article describes a high-performance modeling and simulation approach that evidences the power of microsecond-long Molecular Dynamics simulations for identifying the structural characteristics of two polymers undergoing the LCST phase transition in four different liquid environments. Based on our extensive simulations, the research outcomes predict that 30-PNIPAM and 30-PDEA syndiotactic oligomers display the coil-to-globule transition when mixed with pure glycerol or with the 90:10 glycerol:water mixture with predicted LCST temperatures in the range 360–390 K. As a validation of these predictions, additional simulations for these two oligomers in liquids with a higher content of water, were performed for mixed glycerol:water 50:50 and pure water systems. Our outcomes predict significantly lower LCSTs in the range 290–340 K depending on the oligomer and the glycerol content of the liquid environments.

In a nutshell, our four predictions for the 30-PNIPAM LCST are 370–380 K in pure glycerol, 360–370 K in mixed 90:10 glycerol:water, 310–320 K in mixed 50:50, and 290–300 K in pure water. Hence, while the result of this oligomer in water is in excellent agreement with the existing experimental and computational literature, our predictions for the LCST as the glycerol content by mass increases allowed us to describe a predicted phase diagram for the LCST transition as reported in Figure 3. Currently, there are no experimental observations of this transition for PNIPAM in pure glycerol or glycerol:water solutions with high glycerol content. Simultaneously, our four predictions for the 30-PDEA LCST are 380–390 K in pure glycerol, 360–370 K in mixed 90:10 glycerol:water, 330–340 K in mixed 50:50 glycerol:water, and 290–300 K in pure water. The transition temperature for this oligomer is about 10 K higher than for 30-PNIPAM in equal liquid environments, which is cast into the predicted phase diagram illustrated in Figure 3. To be noted explicitly, currently, there are no experimental observations of PDEA LCST structural transition in glycerol, water or any mixture of these liquids.

Pertaining to our predicted higher than ambient and in the range of boiling water LCSTs, it is worth pointing out that at those temperatures the viscosity of glycerol of about 0.014 N/m^2 is only a small fraction of its value of 0.510 N/m^2 at 304 K. Hence, this steep decrease in the glycerol viscosity most likely enables the coil-to-globule structural collapse of polymers in glycerol yielding a LCST around the predicted 370–380 K or 380–390 K rage depending upon the oligomer. Since the predicted LCST of PNIPAM and PDEA in

glycerol are above the boiling point of water, glycerol is a candidate solvent for industrial applications where polymer phase change behavior at higher than ambient temperatures would be advantageous.

Data availability statement

The original contributions presented in the study are included in the article/Supplementary Material, further inquiries can be directed to the corresponding author.

Author contributions

SH: Data curation, Formal Analysis, Methodology, Software, Validation, Visualization, Writing–original draft. EB-B: Investigation, Methodology, Validation, Conceptualization, Funding acquisition, Project administration, Resources, Supervision, Writing–review and editing.

Funding

The author(s) declare financial support was received for the research, authorship, and/or publication of this article. Funding for this work was provided by the Center for Simulation and Modeling and the Department of Computational and Data Sciences of George Mason University.

Acknowledgments

All simulations were performed on the high performance computing clusters of the Office of Research Computing at George Mason University.

Conflict of interest

The authors declare that the research was conducted in the absence of any commercial or financial relationships that could be construed as a potential conflict of interest.

Publisher's note

Supplementary material

The Supplementary Material for this article can be found online at: https://www.frontiersin.org/articles/10.3389/fnano.2023.1292259/full#supplementary-material

References

Amadei, A., Linssen, A. B. M., and Berendsen, H. J. C. (1993). Essential dynamics of proteins. *Proteins Struct. Funct.* 17, 412–425. doi:10.1002/prot.340170408

Andrews, J., and Blaisten-Barojas, E. (2022). "Workflow for investigating thermodynamic, structural and energy properties of condensed polymer systems," in *Advances in parallel and distributed processing and applications*. Editor H. R. Arabnia (Switzerland: Springer Nature), 1033–1039.

Bayly, C. I., Cieplak, P., Cornell, W., and Kollman, P. A. (1993). A well-behaved electrostatic potential based method using charge restraints for deriving atomic charges: the RESP model. *J. Phys. Chem.* 97, 10269–10280. doi:10.1021/j100142a004

Berendsen, H., Grigera, J. R., and Straatsma, T. P. (1987). The missing term in effective pair potentials. *J. Phys. Chem.* 91, 6269–6271. doi:10.1021/j100308a038

Bharadwaj, S., Niebuur, B.-J., Nothdurft, K., Richtering, W., van der Vegt, N. F. A., and Papadakis, C. M. (2022). Cononsolvency of thermoresponsive polymers: where we are now and where we are going. *Soft Matter* 18, 2884–2909. doi:10.1039/D2SM00146B

Case, D., Cheatham, I., Darden, T., Gohlke, H., Luo, R., Merz, K., et al. (2020). *AmberTools 20 - molecular dynamics simulation*. Available at: https://mybiosoftware.com/ambertools-molecular-dynamics-simulation.html (Accessed August 30, 2023).

Concilio, M., Beyer, V. P., and Becer, C. R. (2022). Thermoresponsive polymers in non-aqueous solutions. *Polym. Chem.* 13, 6423–6474. doi:10.1039/D2PY01147F

Dalgicdir, C., and van der Vegt, N. F. A. (2019). Improved temperature behavior of PNIPAM in water with a modified OPLS model. *J. Phys. Chem. B* 123, 3875–3883. doi:10.1021/acs.jpcb.9b01644

de Oliveira, T. E., Marques, C. M., and Netz, P. A. (2018). Molecular dynamics study of the LCST transition in aqueous poly(N-n-propylacrylamide). *Phys. Chem. Chem. Phys.* 20, 10100–10107. doi:10.1039/c8cp00481a

Doberenz, F., Zeng, K., Willems, C., Zhang, K., and Groth, T. (2020). Thermoresponsive polymers and their biomedical application in tissue engineering - a review. *J. Mater. Chem. B* 8, 607–628. doi:10.1039/C9TB02052G

Du, H., Wickramasinghe, R., and Qian, X. (2010). Effects of salt on the lower critical solution temperature of poly (N-isopropylacrylamide). *J. Phys. Chem. B* 114, 16594–16604. doi:10.1021/jp105652c

Egorov, G. I., Makarov, D. M., and Kolker, A. M. (2013). Volume properties of liquid mixture of water + glycerol over the temperature range from 278.15 to 348.15 K at atmospheric pressure. *Thermochim. Acta* 570, 16–26. doi:10.1016/j.tca.2013.07.012

Eisenhaber, F., Lijnzaad, P., Argos, P., Sander, C., and Scharf, M. (1995). The double cubic lattice method: efficient approaches to numerical integration of surface area and volume and to dot surface contouring of molecular assemblies. *J. Comput. Chem.* 16, 273–284. doi:10.1002/jcc.540160303

Erg Research Group (2015). *Laboratory of theoretical biophysics*. TPPMKTOP Available at: https://erg.biophys.msu.ru/tpp/ (Accessed August 30, 2023).

Essmann, U., Perera, L., Berkowitz, M., Darden, T., Lee, H., and Pedersen, L. (1995). A smooth particle mesh Ewald method. *J. Chem. Phys.* 103, 8577–8593. doi:10.1063/1.470117

Frisch, M., Trucks, G. W., Schlegel, H. B., Scuseria, G. E., Robb, M. A., Cheeseman, J. R., et al. (2013). *Gaussian 09, revision D.01*. Wallingford CT, USA: Gaussian Inc.

Gregory, S. R. (1963). Physical Properties of Glycerine and its solutions *(glycerine producers' association)*. Available at: https://books.google.com/books?id=XpeaGQAACAAJ (Accessed August 30, 2023).

Hanwell, M. D., Curtis, D. E., Lonie, D. C., Vandermeersch, T., Zurek, E., and Hutchison, G. R. (2012). Avogadro: an advanced semantic chemical editor, visualization, and analysis platform. *J. Cheminf.* 4, 17. doi:10.1186/1758-2946-4-17

Hess, B., Bekker, H., and Fraaije, J. (1997). LINCS: a linear constraint solver for molecular simulations. *J. Comp. Chem.* 18, 1463–1472. doi:10.1002/(sici)1096-987x(199709)18:12<1463:aid-jcc4>3.0.co;2-h

Hoover, W. (1985). Canonical dynamics: equilibrium phase-space distributions. *Phys. Rev. A* 31, 1695–1697. doi:10.1103/physreva.31.1695

Hopkins, S., Gogovi, G., Weisel, E., Handler, R., and Blaisten-Barojas, E. (2020). Polyacrylamide in glycerol solutions from an atomistic perspective of the energetics, structure, and dynamics. *AIP Adv.* 10, 085911. doi:10.1063/5.0020850

Idziak, I., Avoce, D., Lessard, D., Gravel, D., and Zhu, X. X. (1999). Thermosensitivity of aqueous solutions of poly(N,N-diethylacrylamide). *Macromolecules* 32, 1260–1263. doi:10.1021/ma981171f

Jolliffe, I. T., and Cadima, J. (2016). Principal component analysis: a review and recent developments. *Philos. Trans. A Math. Phys. Eng. Sci.* 374, 20150202. doi:10.1098/rsta.2015.0202

Jorgensen, W. L., Maxwell, D. S., and Tirado-Rives, J. (1996). Development and testing of the OPLS all-atom force field on conformational energetics and properties of organic liquids. *J. Am. Chem. Soc.* 118, 11225–11236. doi:10.1021/ja9621760

Kang, Y., Joo, H., and Kim, J. S. (2016). Collapse-swelling transitions of a thermoresponsive, single poly(N-isopropylacrylamide) chain in water. *J. Phys. Chem. B* 120, 13184–13192. doi:10.1021/acs.jpcb.6b09165

Lindahl, E., Abraham, M., Hess, B., and van der Spoel, D. (2020). *GROMACS 2020 documentation and source code*. Available at: https://doi.org/10.5281/zenodo.3562512 (Accessed August 30, 2023).

Litvinova, L. S. (2000). "Synthetic polymers: thin layer (planar) chromatography," in *Encyclopedia of separation science*. Editor I. D. Wilson (Netherlands: Academic Press), 4348–4354.

Longhi, G., Lebon, F., Abbate, S., and Fornili, S. L. (2004). Molecular dynamics simulation of a model oligomer for poly(N-isopropylamide) in water. *Chem. Phys. Lett.* 386, 123–127. doi:10.1016/j.cplett.2004.01.045

Micciulla, S., Michalowsky, J., Schroer, M. A., Holm, C., Klitzing, R. V., and Smiatek, J. (2016). Concentration dependent effects of urea binding to poly(N-isopropylacrylamide) brushes: a combined experimental and numerical study. *Phys. Chem. Chem. Phys.* 18, 5324–5335. doi:10.1039/c5cp07544k

Moghadam, S., and Larson, R. G. (2017). Assessing the efficacy of poly(N-isopropylacrylamide) for drug delivery applications using molecular dynamics simulations. *Mol. Pharm.* 14, 478–491. doi:10.1021/acs.molpharmaceut.6b00942

Mu, Y., Nguyen, P. H., and Stock, G. (2005). Energy landscape of a small peptide revealed by dihedral angle principal component analysis. *Proteins Struct. Funct.* 58, 45–52. doi:10.1002/prot.20310

Narang, P., and Venkatesu, P. (2018). Unravelling the role of polyols with increasing carbon chain length and OH groups on the phase transition behavior of PNIPAM. *New J. Chem.* 42, 13708–13717. doi:10.1039/C8NJ02510J

Nosé, S. (1984). A molecular dynamics method for simulations in the canonical ensemble. *Mol. Phys.* 52, 255–268. doi:10.1080/00268978400101201

Nosé, S., and Klein, M. (1983). Constant pressure molecular dynamics for molecular systems. *Mol. Phys.* 50, 1055–1076. doi:10.1080/00268978300102851

Palivec, V., Zadrazil, D., and Heyda, J. (2018). All-atom REMD simulation of poly-N-isopropylacrylamide thermodynamics in water: a model with a distinct 2-state behavior. arXiv:1806.05592v1 [physics.chem-ph]. Available at: https://arxiv.org/abs/1806.05592 (Accessed June 14, 2018).

Pang, X., and Cui, S. (2013). Single-chain mechanics of poly(N,N-diethylacrylamide) and poly(N-isopropylacrylamide): comparative study reveals the effect of hydrogen bond donors. *Langmuir* 29, 12176–12182. doi:10.1021/la403132e

Parrinello, M., and Rahman, A. (1981). Polymorphic transitions in single crystals: a new molecular dynamics method. *J. Appl. Phys.* 52, 7182–7190. doi:10.1063/1.328693

Pérez-Ramirez, H. A., Haro-Pérez, C., and Odriozola, G. (2019). Effect of temperature on the cononsolvency of poly(N-isopropylacrylamide) (PNIPAM) in aqueous 1-propanol. *ACS Appl. Polym. Mater.* 1, 2961–2972. doi:10.1021/acsapm.9b00665

Qin, B., and Arratia, P. E. (2017). Characterizing elastic turbulence in channel flows at low Reynolds number. *Phys. Rev. Fluids* 2, 083302. doi:10.1103/physrevfluids.2.083302

Robertson, M. J., Tirado-Rives, J., and Jorgensen, W. L. (2015). Improved peptide and protein torsional energetics with the opls-aa force field. *J. Chem. Theory Comput.* 11, 3499–3509. doi:10.1021/acs.jctc.5b00356

Rosi, B. P., D'Angelo, A., Buratti, E., Zanatta, M., Tavagnacco, L., Natali, F., et al. (2022). Impact of the environment on the pnipam dynamical transition probed by elastic neutron scattering. *Macromolecules* 55, 4752–4765. doi:10.1021/acs.macromol.2c00177

frontiers | Frontiers in Nanotechnology

TYPE Original Research
PUBLISHED 05 February 2024
DOI 10.3389/fnano.2023.1333127

OPEN ACCESS

EDITED BY
Estela Blaisten-Barojas,
George Mason University, United States

REVIEWED BY
Erick Ulin-Avila,
Center for Engineering and Development CIDESI, Mexico
Filippo Fabbri,
National Research Council (CNR), Italy

*CORRESPONDENCE
Antonija Grubišić-Čabo,
a.grubisic-cabo@rug.nl
Michael S. Fuhrer,
michael.fuhrer@monash.edu

RECEIVED 04 November 2023
ACCEPTED 21 December 2023
PUBLISHED 05 February 2024

CITATION
Grubišić-Čabo A, Kotsakidis JC, Yin Y, Tadich A, Haldon M, Solari S, Riley J, Huwald E, Daniels KM, Myers-Ward RL, Edmonds MT, Medhekar NV, Gaskill DK and Fuhrer MS (2024), Quasi-freestanding AA-stacked bilayer graphene induced by calcium intercalation of the graphene-silicon carbide interface. *Front. Nanotechnol.* 5:1333127. doi: 10.3389/fnano.2023.1333127

Quasi-freestanding AA-stacked bilayer graphene induced by calcium intercalation of the graphene-silicon carbide interface

Antonija Grubišić-Čabo[1,2]*, Jimmy C. Kotsakidis[1,3], Yuefeng Yin[4,5], Anton Tadich[5,6,7], Matthew Haldon[1], Sean Solari[1], John Riley[7], Eric Huwald[7], Kevin M. Daniels[8,9,10], Rachael L. Myers-Ward[11], Mark T. Edmonds[1,5], Nikhil V. Medhekar[4,5], D. Kurt Gaskill[9] and Michael S. Fuhrer[1,5]*

[1]School of Physics and Astronomy, Monash University, Clayton, VIC, Australia, [2]Zernike Institute for Advanced Materials, University of Groningen, Groningen, Netherlands, [3]Laboratory for Physical Sciences, College Park, MD, United States, [4]Department of Materials Science and Engineering, Monash University, Clayton, VIC, Australia, [5]ARC Centre of Excellence in Future Low Energy Electronics Technologies (FLEET), Monash University, Clayton, VIC, Australia, [6]Australian Synchrotron, Melbourne, VIC, Australia, [7]Department of Physics, La Trobe University, Melbourne, VIC, Australia, [8]Department of Electrical and Computer Engineering, University of Maryland, College Park, MD, United States, [9]Institute for Research in Electronics and Applied Physics, University of Maryland, College Park, MD, United States, [10]Fischell Institute for Biomedical Devices, University of Maryland, College Park, MD, United States, [11]US Naval Research Laboratory, Washington, DC, United States

We study quasi-freestanding bilayer graphene on silicon carbide intercalated by calcium. The intercalation, and subsequent changes to the system, were investigated by low-energy electron diffraction, angle-resolved photoemission spectroscopy (ARPES) and density-functional theory (DFT). Calcium is found to intercalate only at the graphene-SiC interface, completely displacing the hydrogen terminating SiC. As a consequence, the system becomes highly n-doped. Comparison to DFT calculations shows that the band dispersion, as determined by ARPES, deviates from the band structure expected for Bernal-stacked bilayer graphene. Instead, the electronic structure closely matches AA-stacked bilayer graphene on calcium-terminated SiC, indicating a spontaneous transition from AB- to AA-stacked bilayer graphene following calcium intercalation of the underlying graphene-SiC interface.

KEYWORDS

graphene, calcium, intercalation, electronic structure, ARPES, DFT

1 Introduction

Graphene, a single layer of graphite Novoselov et al. (2004) is notable for its unique bandstructure with massless Dirac Fermions Novoselov et al. (2005), which give rise to a plethora of exotic physical phenomena, such as a π-Berry phase Zhang et al. (2005); Liu et al. (2011); Hwang et al. (2011), Katsnelson et al. (2006) and an unusual quantum Hall effect Zhang et al. (2005).

In contrast, the most typical form of bilayer graphene, so called AB- or Bernal stacked bilayer graphene (Supplementary Figures S3A, B), has a completely different electronic structure with massive, yet gapless, Dirac fermions, and a Berry phase of 2π Ohta et al. (2006); Partoens and Peeters (2006); McCann and Koshino (2013); Novoselov et al. (2006). In principle, other types of stacking, such as AA-stacking (Supplementary Figures S3C, D), exist. AA-stacking is a metastable stacking, where graphene layers lie directly above one another. Consequently, AA-stacked graphene has an electronic structure which can be considered as a superposition of two single-layer spectra, preserving massless Dirac fermions and a π-Berry phase Liu et al. (2009); Rozhkov et al. (2016). Despite many interesting properties predicted for AA-stacked bilayer graphene, including a recent prediction that it might host a fractional metal state Sboychakov et al. (2021), there are very few experimental realisations Kim et al. (2013); Liu et al. (2009); Caffrey et al. (2016); Endo et al. (2018); de Jong et al. (2018), de Jong et al. (2023). Out of the few reported cases, the majority have been found in lithium intercalated systems Caffrey et al. (2016); Endo et al. (2018), or contained within very small regions otherwise surrounded by AB-stacked graphene de Jong et al. (2018), de Jong et al. (2023).

One of the most promising methods for graphene production in terms of scalability is the growth of graphene on silicon carbide (SiC) which allows formation of large-scale graphene with high carrier mobility Starke and Riedl (2009); Nyakiti et al. (2012); Kruskopf et al. (2016); Emtsev et al. (2009). Graphene on SiC can either be epitaxial, i.e., directly grown on the SiC, with a buffer layer in between the graphene and the SiC interface, or quasi-freestanding graphene–most commonly created via hydrogen intercalation of epitaxial graphene Daniels et al. (2017); Riedl et al. (2009), in which graphene retains the properties expected for the isolated layer Sforzini et al. (2015). Hydrogen is not the only element that can be used to create quasi-freestanding graphene on SiC by means of intercalation Briggs et al. (2019); various other elements can be used, such as gold Sohn et al. (2021); Marchenko et al. (2016), iron Sung et al. (2014); Shen et al. (2018), oxygen Oliveira et al. (2013), lithium Bao et al. (2014); Caffrey et al. (2016); Endo et al. (2018); Virojanadara et al. (2010), magnesium Kotsakidis et al. (2020); Grubišić-Čabo et al. (2021); Kotsakidis et al. (2021), calcium Kotsakidis et al. (2020); Valla et al. (2009); Yang et al. (2014); Endo et al. (2020); Toyama et al. (2022); Ichinokura et al. (2016), antimony Wolff et al. (2019) and ytterbium Watcharinyanon et al. (2013). The majority of the intercalation studies have been done on epitaxial monolayer and bilayer graphene on SiC, with very few intercalation studies on already quasi-freestanding, hydrogen intercalated, graphene Watcharinyanon et al. (2012); Kim et al. (2019); Kotsakidis et al. (2020). Of particular interest to us is calcium intercalated graphene, whose study was inspired by the bulk superconducting graphite intercalation compound CaC_6 Sugawara et al. (2009); Yang et al. (2014); Weller et al. (2005); Emery et al. (2005). The majority of calcium intercalation experiments have been performed on graphene grown on SiC, as this allows for growth of large-area graphene that can be characterised with various surface characterisation techniques, such as X-ray photoelectron spectroscopy (XPS), angle-resolved photoemission spectroscopy (ARPES), low-energy electron diffraction (LEED) and scanning tunnelling microscopy Kotsakidis et al. (2020); Ohta et al. (2006); Kanetani et al. (2012); McChesney et al. (2010). Calcium intercalation is known to strongly n-type dope graphene, an effect which has been extensively studied Ohta et al. (2006); McChesney et al. (2010), however, the impact of calcium intercalation on the structural aspects of graphene and the precise positioning of calcium atoms remained somewhat ambiguous Kotsakidis et al. (2020); Ichinokura et al. (2016); Kanetani et al. (2012). Recent research using XPS by Kotsakidis et al. (2020) has shed light on this, revealing that calcium is situated at the interface between the SiC substrate and graphene buffer layer, with work by Toyama et al. (2022) further confirming that calcium prefers to go to the SiC interface.

In this paper, we report calcium intercalation of quasi-freestanding bilayer graphene (QFSBLG) on SiC. Using a combination of LEED, ARPES and density-functional theory (DFT), calcium is found to intercalate only at the interface between graphene and SiC, fully replacing hydrogen in the structure, and not between the graphene layers. This results in highly n-doped, quasi-freestanding bilayer graphene (Ca-QFSBLG) with a drastically altered electronic structure, as seen by ARPES. Comparison with DFT shows the structure to be in close agreement with AA-stacked bilayer graphene, indicating a spontaneous transition from AB- to AA-stacking, which has not been previously observed for calcium intercalated graphene.

2 Materials and methods

2.1 Sample preparation

QFSBLG samples on SiC were grown on semi-insulating 6H-SiC(0001) substrate as described in Ref. Daniels et al. (2017). Sample preparation, ARPES and LEED measurements were carried out at the Toroidal Analyzer endstation at the Soft X-ray Beamline of the Australian Synchrotron. Samples were introduced to ultra-high vacuum (UHV, base pressure of 1×10^{-10} mbar), and annealed over night at 773–823 K. Sample cleanliness was confirmed by LEED and ARPES. A calcium effusion cell was baked at 423 K overnight and outgassed at 588 K. Once the pressure reached 1×10^{-8} mbar, the effusion cell was inserted into the UHV preparation chamber. Calcium (dendritic pieces, 99.99%, Sigma-Aldrich) was intercalated under graphene following modified recipe from Ref. Kotsakidis et al. (2020): Calcium was evaporated for 15 min, with the calcium cell held at 688 K, and deposited on the graphene/SiC substrate held at room temperature. The thickness of deposited calcium layer was 22 Å, as determined by a quartz crystal microbalance. Following the deposition, the graphene/SiC substrate was annealed at 773 K for 15 min, in order to facilitate calcium intercalation.

2.2 Angle-resolved photoemission spectroscopy and low-energy electron diffraction

Structural characterisation of samples was undertaken using a LEED (OCIVM 3 grid reverse view optics, 200 μm spot size) at room temperature, in the endstation used for ARPES. ARPES measurements used a toroidal-type angle-resolving endstation Broekman et al. (2005) at the Soft X-Ray Beamline of the

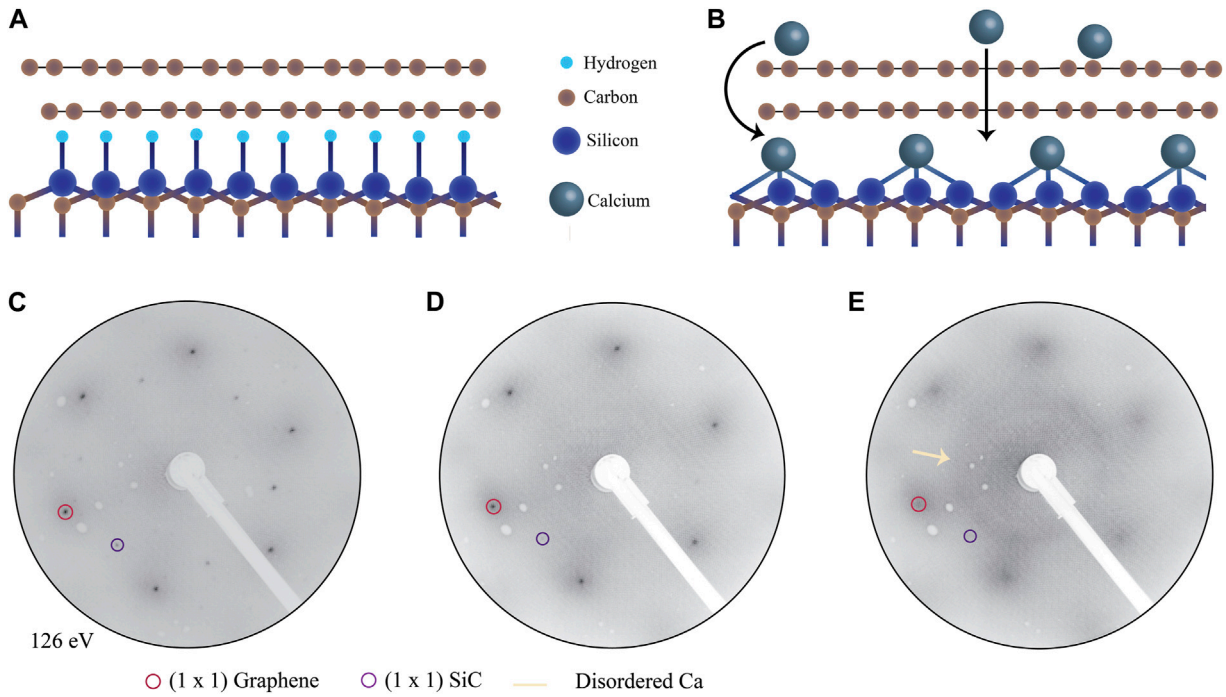

FIGURE 1
Quasi freestanding bilayer graphene (QFSBLG) before and after calcium intercalation. A sketch of QFSBLG before and after intercalation, where hydrogen is replaced by calcium at the SiC interface is shown in **(A,B)**, respectively. **(C)** LEED image of QFSBLG prior calcium intercalation, **(D)** following first, and **(E)** following second calcium intercalation. Red circles indicate the (1 × 1) graphene spots, purple circles indicate the (1 × 1) SiC spots. Yellow arrow points to the ring arising from disordered Ca. All data taken at an incident beam energy of 126 eV and room temperature.

Australian Synchrotron. All ARPES data was taken at room temperature with photon energy ($h\nu$) of 100 eV using linearly polarised light at normal incidence to the sample. The beam spot size was 100 μm × 60 μm. The binding energy (E_{Bin}) scale for all spectra is referenced to the Fermi energy (E_F), determined using the Fermi edge of a gold foil reference sample in electrical contact with the sample. The toroidal analyser permits all polar (Θ) emission angles (−90° to +90°) to be measured along a high-symmetry azimuth (ϕ) of the surface containing the $\bar{\Gamma}$ point. This unique geometry allows for measurement of the Dirac cone along the $\bar{K}$ – $\bar{\Gamma}$ – $\bar{K}$ high-symmetry direction without the need for complex alignment of the spectrometer. Under this geometry, the polarisation vector of the X-rays is entirely contained in the detection plane. The estimated momentum and energy resolution are ≈ 0.02 Å^{-1} and ≈ 150 meV.

2.3 Density-functional theory and tight-binding

First principles density-functional theory calculations were implemented using the Vienna *ab initio* Simulation Package (VASP) to calculate the electronic structure of Ca-QFSBLG Kresse and Furthmüller (1996). The Perdew-Burke-Ernzehof (PBE) form of the generalized gradient approximation (GGA) was used to describe electron exchange and correlation Perdew et al. (1996). A semi-empirical functional (DFT-D2) was employed to describe van der Waals interactions in the system Grimme et al. (2011). The kinetic energy cut-off for the plane-wave basis set was set to 500 eV. We used a 9 × 9 × 1 Γ-centred k-point mesh for sampling the Brillouin zone. The unfolded band structure and Fermi surface were obtained using the KPROJ program based on the k-projection method Chen and Weinert (2018); Chen et al. (2017). Tight-binding calculations were performed in Igor Pro Wavemetrics software based on Ref. Rozhkov et al. (2016) for AA-stacked bilayer graphene, and Refs. Partoens and Peeters (2006); McCann and Koshino (2013) for AB-stacked bilayer graphene. Tight-binding calculations are presented along the $\bar{K}$ – $\bar{\Gamma}$ – $\bar{K}$ high-symmetry direction. Parameters used for tight binding calculations were t = 3.05 (±0.05) and γ_1 = 0.4 for AB-stacked QFSBLG, and t = 2.9 (±0.05) and γ_1 = 0.4 for AA-stacked Ca-QFSBLG.

3 Results and discussion

3.1 Experimental results

QFSBLG samples, Figure 1A, prepared as described in Ref. Daniels et al. (2017) were loaded into the UHV chamber and annealed to remove surface adsorbates, as described in Methods. Following the annealing procedure, LEED data was taken on the clean sample, as shown in Figure 1C. LEED data shows typical diffraction pattern of quasi-freestanding graphene, with only (1 × 1) graphene spots (red circles) and (1 × 1) SiC spots rotated 30° with respect to graphene (purple circles) visible. Following calcium intercalation (Figure 1B), the SiC (1 × 1) spots are less intense compared to the clean QFSBLG, but no other significant changes can

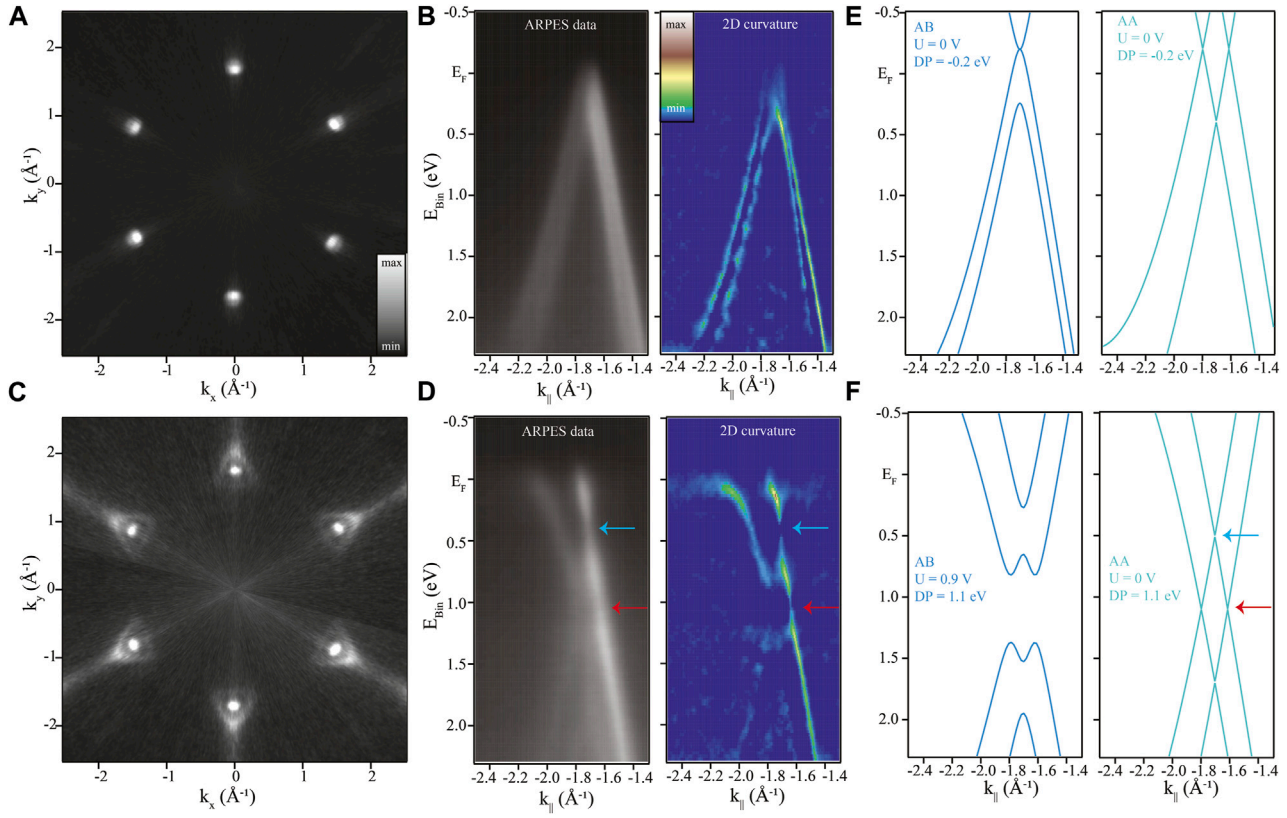

FIGURE 2
ARPES measurements of clean and calcium intercalated quasi-freestanding bilayer graphene (Ca-QFSBLG) after the first intercalation step. **(A)** Fermi surface and **(B)** band structure around the $\bar{K}$ point of QFSBLG, and **(C)** Fermi surface and **(D)** band structure around the $\bar{K}$ point of Ca-QFSBLG. In **(B,D)** both raw ARPES spectra (left) and a 2D curvature of ARPES spectra (right) are shown. Following calcium intercalation, a significant change in the electronic structure and doping level can be seen. **(E)** and **(F)** show tight-binding calculations for AB- (left) and AA-stacked (right) bilayer graphene before and after calcium intercalation, respectively. Red arrows in **(D,F)** indicate location of band crossing between the top and bottom layer band, and a lack of the band gap for AA-stacked bilayer graphene. Blue arrows in **(D,F)** show the Dirac point in the top graphene layer which appears ungapped.

be seen in LEED, as shown in Figure 1D. After the second intercalation step (Figure 1E) drastic changes can be observed in the LEED pattern: (1 × 1) SiC spots are almost completely gone, while (1 × 1) graphene spots are much weaker and broader. Blurring of the graphene (1 × 1) spots suggests additional scattering, likely from calcium atoms accumulating on the surface of the sample in a disordered manner. A new feature can also be observed in the diffraction pattern in Figure 1E, a diffuse ring, marked by a yellow arrow, with a radius corresponding to that of a $(\sqrt{3} \times \sqrt{3})$R30° calcium structure. Ring like features observed in LEED usually point towards rotationally disordered system Emtsev et al. (2008), suggesting calcium is not ordered either under graphene or on its surface. This is in contrast to previous LEED data on calcium intercalated graphene on SiC, where a sharp single domain $(\sqrt{3} \times \sqrt{3})$R30° LEED pattern coming from calcium intercalation is observed Kanetani et al. (2012); Kotsakidis et al. (2020); Toyama et al. (2022). One possible explanation for this discrepancy is that in our system, disorder comes from calcium that did not intercalate, but is instead deposited on the surface of the sample where it does not order. Another possibility is that while calcium is replacing hydrogen at the SiC interface, it does so without rotational order, though the reason for this difference in structure is not clear.

Following structural characterization by LEED, we proceed with the electronic structure investigation using ARPES Damascelli (2004) which allows direct imaging of the electronic bands. Due to an increase in observed disorder for the second intercalation step in LEED (Figure 1E) we will only focus on the first intercalation step for the ARPES investigation. Figure 2 shows intercalation induced changes in the electronic structure of graphene, as observed by ARPES. Changes are tracked in the energy–momentum cuts taken at the Fermi surface (Figures 2A, C) and along the $\bar{K} - \bar{\Gamma} - \bar{K}$ high-symmetry direction (Figures 2B, D). In order to enhance the dispersive features of graphene around the $\bar{K}$ point, we use a two-dimensional (2D) curvature analysis technique Zhang et al. (2011), shown in Figures 2B, D, on the right. The Fermi surface map, Figure 2A, shows the first Brillouin zone of pristine QFSBLG prior calcium intercalation, with six hole pockets visible at the Brillouin zone boundary. As expected for the case of bilayer graphene Ohta et al. (2006), two sets of bands are visible in the energy dispersion data, Figure 2B. Since the samples are p-doped, the Dirac point is located above the Fermi level (0.20 eV, Supplementary Material), which can be clearly seen in the energy dispersion and the 2D curvature data (Figure 2B).

Upon calcium intercalation, profound changes can be observed in the electronic structure: two sets of electron pockets can be seen at the Fermi surface (Figure 2C), and system exhibits high levels of

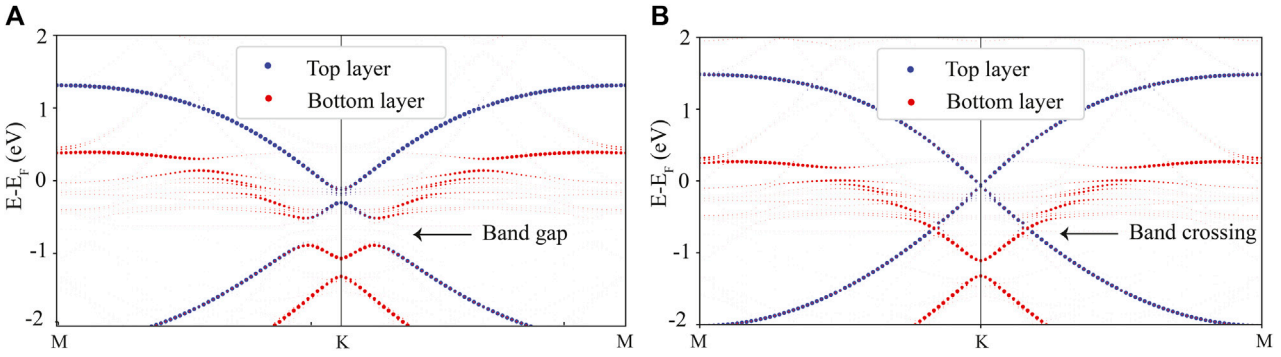

FIGURE 3
DFT calculations for calcium intercalated QFSBLG. The unfolded band structure of calcium intercalated bilayer graphene for the case of AB- and AA-stacking is shown in **(A)** and **(B)**, respectively. The contribution from the top graphene layer is shown in blue, and from the bottom layer in red. Arrows indicate a band gap for the case of AB-stacking, **(A)**, and a band crossing for the case of AA-stacking in Ca-QFSBLG, **(B)**.

n-doping (Figure 2D). In order to better understand the dispersions and changes arising from calcium intercalation, we compare our experimental data to simple tight-binding models for AA- and AB-stacked graphene (Figures 2E, F) Rozhkov et al. (2016); Partoens and Peeters (2006). The same model was used to estimate Dirac point position, doping, Fermi wavevector and Fermi velocity. We used the band position data obtained from momentum dispersion curves, to refine the tight-binding model, and select the appropriate graphene stacking. More information about this can be found in the Supplementary Material. Prior to calcium intercalation, the system is found to be p-doped, with the Dirac point located at DP = (0.20 ± 0.02) eV above the Fermi level, and a Fermi wavevector (k_F) value of k_F = (0.057 ± 0.007) Å^{-1}, corresponding to a hole carrier density of n_h^{total} = (5.17 ± 0.08) × 10^{12} cm^{-2}, in agreement with literature values for hydrogen intercalated graphene on SiC Riedl et al. (2009); Sforzini et al. (2015). Following calcium intercalation (Figures 2C, D) the sample is transformed into highly n-doped system in which no clear band gap can be seen. This structure is in stark contrast to the C_6CaC_6 electronic structure, where the ordered calcium phase gives rise to a folding of the π bands of graphene, resulting in the folded bands appearing close to the $\bar{\Gamma}$ point Kanetani et al. (2012); Toyama et al. (2022); Mazin and Balatsky (2010). In the case of Ca-QFSBLG, no states are observed at the $\bar{\Gamma}$ point, supporting the interpretation that in our case calcium is not ordered in C_6CaC_6 structure, in agreement with the LEED data (Figures 1D, E). Absence of the signatures of C_6CaC_6 structure implies that calcium is not intercalated between the layers, in agreement with recent work by Kotsakidis et al. (2020). Rather, we instead observe a quasi-freestanding bilayer graphene that is n-doped. Nevertheless, there are several discrepancies between our results (Figure 2D) and what is expected from simply n-doped (quasi-freestanding) bilayer graphene Ohta et al. (2006). The most obvious discrepancy is a lack of band gap in the system (see red and blue arrows in Figure 2D), which is expected for the simple case of AB-stacked bilayer graphene Ohta et al. (2006); Grubišić-Čabo et al. (2021). This is reminiscent of the structure expected for AA-stacked bilayer graphene where a band gap is not expected, and the electronic bands still have massless character as for the case of monolayer graphene Rozhkov et al. (2016). Taking this into the account, we modelled both AA- and AB-stacked bilayer graphene with tight-binding (Figures 2E, F) and DFT (Figure 3). From the tight-binding model, the best agreement was obtained for AA-stacked bilayer graphene, where the inner band Fermi wavevector was k_F^{inner} = (0.086 ± 0.007) Å^{-1}, and the outer band was k_F^{outer} = (0.280 ± 0.007) Å^{-1}. These values correspond to a total electron density of n_e^{total} = n_e^{inner}+n_e^{outer} = (1.37 ± 0.06) × 10^{14} cm^{-2}, a two orders of magnitude increase in carrier concentration with respect to the pristine QFSBLG. The aforementioned dramatic increase in the carrier concentration is accompanied with small reduction in Fermi velocity of graphene–Ca-QFSBLG has Fermi velocity v_F = (0.93 ± 0.02) × 10^6 ms^{-1}, while QFSBLG has Fermi velocity v_F = (0.99 ± 0.02) × 10^6 ms^{-1}, suggesting that no significant renormalisaiton of Fermi velocity due to transformation of stacking Li et al. (2010), change of the dielectric constant of the graphene's surroundings Hwang et al. (2012), or many-body interactions Elias et al. (2011) takes place. Lastly, while the observed increase in the carrier density is significant, it is lower than values observed for the case when calcium goes both to the SiC interface and in between the sheets of bilayer graphene Toyama et al. (2022), thus underpinning the notion of intercalation occurring solely at the interface of our system.

3.2 Theoretical results

We further examine the nature of stacking in Ca-QFSBLG by performing DFT calculations of the electronic structure of AB- and AA-stacked Ca-QFSBLG. We first calculate the calcium intercalation energy based on Eq. 1 as follows:

$$E_I = E(SiC/graphene) + E(Ca) - E(SiC/graphene + Ca), \quad (1)$$

where E_I is the intercalation energy, E (*SiC/graphene*), E (*Ca*) and E (*SiC/graphene* + *Ca*) are the energy of SiC/graphene heterostructure (SiC covalently bonded with graphene plus a monolayer graphene), atomic energy of calcium in its bulk state, and the energy of SiC/graphene system upon calcium intercalation, respectively. Once calcium is placed below bilayer graphene, a small difference is found in the formation energy between the AA- and AB-stacked bilayer graphene, as shown in Table 1, with AB-stacking being slightly favourable. This small difference in formation energy suggests it is plausible that AA-stacking could

TABLE 1 Calculation for intercalation energy, AA- vs. AB-stacking, using different van der Waals corrections.

Stacking type	DFT-D2 energy (eV/Ca atom)	DFT-D3 energy (eV/Ca atom)
AA	0.94	1.08
AB	0.98	1.09

indeed be a stable phase in Ca-QFSBLG, similar to what has been observed for the case of lithium intercalation Watcharinyanon et al. (2012); Caffrey et al. (2016). As both structures appear energetically stable, and are close in the formation energy, DFT band structure calculations were performed for AA- and AB-stacking in order to determine which structure fits experimental ARPES data better.

The unfolded band structure of AA- and AB-stacked Ca-QFSBLG is shown in Figure 3. For the case of AB-stacked Ca-QFSBLG (Figure 3A), a large band gap, approximately 0.38 eV in size, is found between the top of the valence band and bottom of a conduction band, situated 0.51 eV below the Fermi level. This structure is similar to the one observed for magnesium intercalated graphene on SiC Grubišić-Čabo et al. (2021), where a band gap of 0.36 eV was observed. In the case of AA-stacked bilayer graphene (Figure 3B), the structure is markedly different, and no band gap is found between the top of the valence band and bottom of a conduction band. Instead, a smaller 0.20 eV gap is identified 1.05 eV below the Fermi level located only in the bottom graphene layer. In contrast, the top graphene layer is gapless, and nearly indistinguishable from the pristine monolayer graphene. The latter structure is in good agreement with the experimental data shown in Figure 2, particularly in the region where the top- and bottom-layer derived bands cross at finite momentum (red arrows in Figures 2D, F) and the Dirac point of the top graphene layer (blue arrows in Figures 2D, F), in agreement with our experimental ARPES results which show Ca-QFSBLG as AA-stacked.

The interaction distance between intercalated calcium atoms and graphene plays a crucial role in driving the electronic structure differences between AA-stacked and AB-stacked systems. In the AA-stacked system with calcium intercalation, we observed a larger separation between the graphene layers and calcium atoms for AA-stacked configuration (2.45 Å) in comparison to the AB-stacked configuration (2.33 Å, Supplementary Figure S3). This observation may provide a partial explanation for the diminished impact on the top layer during the doping process.

4 Conclusion

Calcium intercalation was successfully achieved in quasi-freestanding bilayer graphene on hydrogenated SiC, resulting in significant changes to the system. Upon calcium intercalation, calcium replaced hydrogen at the SiC interface, leading to a switch from p-type doping to n-type doping. This transition was accompanied with almost two orders of magnitude change in the carrier concentration, going from $n_h^{total} = 5.17 \times 10^{12}$ cm^{-2} to $n_e^{total} = 1.37 \times 10^{14}$ cm^{-2}, while retaining the quasi-freestanding nature, and exhibiting minimal change of the Fermi velocity. Structurally, the intercalation process resulted in a transformation from AB-stacked to AA-stacked bilayer graphene, a shift facilitated by a small difference in the formation energy between the two stacking types. As a result, the electronic band structure is significantly altered. The top layer of graphene is nearly indistinguishable from a pristine monolayer, retaining the ungapped Dirac point. While previous reports show indirect evidence of inhomogeneous AA- and AB-stacked regions in epitaxial graphene following lithium intercalation and de-intercalation, to our knowledge, this is the first report of the preparation of large-area, uniform quasi-freestanding AA-stacked graphene following calcium intercalation. This opens the door to further study of the properties of this distinct new graphene system with its unique band structure.

Data availability statement

The datasets presented in this study can be found in online repositories. The names of the repository/repositories and accession number(s) can be found below: Zenodo: https://doi.org/10.5281/zenodo.10071225.

Author contributions

AG-C: Formal Analysis, Investigation, Visualization, Writing–original draft, Writing–review and editing, Conceptualization. JK: Conceptualization, Investigation, Writing–review and editing. YY: Formal Analysis, Writing–review and editing. AT: Data curation, Formal Analysis, Investigation, Resources, Software, Writing–review and editing. MH: Investigation, Writing–review and editing. SS: Investigation, Writing–review and editing. JR: Data curation, Resources, Writing–review and editing. EH: Resources, Writing–review and editing. KD: Resources, Writing–review and editing. RM-W: Resources, Writing–review and editing. ME: Investigation, Supervision, Writing–review and editing. NM: Formal Analysis, Supervision, Writing–review and editing. DG: Resources, Supervision, Writing–review and editing. MF: Conceptualization, Funding acquisition, Supervision, Writing–original draft, Writing–review and editing, Project administration.

Funding

The author(s) declare financial support was received for the research, authorship, and/or publication of this article. This work was supported by the Australian Research Council under awards DP150103837, DP200101345 and FL120100038. JK was supported by the Australian Government Research Training Program, and the Monash Centre for Atomically Thin Materials. YY and NM were supported by the Australian Research Council (CE17010039). DG, RM-W, and KD were supported by core programs at the U.S. Naval Research Laboratory funded by the Office of Naval Research.

Acknowledgments

This research was undertaken on the Soft X-ray spectroscopy beamline at the Australian Synchrotron, part of ANSTO. YY and NM gratefully acknowledge the computational support from the National Computing Infrastructure and Pawsey Supercomputing Facilities. Preprint version of this article was published on arXiv repository as Grubišić-Čabo et al. (2023).

Conflict of interest

The authors declare that the research was conducted in the absence of any commercial or financial relationships that could be construed as a potential conflict of interest.

Publisher's note

All claims expressed in this article are solely those of the authors and do not necessarily represent those of their affiliated organizations, or those of the publisher, the editors and the reviewers. Any product that may be evaluated in this article, or claim that may be made by its manufacturer, is not guaranteed or endorsed by the publisher.

Supplementary material

The Supplementary Material for this article can be found online at: https://www.frontiersin.org/articles/10.3389/fnano.2023.1333127/full#supplementary-material

References

Bao, W., Wan, J., Han, X., Cai, X., Zhu, H., Kim, D., et al. (2014). Approaching the limits of transparency and conductivity in graphitic materials through lithium intercalation. *Nat. Commun.* 5, 4224. doi:10.1038/ncomms5224

Briggs, N., Gebeyehu, Z. M., Vera, A., Zhao, T., Wang, K., De La Fuente Duran, A., et al. (2019). Epitaxial graphene/silicon carbide intercalation: a minireview on graphene modulation and unique 2D materials. *Nanoscale* 11, 15440–15447. doi:10.1039/C9NR03721G

Broekman, L., Tadich, A., Huwald, E., Riley, J., Leckey, R., Seyller, T., et al. (2005). First results from a second generation toroidal electron spectrometer. *J. Electron Spectrosc. Relat. Phenom.* 144-147, 1001–1004. doi:10.1016/j.elspec.2005.01.022

Caffrey, N. M., Johansson, L. I., Xia, C., Armiento, R., Abrikosov, I. A., and Jacobi, C. (2016). Structural and electronic properties of Li-intercalated graphene on SiC(0001). *Phys. Rev. B* 93, 195421. doi:10.1103/PhysRevB.93.195421

Chen, M., and Weinert, M. (2018). Layer *k*-projection and unfolding electronic bands at interfaces. *Phys. Rev. B* 98, 245421. doi:10.1103/PhysRevB.98.245421

Chen, M. X., Chen, W., Zhang, Z., and Weinert, M. (2017). Effects of magnetic dopants in $Li_{0.8}M_{0.2}OH$ FeSe (M=Fe, Mn, Co): density functional theory study using a band unfolding technique. *Phys. Rev. B* 96, 245111. doi:10.1103/PhysRevB.96.245111

Damascelli, A. (2004). Probing the electronic structure of complex systems by ARPES. *Phys. Scr.* T109, 61. doi:10.1238/Physica.Topical.109a00061

Daniels, K. M., Jadidi, M. M., Sushkov, A. B., Nath, A., Boyd, A. K., Sridhara, K., et al. (2017). Narrow plasmon resonances enabled by quasi-freestanding bilayer epitaxial graphene. *2D Mat.* 4, 025034. doi:10.1088/2053-1583/aa5c75

de Jong, T. A., Krasovskii, E. E., Ott, C., Tromp, R. M., van der Molen, S. J., and Jobst, J. (2018). Intrinsic stacking domains in graphene on silicon carbide: a pathway for intercalation. *Phys. Rev. Mat.* 2, 104005. doi:10.1103/PhysRevMaterials.2.104005

de Jong, T. A., Visser, L., Jobst, J., Tromp, R. M., and van der Molen, S. J. (2023). Stacking domain morphology in epitaxial graphene on silicon carbide. *Phys. Rev. Mat.* 7, 034001. doi:10.1103/PhysRevMaterials.7.034001

Elias, D. C., Gorbachev, R. V., Mayorov, A. S., Morozov, S. V., Zhukov, A. A., Blake, P., et al. (2011). Dirac cones reshaped by interaction effects in suspended graphene. *Nat. Phys.* 7, 701–704. doi:10.1038/nphys2049

Emery, N., Hérold, C., d'Astuto, M., Garcia, V., Bellin, C., Marêché, J. F., et al. (2005). Superconductivity of bulk CaC_6. *Phys. Rev. Lett.* 95, 087003. doi:10.1103/PhysRevLett.95.087003

Emtsev, K. V., Bostwick, A., Horn, K., Jobst, J., Kellogg, G. L., Ley, L., et al. (2009). Towards wafer-size graphene layers by atmospheric pressure graphitization of silicon carbide. *Nat. Mat.* 8, 203–207. doi:10.1038/nmat2382

Emtsev, K. V., Speck, F., Seyller, T., Ley, L., and Riley, J. D. (2008). Interaction, growth, and ordering of epitaxial graphene on SiC{0001} surfaces: a comparative photoelectron spectroscopy study. *Phys. Rev. B* 77, 155303. doi:10.1103/PhysRevB.77.155303

Endo, Y., Fukaya, Y., Mochizuki, I., Takayama, A., Hyodo, T., and Hasegawa, S. (2020). Structure of superconducting Ca-intercalated bilayer graphene/SiC studied using total-reflection high-energy positron diffraction. *Carbon* 157, 857–862. doi:10.1016/j.carbon.2019.10.070

Endo, Y., Ichinokura, S., Akiyama, R., Takayama, A., Sugawara, K., Nomura, K., et al. (2018). Weak localization in bilayer graphene with Li-intercalation/desorption. *J. Phys. Condens. Matter.* 30, 305701. doi:10.1088/1361-648x/aaccc4

Grimme, S., Ehrlich, S., and Goerigk, L. (2011). Effect of the damping function in dispersion corrected density functional theory. *J. Comput. Chem.* 32, 1456–1465. doi:10.1002/jcc.21759

Grubišić-Čabo, A., Kotsakidis, J. C., Yin, Y., Tadich, A., Haldon, M., Solari, S., et al. (2021). Magnesium-intercalated graphene on SiC: highly n-doped air-stable bilayer graphene at extreme displacement fields. *Appl. Surf. Sci.* 541, 148612. doi:10.1016/j.apsusc.2020.148612

Grubišić-Čabo, A., Kotsakidis, J. C., Yin, Y., Tadich, A., Haldon, M., Solari, S., et al. (2023). Quasi-free-standing AA-stacked bilayer graphene induced by calcium intercalation of the graphene-silicon carbide interface. *arXiv.* 2311.02528.

Hwang, C., Park, C.-H., Siegel, D. A., Fedorov, A. V., Louie, S. G., and Lanzara, A. (2011). Direct measurement of quantum phases in graphene via photoemission spectroscopy. *Phys. Rev. B* 84, 125422. doi:10.1103/PhysRevB.84.125422

Hwang, C., Siegel, D. A., Mo, S.-K., Regan, W., Ismach, A., Zhang, Y., et al. (2012). Fermi velocity engineering in graphene by substrate modification. *Sci. Rep.* 2, 590. doi:10.1038/srep00590

Ichinokura, S., Sugawara, K., Takayama, A., Takahashi, T., and Hasegawa, S. (2016). Superconducting calcium-intercalated bilayer graphene. *ACS Nano* 10, 2761–2765. doi:10.1021/acsnano.5b07848

Kanetani, K., Sugawara, K., Sato, T., Shimizu, R., Iwaya, K., Hitosugi, T., et al. (2012). Ca intercalated bilayer graphene as a thinnest limit of superconducting C_6Ca. *PNAS* 109, 19610–19613. doi:10.1073/pnas.1208889109

Katsnelson, M. I., Novoselov, K. S., and Geim, A. K. (2006). Chiral tunnelling and the Klein paradox in graphene. *Nat. Phys.* 2, 620–625. doi:10.1038/nphys384

Kim, H., Dugerjav, O., Lkhagvasuren, A., and Seo, J. M. (2019). Doping modulation of quasi-free-standing monolayer graphene formed on SiC(0001) through $Sn_{1-x}Ge_x$ intercalation. *Carbon* 144, 549–556. doi:10.1016/j.carbon.2018.12.084

Kim, K. S., Warlter, A. L., Moreschini, L., Seyller, T., Horn, K., Rotenberg, E., et al. (2013). Coexisting massive and massless Dirac fermions in symmetry-broken bilayer graphene. *Nat. Mat.* 12, 887–892. doi:10.1038/nmat3717

Kotsakidis, J. C., Currie, M., Grubišić-Čabo, A., Tadich, A., Myers-Ward, R. L., DeJarld, M., et al. (2021). Increasing the rate of magnesium intercalation underneath epitaxial graphene on 6H-SiC(0001). *Adv. Mat. Interfaces* 8, 2101598. doi:10.1002/admi.202101598

Kotsakidis, J. C., Grubišić-Čabo, A., Yin, Y., Tadich, A., Myers-Ward, R. L., DeJarld, M., et al. (2020). Freestanding n-doped graphene via intercalation of calcium and magnesium into the buffer layer–SiC(0001) interface. *Chem. Mat.* 32, 6464–6482. doi:10.1021/acs.chemmater.0c01729

Kresse, G., and Furthmüller, J. (1996). Efficiency of ab-initio total energy calculations for metals and semiconductors using a plane-wave basis set. *Comput. Mat. Sci.* 6, 15–50. doi:10.1016/0927-0256(96)00008-0

Kruskopf, M., Pakdehi, D. M., Pierz, K., Wundrack, S., Stosch, R., Dziomba, T., et al. (2016). Comeback of epitaxial graphene for electronics: large-area growth of bilayer-free graphene on SiC. *2D Mat.* 3, 041002. doi:10.1088/2053-1583/3/4/041002

Li, G., Luican, A., Lopes dos Santos, J. M. B., Castro Neto, A. H., Reina, A., Kong, J., et al. (2010). Observation of van Hove singularities in twisted graphene layers. *Nat. Phys.* 6, 109–113. doi:10.1038/nphys1463

Liu, Y., Bian, G., Miller, T., and Chiang, T.-C. (2011). Visualizing electronic chirality and Berry phases in graphene systems using photoemission with circularly polarized light. *Phys. Rev. Lett.* 107, 166803. doi:10.1103/PhysRevLett.107.166803

Liu, Z., Suenaga, K., Harris, P. J. F., and Iijima, S. (2009). Open and closed edges of graphene layers. *Phys. Rev. Lett.* 102, 015501. doi:10.1103/PhysRevLett.102.015501

Marchenko, D., Varykhalov, A., Sánchez-Barriga, J., Seyller, T., and Rader, O. (2016). Rashba splitting of 100 meV in Au-intercalated graphene on SiC. *Appl. Phys. Lett.* 108, 172405. doi:10.1063/1.4947286

Mazin, I., and Balatsky, A. (2010). Superconductivity in Ca-intercalated bilayer graphene. *Philos. Mag. Lett.* 90, 731–738. doi:10.1080/09500839.2010.487473

McCann, E., and Koshino, M. (2013). The electronic properties of bilayer graphene. *Rep. Prog. Phys.* 76, 056503. doi:10.1088/0034-4885/76/5/056503

McChesney, J. L., Bostwick, A., Ohta, T., Seyller, T., Horn, K., González, J., et al. (2010). Extended van Hove singularity and superconducting instability in doped graphene. *Phys. Rev. Lett.* 104, 136803. doi:10.1103/PhysRevLett.104.136803

Novoselov, K., Geim, A., Morozov, S., Jiang, D., Zhang, Y., Dubonos, S., et al. (2004). Electric field effect in atomically thin carbon films. *Science* 80, 306666–306669. doi:10.1126/science.1102896

Novoselov, K. S., Geim, A. K., Morozov, S. V., Jiang, D., Katsnelson, M. I., Grigorieva, I. V., et al. (2005). Two-dimensional gas of massless Dirac fermions in graphene. *Nature* 438, 197–200. doi:10.1038/nature04233

Novoselov, K. S., McCann, E., Morozov, S. V., Fal'ko, V. I., Katsnelson, M. I., Zeitler, U., et al. (2006). Unconventional quantum Hall effect and Berry's phase of 2π in bilayer graphene. *Nat. Phys.* 2, 177–180. doi:10.1038/nphys245

Nyakiti, L., Wheeler, V., Garces, N., Myers-Ward, R., Eddy, C., and Gaskill, D. (2012). Enabling graphene-based technologies: toward wafer-scale production of epitaxial graphene. *MRS Bull.* 37, 1149–1157. doi:10.1557/mrs.2012.180

Ohta, T., Bostwick, A., Seyller, T., Horn, K., and Rotenberg, E. (2006). Controlling the electronic structure of bilayer graphene. *Science* 313, 951–954. doi:10.1126/science.1130681

Oliveira, M. H., Schumann, T., Fromm, F., Koch, R., Ostler, M., Ramsteiner, M., et al. (2013). Formation of high-quality quasi-free-standing bilayer graphene on SiC(0001) by oxygen intercalation upon annealing in air. *Carbon* 52, 83–89. doi:10.1016/j.carbon.2012.09.008

Partoens, B., and Peeters, F. M. (2006). From graphene to graphite: electronic structure around the *K* point. *Phys. Rev. B* 74, 075404. doi:10.1103/PhysRevB.74.075404

Perdew, J. P., Burke, K., and Ernzerhof, M. (1996). Generalized gradient approximation made simple. *Phys. Rev. Lett.* 77, 3865–3868. doi:10.1103/PhysRevLett.77.3865

Riedl, C., Coletti, C., Iwasaki, T., Zakharov, A. A., and Starke, U. (2009). Quasi-free-standing epitaxial graphene on SiC obtained by hydrogen intercalation. *Phys. Rev. Lett.* 103, 246804. doi:10.1103/PhysRevLett.103.246804

Rozhkov, A., Sboychakov, A., Rakhmanov, A., and Nori, F. (2016). Electronic properties of graphene-based bilayer systems. *Phys. Rep.* 648, 1–104. doi:10.1016/j.physrep.2016.07.003

Sboychakov, A. O., Rakhmanov, A. L., Rozhkov, A. V., and Nori, F. (2021). Bilayer graphene can become a fractional metal. *Phys. Rev. B* 103, L081106. doi:10.1103/PhysRevB.103.L081106

Sforzini, J., Nemec, L., Denig, T., Stadtmüller, B., Lee, T.-L., Kumpf, C., et al. (2015). Approaching truly freestanding graphene: the structure of hydrogen-intercalated graphene on 6H-SiC(0001). *Phys. Rev. Lett.* 114, 106804. doi:10.1103/PhysRevLett.114.106804

Shen, K., Sun, H., Hu, J., Hu, J., Liang, Z., Li, H., et al. (2018). Fabricating quasi-free-standing graphene on a SiC(0001) surface by steerable intercalation of iron. *J. Phys. Chem. C* 122, 21484–21492. doi:10.1021/acs.jpcc.8b06789

Sohn, Y., Shin, W. J., Ryu, S. H., Huh, M., Cha, S., and Kim, K. S. (2021). Graphene p-n junction formed on SiC(0001) by Au intercalation. *J. Korean Phys. Soc.* 78, 40–44. doi:10.1007/s40042-020-00010-0

Starke, U., and Riedl, C. (2009). Epitaxial graphene on SiC(0001) and SiC(000$\bar{1}$): from surface reconstructions to carbon electronics. *J. Condens. Matter Phys.* 21, 134016. doi:10.1088/0953-8984/21/13/134016

Sugawara, K., Sato, T., and Takahashi, T. (2009). Fermi-surface-dependent superconducting gap in C_6Ca. *Nat. Phys.* 5, 40–43. doi:10.1038/nphys1128

Sung, S. J., Yang, J. W., Lee, P. R., Kim, J. G., Ryu, M. T., Park, H. M., et al. (2014). Spin-induced band modifications of graphene through intercalation of magnetic iron atoms. *Nanoscale* 6, 3824–3829. doi:10.1039/C3NR04178F

Toyama, H., Akiyama, R., Ichinokura, S., Hashizume, M., Iimori, T., Endo, Y., et al. (2022). Two-dimensional superconductivity of Ca-intercalated graphene on SiC: vital role of the interface between monolayer graphene and the substrate. *ACS Nano* 16, 3582–3592. doi:10.1021/acsnano.1c11161

Valla, T., Camacho, J., Pan, Z.-H., Fedorov, A. V., Walters, A. C., Howard, C. A., et al. (2009). Anisotropic electron-phonon coupling and dynamical nesting on the graphene sheets in superconducting CaC_6 using angle-resolved photoemission spectroscopy. *Phys. Rev. Lett.* 102, 107007. doi:10.1103/PhysRevLett.102.107007

Virojanadara, C., Watcharinyanon, S., Zakharov, A. A., and Johansson, L. I. (2010). Epitaxial graphene on 6*H*-SiC and Li intercalation. *Phys. Rev. B* 82, 205402. doi:10.1103/PhysRevB.82.205402

Watcharinyanon, S., Johansson, L., Zakharov, A. A., and Virojanadara, C. (2012). Studies of Li intercalation of hydrogenated graphene on SiC(0001). *Surf. Sci.* 606, 401–406. doi:10.1016/j.susc.2011.10.023

Watcharinyanon, S., Johansson, L. I., Xia, C., and Virojanadara, C. (2013). Ytterbium oxide formation at the graphene–SiC interface studied by photoemission. *J. Vac. Sci. Technol. A* 31, 020606. doi:10.1116/1.4792040

Weller, T. E., Ellerby, M., Saxena, S. S., Smith, R. P., and Skipper, N. T. (2005). Superconductivity in the intercalated graphite compounds C_6Yb and C_6Ca. *Nat. Phys.* 1, 39–41. doi:10.1038/nphys0010

Wolff, S., Roscher, S., Timmermann, F., Daniel, M. V., Speck, F., Wanke, M., et al. (2019). Quasi-freestanding graphene on SiC(0001) by Ar-mediated intercalation of antimony: a route toward intercalation of high-vapor-pressure elements. *Ann. Phys.* 531, 1900199. doi:10.1002/andp.201900199

Yang, S.-L., Sobota, J. A., Howard, C. A., Pickard, C. J., Hashimoto, M., Lu, D. H., et al. (2014). Superconducting graphene sheets in CaC_6 enabled by phonon-mediated interband interactions. *Nat. Commun.* 5, 3493. doi:10.1038/ncomms4493

Zhang, P., Richard, P., Qian, T., Xu, Y.-M., Dai, X., and Ding, H. (2011). A precise method for visualizing dispersive features in image plots. *Rev. Sci. Instrum.* 82, 043712. doi:10.1063/1.3585113

Zhang, Y., Tan, Y.-W., Stormer, H. L., and Kim, P. (2005). Experimental observation of the quantum Hall effect and Berry's phase in graphene. *Nature* 438, 201–204. doi:10.1038/nature04235

frontiers | Frontiers in Nanotechnology

TYPE Mini Review
PUBLISHED 06 March 2024
DOI 10.3389/fnano.2024.1320503

OPEN ACCESS

EDITED BY
Theresa Schoetz,
University of Illinois at Urbana-Champaign, United States

REVIEWED BY
Svetlozar Ivanov,
Technische Universität Ilmenau, Germany

*CORRESPONDENCE
Neus Domingo,
ndomingo@ornl.gov

RECEIVED 12 October 2023
ACCEPTED 15 February 2024
PUBLISHED 06 March 2024

CITATION
Domingo N (2024), Understanding piezocatalysis, pyrocatalysis and ferrocatalysis. *Front. Nanotechnol.* 6:1320503. doi: 10.3389/fnano.2024.1320503

Understanding piezocatalysis, pyrocatalysis and ferrocatalysis

Neus Domingo*

Functional Atomic Force Microscope Group, Center for Nanophase Materials Sciences, Oak Ridge National Laboratory, Oak Ridge, TN, United States

The last decade has witnessed the emergence of the application of piezoelectric and ferroelectric materials for catalytic and photocatalytic applications that harness light, thermal and mechanical energy into chemical reactions. This article surveys the different concepts of pyro- and piezocatalysis and differences with respect to ferrocatalysis and switchable catalysis and delves into the current understanding of the mechanisms underlying piezocatalysis. The outlook for advancing in the surface science studies required for the design of new and better catalysts based on polar electromechanically active materials is discussed in the context of the state of the art experimental studies and potential future nanoscience developments.

KEYWORDS

ferrocatalysis, ferroelectrics, photocatalysis, piezocatalysis, pyrocatalysis

1 Introduction

Catalysis, a multidisciplinary field by nature covering areas from physics to chemistry and biology and at the base of the chemical industry, uses catalysts as materials to intermediate chemical reactions that lead to the final reaction product through lower energetic pathways. In photogenerated catalysis, the photocatalytic activity of a material depends on the ability of the catalyst to create electron/hole pairs upon light absorption to accelerate desired reactions. A primary practical application is based on the discovery of photocatalytic water splitting by titanium dioxide (TiO_2), a process of artificial photosynthesis that generates hydrogen (and oxygen) from water and light (Fujishima and Honda, 1972; Man, Su et al., 2011; Zhao and Liu, 2014; Lampimäki, Schreiber et al., 2015). The problem of photocatalysts is that they must meet restrictive bandgap requirements, and typically need dopants and/or additional co-catalysts to optimize their performance. Moreover, heterogeneous catalysis on surfaces is highly selective, since the catalysts efficiency is limited by the Sabatier principle which balances the catalytic efficiency against the optimal strength of the adsorbate-surface interaction (Medford, Vojvodic et al., 2015) and available active sites, and thus its optimization for each chemical reaction requires a dedicated research effort.

While photocatalysis is a straightforward green methodology to convert light to chemical energy, there are other possible sources of charge to be exploited to harvest green energy for catalysis applications. In this regard, electromechanically active oxide perovskites are emerging as one of the most promising material systems to open new opportunities in the area of catalysis (Kim, Nguyen et al., 2018; Li, Li et al., 2020; X.-K. Wei, Domingo et al., 2022). In this class of materials, the polarization is coupled to strain and temperature fields therefore making it possible to create polarization by means of mechanical and thermal energy. In this mini review, we will sketch the state of the art in the understanding of the fundamental mechanisms of ferrocatalytisis, piezocatalysis and

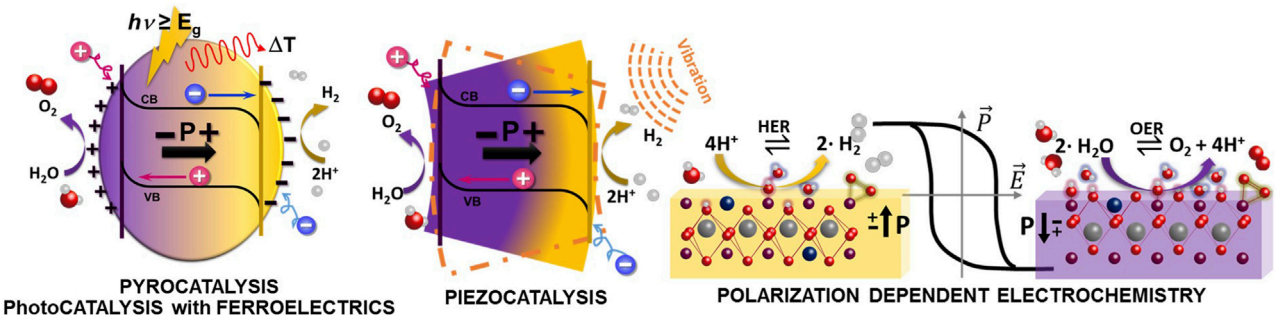

FIGURE 1
Illustration of the different concepts of pyrocatalysis, photocatalysis based on ferroelectric materials and piezocatalysis. The right panel illustrates the selectivity of ferroelectric surfaces to drive oxidation and reduction reactions as a function of the ferroelectric polarization.

pyrocatalysis and discuss the current research gaps and potential future developments in the field.

2 Polarization assisted catalysis

Polarization assisted catalysis is an emerging catalysis field that embraces the use of pyroelectric, piezoelectric and ferroelectric materials to harvest light, thermal and mechanical energy into chemical reactions. These different concepts sketched in Figure 1 have been coined in the last decade to refer to different mechanisms in which these polar and electromechanical active materials are observed to enhance catalytic efficiency in different type of redox reactions. Piezoelectric materials are generally non-centrosymmetric crystals that can create electrical dipoles as a response to an applied mechanical stress or deformation, leading to the emergence of a voltage drop across the material (also called piezopotential), based on the different charges accumulated on opposite surfaces. These are electromechanical active materials that will also deform under applied electric fields due to the inverse piezoelectric effect. A crystal that poses spontaneous polarization even under unstrained conditions is defined as a pyroelectric material, and its electric polarization changes as a function of temperature. A subclass of pyroelectric materials are ferroelectrics, exhibiting an spontaneous polarization that can be reversed upon the application of an electric field giving rise to ferroelectric hysteresis loops. Both, pyroelectric and ferroelectric materials are also piezoelectric and thus its polarization can be modulated by mechanical stress.

2.1 Piezocatalysis and pyrocatalysis

In piezoelectric and pyroelectric materials, the change of its polar state creates a bound charge on the surfaces with stray electric fields that need to be compensated to reach stability, a property that has been exploited to build up piezoelectric nanogenerators by short-circuiting opposite surfaces (Wang and Song, 2006). However, when the polar materials are exposed to ambient, the most relevant screening mechanism is the appearance of surface adsorbates layers composed by different types of ionic species and dipolar chemical groups that compensate the surface stray electric fields. Being a subclass of piezoelectrics, ferroelectric materials are known to show the highest piezoelectric coefficients and also spontaneous stray electric fields that need to be compensated to stabilize the ferroelectric polarization. Thus, similar to photocatalysis, the thermal or mechanical induced change of polarization in any pyroelectric or piezoelectric material can be regarded as a source of potential that can lead to the accumulation of charge at the surfaces available to accelerate catalytic reactions, leading to "pyroelectrocatalysis" (Kakekhani and Ismail-Beigi, 2016; Wu, Mao et al., 2016) and "piezoelectrochemical" effects (Starr and Wang, 2013; Starr and Wang, 2015; Zhang, Xie et al., 2017; Wu, Qin et al., 2018; Liang, Yan et al., 2019; Yu, Liu et al., 2019) respectively. The efficiency of polar materials to implement pyrocatalysis and piezocatalysis will strongly depend on the balance between the polarization change (instantaneous upon the change of temperature and strain), the screening dynamics and the charge generation rates as compared to the physical chemical features of the reactions to catalyze.

However, the piezopotentials and pyroelectric potential differences created by thermal and mechanical changes in dielectric piezoelectrics cannot supply enough charges for efficient catalytic processes on their own, so most of the times practical applications are based on semiconductor piezoelectrics [and dopped ferroelectric (Dubey, Keat et al., 2022)] materials that can provide free and photoinduced carriers to enhance the catalytic reactivity (Mushtaq, Chen et al., 2018). In this case, the internal generated electric fields, similar to the concept of piezotronics and piezo-phototronics, are expected to regulate charge carrier transport behavior and force the free charges to move towards opposite directions, inhibiting the recombination of photocharge carriers and enabling more holes and electrons to reach the active sites on opposite surfaces of the catalysts for the redox reaction.

2.2 Ferrocatalysis and switchable catalysis

Ferroelectric materials are also known as wide band gap semiconductors and show a permanent internal polarization that can be rotated through the application of an electric field. This polarization leads to a discontinuity on the electric fields at their surface that needs to be screened to ensure their stability (Sergei, Yunseok et al., 2018). Archetypal ferroelectrics show polarization

values in the range of $P \in (10\text{-}70)\ \mu C{\cdot}cm^{-2}$, leading to stray electric fields of the order of $E = 1{\cdot}e^{10}$ V/m on the surface (~1.1 V at 1 nm above the surface for $p = 10\ \mu C\ cm^{-2}$). The most efficient way to cancel the electric field is the accumulation of equal amounts of compensating opposite charges, that would be the charge equivalent to about 1.5 electrons/nm^2 for a ferroelectric material with $p = 25\ \mu C\ cm^{-2}$ like $BaTiO_3$ (~2.8V nm^{-1}, enough field for water splitting). This can be achieved by internal screening mechanisms such as band bending near the surface to accumulate electrons, holes or ionic charges as oxygen vacancies, or by the adsorption of external species. In UHV, the adsorbates are species found in the bulk such as oxygen anions while in ambient conditions the range of available species is much wider. Among all the external adsorbates, water molecules either physisorbed or dissociated play the major role (Segura, Domingo et al., 2013; Cordero-Edwards, Rodríguez et al., 2016), since as a polar molecule is sensitive to the stray electric fields and can dissociate on the surface forming hydroxyls or providing ionic charges. Other known active species include carbonated organic molecules, with different carboxylic groups and Si oxides, or other salts formed from ions contained in the material. So far, the race towards understanding the interplay between ferroelectricity and surface electrochemistry still faces crucial unresolved issues, since at the nanoscale the ferroelectric state is fundamentally inseparable from the electrochemical state of the surface (Yang, Morozovska et al., 2017) and determines ferroelectric switching dynamics (Spasojevic, Verdaguer et al., 2022). This coupling has strong impact on the application of ferroelectric materials in nanodevices such as Tunnel Junctions (Lu, Lipatov et al., 2014; Guo, Wang et al., 2017) since it can create an imprint in the ferroelectric state (Lee, Kim et al., 2016) or alter associated fundamental physical properties such as tunnelling eletroresistance (Gruverman, Wu et al., 2009). On the other hand, it also opens the door to chemically control the ferroelectric polarization (Wang, Fong et al., 2009).

Finally, the family of ferroelectric materials has been targeted as a new generation of exciting heterogeneous catalysts for (electro) chemical reactions involving OER (Hong, Risch et al., 2015; Hwang, Rao Reshma et al., 2017; Wei, Rao et al., 2019; Sun, Alonso et al., 2021; Wang, Adiga et al., 2021; Zhang, Jeerh et al., 2021), and HER since i) some recent works demonstrate the feasibility to use strain to tune the electroactive sites in oxide perovskites for applications in electrocatalysis (Hwang, Feng et al., 2019) and ii) polar materials are known to show specific electrochemical reactivity of their surfaces as a function of the ferroelectric polarization, as depicted in the right panel of Figure 1 (Kalinin, Bonnell et al., 2004; Cordero-Edwards, Rodríguez et al., 2016; Li, Zhao et al., 2017; Domingo, Gaponenko et al., 2019; Tian, Wang et al., 2022). Thus, polarization becomes a switch to control surface chemical activity since the polarization direction (out of plane vs. in plane) modifies the surface strain and the polarization sense (or polarity, changing between up or down) can selectively change the reactions between oxidation and reduction. In this regard, catalysis based on ferroelectrics promises a controllable chemical reaction with boosted efficiency (Wan, Ge et al., 2021). However, the study of catalytic processes on polar surfaces is challenging, and therefore only a few *ab initio* and DFT studies of FE surface chemistry are available (Geneste and Dkhil, 2009; Rakotovelo, Moussounda et al., 2009; Sanna, Hölscher et al., 2012; Li, Wang et al., 2014; Tymińska, Wu et al., 2017). A direct consequence of the tunable surface electrochemistry of polar materials is the fact that polarization becomes a switch to adjust surface catalytic properties, thus opening a door to design and implement catalytic loops enabled by alternating two polarization states, overcoming the Sabatier principle. These catalytic loops could drive reactions that are otherwise impossible to achieve using a fixed substrate. Even though the exploitation of polar materials for switchable surface chemistry has recently been theoretically proposed (Kakekhani and Ismail-Beigi, 2015; Kakekhani, Ismail-Beigi et al., 2016; Efe, Spaldin et al., 2021), there has been no direct experimental verification. Ferroelectric materials, as a subgroup of piezoelectric and pyroelectric materials show spontaneous electric polarization that can be rotated by the application of electric fields but these requires the use of electrodes on the surfaces. It is important to note that since polarization is coupled to strain and temperature fields, it is possible to create polarization by means of mechanical and thermal energy, but these fields cannot switch polarisation between two different ferroelectric states as required for switchable surface chemistry.

2.3 Flexoelectricity to harness mechanical energy

A completely new approach as a renewable source of electrons is the mechanical energy obtained from environmental noise or friction by movement (triboelectricity). In this sense, "piezotronics" has recently emerged as a promising pragmatic area for low power consumption devices, and was proposed as a mechanism to engineer photoelectrochemical (PEC) cells (Yu and Wang, 2018). It exploits the polarization induced in piezoelectric materials under applied forces and thus it is limited to the use of non-centrosymmetric materials. Opposite to this, flexoelectricity is a universal property of materials whereby they generate a polarization and associated (free and structural) charge displacement when subjected to an inhomogeneous deformation such as bending, creating strain gradients. Moreover, the ubiquitous presence of strain gradients compels us to include flexoelectric effects in any serious attempt to understand the fundamental underlying mechanisms behind any mechanical-to-chemical energy conversion process. Flexoelectric effects are expected to be favored in ferroelectric materials due to their high dielectric permittivity, but we have demonstrated that they can also be surprisingly huge in oxide semiconductors with metal electrodes (Narvaez, 2016; Narvaez, Vasquez-Sancho et al., 2016), paving the way to exploit flexoelectricity at the macroscale by the design of the proper heterostructures and interface engineering. Of importance, flexoelectricity strongly couples to ferroelectricity leading to some of the most recent advances in nanoscale ferroelectrics such as the demonstration of flexoelectricity as an effective field for ferroelectric polarization switching (Lu, Bark et al., 2012; Bhaskar, Banerjee et al., 2016).

Recently, there has been a growing interest on the application of 2D and low dimensional materials for catalytic applications due to its huge surface to volume ratio (Wei, Domingo et al., 2022). While most of these materials are centrosymmetric, its characteristic geometry is expected to enable the appearance of huge strain gradients and eventually significant flexoelectric fields. In this regard, some recent studies of flexocatalysis in 2D

TABLE 1 Comparison of the piezocatalysis mechanisms.

	Energy band theory	Screening charge effect
Origin of charges in the catalytic reaction	Material internal charges	External screening charges
Mechanism	Mechanical excitation	Change of polarization
"Piezopotential" role	"Gate" to initiate the reaction by adjusting the band structure and controlling the internal charge carrier flow	Triggers the specific reaction by exceeding the redox potential
Catalytic efficiency	Catalytic capacity determined by the band level, similar to photocatalysis	Catalytic activity determined by piezopotential, similar to electrolysis

centrosymmetric semiconductors already demonstrate the efficiency of this materials to drive redox reactions under ultrasonic stimulation (Wu, Liu et al., 2023).

3 Discussion

3.1 Enhanced efficiency of piezo and ferroelectric materials in catalytic applications

In the last few years, there has been an explosion of experimental studies on the enhanced efficiency of piezoelectric and ferroelectric materials for catalytic applications, mainly in the field of environmental remediation (e.g., organic pollutant decontamination) (Liu, Qi et al., 2023), but also for energy production (Zhang, Xie et al., 2017) from water splitting and CO_2 reduction and materials synthesis (selective growth/deposition and organic synthesis) (Ren, Peng et al., 2023). In all cases, the catalysts are nanoparticles, nanowires or nanoplates/nanosheets and the catalytic activity is accelerated by the use of light and sonication, which is expected to maximize photocatalytic carriers and create polarization induced internal electric fields (piezopotential changes) within the material that play a crucial role in charge separation and transport of free and photo-carriers in these materials. Similar effects are also observed in dye degradation when the solution is subjected to thermal cycling in pyrocatalytic applications (Singh, Sharma et al., 2023). However, while all these experimental works demonstrate the enhanced catalytic efficiency of such combinations in unison, the mechanisms behind piezocatalysis are still under debate and there is a lack of fundamental studies to understand the coupling of induced bulk electric fields and chemical reactions at the interface. Moreover, in most of the cases, the mechanism by which sonication induces piezopotentials in the nanoparticles is speculative and based on simulations. Finally, there is also a sever lack of knowledge of distribution of the different redox active sites within the nanocatalysts, also associated with low understanding of the ferroelectric domain structure of the nanoparticles and nanosheets.

3.2 Energy band theory vs. screening charge effect

Considering that piezoelectric and ferroelectric materials under strain changes transform mechanical energy into a piezopotential, one can find two distinguishable mechanisms in the literature on the piezopotential coupling to catalysis (Wang, Han et al., 2022; Meng, Liu et al., 2023), with its main features summarized in Table 1. The first one, called the "energy band theory" is inspired by photocatalysis, and identifies the piezopotential as a gate to initiate the reaction by adjusting the band structure and controlling the internal charge carrier flow to the catalyst surface to allow the reaction. In this case, the catalytical process uses the material internal charges and the band level determines the catalytic capacity. By contrast, another mechanism called "screening charge effect" can be considered, which emphasizes the critical role of the piezopotential on generating external screening charges in the form of external surface charge adsorbates from external molecules. In this case, the piezopotential should exceed the required Gibbs free energy change to trigger a specific reaction (i.e., reaching the redox potential for the reaction) (Su, Wang et al., 2021) determining the catalytic activity very similar to the process of electrolysis. Also, now the charges participating in the redox reaction are surface adsorbates rather than internal carriers from the material (i.e., there is no charge transfer through the interface) (Dubey, Keat et al., 2022). While experimental works have been able to identify specific chemical compounds participating the overall chemical pathway of the reaction (by using specific blocking agents limiting the catalytic performance), the origin of the involved charge is not yet reasonably explained. Moreover, in some aspects both theories are contradictory, since in the second case the dynamic screening behavior is beneficial for piezocatalyis while the former demonstrates that capacitive current induced by screening phenomena would lead to adverse effects for piezocatalysis.

3.3 Ferroelectric structure at the nanoscale

One of the key elements for the understanding of the role of ferroelectric materials in piezocatalytic and photocatalytic applications is the ferroelectric domain structure of the nanocatalysts units. The most simple approach is to consider that the nanostructures are single crystal domains with a uniform polarization. However, ferroelectric polarization is extremely sensitive to boundary conditions and size effects, and the stability of a single domain can be strongly compromised at the nanoscale in single particles or nanosheets, where the surface to volume ratio is maximized and the strain cannot be tunned with a substrate. Moreover, some theoretical studies of ferroelectric nanoparticle domain configuration predict the formation of complex topological structures such as hopfions (Luk'yanchuk, Tikhonov et al., 2020). In this regard, it is important to take into account the local ferroelectric nanostructure, including the

presence of domain walls and polarization rotation effects, morphotropic phase boundaries and defects manipulation and configuration (Meng, Liu et al., 2023). Functional studies of individual nanoscale entities are scarce and most of the times fall in the limit of spatial resolution. The most common study is based on structural spectroscopies or the change of work function between dark and illumination conditions that points to the appearance of a piezopotential due to photocharge separation. Beyond that, piezoelectric force microscopy and ferroelectric switching spectroscopy measurements are in general doubtful and cannot be extrapolated to the behavior of a single nanoparticles in the solution.

3.4 The effect of mechanical stimulation methods

There are several different mechanical stimulation methods available for catalytic processes, roughly divided into high-frequency ultrasonication, low-frequency shear force or mechanical bending. While the efficiency is typically maximized by ultrasonication at frequencies around 40 kHz, practical implementation of this methodology at the industrial scale is hindered by its high energy input. In these cases, the applied sonication frequency can maximize the piezopotential when it matches the resonance frequency of the nanostructure (You, Wu et al., 2019).

However, the piezoelectric effect in non-centrosymmetric crystalline materials is based on the piezoelectric tensor that correlates the application of a directional strain with the appearance of an electric field. Ultrasonic vibrations create intense pressure by the collapse of cavitation bubbles deforming the catalysts via a periodic external strain. Still, the effect of every single nanocatalytic unit is divers and there are only theoretical simulations available on the predicted piezopotential obtained. In this regard, strain gradients and associated flexoelectric effects cannot be neglected and should be included in the study of piezocatalysis.

Finally, the sonication processes are also known to accelerate the chemical reactions by maximizing the interaction time between reactants (in this case, the external molecules and the piezocatalysts), so it can have an important role in breaking the capacitive double layer and preventing the stabilization of screening charge at the surface of the piezoelectric and ferroelectric materials, thus enhancing the surface reactivity.

3.5 Research gaps and future challenges

Advances for the control and design of better piezocatalysts urgently require a deeper understanding of the underlying mechanism that should take into account the different time scales of all the processes involved in the two cases. In this regard, while the formation of piezoelectric potential and photocarriers can be considered instantaneous, the time constants for the mobility of internal carriers, the activation of different internal and external screening mechanisms, the stabilization of capacitive double layers at the surface of the catalysts and the chemical reaction times should be carefully balanced. In order to delve into a better knowledge of the coupling between internal electric fields and surface chemical reactions it is urgent to develop new characterization tools that allow fundamental studies of this coupling with nanoscale resolution, to correlate functional properties with chemical composition and reaction dynamics. To this end, it is important to control the ferroelectric state of the surface and isolate and identify the active sites of reduction and oxidation paths of the reactions and their local correlation with the polarization, as well as the size effect of the nanostructures on the ferroelectric and piezoelectric configuration. Up to now, pollutant decontamination has probably been the straightforward benchmarking application due to its direct correlation with reduction and oxidation reactions. However, its efficiency for market applications for CO2 reduction or water splitting are still to be demonstrated. Nonetheless, the singular role of piezoelectric and ferroelectric materials in this field is that they open a new paradigm by coupling the chemical reactions with bulk materials functional properties and new ways of energy harvesting. So, while there are evidences of their ability to reduce CO2 and water splitting, more fundamental research needs to be driven in order to enhance their efficiency and make it competitive enough. Only with a better understanding of the associated surface science underlying piezocatalytic and ferrocatalytic processes it will be possible to advance in the prediction, design and improvement of nanomaterials for such applications as well as future advances in biomedical applications (Chen, Zhu et al., 2023; Wang, Zhang et al., 2023).

Author contributions

ND: Conceptualization, Formal Analysis, Investigation, Resources, Validation, Visualization, Writing–original draft.

Funding

The author(s) declare financial support was received for the research, authorship, and/or publication of this article. This work was supported by Center for Nanophase Materials Sciences (CNMS), which is a U.S. Department of Energy, Office of Science User Facility at Oak Ridge National Laboratory.

Licenses and permissions

Conflict of interest

The author ND is an employee of Oak Ridge National Laboratory, managed by UT-Battelle LLC, an M&O contractor for the U.S. Department of Energy.

Publisher's note

References

Bhaskar, U. K., Banerjee, N., Abdollahi, A., Wang, Z., Schlom, D. G., Rijnders, G., et al. (2016). A flexoelectric microelectromechanical system on silicon. *Nat. Nanotechnol.* 11 (3), 263–266. doi:10.1038/nnano.2015.260

Chen, S., Zhu, P., Mao, L., Wu, W., Lin, H., Xu, D., et al. (2023). Piezocatalytic medicine: an emerging frontier using piezoelectric materials for biomedical applications. *Adv. Mater.* 35 (25), 2208256. doi:10.1002/adma.202208256

Cordero-Edwards, K., Rodríguez, L., Calò, A., Esplandiu, M. J., Pérez-Dieste, V., Escudero, C., et al. (2016). Water affinity and surface charging at the z-cut and y-cut LiNbO3 surfaces: an ambient pressure X-ray photoelectron spectroscopy study. *J. Phys. Chem. C* 120 (42), 24048–24055. doi:10.1021/acs.jpcc.6b05465

Domingo, N., Gaponenko, I., Stucki, N., Cordero-Edwards, K., Pérez-Dieste, V., Escudero, C., et al. (2019). Surface charged species and electrochemistry of ferroelectric thin films. *Nanoscale* 11, 17920–17930. doi:10.1039/c9nr05526f

Dubey, A., Keat, C. H., Shvartsman, V. V., Yusenko, K. V., Castillo, M. E., Buzanich, A. G., et al. (2022). Mono-Di-and tri-valent cation doped BiFe0.95Mn0.05O3 nanoparticles: ferroelectric photocatalysts. *Adv. Funct. Mater.* 32 (43), 2207105. doi:10.1002/adfm.202207105

Efe, I., Spaldin, N. A., and Gattinoni, C. (2021). On the happiness of ferroelectric surfaces and its role in water dissociation: the example of bismuth ferrite. *J. Chem. Phys.* 154 (2), 024702. doi:10.1063/5.0033897

Fujishima, A., and Honda, K. (1972). Electrochemical photolysis of water at a semiconductor electrode. *Nature* 238, 37–38. doi:10.1038/238037a0

Geneste, G., and Dkhil, B. (2009). Adsorption and dissociation of H2O on in-plane-polarized BaTiO3 (001) surfaces and their relation to ferroelectricity. *Phys. Rev. B* 79 (23), 235420. doi:10.1103/physrevb.79.235420

Gruverman, A., Wu, D., Lu, H., Wang, Y., Jang, H. W., Folkman, C. M., et al. (2009). Tunneling electroresistance effect in ferroelectric tunnel junctions at the nanoscale. *Nano Lett.* 9 (10), 3539–3543. doi:10.1021/nl901754t

Guo, R., Wang, Y., Yoong, H. Y., Chai, J., Wang, H., Lin, W., et al. (2017). Effect of extrinsically introduced passive interface layer on the performance of ferroelectric tunnel junctions. *ACS Appl. Mater. Interfaces* 9 (6), 5050–5055. doi:10.1021/acsami.6b15564

Hong, W. T., Risch, M., Stoerzinger, K. A., Grimaud, A., Suntivich, J., and Shao-Horn, Y. (2015). Toward the rational design of non-precious transition metal oxides for oxygen electrocatalysis. *Energy & Environ. Sci.* 8 (5), 1404–1427. doi:10.1039/c4ee03869j

Hwang, J., Feng, Z., Charles, N., Wang, X. R., Lee, D., Stoerzinger, K. A., et al. (2019). Tuning perovskite oxides by strain: electronic structure, properties, and functions in (electro)catalysis and ferroelectricity. *Mater. Today* 31, 100–118. doi:10.1016/j.mattod.2019.03.014

Hwang, J., Rao Reshma, R., Giordano, L., Katayama, Y., Yu, Y., and Shao-Horn, Y. (2017). Perovskites in catalysis and electrocatalysis. *Science* 358 (6364), 751–756. doi:10.1126/science.aam7092

Kakekhani, A., and Ismail-Beigi, S. (2015). Ferroelectric-based catalysis: switchable surface chemistry. *ACS Catal.* 5 (8), 4537–4545. doi:10.1021/acscatal.5b00507

Kakekhani, A., and Ismail-Beigi, S. (2016). Ferroelectric oxide surface chemistry: water splitting via pyroelectricity. *J. Mater. Chem. A* 4 (14), 5235–5246. doi:10.1039/c6ta00513f

Kakekhani, A., Ismail-Beigi, S., and Altman, E. I. (2016). Ferroelectrics: a pathway to switchable surface chemistry and catalysis. *Surf. Sci.* 650, 302–316. doi:10.1016/j.susc.2015.10.055

Kalinin, S. V., Bonnell, D. A., Alvarez, T., Lei, X., Hu, Z., Shao, R., et al. (2004). Ferroelectric lithography of multicomponent nanostructures. *Adv. Mater.* 16 (9-10), 795–799. doi:10.1002/adma.200305702

Kim, S., Nguyen, N., and Bark, C. (2018). Ferroelectric materials: a novel pathway for efficient solar water splitting. *Appl. Sci.* 8 (9), 1526. doi:10.3390/app8091526

Lampimäki, M., Schreiber, S., Zelenay, V., Křepelová, A., Birrer, M., Axnanda, S., et al. (2015). Exploring the environmental photochemistry on the TiO2(110) surface *in situ* by near ambient pressure X-ray photoelectron spectroscopy. *J. Phys. Chem. C* 119 (13), 7076–7085. doi:10.1021/jp511340n

Lee, H., Kim, T. H., Patzner, J. J., Lu, H., Lee, J.-W., Zhou, H., et al. (2016). Imprint control of BaTiO3 thin films via chemically induced surface polarization pinning. *Nano Lett.* 16 (4), 2400–2406. doi:10.1021/acs.nanolett.5b05188

Li, R., Zhao, Y., and Li, C. (2017). Spatial distribution of active sites on a ferroelectric PbTiO3 photocatalyst for photocatalytic hydrogen production. *Faraday Discuss.* 198 (0), 463–472. doi:10.1039/c6fd00199h

Li, X., Wang, B., Zhang, T.-Y., and Su, Y. (2014). Water adsorption and dissociation on BaTiO3 single-crystal surfaces. *J. Phys. Chem. C* 118 (29), 15910–15918. doi:10.1021/jp5051386

Li, Y., Li, J., Yang, W., and Wang, X. (2020). Implementation of ferroelectric materials in photocatalytic and photoelectrochemical water splitting. *Nanoscale Horizons* 5 (8), 1174–1187. doi:10.1039/d0nh00219d

Liang, Z., Yan, C.-F., Rtimi, S., and Bandara, J. (2019). Piezoelectric materials for catalytic/photocatalytic removal of pollutants: recent advances and outlook. *Appl. Catal. B Environ.* 241, 256–269. doi:10.1016/j.apcatb.2018.09.028

Liu, J., Qi, W., Xu, M., Thomas, T., Liu, S., and Yang, M. (2023). Piezocatalytic techniques in environmental remediation. *Angew. Chem. Int. Ed.* 62 (5), e202213927. doi:10.1002/anie.202213927

Lu, H., Bark, C. W., Esque de los Ojos, D., Alcala, J., Eom, C. B., Catalan, G., et al. (2012). Mechanical writing of ferroelectric polarization. *Science* 336 (6077), 59–61. doi:10.1126/science.1218693

Lu, H., Lipatov, A., Ryu, S., Kim, D. J., Lee, H., Zhuravlev, M. Y., et al. (2014). Ferroelectric tunnel junctions with graphene electrodes. *Nat. Commun.* 5, 5518. doi:10.1038/ncomms6518

Luk'yanchuk, I., Tikhonov, Y., Razumnaya, A., and Vinokur, V. M. (2020). Hopfions emerge in ferroelectrics. *Nat. Commun.* 11 (1), 2433. doi:10.1038/s41467-020-16258-w

Man, I. C., Su, H.-Y., Calle-Vallejo, F., Hansen, H. A., Martínez, J. I., Inoglu, N. G., et al. (2011). Universality in oxygen evolution electrocatalysis on oxide surfaces. *ChemCatChem* 3 (7), 1159–1165. doi:10.1002/cctc.201000397

Medford, A. J., Vojvodic, A., Hummelshøj, J. S., Voss, J., Abild-Pedersen, F., Studt, F., et al. (2015). From the Sabatier principle to a predictive theory of transition-metal heterogeneous catalysis. *J. Catal.* 328, 36–42. doi:10.1016/j.jcat.2014.12.033

Meng, N., Liu, W., Jiang, R., Zhang, Y., Dunn, S., Wu, J., et al. (2023). Fundamentals, advances and perspectives of piezocatalysis: a marriage of solid-state physics and catalytic chemistry. *Prog. Mater. Sci.* 138, 101161. doi:10.1016/j.pmatsci.2023.101161

Mushtaq, F., Chen, X., Hoop, M., Torlakcik, H., Pellicer, E., Sort, J., et al. (2018). Piezoelectrically enhanced photocatalysis with BiFeO3 nanostructures for efficient water remediation. *iScience* 4, 236–246. doi:10.1016/j.isci.2018.06.003

Narvaez, J. (2016). Bellaterra, Spain. Universitat Autònoma de Barcelona, *Flexoelectricity in single crystals*

Narvaez, J., Vasquez-Sancho, F., and Catalan, G. (2016). Enhanced flexoelectric-like response in oxide semiconductors. *Nature* 538 (7624), 219–221. doi:10.1038/nature19761

Rakotovelo, G., Moussounda, P. S., Haroun, M. F., Légaré, P., Rakotomahevitra, A., Rakotomalala, M., et al. (2009). Adsorption of CO, CO2 and NO molecules on a BaTiO3 (001) surface. *Surf. Sci.* 603 (9), 1221–1228. doi:10.1016/j.susc.2009.03.006

Ren, Z., Peng, Y., He, H., Ding, C., Wang, J., Wang, Z., et al. (2023). Piezoelectrically mediated reactions: from catalytic reactions to organic transformations. *Chin. J. Chem.* 41 (1), 111–128. doi:10.1002/cjoc.202200443

Sanna, S., Hölscher, R., and Schmidt, W. G. (2012). Polarization-dependent water adsorption on the LiNbO3 (0001) surface. *Phys. Rev. B* 86 (20), 205407. doi:10.1103/physrevb.86.205407

Segura, J. J., Domingo, N., Fraxedas, J., and Verdaguer, A. (2013). Surface screening of written ferroelectric domains in ambient conditions. *J. Appl. Phys.* 113 (18), 187213. doi:10.1063/1.4801983

Sergei, V. K., Yunseok, K., Dillon, D. F., and Anna, N. M. (2018). Surface-screening mechanisms in ferroelectric thin films and their effect on polarization dynamics and domain structures. *Rep. Prog. Phys.* 81 (3), 036502. doi:10.1088/1361-6633/aa915a

Singh, G., Sharma, M., Sharma, J. D., Kumar, S., and Vaish, R. (2023). Ferroelectric ceramics for pyrocatalytic applications. *Prog. Solid State Chem.* 72, 100428. doi:10.1016/j.progsolidstchem.2023.100428

Spasojevic, I., Verdaguer, A., Catalan, G., and Domingo, N. (2022). Effect of humidity on the writing speed and domain wall dynamics of ferroelectric domains. *Adv. Electron. Mater.* 8 (6), 2100650. doi:10.1002/aelm.202100650

Starr, M. B., and Wang, X. (2013). Fundamental Analysis of piezocatalysis process on the surfaces of strained piezoelectric materials. *Sci. Rep.* 3, 2160. doi:10.1038/srep02160

Starr, M. B., and Wang, X. (2015). Coupling of piezoelectric effect with electrochemical processes. *Nano Energy* 14, 296–311. doi:10.1016/j.nanoen.2015.01.035

Su, R., Wang, Z., Zhu, L., Pan, Y., Zhang, D., Wen, H., et al. (2021). Strain-engineered nano-ferroelectrics for high-efficiency piezocatalytic overall water splitting. *Angew. Chem. Int. Ed.* 60 (29), 16019–16026. doi:10.1002/anie.202103112

Sun, C., Alonso, J. A., and Bian, J. (2021). Recent advances in perovskite-type oxides for energy conversion and storage applications. *Adv. Energy Mater.* 11 (2). doi:10.1002/aenm.202000459

Tian, Y., Wang, A., Wei, Y., Pei, M., Cao, R., Gu, Z., et al. (2022). Large-area printing of ferroelectric surface and super-domain for solar water splitting. *Adv. Funct. Mater.* 32, 2111180. doi:10.1002/adfm.202111180

Tymińska, N., Wu, G., and Dupuis, M. (2017). Water oxidation on oxygen-deficient barium titanate: a first-principles study. *J. Phys. Chem. C* 121 (15), 8378–8389. doi:10.1021/acs.jpcc.6b12425

Wan, T. L., Ge, L., Pan, Y., Yuan, Q., Liu, L., Sarina, S., et al. (2021). Catalysis based on ferroelectrics: controllable chemical reaction with boosted efficiency. *Nanoscale* 13 (15), 7096–7107. doi:10.1039/d1nr00847a

Wang, K., Han, C., Li, J., Qiu, J., Sunarso, J., and Liu, S. (2022). The mechanism of piezocatalysis: energy band theory or screening charge effect? *Angew. Chem. Int. Ed.* 61 (6), e202110429. doi:10.1002/anie.202110429

Wang, L., Adiga, P., Zhao, J., Samarakoon, W. S., Stoerzinger, K. A., Spurgeon, S. R., et al. (2021). Understanding the electronic structure evolution of epitaxial $LaNi_{1-x}Fe_xO_3$ thin films for water oxidation. *Nano Lett.* 21 (19), 8324–8331. doi:10.1021/acs.nanolett.1c02901

Wang, L., Zhang, S., Zhang, Y., and An, Q. (2023). Piezodynamic therapy: mechanisms and biomedical applications. *Nano Energy* 110, 108342. doi:10.1016/j.nanoen.2023.108342

Wang, R. V., Fong, D. D., Jiang, F., Highland, M. J., Fuoss, P. H., Thompson, C., et al. (2009). Reversible chemical switching of a ferroelectric film. *Phys. Rev. Lett.* 102 (4), 047601. doi:10.1103/physrevlett.102.047601

Wang, Z. L., and Song, J. (2006). Piezoelectric nanogenerators based on zinc oxide nanowire arrays. *Science* 312 (5771), 242–246. doi:10.1126/science.1124005

Wei, C., Rao, R. R., Peng, J., Huang, B., Stephens, I. E. L., Risch, M., et al. (2019). Recommended practices and benchmark activity for hydrogen and oxygen electrocatalysis in water splitting and fuel cells. *Adv. Mater.* 31 (31), 1806296. doi:10.1002/adma.201806296

Wei, X.-K., Domingo, N., Sun, Y., Balke, N., Dunin-Borkowski, R. E., and Mayer, J. (2022). Progress on emerging ferroelectric materials for energy harvesting, storage and conversion. *Adv. Energy Mater.* 12, 2201199. doi:10.1002/aenm.202201199

Wei, X.-K., Domingo, N., Sun, Y., Balke, N., Dunin-Borkowski, R. E., and Mayer, J. (2022). Progress on emerging ferroelectric materials for energy harvesting, storage and conversion. *Adv. Energy Mater.* 2022, 01199. doi:10.1002/aenm.202201199

Wu, J., Mao, W., Wu, Z., Xu, X., You, H., Xue, A. X., et al. (2016). Strong pyro-catalysis of pyroelectric BiFeO3 nanoparticles under a room-temperature cold–hot alternation. *Nanoscale* 8 (13), 7343–7350. doi:10.1039/c6nr00972g

Wu, J., Qin, N., and Bao, D. (2018). Effective enhancement of piezocatalytic activity of BaTiO3 nanowires under ultrasonic vibration. *Nano Energy* 45, 44–51. doi:10.1016/j.nanoen.2017.12.034

Wu, T., Liu, K., Liu, S., Feng, X., Wang, X., Wang, L., et al. (2023). Highly efficient flexocatalysis of two-dimensional semiconductors. *Adv. Mater.* 35 (3), 2208121. doi:10.1002/adma.202208121

Yang, S. M., Morozovska, A. N., Kumar, R., Eliseev, E. A., Cao, Y., Mazet, L., et al. (2017). Mixed electrochemical-ferroelectric states in nanoscale ferroelectrics. *Nat. Phys.* 13, 812–818. doi:10.1038/nphys4103

You, H., Wu, Z., Zhang, L., Ying, Y., Liu, Y., Fei, L., et al. (2019). Harvesting the vibration energy of BiFeO3 nanosheets for hydrogen evolution. *Angew. Chem. Int. Ed.* 58 (34), 11779–11784. doi:10.1002/anie.201906181

Yu, D., Liu, Z., Zhang, J., Li, S., Zhao, Z., Zhu, L., et al. (2019). Enhanced catalytic performance by multi-field coupling in KNbO3 nanostructures: piezo-photocatalytic and ferro-photoelectrochemical effects. *Nano Energy* 58, 695–705. doi:10.1016/j.nanoen.2019.01.095

Yu, Y., and Wang, X. (2018). Piezotronics in photo-electrochemistry. *Adv. Mater.* 30 (43), 1800154. doi:10.1002/adma.201800154

Zhang, M., Jeerh, G., Zou, P., Lan, R., Wang, M., Wang, H., et al. (2021). Recent development of perovskite oxide-based electrocatalysts and their applications in low to intermediate temperature electrochemical devices. *Mater. Today* 49, 351–377. doi:10.1016/j.mattod.2021.05.004

Zhang, Y., Xie, M., Adamaki, V., Khanbareh, H., and Bowen, C. R. (2017). Control of electro-chemical processes using energy harvesting materials and devices. *Chem. Soc. Rev.* 46 (24), 7757–7786. doi:10.1039/c7cs00387k

Zhao, W.-N., and Liu, Z.-P. (2014). Mechanism and active site of photocatalytic water splitting on titania in aqueous surroundings. *Chem. Sci.* 5 (6), 2256–2264. doi:10.1039/c3sc53385a

frontiers | Frontiers in Nanotechnology

TYPE Original Research
PUBLISHED 04 April 2024
DOI 10.3389/fnano.2024.1366542

OPEN ACCESS

EDITED BY
Neha Kaushik,
University of Suwon, Republic of Korea

REVIEWED BY
Rita Rizzoli,
CNR—Institute for Microelectronics and Microsystems (IMM), Italy
Carla Bittencourt,
University of Mons, Belgium

*CORRESPONDENCE
Petra Rudolf,
p.rudolf@rug.nl

RECEIVED 06 January 2024
ACCEPTED 11 March 2024
PUBLISHED 04 April 2024

CITATION
Zehra T, Syari'ati A, Ivashenko O, Bignardi L, Van Dorp WF, De Hosson JTM and Rudolf P (2024), Graphene growth from photo-polymerized bi-phenylthiol self-assembled monolayers.
Front. Nanotechnol. 6:1366542.
doi: 10.3389/fnano.2024.1366542

Graphene growth from photo-polymerized bi-phenylthiol self-assembled monolayers

Tashfeen Zehra, Ali Syari'ati, Oleksii Ivashenko, Luca Bignardi, Willem F. Van Dorp, Jeff T. M. De Hosson and Petra Rudolf*

Zernike Institute for Advanced Materials, University of Groningen, Groningen, Netherlands

We present an enhanced methodology for the synthesis of graphene, from photo-polymerized self-assembled monolayers (SAMs) of 1,1′-biphenyl-4-thiol on both electropolished and oxidized copper substrates. The SAMs were subjected to a two-step process involving light-induced polymerization followed by annealing in a vacuum furnace to yield the two-dimensional solid. Comprehensive characterization using contact angle measurements, X-ray photoelectron spectroscopy, and Raman spectroscopy, as well as scanning electron and transmission electron microscopy, provided conclusive evidence of growth of single-layer graphene. Notably, our findings revealed superior quality graphene on oxidized copper substrates compared to their electropolished counterparts, highlighting the impact of substrate choice on the quality of the resultant material.

KEYWORDS

graphene growth, bi-phenylthiol, self-assembled monolayers, photopolymerization, X-ray photoelectron spectroscopy, Raman spectroscopy, transmission electron microscopy, contact angle measurements

1 Introduction

Graphene has surprised the scientific community because never before a single material was found to exhibit such a plethora of extraordinary properties (Novoselov et al., 2013; Akinwande et al., 2017), making it an unparalleled candidate for a diverse range of applications, including in electronics, sensors, and coatings (Novoselov et al., 2004; Novoselov et al., 2005; Zhang et al., 2005; Berger et al., 2004; Wang et al., 2008). As a consequence, numerous synthesis techniques have emerged in recent years, encompassing methods such as chemical exfoliation of graphite, reduction of graphite oxide, thermal graphitization of silicon carbide, and chemical vapor deposition (CVD) growth on metallic substrates (Dikin et al., 2007; Gilje et al., 2007; Emtsev et al., 2009; Li et al., 2009; Bae et al., 2010; Gengler et al., 2010; Batzill, 2012). One method that has received relatively modest attention is the growth of graphene from self-assembled monolayers (SAMs) (Turchanin et al., 2011; Rhinow et al., 2012; Angelova et al., 2013; Matei et al., 2013), even though it is relatively simple and easily upscalable. Growing graphene from self-assembled monolayers has the advantage that an SAM comprises a well-defined amount of carbon, and with the right choice of molecules, the thickness is controllable from single-layer to few-layer (FL) graphene. Previous work by Turchanin et al. (2011); Rhinow et al. (2012); Angelova et al. (2013); Matei et al. (2013) demonstrated the successful generation of graphene from a 1,1′-biphenyl-4-thiol (BPT) SAM, first polymerized through electron irradiation in ultrahigh vacuum (UHV~10^{-10} mbar) and then heated to approximately 1,273 K to transform the

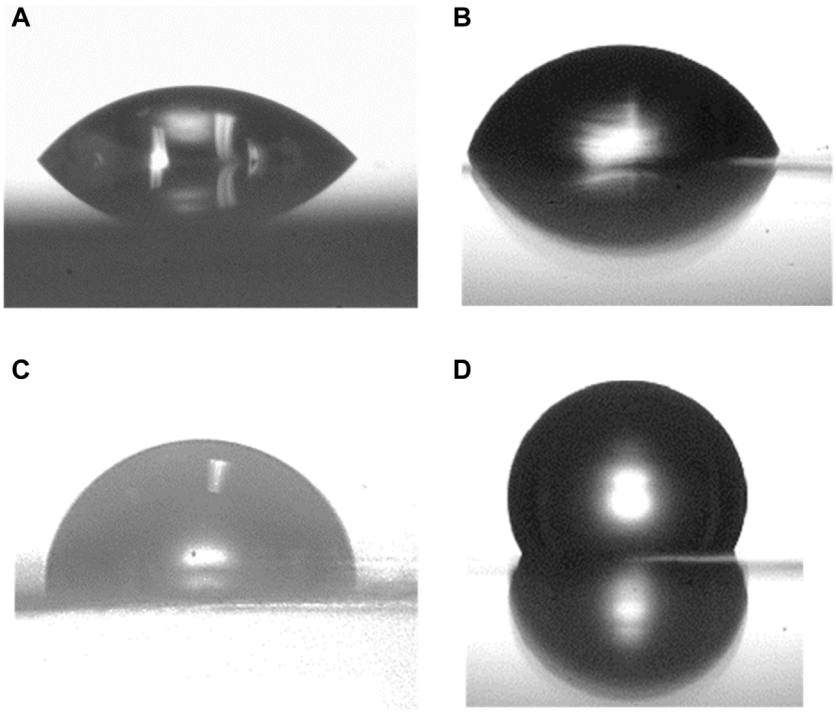

FIGURE 1
Water contact angle measured on electropolished copper foil **(A)**, **(C)** and oxidized **(B)**, **(D)** Cu substrates before and after self-assembly of a BPT monolayer.

cross-linked molecules into a continuous honeycomb sheet. Of particular significance is the polymerization step, as 1,1′-biphenyl-4-thiol desorbs at 400 K (Matei et al., 2013), but graphene production requires higher temperatures. By increasing the molecular weight through cross-linking, the precursor is found to remain on the surface for further processing. Experiments on Au (Turchanin et al., 2011) revealed that the resulting graphene was nano-crystalline, but those on Cu revealed that domains spanning several micrometers were formed (Matei et al., 2013).

Motivated by these promising results, we explored a more straightforward method that eliminates, in principle, the need for ultrahigh vacuum, rendering it a cost-effective alternative. In our approach, SAM molecules are polymerized using light, and a high-vacuum oven is employed for subsequent transformation into graphene. We prove that light-induced polymerization is equally successful as electron beam-induced polymerization and demonstrate micrometer-sized domains on oxidized Cu. Although our experiments were performed in ultrahigh vacuum for polymerization, this approach does not necessitate such stringent vacuum conditions (contrary to electron beam irradiation) for graphene production from adsorbed molecules and may open the door to the production of BN-doped graphene (Belser et al., 2023) with larger domain sizes and on insulating surfaces.

2 Experimental details

The two types of substrates used in these experiments were polycrystalline copper foils (thickness 25 µm, 99.99% purity, Goodfellow) either left with their native oxide or cleaned by electropolishing before assembling the 1,1′-biphenyl-4-thiol (BPT) monolayer. For electropolishing, the copper foils, connected to the positive terminal of the power supply (E0300-0.1-L, Delta Elektronika), were immersed in the electrolyte (copper foil as the anode), an aqueous solution (2:1:1) of phosphoric acid (85 wt% in H_2O, Sigma-Aldrich) and acetic acid (99%, Sigma-Aldrich). After 5 min of 2.5 V applied to the system, the surface oxide dissolved in the electrolyte. A hydrogen reduction reaction took place at the cathode. After electropolishing, the surface was smooth and showed no more traces of oxide, as confirmed by X-ray photoelectron spectroscopy (XPS). The electropolished foils were thoroughly rinsed with Milli-Q water, ethanol, and chloroform before immersion in the BPT solution. Copper foils covered by the native oxide were thoroughly rinsed with ethanol and chloroform before immersion in the BPT solution. We refer to these substrates as electropolished and oxidized copper in the following sections.

Monolayers of 1,1′-biphenyl-4-thiol (97%, Sigma-Aldrich) were prepared by self-assembly from a 0.5 mM solution of chloroform (≥99.0% purity, Lab-Scan) by immersing the substrates for 24 h in the dark, at room temperature. After surface functionalization, the substrates were rinsed with chloroform, thoroughly dried with an argon gas stream (5.0 purity, Linde), and used for contact angle measurements or introduced immediately into the UHV system (base pressure ~9×10^{-10} mbar). There, the SAMs were first characterized by XPS and then irradiated using a commercial He-I discharge lamp (HIS-13, Omicron Focus, photon energy 21.22 eV), operating at a pressure of ~10^{-8} mbar, to induce polymerization. After polymerization, the samples were transferred to a vacuum furnace (EHA 12/150B, Carbolite Gero), operating at a base pressure of ~10^{-5} mbar, where they were annealed at 1,100 K to induce graphene growth.

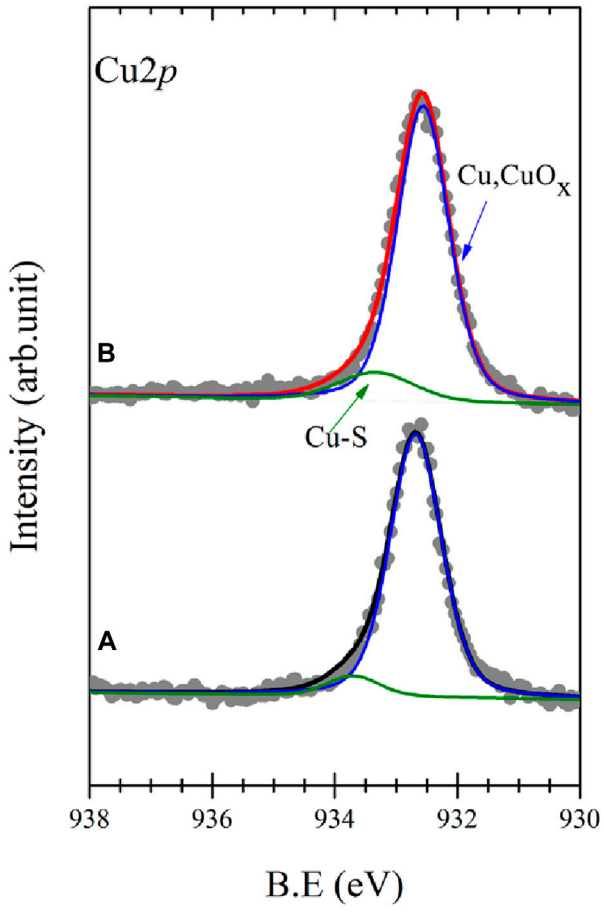

FIGURE 2
XPS spectra of the Cu2$p_{3/2}$ core level region of a self-assembled monolayer of BPT on electropolished **(A)** and oxidized copper **(B)**; raw data (●) and fit (—).

Contact angle (CA) measurements were made with a homemade microscope–goniometer setup, first on the bare substrates and then again after assembling the SAMs. A 2-μL drop of Milli-Q water was used as the measuring liquid (sessile drop method) (Mittal, 2003). A total of five to seven spots on each sample were measured, and the contact angle was averaged. Analysis was done by applying a baseline and an elliptical curve fitting of the water–air contact profile. The uncertainty in the measurements is ± 2°. XPS spectra were collected by employing a monochromatic Al K_α X-ray source ($h\nu$ = 1486.6 eV) and a hemispherical electron analyzer (Scienta R4000) at a base pressure of ~9×10^{-10} mbar. The X-rays illuminated the whole width of the sample; the overall experimental resolution was 0.4 eV. XPS spectra analysis was done using the least squares curve fitting program WinSpec developed at the LISE, University of Namur, Belgium, and included a Shirley baseline subtraction and a peak deconvolution using a linear combination of Gaussian and Lorentzian functions, taking into account the experimental resolution. The spectra were fitted with a minimum number of peaks consistent with the structure of the molecules on the surface. Binding energies of isolated peaks are given at ±0.05 eV; when more than one component was needed to reproduce the raw data, the error in the component position was ±0.1 eV. The uncertainties in the intensity determinations were approximately 1%. All measurements were taken on freshly prepared samples; three samples were measured in each case to check for reproducibility. Raman spectra in the range of 500–3,000 cm^{-1} were collected with an Olympus BX51 microscope fiber-coupled to an Andor Technology DU416A-LDC-DD camera coupled to a Shamrock 163 spectrograph, and 500 L/mm blazed grating was carried out at 750 nm. A HeNe laser (Thorlabs, random polarization) with a wavelength of 632.8 nm was used; the laser power was 9 mW and the focus spot measured 2 μm. Each spectrum was the average of 40 scans (0.5 s per scan) collected at 4 cm^{-1} resolution. Spectra were collected at five different spots of each sample to check for homogeneity. Transmission electron microscopy (TEM) images were acquired with a JEOL 2010F TEM, equipped with a field emission gun and operated at 200 keV. TEM images in the bright field mode and diffraction patterns were collected with a Gatan CCD camera. Scanning electron microscopy (SEM) analysis was performed using a JEOL JSM-7000F microscope equipped with a field emission source operated at 5 kV. Other SEM images (suspended graphene on TEM grids) were collected using a Philips XL30S microscope equipped with a field emission source operated at 5 kV.

3 Results and discussion

Contact angle measurements provided initial information on the quality of the self-assembled monolayers of BPT on electropolished and oxidized copper. The wetting properties of the sample's surface change when the surface is functionalized. In a well-ordered SAM, the exposed part of the BPT is hydrophobic; therefore, a higher CA is expected for functionalized surfaces. The contact angle of the bare electropolished Cu substrate (Figure 1A) is (40 ± 2)°, while, as seen in Figure 1C, that of the BPT-functionalized surface is (96 ± 2)°, *i.e.*, higher, as anticipated.

The oxidized substrates showed a similar result, as seen from the comparison of Figures 1B, D): the BPT-functionalized oxidized Cu exhibits a CA of (114 ± 2)°, which is higher than that observed for the substrate prior to functionalization (76 ± 2)°. The difference in the contact angle between the BPT SAMs on electropolished and oxidized Cu depends on the intermolecular forces between molecules. In fact, Ron et al. (1998) and Laibinis and Whitesides (1992) reported that lower CA values are indicative of less densely packed SAMs. Consequently, our results suggest a more closely packed arrangement of the SAMs on the oxidized Cu surface.

Our observations for the bare oxidized substrate align with those of Gottardi et al. (2015), who oxidized Cu (111) in air and identified the formed oxide phase as Cu_2O. Indeed, the contact angle determined for the bare oxidized surface is consistent with that (70 ± 2)° reported by Cabrita et al. (2010) for Cu_2O, while these authors also found that the CAs for oxides like CuO and CuO/Cu(OH) are smaller. Hence, based on the value of the contact angle, we deduce that the oxide phase present in copper in our studies is primarily Cu_2O.

To corroborate the structural integrity of the BPT molecules in the SAMs, X-ray photoelectron spectroscopy (XPS) was carried out. Figures 2A, B display the Cu2$p_{3/2}$ core level region for a pristine BPT SAM on electropolished and oxidized surfaces, respectively. Two components are discernible in these spectra: the main component at 932.7 eV and a shoulder attributable to Cu bound to S at 933.5 eV. Concerning the former, we note that since both Cu and Cu_2O exhibit a main component at this same binding energy (Ron et al., 1998), a precise differentiation between these oxidation

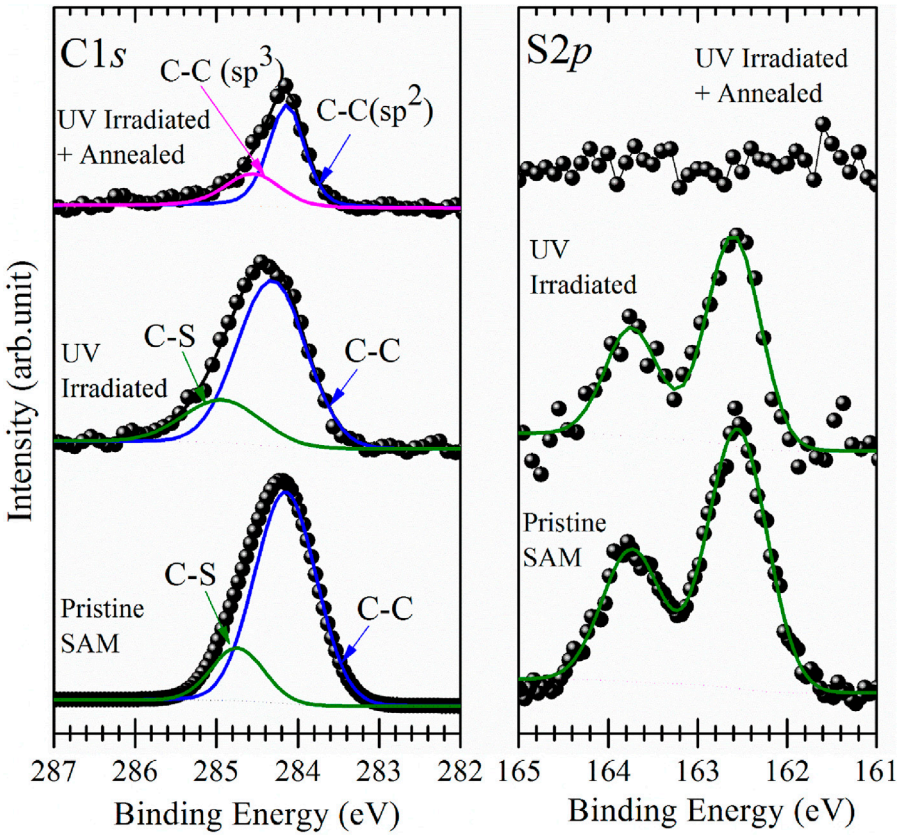

FIGURE 3
XPS spectra of the C1*s* (left panel) and S2*p* (right panel) core level regions of self-assembled monolayers of BPT on electropolished copper foil as prepared (bottom), after irradiation with UV light for 6 h, and after annealing to 1,100 K; raw data (●) and fit (—).

states proves challenging. However, for oxidized copper (Figure 2B), the main component displays a slightly larger full width at half maximum (FWHM)—0.67 eV for oxidized and 0.6 eV for electropolished Cu—and a wider scan of the Cu2*p* core level region (Supplementary Figure S1) also shows a small satellite peak at around 945 eV in binding energy. Both the higher FWHM and the presence of the small satellite peak are characteristic of Cu_2O, consistent with the contact angle measurements. The fact that a component due to Cu-S bonds can be discerned, points to the formation of thiolates.

Figures 3, 4 display the C1*s* (left panels) and S2*p* (right panels) spectra for BPT self-assembled monolayers on electropolished and oxidized copper as prepared, after photopolymerization and after annealing.

For the as-prepared BPT SAM on electropolished copper, the C1*s* photoemission line (Figure 3, left panel, bottom spectrum) exhibits a main component at a binding energy of 284.2 eV, attributed to the aromatic carbon of the biphenyl rings, and a smaller component due to the C-S bonds at 284.8 eV (Matei et al., 2013). Remarkably, the C1*s* spectrum for the as-prepared BPT SAM on oxidized copper (Figure 4, left panel, bottom spectrum) is nearly identical, with the main component at a BE of 284.3 eV and the smaller component due to C-S bonds at 284.9 eV. The S2*p* intensity peaks are at 162.5 eV (Figure 3, right panel) for the BPT SAM on electropolished copper and at 162.6 eV (Figure 4, right panel) for the BPT-SAM on oxidized copper, indicating the formation of thiolates (Laibinis et al., 1991) in both cases. Notably, no evidence for oxidized sulfur or metal sulfides was found at higher binding energies, confirming the structural integrity of the BPT molecules on both surfaces.

If the SAM is well-packed, the photoelectrons from the S atoms will be attenuated when passing through the biphenyl layer. To evaluate the attenuation of these photoelectrons, we calculated the intensity ratio I_{C1s}/I_{S2p} for both BPT SAMS and found I_{C1s}/I_{S2p} = 9:1 for the one on electropolished Cu and I_{C1s}/I_{S2p} = 8:1 for that on oxidized Cu. The lower ratio observed for the latter suggests that S2*p* photoelectrons experience less attenuation by the SAM, indicating a configuration where the molecules are more inclined toward the substrate surface because the adsorption sites are farther apart, and the biphenyl layer is, therefore, thinner. Such a scenario has been observed for oxidized Cu(111), where the oxide is arranged in a distorted Cu(100)-($\sqrt{2}$x$\sqrt{2}$)R45° superstructure (Gottardi et al., 2015). Although the surfaces are polycrystalline in the present case (*vide infra*), it is reasonable to infer that the distinct I_{C1s}/I_{S2p} ratios arise from a different packing of BPT on the two surfaces. The XPS results, therefore, support the successful deposition of well-organized SAMs on both substrates, as corroborated by the contact angle measurements.

Following self-assembly and XPS characterization, the SAMs were polymerized with UV light. The polymerization step is needed to prevent desorption of individual BPTs from the surface during annealing (Matei et al., 2013), the essential step for the transformation of the SAM into graphene. To find out the

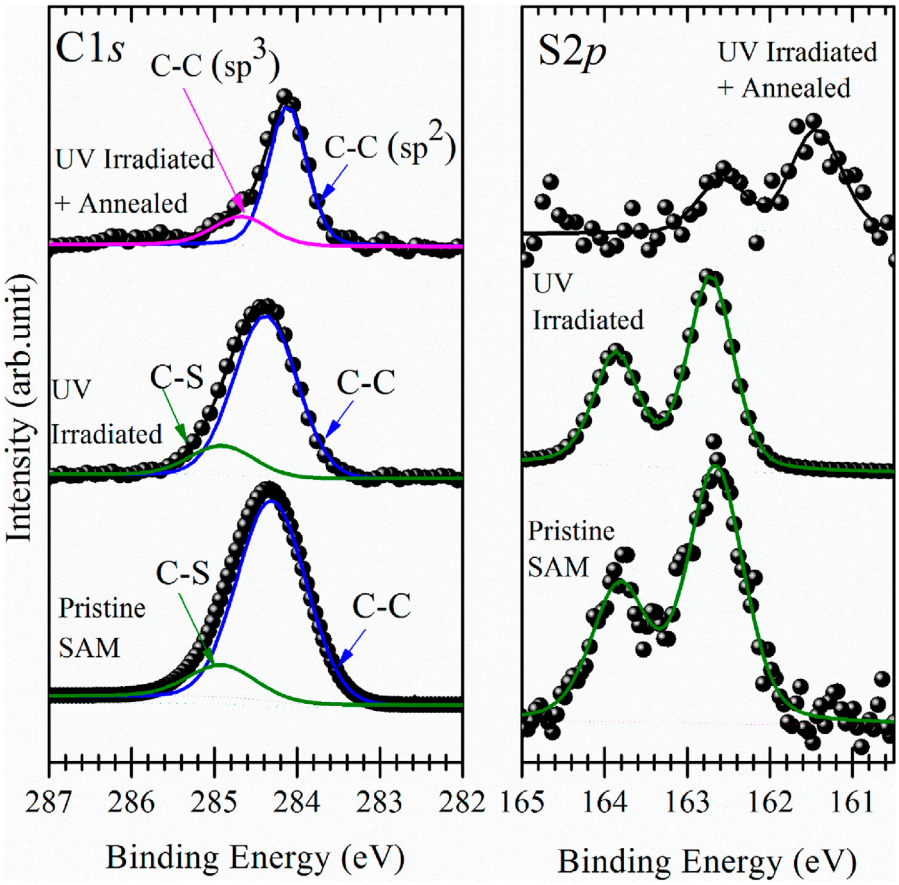

FIGURE 4
XPS spectra of the C1*s* (left panel) and S2*p* (right panel) core level regions of self-assembled monolayers of BPT on oxidized copper foil as prepared (bottom), after irradiation with UV light for 6 h, and after annealing to 1,100 K; raw data (●) and fit (—).

optimal irradiation time, the samples were exposed to UV light (He I = 21.22 eV) for durations ranging from 1 to 12 h.

Pristine BPT SAMs and UV-irradiated (polymerized) samples show no major differences in the C1*s* and S2*p* spectra presented in Figures 3, 4. Since UV light causes emission of secondary electrons, it is reasonable to assume that the same effects as observed for electron beam irradiation occur (Turchanin et al., 2009; Yildirim et al., 2017), namely, dehydrogenation and cross-linking of the phenyl rings in such a way that they maintain their aromatic structure. For both substrates, the main C1*s* component shifted to a slightly higher BE (0.2 eV for the SAM on electropolished and 0.1 eV for the SAM on oxidized Cu foil). The decrease in the S2*p* spectral intensity, and hence in the amount of sulfur, was negligible after polymerization, and like for the C1*s* photoemission line, we saw a small shift (0.1 eV) of the S2*p* line to a higher BE after UV irradiation.

After photopolymerization, each SAM was subjected to annealing at 1,100 K. Thereafter, the carbon remaining on the surface was assessed using XPS as a function of UV irradiation time, as depicted in Figure 5 for the SAM on electropolished Cu. Notably, the sample that remained unexposed to light experienced nearly complete carbon loss during annealing. For samples irradiated for 2 or 4 h, an 80% decrease in the C1*s* intensity indicated incomplete polymerization of the SAM after 4 h of irradiation. Longer irradiation times (5–12 h) resulted in approximately 35% of the initial carbon remaining on the surface after annealing. This percentage closely aligns with the 30% reported by Matei et al. (2013) after electron-induced polymerization followed by annealing. Given that irradiation times exceeding 6 h did not yield a difference in the resulting carbon coverage, 6 h of irradiation was deemed sufficient.

The top curves in Figures 3, 4 present the C1*s* and S2*p* XPS spectra collected after annealing of the polymerized SAMs. While the amount of carbon on the surface did not change with polymerization, for the annealed samples, a loss of C was evident. To estimate the changes in carbon intensities, we used the ratio of the C and Cu XPS signals I_{C1s}/I_{Cu2p}. For the sample on oxidized Cu, a value of 0.98 was found. For reference purposes, we also prepared graphene on electropolished Cu by chemical vapor deposition (CVD), following the procedure described in Gottardi et al. (2015), which yields a single layer of graphene, and found an intensity ratio I_{C1s}/I_{Cu2p} of 0.97 for this sample. Since the Cu intensity is attenuated by the oxide on oxidized Cu, we can conclude that there is slightly more than a single layer of carbon on the oxidized Cu surface after annealing the polymerized BPT SAM. In contrast, for BPT molecules on electropolished copper foils, after polymerization and annealing, the I_{C1s}/I_{Cu2p} ratio is found to be 0.56, significantly lower than for CVD-grown graphene on the same surface. A possible reason for such a reduced amount of carbon is desorption of non-polymerized molecules (Turchanin et al., 2013). We cannot be certain whether it is the UV

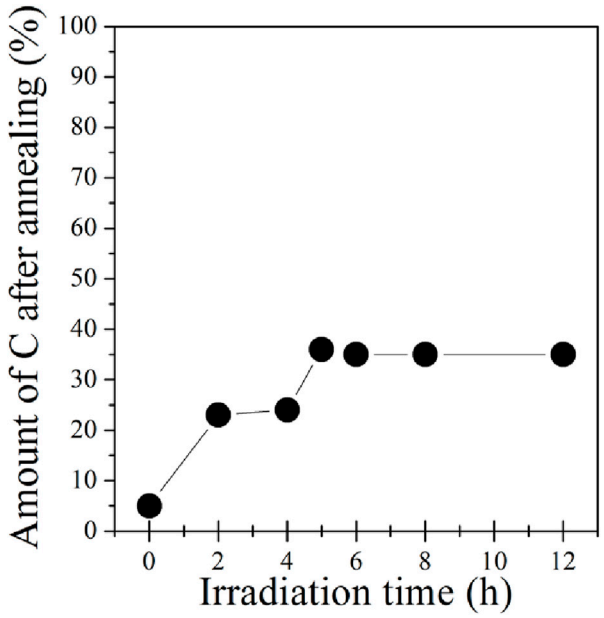

FIGURE 5
Relative amount of carbon remaining after annealing to 1,100 K of BPT SAMs on an electropolished copper foil that had been previously polymerized by UV irradiation, plotted as a function of UV irradiation time. 100% corresponds to the amount of carbon detected for the freshly assembled BPT before light exposure and annealing.

photons or the secondary electrons or both that cause polymerization in our case; however, since the secondary electron yield of Cu is higher than that for copper oxides (Aguilera et al., 2013), if only secondary electrons were involved, there should be more non-polymerized BPT on oxidized copper than on electropolished Cu.

For the C1*s* lineshape, we first observe that the full width at half maximum (FWHM) of the main component of the annealed photopolymerized SAM on electropolished Cu (Figure 3, left panel, top curve) as well as on oxidized Cu (Figure 4 left panel top curve) has decreased to half the value it had in after polymerization and amounts now to 0.5 eV. Since the lineshape and binding energy of both samples very closely resemble those of CVD-grown graphene (Bignardi, 2013), we attribute the main component to sp^2-hybridized carbon and the smaller component to sp^3-hybridized carbon.

As seen in Figure 4 (right panel, top curve), sulfur is detected in the XPS spectrum after annealing the photopolymerized BPT SAM on oxidized copper, while no traces of sulfur were found for the one on electropolished copper foils (Figure 3, right panel, top curve). Compared to the spectrum before annealing, the sulfur signal shows a 65% decrease in the intensity, and the peak maximum shifts to a BE of 161.5 eV, typical of copper sulfides. This confirms the breaking of C-S bonds during annealing (Matei et al., 2013), as already concluded from the shape of the C1*s* photoemission line of the photopolymerized BPT SAM on oxidized copper. It is reasonable to assume that because of the higher amount of carbon present on the oxidized surface after annealing, sulfur atoms are blocked by the carbon layer on top and cannot desorb even at high temperatures,

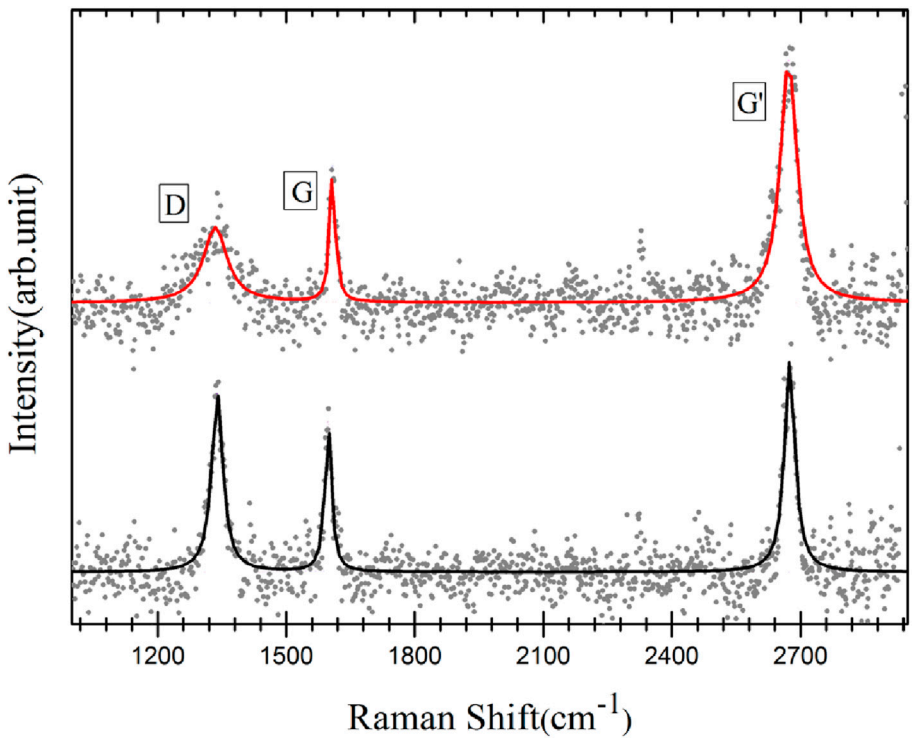

FIGURE 6
Raman spectra acquired after annealing photo-polymerized 1, 1′, biphenyl-4-thiol SAMs on electropolished (black curve) and oxidized copper foil (red curve); raw data (●) and fit (—).

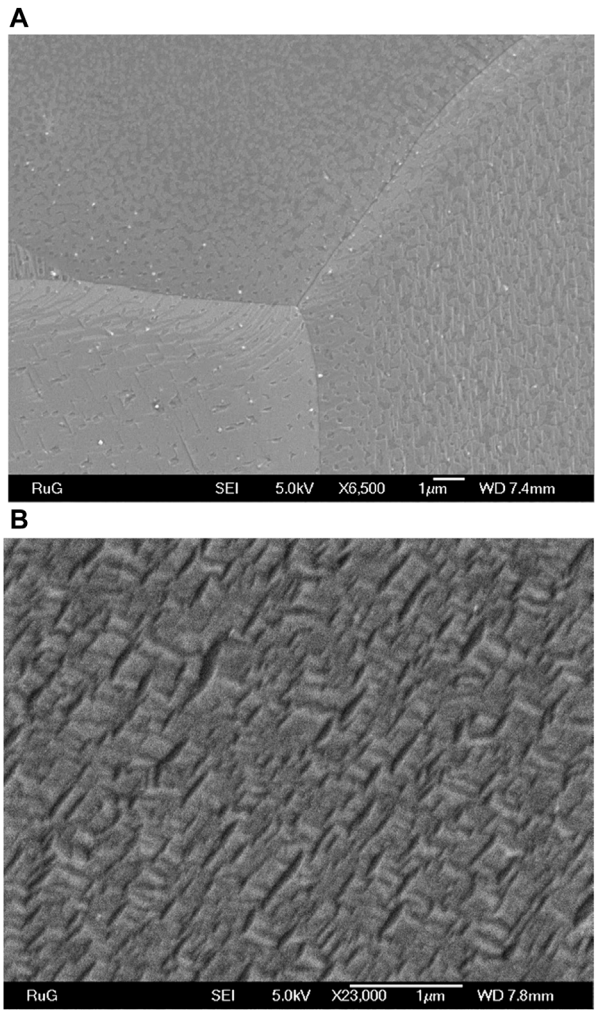

FIGURE 7
Scanning electron microscopy of **(A)** graphene on electropolished Cu foil and **(B)** graphene on Cu_2O/Cu foil produced by annealing a photo-polymerized BPT SAM.

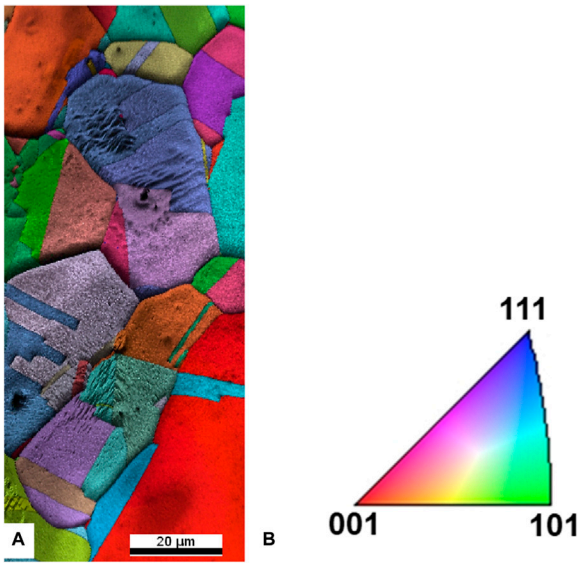

FIGURE 8
Electron backscattering diffraction map obtained on graphene on electropolished Cu foil **(A)** and the relation between false color coding and crystallographic orientation **(B)**.

while on electropolished copper, they can easily desorb because the carbon layer is incomplete.

From CA and XPS measurements of the polymerized and annealed BPT SAMs, the presence of graphitized carbon was established. To ascertain whether the carbon layer is indeed graphene, Raman spectroscopy was performed. Graphene typically exhibits distinct Raman features, namely, the D band, the G band, and the G′ band (Ferrari et al., 2006; Malard et al., 2009). The D band is a measure of the number of defects and, therefore, provides an insight into the quality of the material, while the position and shape of the G′ band as well as the ratio between the intensities of the G and the G' bands give information about the number of graphene layers (Ferrari et al., 2006; Malard et al., 2009; Lucchese et al., 2010). A ratio $I_{G'}/I_G$ ~ 2–3 is found for monolayer graphene, $2 > I_{G'}/I_G > 1$ for bilayer graphene, and $I_{G'}/I_G < 1$ for multilayer graphene. Figure 6 presents the Raman spectra acquired on the polymerized BPT SAMs on electropolished (black curve) and oxidized copper foil (red curve) after annealing. The relative intensity and position of the peaks were consistent throughout each sample. One can clearly see the fingerprints of graphene: the G band at 1,607 cm^{-1}, the D band at 1,335 cm^{-1}, and the G′ band at 2,672 cm^{-1}. For graphene grown on oxidized copper, the ratio $I_{G'}/I_G$ is ~ 2, pointing to a single layer of graphene. The lower intensity of the D band indicates that graphene grown on oxidized copper foil has fewer defects and, therefore, is of better quality than that grown on electropolished copper. The average distance between two point defects in the graphene layer was estimated using the intensity ratio of the G and D peaks (Lucchese et al., 2010). For the graphene on the oxidized substrate, the ratio I_D/I_G ~ 0.3 implies an average distance between point defects of *ca.* 20 nm, while for electropolished substrates, I_D/I_G ~ 1.1 gives an average distance of *ca.* 10 nm. These results align with the findings of Gottardi et al. 2015, who demonstrated that CVD-grown graphene on oxidized Cu(111) is of higher quality than that grown on electropolished substrates. Furthermore, analysis of the G′ band of graphene on oxidized copper foil (red curve) shows that it can be fitted with a single Lorentzian with a full width at half maximum of 46 cm^{-1}, confirming single-layer graphene growth (Ferrari et al., 2006; Bignardi et al., 2013) already deduced from the XPS results.

To explore the morphological properties of graphene grown on both substrates, we performed scanning electron microscopy. Figure 7A displays the SEM image of graphene grown on electropolished copper foil. As already inferred from the XPS data, graphene does not form a continuous layer. Instead, the island density varies depending on the grain orientations of the foil. These results are consistent with graphene grown by chemical vapor deposition (CVD) on polycrystalline copper foil (Wood et al., 2011), where the most favorable orientation for graphene growth is Cu(111), followed by growth on high-index facets, while Cu(100) has been identified as the least favorable orientation with a slow graphene growth rate. In Figure 7A, three large distinct crystalline orientations are observed. The grain at the bottom left of the image exhibits continuous film growth with only few very small holes in the

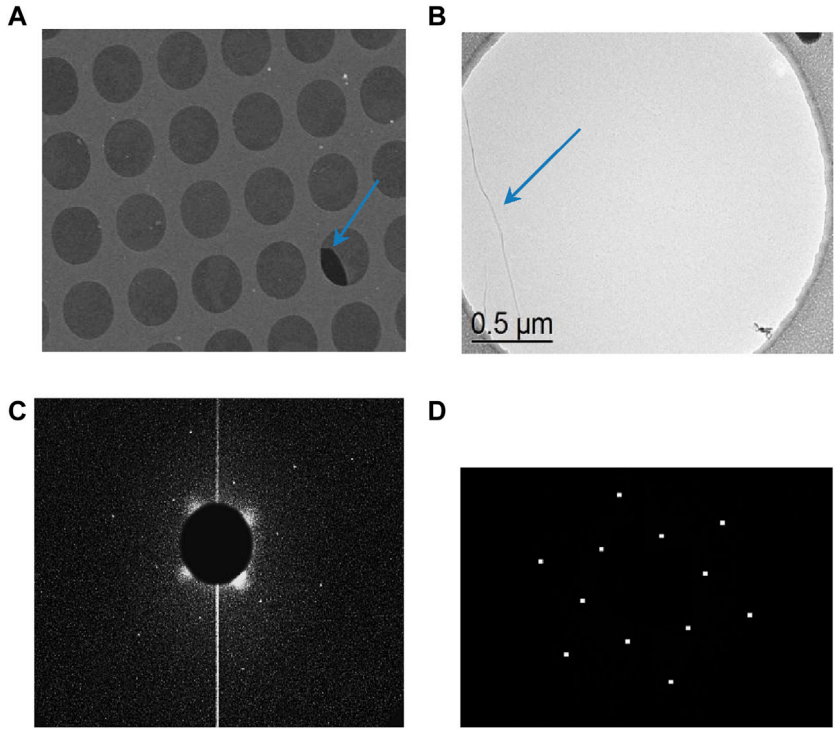

FIGURE 9
TEM of graphene grown by annealing a polymerized BPT SAM on oxidized Cu and transferred to TEM grids. **(A)** Overview of approximately 250 μm^2 area of the TEM grid; **(B)** detailed image of a single layer of suspended graphene; **(C)** electron diffraction pattern obtained on the area shown in panel **(B)**; **(D)** same electron diffraction pattern as **(C)** after background subtraction.

film, while other grains clearly show island formation. To understand these morphological differences, we determined the structure of the copper surface using electron backscattering diffraction (EBSD), as shown in Figure 8A. We found that the electropolished Cu foil consists of multiple orientations, with grain sizes ranging between 50 and 100 μm. Approximately 28% of the grains were oriented (001), 11% (101) and 2.5% (111), while the rest of the area consisted of high-index facets. The grains exhibiting island growth (Figure 7A) were closer to Cu(100) in orientation than the grains exhibiting continuous growth, which was close to Cu(111). This proves that the reduced diffusion on Cu(100) (Wood et al., 2011) is reflected also in the quality of the graphene produced by our method. Figure 7B shows the SEM image of graphene grown by annealing the polymerized BPT SAM on oxidized copper. Here, the layer is continuous and covers the entire surface; no holes can be seen. This explains the lower defect density deduced from the Raman spectra.

Further details concerning the structural properties of the grown graphene can be gained from transmission electron microscopy. For this purpose, the graphene layer needs to be transferred to TEM grids, as described in Bignardi et al. (2013). We were unable to transfer graphene grown on electropolished copper as it was not a continuous film, and graphene islands spread in the etchant solution. The graphene grown on oxidized copper was successfully transferred. Figure 9A shows the TEM micrograph of the suspended graphene; more than 90% of the 2-μm holes are covered. During transfer to the TEM grid, the sheets can fold or break, as seen in Figure 9A, where one hole is not fully covered and the rupture in the sheet is indicated with a blue arrow. During the transfer procedure, some defects like wrinkles and folding of sheets can occur (Bignardi et al., 2013); Figures 9A, B provides a detailed view of suspended graphene, revealing a wrinkle in the graphene sheet. The electron diffraction pattern collected from this sample is presented in Figure 9C. After background subtraction (Figure 9D), a single set of hexagonal spots is visible, indicating that the graphene layer is single crystalline in the measured region. However, this observation is not representative of the entire graphene layer; in fact, only 10% of the free-standing graphene in the 2-μm-diameter circular holes was found to be a single domain, and 90% exhibited a multidomain structure, explaining the observed defect peak D intensity in the Raman data.

4 Conclusion

In conclusion, we developed an improved method for graphene synthesis on copper foils through the annealing of self-assembled monolayers of 1,1′-biphenyl-4-thiol, previously polymerized using UV light rather than an electron beam. On the electropolished Cu foil, we found that the quality of the obtained graphene strongly depends on the crystallographic orientation of the grains, and a continuous layer was obtained only on Cu(111), while other orientations showed growth of small islands. Interestingly, oxidized Cu foils yielded superior graphene quality with the formation of a continuous layer and approximately 10% of the grains exceeding 2 μm in size. However, it is noteworthy that achieving such high-quality graphene required temperatures comparable

to those used in CVD growth. This synthesis route opens the way for graphene preparation via self-assembly of precursor molecules on insulating substrates, provided they exhibit similar catalytic properties leading to graphitization, as observed with the Cu_2O surface studied in this work. The next challenge will be to verify whether this method is also suitable for producing doped graphene and, if yes, whether a certain arrangement of the doping atoms in the precursor molecule can be preserved in the resulting graphene.

Data availability statement

The original contributions presented in the study are included in the article/Supplementary Material; further inquiries can be directed to the corresponding author.

Author contributions

TZ: data curation, formal analysis, funding acquisition, investigation, validation, visualization, writing–original draft, and writing–review and editing. AS: data curation, formal analysis, investigation, writing–original draft, and writing–review and editing. OI: data curation, formal analysis, investigation, writing–original draft, and writing–review and editing. LB: data curation, investigation, writing–original draft, and writing–review and editing. WV: data curation, formal analysis, investigation, writing–original draft, and writing–review and editing. JH: resources, supervision, validation, writing–original draft, and writing–review and editing. PR: conceptualization, methodology, project administration, resources, supervision, validation, writing–original draft, and writing–review and editing.

Funding

The author(s) declare that financial support was received for the research, authorship, and/or publication of this article. TZ acknowledges the Schlumberger Foundation's *Faculty for the Future* program for supporting her PhD study. This work was performed within the "Top Research School" program of the Zernike Institute for Advanced Materials under the Bonus Incentive Scheme (BIS) of the Netherlands' Ministry of Education, Science, and Culture.

Acknowledgments

The authors thank Wesley R. Browne for support with the Raman measurements and Petra Reinke for insightful discussions. Preliminary studies by the bachelor students Roban van Herk, André Mintjes, and Estela Moretón Alfonsin are gratefully acknowledged.

Conflict of interest

The authors declare that the research was conducted in the absence of any commercial or financial relationships that could be construed as a potential conflict of interest.

Publisher's note

Supplementary material

The Supplementary Material for this article can be found online at: https://www.frontiersin.org/articles/10.3389/fnano.2024.1366542/full#supplementary-material

References

Aguilera, L., Montero, I., Dávila, M. E., Ruiz, A., Galán, L., Nistor, V., et al. (2013). CuO nanowires for inhibiting secondary electron emission. *J. Phys. D. Appl. Phys.* 46, 165104. doi:10.1088/0022-3727/46/16/165104

Akinwande, D., Brennan, C. J., Bunch, J. S., Egberts, P., Felts, J. R., Gao, H., et al. (2017). A review on mechanics and mechanical properties of 2D materials—graphene and beyond. *Extreme Mech. Lett.* 13, 42–77. doi:10.1016/j.eml.2017.01.008

Angelova, P., Vieker, H., Weber, N.-E., Matei, D., Reimer, O., Meier, I., et al. (2013). A universal scheme to convert aromatic molecular monolayers into functional carbon nanomembranes. *ACS Nano* 7 (8), 6489–6497. doi:10.1021/nn402652f

Bae, S., Kim, H., Lee, Y., Xu, X., Park, J.-S., Zheng, Y., et al. (2010). Roll-to-roll production of 30-inch graphene films for transparent electrodes. *Nat. Nanotechnol.* 5 (8), 574–578. doi:10.1038/nnano.2010.132

Batzill, M. (2012). The surface science of graphene: metal interfaces, CVD synthesis, nanoribbons, chemical modifications, and defects. *Surf. Sci. Rep.* 67, 83–115. doi:10.1016/j.surfrep.2011.12.001

Belser, A., Greulich, K., Klein, M., Gruninger, P., Sättele, M. S., Fingerle, M., et al. (2023). Planar BN-doped nanographenes on reactive metal surfaces: a promising pathway for the preparation of BN-doped graphene layers. *ACS Appl. Electron. Mat.* 5, 5193–5201. doi:10.1021/acsaelm.3c00924

Berger, C., Song, Z., Li, T., Li, X., Ogbazghi, A. Y., Feng, R., et al. (2004). Ultrathin epitaxial graphite: 2D electron gas properties and a route toward graphene-based nanoelectronics. *J. Phys. Chem. B* 108, 19912–19916. doi:10.1021/jp040650f

Bignardi, L. (2013). "Electronic and structural properties of graphene/metal interphases,". PhD thesis (Groningen, Netherlands: University of Groningen). ISNBNs 9789036762588.

Bignardi, L., van Dorp, W. F., Gottardi, S., Ivashenko, O., Dudin, P., Barinov, A., et al. (2013). Microscopic characterisation of suspended graphene grown by chemical vapour deposition. *Nanoscale* 5 (13), 9057–9061. doi:10.1039/C3NR02386A

Cabrita, J. F., Viana, A. S., and Abrantes, L. M. (2010). Copper protection by phosphonic acid self-assembled monolayers. *Corros. Prot. Mat.* 29 (4), 114–119.

Dikin, D. A., Stankovich, S., Zimney, E. J., Piner, R. D., Dommett, G. H. B., Evmenenko, G., et al. (2007). Preparation and characterization of graphene oxide paper. *Nature* 448, 457–460. doi:10.1038/nature06016

Emtsev, K. V., Bostwick, A., Horn, K., Jobst, J., Kellogg, G. L., Ley, L., et al. (2009). Towards wafer-size graphene layers by atmospheric pressure graphitization of silicon carbide. *Nat. Mat.* 8 (3), 203–207. doi:10.1038/nmat2382

Ferrari, A. C., Meyer, J. C., Scardaci, V., Casiraghi, C., Lazzeri, M., Mauri, F., et al. (2006). Raman spectrum of graphene and graphene layers. *Phys. Rev. Lett.* 97, 187401. doi:10.1103/PhysRevLett.97.187401

Gengler, R. Y. N., Spyrou, K., and Rudolf, P. (2010). A roadmap to high quality chemically prepared graphene. *J. Phys. D. Appl. Phys.* 43 (37), 374015. doi:10.1088/0022-3727/43/37/374015

Gilje, S., Han, S., Wang, M., Wang, K. L., and Kaner, R. B. (2007). A chemical route to graphene for device applications. *Nano Lett.* 7 (11), 3394–3398. doi:10.1021/nl0717715

Gottardi, S., Müller, K., Bignardi, L., Moreno-López, J. C., Pham, T. A., Ivashenko, O., et al. (2015). Comparing graphene growth on Cu(111) versus oxidized Cu(111). *Nano Lett.* 15 (2), 917–922. doi:10.1021/nl5036463

Laibinis, P. E., and Whitesides, G. M. (1992). Self-assembled monolayers of n-alkanethiolates on copper are barrier films that protect the metal against oxidation by air. *J. Am. Chem. Soc.* 114, 9022–9028. doi:10.1021/ja00049a038

Laibinis, P. E., Whitesides, G. M., Allara, D. L., Tao, Y.-T., Parikh, A. N., and Nuzzo, R. G. (1991). Comparison of the structures and wetting properties of self-assembled monolayers of n-alkanethiols on the coinage metal surfaces, copper, silver, and gold. *J. Am. Chem. Soc.* 113 (19), 7152–7167. doi:10.1021/ja00019a011

Li, X., Cai, W., An, J., Kim, S., Nah, J., Yang, D., et al. (2009). Large-area synthesis of high-quality and uniform graphene films on copper foils. *Science* 324, 1312–1314. doi:10.1126/science.1171245

Lucchese, M. M., Stavale, F., Martins Ferreira, E. H., Vilani, C., Moutinho, M. V. O., Capaz, R. B., et al. (2010). Quantifying ion-induced defects and Raman relaxation length in graphene. *Carbon* 48, 1592–1597. doi:10.1016/j.carbon.2009.12.057

Malard, L. M., Pimenta, M. A., Dresselhaus, G., and Dresselhaus, M. S. (2009). Raman spectroscopy in graphene. *Phys. Rep.* 473 (5-6), 51–87. doi:10.1016/j.physrep.2009.02.003

Matei, D. G., Weber, N.-E., Kurasch, S., Wundrack, S., Woszczyna, M., Grothe, M., et al. (2013). Functional single-layer graphene sheets from aromatic monolayers. *Adv. Mat.* 25 (30), 4146–4151. doi:10.1002/adma.201300651

K. L. Mittal (2003). *Contact angle, wettability and adhesion* (Utrecht: VSP).

Novoselov, K. S., Fal'ko, V. I., Colombo, L., Gellert, P. R., Schwab, M. G., and Kim, K. (2013). A roadmap for graphene. *Nature* 490, 192–200. doi:10.1038/nature11458

Novoselov, K. S., Geim, A. K., Morozov, S. V., Jiang, D., Katsnelson, M. I., Grigorieva, I. V., et al. (2005). Two-dimensional gas of massless Dirac fermions in graphene. *Nature* 438, 197–200. doi:10.1038/nature04233

Novoselov, K. S., Geim, A. K., Morozov, S. V., Jiang, D., Zhang, Y., Dubonos, S. V., et al. (2004). Electric field effect in atomically thin carbon films. *Science* 306, 666–669. doi:10.1126/science.1102896

Rhinow, D., Weber, N. E., and Turchanin, A. (2012). Atmospheric pressure, temperature-induced conversion of organic monolayers into nanocrystalline graphene. *J. Phys. Chem. C* 116 (22), 12295–12303. doi:10.1021/jp301877p

Ron, H., Cohen, H., Matlis, S., Rappaport, M., and Rubinstein, I. (1998). Self-assembled monolayers on oxidized metals. 4. superior n -alkanethiol monolayers on copper. *J. Phys. Chem. B* 102 (49), 9861–9869. doi:10.1021/jp9827072

Turchanin, A., Käfer, D., El-Desawy, M., Wöll, C., Witte, G., and Gölzhäuser, A. (2009). Molecular mechanisms of electron-induced cross-linking in aromatic SAMs. *Langmuir* 25 (13), 7342–7352. doi:10.1021/la803538z

Turchanin, A., Weber, D., Büenfeld, M., Kisielowski, C., Fistul, M. V., Efetov, K. B., et al. (2011). Conversion of self-assembled monolayers into nanocrystalline graphene: structure and electric transport. *ACS Nano* 5 (5), 3896–3904. doi:10.1021/nn200297n

Wang, X., Zhi, L., and Müllen, K. (2008). Transparent, conductive graphene electrodes for dye-sensitized solar cells. *Nano Lett.* 8 (1), 323–327. doi:10.1021/nl072838r

Wood, J. D., Schmucker, S. W., Lyons, A. S., Pop, E., and Lyding, J. W. (2011). Effects of polycrystalline Cu substrate on graphene growth by chemical vapor deposition. *Nano Lett.* 11 (11), 4547–4554. doi:10.1021/nl201566c

Yildirim, C., Füser, M., Terfort, A., and Michael Zharnikov, M. (2017). Modification of aromatic self-assembled monolayers by electron irradiation: basic processes and related applications. *J. Phys. Chem. C* 121 (1), 567–576. doi:10.1021/acs.jpcc.6b11269

Zhang, Y. B., Tan, Y.-W., Stormer, H. L., and Kim, P. (2005). Experimental observation of the quantum Hall effect and Berry's phase in graphene. *Nature* 438, 201–204. doi:10.1038/nature04235

frontiers | Frontiers in Nanotechnology

TYPE Review
PUBLISHED 15 May 2024
DOI 10.3389/fnano.2024.1371386

OPEN ACCESS

EDITED BY
Estela Blaisten-Barojas,
George Mason University, United States

REVIEWED BY
Matthew William Daniels,
National Institute of Standards and Technology (NIST), United States
Mutsumi Kimura,
Ryukoku University, Japan

*CORRESPONDENCE
Sayani Majumdar,
sayani.majumdar@tuni.fi

RECEIVED 16 January 2024
ACCEPTED 15 April 2024
PUBLISHED 15 May 2024

CITATION
Majumdar S (2024), Harnessing ferroic ordering in thin film devices for analog memory and neuromorphic computing applications down to deep cryogenic temperatures.
Front. Nanotechnol. 6:1371386.
doi: 10.3389/fnano.2024.1371386

Harnessing ferroic ordering in thin film devices for analog memory and neuromorphic computing applications down to deep cryogenic temperatures

Sayani Majumdar*

Faculty of Information Technology and Communication Sciences, Tampere University, Tampere, Finland

The future computing beyond von Neumann era relies heavily on emerging devices that can extensively harness material and device physics to bring novel functionalities and can perform power-efficient and real time computing for artificial intelligence (AI) tasks. Additionally, brain-like computing demands large scale integration of synapses and neurons in practical circuits that requires the nanotechnology to support this hardware development, and all these should come at an affordable process complexity and cost to bring the solutions close to market rather soon. For bringing AI closer to quantum computing and space technologies, additional requirements are operation at cryogenic temperatures and radiation hardening. Considering all these requirements, nanoelectronic devices utilizing ferroic ordering has emerged as one promising alternative. The current review discusses the basic architectures of spintronic and ferroelectric devices for their integration in neuromorphic and analog memory applications, ferromagnetic and ferroelectric domain structures and control of their dynamics for reliable multibit memory operation, synaptic and neuronal leaky-integrate-and-fire (LIF) functions, concluding with their large-scale integration possibilities, challenges and future research directions.

KEYWORDS

neuromorphic, ferroelectric, spintronics, nanotechnology, non-volatile (NV) memory

Introduction

The future of computing beyond Complementary Metal Oxide Semiconductor (CMOS) era requires extensive use of material and device physics to perform computation at the atomic level (Manipatruni, 2018; Chen, 2022). Development of neuromorphic computing hardware, that is devices with bio-plausible functionalities for implementing neural network operations in hardware, requires different kinds of volatile and non-volatile memories to implement synaptic and neuronal functionalities. While synaptic plasticity, runtime weight update and supervised learning require well-controlled, multilevel conductance in nanoscale devices with long and short-term synaptic potentiation and depression, neuronal leaky-integrate-and-fire (LIF) activity demands accumulative nature of switching from one conductance state to the other and a finite decay rate of conductance states to return to its previous condition rather quickly.

For achieving multilevel conductance states, different physical phenomenon has been actively investigated by the scientists. This includes resistive random-access memories

(RRAMs), phase-change memories (PCMs), conduction bridge memories (CBRAMs), magnetic random-access memories (MRAMs), ferroelectric random-access memories (FeRAMs) and so on (Xia, 2019; Ielmini, 2020; Majumdar, 2022b). Each technology provides some advantages and some challenges in terms of operational voltage requirement, speed, scalability, reliability, endurance, yield, manufacturability, cost etc. and no single technology has so far been able to provide solutions for all the requirements for high-performance memories and in-memory-computing (IMC). In the current review article, we will focus on the last two categories of emerging CMOS-compatible memories, i.e., MRAMs and FeRAMs as multilevel memories and their implementation in certain application areas that shows utilization of ferroic ordering can have significant advantage in non-volatile memory (NVM) and neuromorphic hardware development, operating down to deep cryogenic temperature.

Ferromagnetic (FM) and ferroelectric (FE) material based programmable memory devices can represent multiple conductance states due to their switchable polarization and internal domain structures that can be programmed controllably utilizing magnetic or electric field. These switched polarization states can retain their polarization after the applied field is withdrawn, and thus they can work as multi-level memory and synaptic devices for implementing neuromorphic functionalities. The multi-domain switching dynamics of FM or FE thin films are fundamentally different from most other memristive devices that involves electroforming processes and significant ion motion (in case of RRAMs or CBRAMs) or switching between crystalline and amorphous phases (like PCMs). Analog resistive states in FM or FE thin film devices are due to the non-coherent switching of the polarized domains, with polarization up and down states representing device On and Off states and mixed polarization phases leading to intermediate conductance states. Based on device architectures and operating principles, large conductance range, fast switching, programmable retention and power efficiency can be achieved in Ferroic devices. In particular, devices with ferromagnetic ordering can provide excellent endurance and more energy-efficient writing, due to the spin-based nature of magnetization switching with no charge movements in MRAMs (Grollier, 2020) while ferroelectric field-effect transistor (FeFET) technology offer large dynamic conductance range, analog operation and excellent CMOS compatibility (Jerry, 2017; Mulaosmanovic, 2017; Khan, 2020).

Traditionally, spintronic MRAMs and FeRAMs have been implemented as binary memory components. However, due to growing interest in neuromorphic device functionalities, it is of high relevance to investigate their multi-domain switching properties for replicating synaptic plasticity and membrane potential modulation for neuronic functionalities. Interestingly, the multidomain switching mechanisms of ferroic materials has resemblance with biological neural systems, like accumulative and stochastic nature of switching, providing the very promising possibilities for incorporating both short- and long-term memory operations that can be utilized to develop bio-realistic hardware primitives.

In addition to the need for multibit storage and computing, memories operating at cryogenic temperatures are becoming critical components for high performance computing (HPC), quantum technologies, space and superconducting electronics. For HPC, one significant demand is memories with capacities for handling of larger and faster data systems for applications such as data analytics and machine learning. Computing at cryogenic temperature has the potential to provide these functionalities through improvements in cycling time, power consumption, and higher compute density.

For quantum computers, there are three major components, quantum bits or qubits, a control processor, and a memory block. In the present-day quantum computers, a conventional computer operating at room temperature is used as the control processor. Long cables connect the qubits to the control processor. Although working satisfactorily for a small number of qubits, scalability of this architecture to even a few hundreds of qubits would be a big challenge due to the requirement of a large number of cables to maintain a connection between the room-temperature control processor and the qubits at cryogenic temperature. One way of circumventing the scaling issue is to place the control processor at a temperature close to that of the qubits. However, when the control processor is at 4 K or below, types of memories that can be used in conjunction with quantum computers, also become limited. Interconnects between the room-temperature memories and the cryogenic control processor would cause a significant thermal leakage and could generate thermal noise that is large enough to destroy the quantum states of the noise-sensitive qubits. This necessitates use of cryogenic memories compatible with the control processors (Wang, 2020a). Space technologies additionally require radiation hardening of the memory components to operate without degradation or failure under harsh space conditions.

Considering the needs for high-performance multi-level storage and processing at cryogenic temperatures, devices harnessing ferroic ordering can provide an excellent solution (Grollier, 2020). In the current review, we focus our discussions on reliable reproduction and stability of multilevel states that could lead to successful implementations of neural functionalities. In ferroic components, high endurance is a general feature that is linked to the non-destructive nature of the multidomain switching. However, in actual practice, limited endurance is observed often due to various factors like structural defects, grain and phase boundaries, dislocations and disorders in the thin film materials that lead to unwanted charge and ion migration, vacancy and trap related charging of devices during frequent field cycling and eventually cause early breakdowns. It has been observed in recent studies (Hur, 2022; Bohuslavskyi, 2024) that lowering the operating temperature can successfully circumvent many such leakage current issues and can prolong the device lifetimes. Additionally, higher spin-polarization (Garcia, 2004; Majumdar, 2008) and stability of mixed polarization states in ferromagnets at cryogenic temperatures (Majumdar, 2012a) cause better analog device performance. It can be, therefore predicted that, ferroic-based analog memory devices could provide a promising pathway toward implementation of energy efficient neuro-inspired computing hardware with potential advantages of high endurance and reliability, especially at cryogenic temperatures. Although some of the ferroic materials based NVM devices have larger cell areas than RRAMs and PCMs, their rich device physics can be utilized to compute with smaller number of components in large and complex neural circuits.

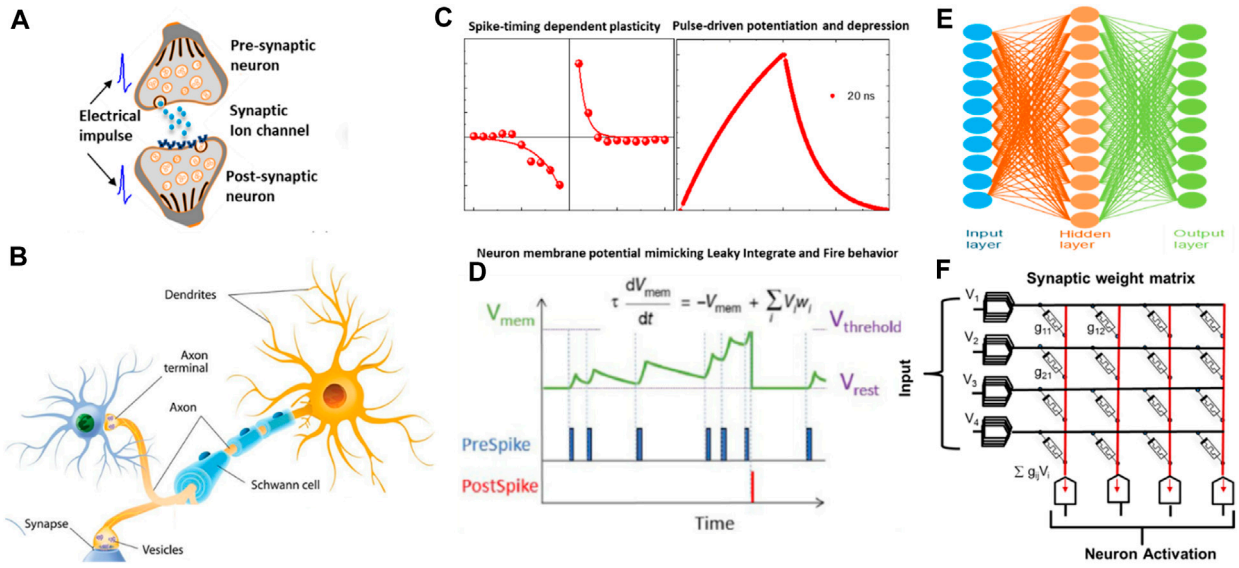

FIGURE 1
Schematic representation of a biological neural network and its electronic counterpart. **(A)** A biological synapse and it is response to electrical impulses arriving from the neurons. **(B)** A biological neuron cell body. **(C)** Synapse and **(D)** neuron characteristics. The neuron activation is influenced by its membrane potential, with multiple incoming spikes accumulating and increasing the potential to eventually cross a threshold and fire. These dynamics can be described using a leaky integrate-fire (LIF) neuron model. Neurons are interconnected by synapses, which in electronic circuits can be integrated into crossbar devices with multiple, programmable conductance states. Spike timing dependence plasticity (STDP) and pulse driven potentiation and depression of a synapse help to obtain bio-plausible learning based on synaptic plasticity. **(E)** A schematic of a neural network and it is hardware implementation in **(F)** crossbar arrays of synaptic weight elements and neurons.

Digital electronics vs neuromrphic hardware

Digital electronic components like memories and logic devices operate in "1" and "0" states, where state "1" generally represents presence of a charge or current and state "0" represents absence of it. In the rapidly evolving landscape of semiconductor technology, the demand for high-performance, energy-efficient, and non-volatile memory solutions (NVMs) has grown exponentially. NVMs play a pivotal role in modern electronics, serving as storage elements for data retention even when power is switched off. Traditional NVMs, like flash memory, have been widely adopted for their non-volatile characteristics but currently they are facing limitations in terms of scalability, energy efficiency and endurance. In ferromagnetic or ferroelectric components, an external magnetic or electric field respectively controls the direction of electron spins or electric dipoles and play a major role in determining device "1" and "0" states. In both kind of devices, with ferroic ordering, "up" or "down" spin states or electric polarization states are rather easy to control and maintain. Therefore, ferroic ordering based binary memories became a matured technology like magnetic or ferroelectric random-access memories in these domains.

For neuromorphic or analog computing applications, it is still possible to use binary memories. However, we must keep in mind that similar to biological synapses in the brain, synaptic weights in neural networks are analog in nature rather than binary and hence to replicate a synapse, multiple memory devices are needed to store one single synaptic weight. This increases the area footprint, required read/write energy, and complicates the circuits. To avoid such issues, it is therefore, of utmost importance to store multiple bits of information in the single cell of memories. By utilizing the multidomain structures of ferromagnetic or ferroelectric thin films, it is possible to have reasonable control over multi-conductance states that can make these devices suitable as analog, volatile or non-volatile memories and synapses with programmable plasticity, i.e., long or short-term retention properties of multiple conductance states that can be tuned by the input pulse parameters. Figure 1 shows a biological neural network, the mechanism of synaptic weight change in biological systems and its electronic counterpart that is implemented in crossbar arrays of synaptic weight elements and neuron dynamics using a leaky-integrate-fire (LIF) neuron model.

One key challenge of analog memory, however, is reproducibility and retention of the intermediate states, especially in scaled devices. Due to inherent randomness in domain switching in ferroic devices, we observe a finite distribution of intermediate states under identical pulse programming condition that restricts their bit resolution. At room temperature, higher mobility of ferroic domains together with other defect related effects like movement of trapped charges and vacancies thus make control of analog states even more challenging. At deep cryogenic temperature, on the other hand, lack of thermal energy makes the domain rotation more restricted leading to less bit flips and effectively more control over the intermediate mixed domain states in the ferroic devices. In previous works, with ferromagnetic half-metal-based spin-valves (Majumdar, 2006; Majumdar, 2012b), and magnetic tunnel junctions (MTJ) (Garcia, 2004), sizable resistance switching effects were observed at 4K that decayed substantially with increase in temperature. Even with higher spin-polarized electrodes (Majumdar, 2008; Angervo, 2022), no performance improvements at 300 K were observed. Better

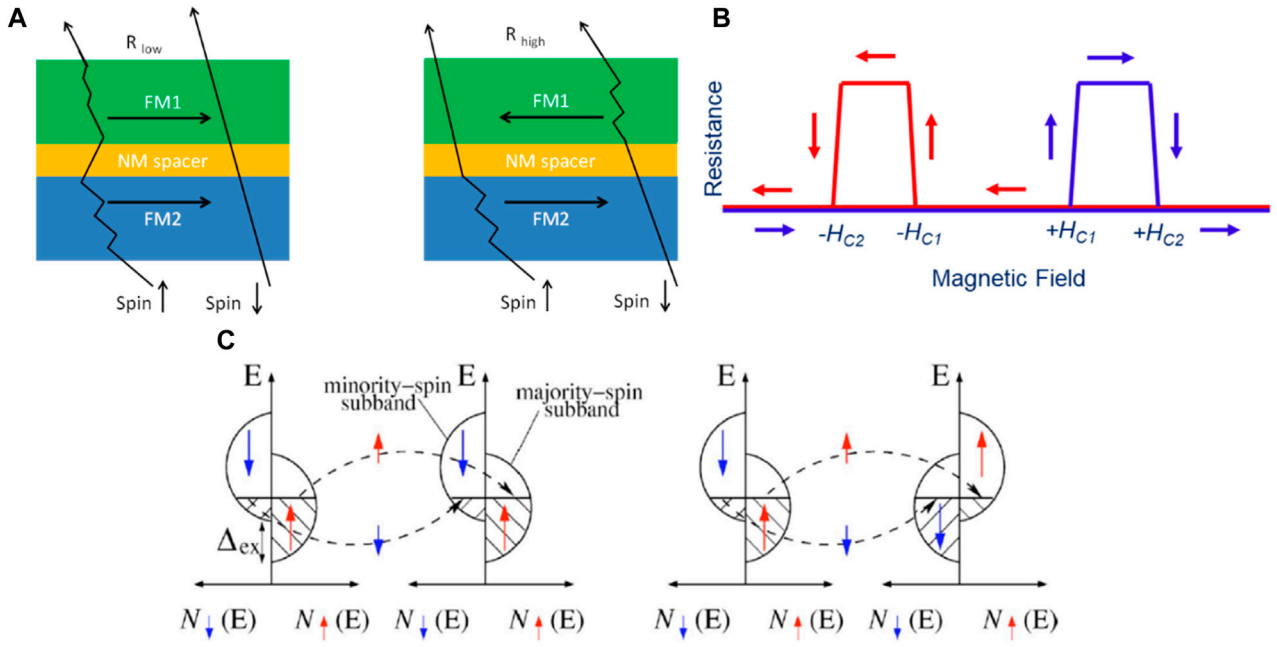

FIGURE 2
(A) Schematic diagram of a spin-valve architecture for parallel and antiparallel alignments of the two ferromagnetic electrodes showing spin dependent scattering at the two electrodes. **(B)** Change in electrical resistance of the spin valve due to forward and reverse sweeping of the magnetic fields. **(C)** Schematic diagram showing spin polarized tunneling of carriers between the two ferromagnetic electrodes with different spin resolved density of states. Adapted from Majumdar 2017, 2018a.

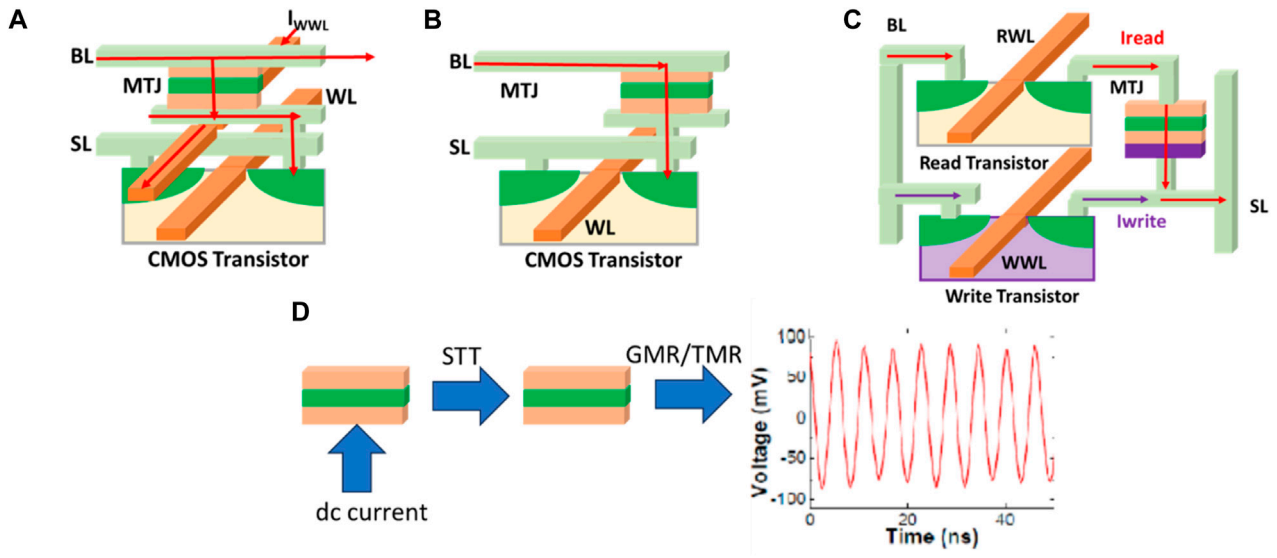

FIGURE 3
Schematic diagram of different MRAM structures and their operating principles. Schematics of **(A)** conventional MRAM architecture where magnetic field is used for writing, **(B)** spin-transfer-torque MRAM where spin polarized current is used for writing **(C)** and spin-orbit torque MRAM (SOT MRAM) where two separate read and write paths are used and **(D)** spin-toque nano oscillators (STNO) where a dc current causes precision of the magnetic layer producing spin-transfer torque which upon passing through a GMR/TMR layer produces an oscillating voltage.

performance of such devices at cryogenic temperatures were considered a bottleneck at that time. Now, in the age of high-performance computing, quantum computing and space technologies, when memories working at deep cryogenic temperatures are becoming a major focus for development, these works can provide an important design clue about how we can take advantage of ferroic ordering at low temperatures to design most efficient analog memory and neuromorphic systems.

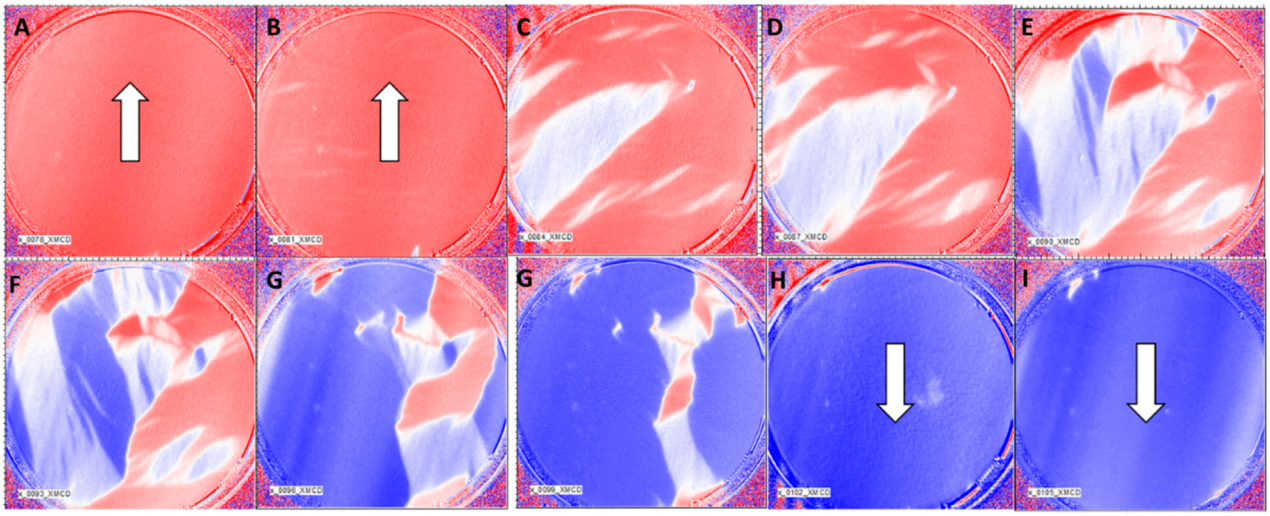

FIGURE 4
Magnetic domain imaging using photoemission electron microscopy (PEEM), with magnetic contrast from x-ray magnetic circular dichroism (XMCD) technique (XMCD-PEEM) at 40 K. The images were taken from $La_{0.5}Sr_{0.5}MnO_3$ thin films of 20 nm thickness. In order to study the local magnetic switching of the magnetic domains in the films, XMCD-PEEM images were recorded in a varying magnetic field between +10 mT (A) to −10 mT (I). The results show that at saturated magnetization states, the samples are homogeneously magnetized. However, when the in-plane magnetic field was varied between the saturation values, a clear domain wall formation between parallel and antiparallelly aligned domains of the LSMO film surface was seen. With further increase of magnetic fields, more and more domains changed their orientation resulting in sharp change in magnetic contrast image. Adapted from Majumdar 2024. **(A–F)** represents XMCD images under different magnetic fields showing gradual magnetic domain rotaion.

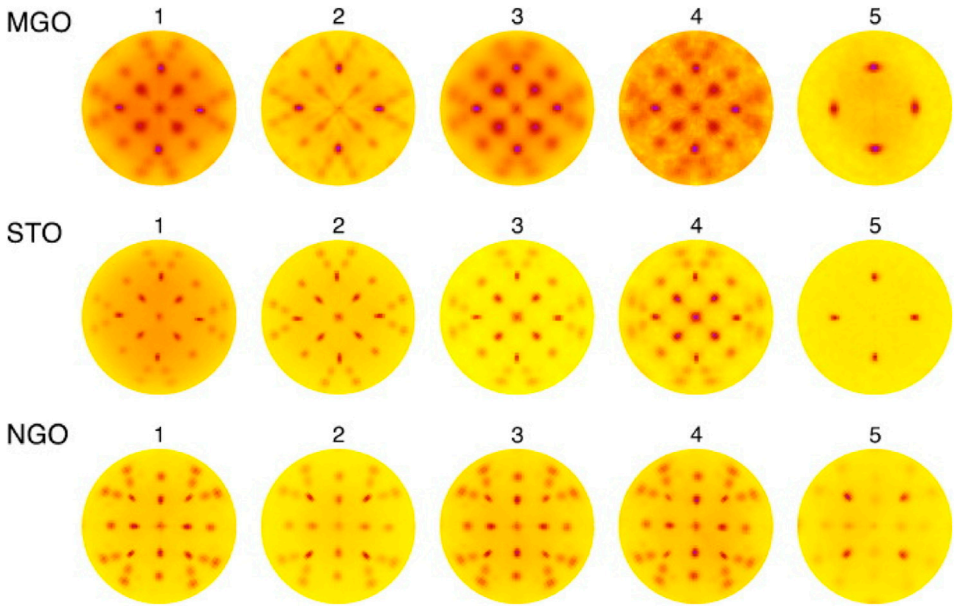

FIGURE 5
X-ray pole figures of the (1 1 0) reflection at 2θ = 32.76° of as deposited LSMO films deposited on MgO, STO and NGO substrates using deposition parameters shown in Table 1. Reproduced with permission from Majumdar 2012a.

Physics of spintronic devices for analog memory and neuromorphic computing

Spintronic devices can work as binary resistive switching or memristive devices by storing digital or analog information in their magnetic domain textures (Finocchio, 2021). Among spintronic devices, magnetic tunnel junctions (MTJs) are extensively studied that exhibited reliable memory read and write performances in device dimension down to tens of nanometers (Ikegawa, 2020). MTJs have mostly been used to work as binary memory with high accuracy and thermal stability, ultrafast operation and nearly infinite endurance. However, having controllable multilevel conductance in

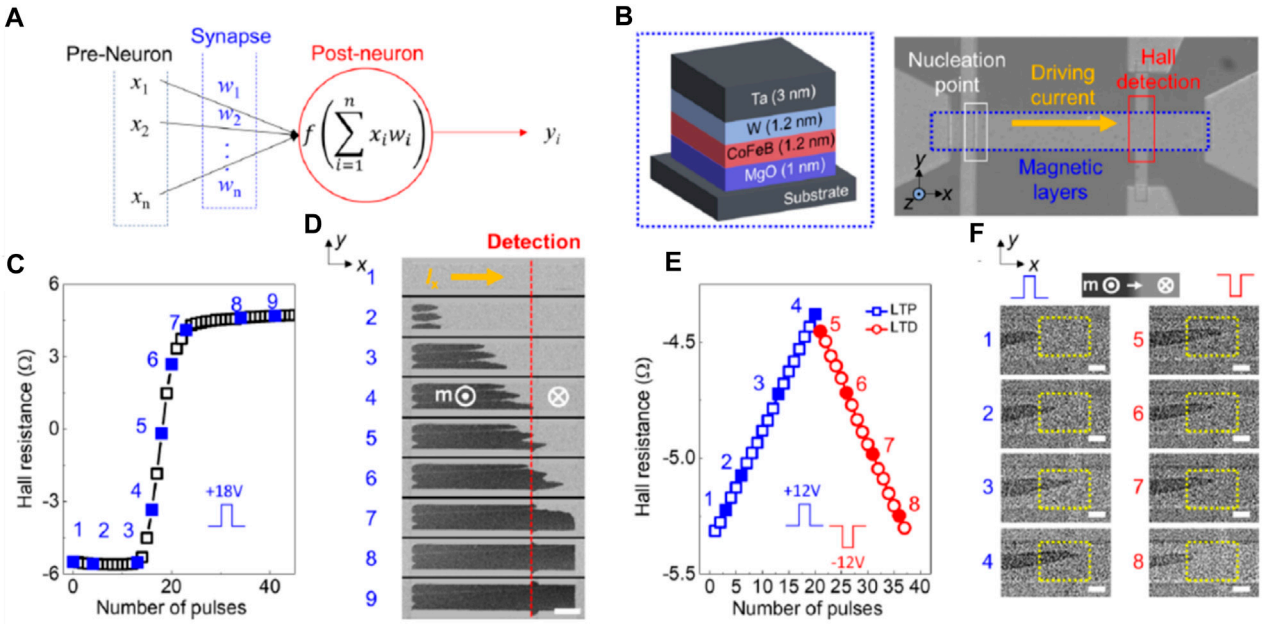

FIGURE 6
Representative spin neuron and weight functions. **(A)** Schematic of the perceptron, part of the artificial neural network; **(B)** schematic of the MgO/CoFeB/W structure and an optical image of the patterned Hall bar device with the measurement configuration; **(C)** representative Hall resistance determined by the position of the current-driven DW; and **(D)** corresponding MOKE images for each state (marked as blue numbers). The light and dark gray colors in the MOKE images represent the +z and −z magnetization domains, respectively; **(E)** typical LTP/LTD functions of the Hall resistance modulated by potentiation/depression training pulses ±12 V in amplitude with a fixed pulse width of 50 ms; **(F)** corresponding MOKE images for each state (marked by blue numbers for potentiation and red for depression). (Figure reproduced with permission from Yang, 2021).

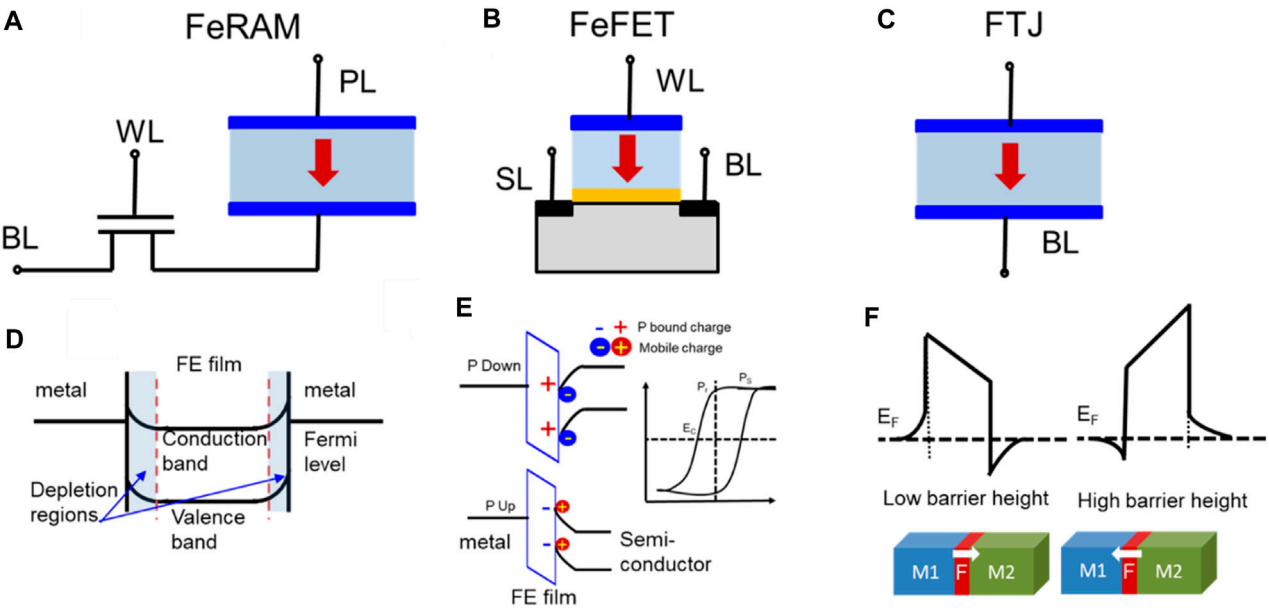

FIGURE 7
Schematics of Ferroelectric memory devices consisting of **(A)** one-transistor-one-capacitor (1T1C) cell known as FeRAM where the non-volatile data storage takes place in the ferroelectric capacitor while the MOSFET acts as a switch, **(B)** one-transistor FeFET memories where the ferroelectric layer is integrated in the MOSFET gate stack. In FeFETs FE polarization charge determines devices On, Off and non-volatility of polarization charges determines memory properties and **(C)** an FTJ, analogous to an MTJ, where change in the direction of FE polarization in the ultrathin FE tunnel barrier, sandwiched between two metals with different work functions, causes an asymmetric barrier potential. This results in modifications of barrier heights for the tunneling electrons for the two-polarization direction, causing resistive switching. **(D–F)** Schematics of the corresponding device band diagrams. Figure reproduced from Majumdar 2022a.

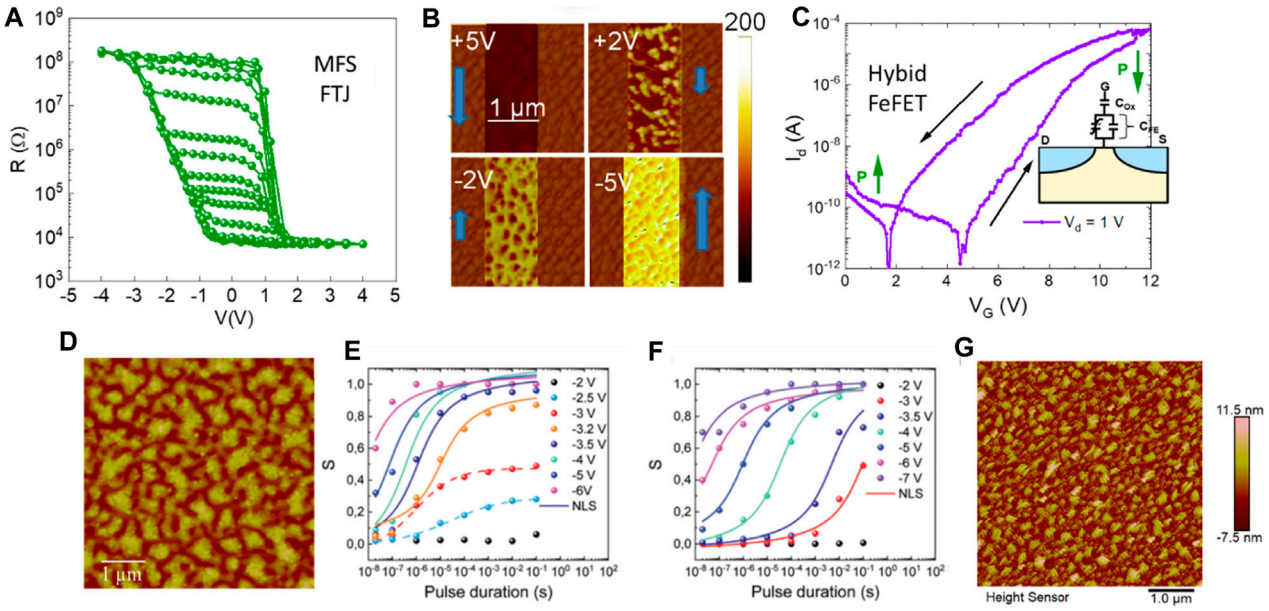

FIGURE 8
Multiple conductance states due to complete or partial polarization rotation in ferroelectric devices. **(A)** Memristive behaviour from FTJs upon programming with different voltages. When scanning between −4 V and +4 V, the devices showed large On/Off ratio of $>10^4$, however for operation within smaller voltage range, the device started showing reduced resistance switching, indicating partial FE domain rotation. **(B)** Electrical data of **(A)** further verified by piezo-force microscope data showing partial domain rotation, shown by bright and dark regions. **(C)** Analog nature of drain current switching in FeFETs with hybrid FE/DE gate layer. Inset showing the FeFET schematics. **(D–G)** Polycrystalline ferroelectric morphology dependent domain switching dynamics where low temperature annealing led to bigger crystallites separated by wide grain boundaries, as shown in the image **(D)** using AFM compared to the film with higher annealing temperature, shown in the image **(G)**. The low temp annealed film domain switching dynamics could only be fitted with nucleation limited switching (NLS) model **(E)** only when applying larger electric fields compared to the high temperature annealed films **(F)**, concluding microstructure dependence of analog conductance in FTJs. (Figure reproduced from Majumdar, 2019a; Majumdar, 2019b; Majumdar, 2023; Majumdar, 2021).

MTJs is possible based on the controllable switching properties of magnetic moments of the ferromagnetic "free electrode" of an MTJ. In the following sections, we will discuss analog conductivity in spintronic components due to possibilities of information storage based on ferromagnetic domain wall motions. However, before going to the details of multilevel data storage, we need to discuss the common spintronic device architectures, operation principles and potential for integration in a scalable technology and then discuss their properties that makes them suitable as analog memories and synaptic weight elements.

Spin-Valves and Magnetic Tunnel Junctions (MTJs): Spin valves are devices where a non-magnetic thin film is sandwiched between two FM electrodes with different coercive fields H_{C1} and H_{C2}. When a spin valve is placed in an external magnetic field (H), the magnetic domains of the two ferromagnetic electrodes aligns themselves as per their coercive fields (H_C) and their net spin direction become either parallelly (P) or antiparallelly (AP) aligned (as shown schematically in Figure 2A). When H is between the coercive fields of the electrodes, *i.e.*, $H_{C1} < H < H_{C2}$, the two electrodes reach an antiparallel alignment. Once H is higher than both the coercive fields, $H > H_{C1}$ *and* H_{C2}, the two electrodes attain a parallel configuration. The spin polarized carriers entering the device through one of the FM electrodes leave the device through the counter electrode and in the transit, they face spin dependent scattering within the device. When the two FMs are parallelly aligned, one of the spin directions can pass without suffering significant scattering leading to a device low resistance (ON) state while for antiparallel alignment, both spin directions suffer significant scattering leading to a high resistance (OFF) state, as shown schematically in Figure 2B. The change in resistance arising from this resistance bi-stability gives rise to the giant magnetoresistance ratio (GMR) in spin-valves.

$$GMR = \frac{R_{high} - R_{low}}{R_{low}} \quad (1)$$

The two FM electrodes inject and detect spin polarized carriers while the non-magnetic spacer decouples the two FM electrodes to ensure independent switching of their magnetic moments. Simultaneously, the spacer should allow unhindered transport of spin polarized carriers. Based on the applied magnetic field, electrical resistance of a spin valve switches between high and low resistance states leading to GMR effect. GMR is defined in Equation 1, where the R_{high} and R_{low} is the high and low resistance of the spin valve respectively. A magnetic tunnel junction (MTJ) is a similar architecture as a spin valve, however the non-magnetic spacer in an MTJ is an ultrathin layer of an insulating material (typically <5 nm) through which spin polarized carriers can quantum mechanically tunnel from one electrode to the counter electrode (Figure 2C). The magnetoresistance, thus obtained in an MTJ, is known as tunneling magnetoresistance (TMR). In an MTJ, one electrode's magnetization is generally fixed known as the pinned layer while the other electrode's magnetization can rotate freely. This

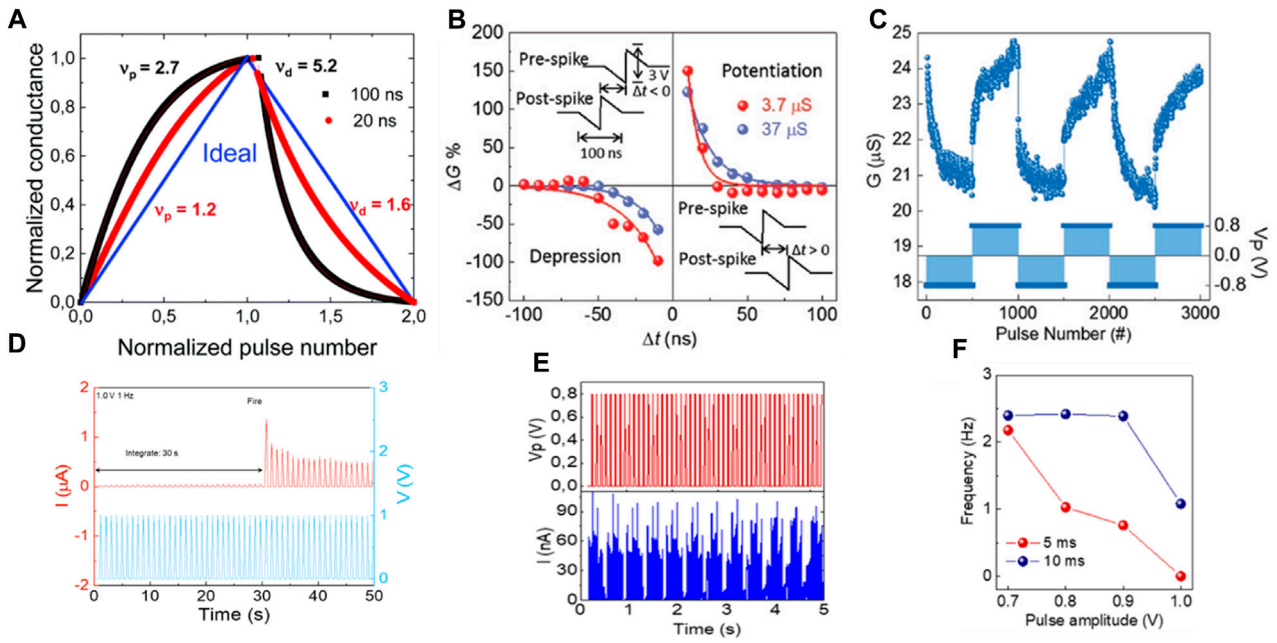

FIGURE 9
Synaptic potentiation and depression due to different applied pulse trains. **(A)** Plot of normalized conductance vs normalized pulse number for 100 ns and 20 ns pulse trains in an FTJ synapse device showing improvement in linearity for excitation with shorter pulses. **(B)** STDP of FTJ synapses when pulses of 3 V amplitude and 100 ns duration was applied with pre and post synaptic pulse delay varying between 100 ns and 20 ns range. **(C)** Synaptic potentiation and depression due to application of symmetric and identical pulse trains of 0.8 V magnitude. **(D)** Neuronal leaky-integrate-and-fire (LIF) response from an FTJ showing under excitation with identical subthreshold pulses (of 1 V magnitude), polarization switching happens after accumulating certain number of pulses. **(E)** oscillatory current response in an FTJ neuron when excited with 0.8 V pulses. **(F)** neuronal current oscillation frequency depending on excitation pulse magnitude.

layer is called free layer. In Jullier's formalism (Julliere, 1975), TMR is defined as

$$TMR = \frac{2P_1P_2}{1 - P_1P_2} \tag{2}$$

In this formalism, it is assumed that spin-polarized carriers travel from one spin polarized electrode to the other without suffering any spin flip and P_1 and P_2 represent spin polarization of electrode 1 and 2, respectively. P is defined as

$$P = \frac{N(\uparrow) - N(\downarrow)}{N(\uparrow) + N(\downarrow)} \tag{3}$$

where $N(\uparrow)$ and $N(\downarrow)$ represents density of states at the Fermi level of the up ($\uparrow$) and down ($\downarrow$) spin carriers. TMR can also be calculated using the tunneling currents, as shown in Eq. 4, where $G_{\uparrow\uparrow}$ and $G_{\uparrow\downarrow}$ represent the junction conductance for the parallel and anti-parallel configuration of the electrodes respectively,

$$TMR = \frac{G_{\uparrow\uparrow} - G_{\uparrow\downarrow}}{G_{\uparrow\downarrow}} \tag{4}$$

However, it is important to note that in all these formalisms, only the effect of the electrodes have been considered. In reality, the interface between the electrodes and the barrier plays a vital role (Majumdar, 2011; Majumdar, 2018a). Spin scattering, trapping, filtering effects at the interfaces are significant in most practical devices and often determine the critical parameters like device performance over large temperature range, reliability, endurance, yield, etc. Also, for multilevel memories, internal magnetic domain structures of the ferromagnetic thin films, based on their fabrication processes, substrate-induced strain states etc. need to be analyzed carefully. Additionally, based on the magnetic memory component architecture, like the spin-transfer-torque MRAM (STT-MRAM), spin-orbit-torque MRAM (SOT-MRAM) or magnetic nano oscillators (Figure 3), different readout current and switching functionalities can be obtained.

Spin-transfer torque MRAM (STT-MRAM): One of the most common spintronic memory components is STT-MRAM. STT magnetization switching, first reported by Berger (Berger, 1996) and Slonczwski (Slonczwski, 1996), arises due to an interaction between magnetization and a spin-polarized current. Here, an exchange of angular momentum between the spins of local magnetic moment and free electrons passing through MTJs gives rise to large magnetoresistance (MR) effect, as shown in Figure 3B. When the two electrodes switch from AP to P configuration, electrons flow from the pinned layer to the free layer. Electrons passing through the pinned layer have the same spin direction as that of the magnetization in the pinned layer and therefore the current is spin polarized. This spin-polarized current exerts STT on the magnetization of the free layer, forcing the magnetization of the free layer to switch. In the reverse switching process, electrons flow from the free layer to the pinned layer. When the electrons pass through the free layer, the electrons with the same spin direction as that of the magnetization in the pinned layer pass through, however, the electrons with the opposite spin direction are reflected at the boundary of barrier and the pinned layer and injected back into the

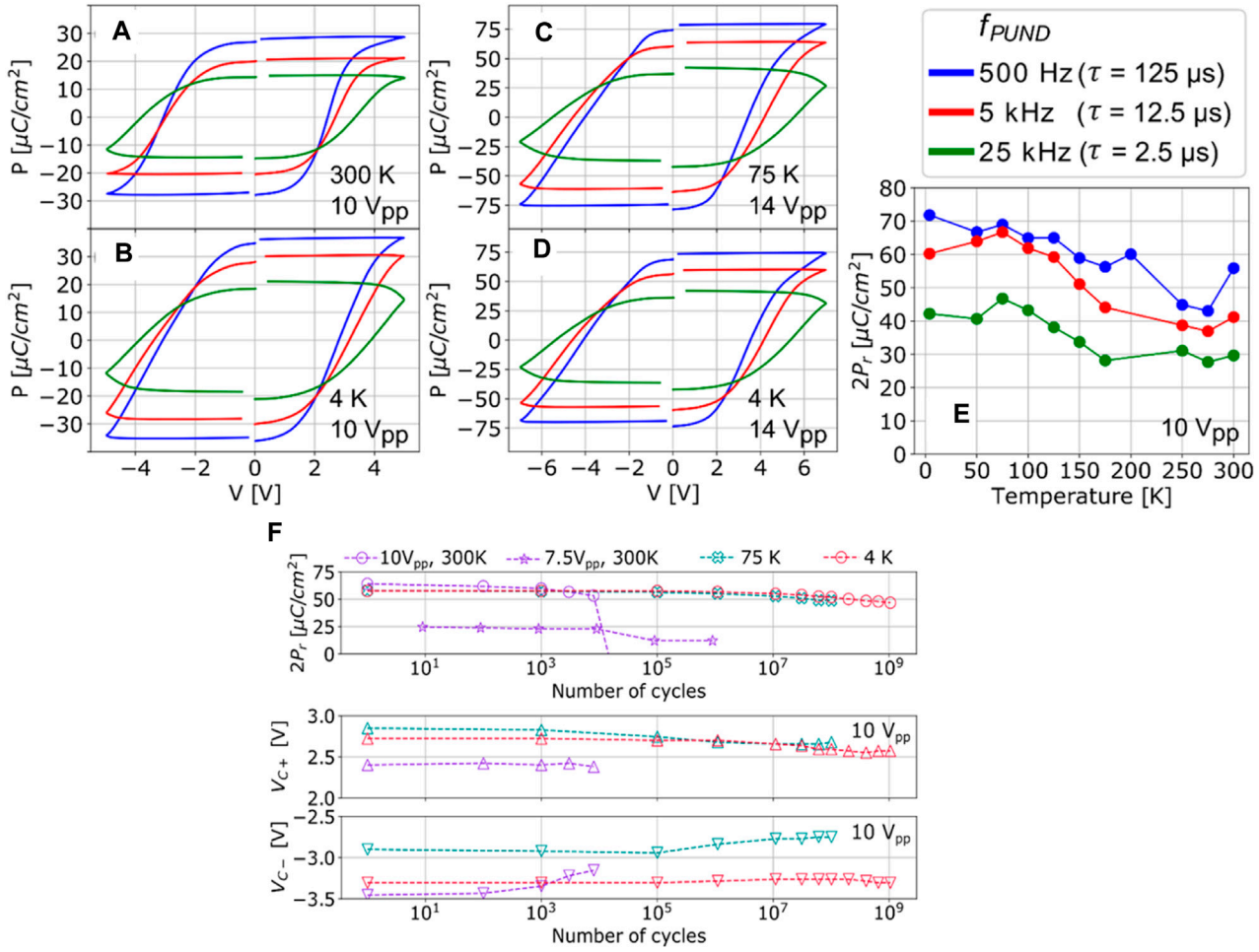

FIGURE 10
(A, B) *P-V* characteristics of HZO devices at fixed magnitude of 10 Vpp and different frequencies of 500 Hz, 5 kHz and 25 kHz at 300 K and 4 K. **(C, D)** P-V characteristics with the critical pulse amplitudes (close to breakdown) of 14 Vpp at different frequencies at 75 K and 4 K. $2P_r$ as high as 150 μCcm^{-2} was measured at 4 K and 75 K. **(E)** $2P_r$ as a function of temperature T at 10 Vpp and different frequencies. **(F)** (Top) The polarization as a function of cycling with 10 Vpp at 100 kHz at 500 Hz frequency for 300 K, 75 K, and 4 K (circles). Additionally, 300 K data for 7.5 Vpp measured using the same frequency. (Bottom) The evolution of Vc+ and Vc-as function of switching cycles for different temperatures. Adapted from Bohuslavskyi 2024.

free layer. This reflected current exerts STT on the magnetization of the free layer, and eventually switch the magnetization of the free layer. STT switching on all-metallic spin valve structures with a Cu spacer was reported by Katine et al. (Katine et al., 2000) rather than the MTJs with MgO barrier. The critical properties for operational suitability of an STT-MRAM cell for a particular memory design and node are its resistance, TMR value, switching current and thermal stability. One key challenge for STT-MRAM being the simultaneous achievement of low switching current and high thermal stability (Kawahara, 2012).

Spin-orbit torque MRAM (SoT-MRAM): In a spin-orbit-torque MRAM (SOT-MRAM) cell, the main mechanism is the spin–orbit torque (SOT) working on the principle of spin hall effect. In SOT MRAM technology, a charge current passing through the heavy metal electrode of the MTJ results in spin accumulation in the free-layer of the MTJ due to the spin-orbit interaction. This causes reversal of the free-layer magnetization to either P or AP state, based on the current direction relative to the free-layer easy axis. SOTs unique switching mechanism is reflected in an advantage over STT-MRAM cell due to its separate paths for read and write operation, as shown in Figure 3C. These paths can be optimized independently leading to the possibility to get improvement in write current and write latency in SOT-MRAM cell. Moreover, SOT-MRAMs show more symmetric write operation due to its spin hall effect switching mechanism, compared to STT-MRAM and offer a lower resistance write path than STT-MRAM to allow faster write operations without effecting dielectric breakdown of SOT-MRAM. The transient analysis at the cell level shows pulse width of 5 ns can be adopted for both STT and SOT to work in the precisional regime. STT-MRAM architecture is nearly 50% area-efficient and 74% leakage power-efficient, compared to SOT-MRAM. However, SOT-MRAM cells are 4× faster and more reliable in terms of read disturbance and dielectric breakdown compared to STT-MRAMs. At the architectural level SOT-MRAM found to be performing more efficiently than the STT-MRAM in terms of read/write energy, read/write latency at the expense of marginal increase in chip-area and leakage-power dissipation (Saha, 2022).

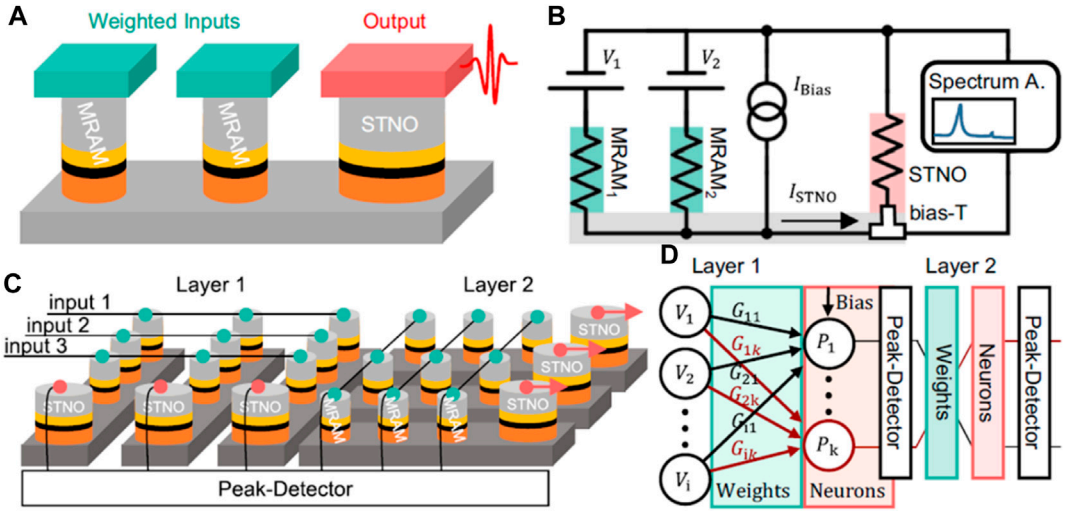

FIGURE 11
Schematic representation of an MRAM based weighted spin torque nano-oscillators (WSTNO). **(A)** WSTNO consists of two MRAM memories as weights and a larger nanopillar as an STNO. The MRAMs work as non-volatile weight elements and the STNO work to transfer non-linear function of the neuron. **(B)** Schematic of the equivalent circuit of the demonstrated system. The input voltages, V_1 and V_2 are multiplied by the MRAM conductance and used to excite the STNO. The STNO current is converted non-linearly into an oscillating output power. **(C, D)** Schematics of two layers with 3 inputs and 3 outputs each demonstrating the scaling of the suggested neuromorphic circuit consisting of a crossbar array of MRAMs and STNOs at the output of each layer. The number of inputs, outputs and layers can be scaled, increasing the footprint linearly. Reproduced with permission from Böhnert 2023.

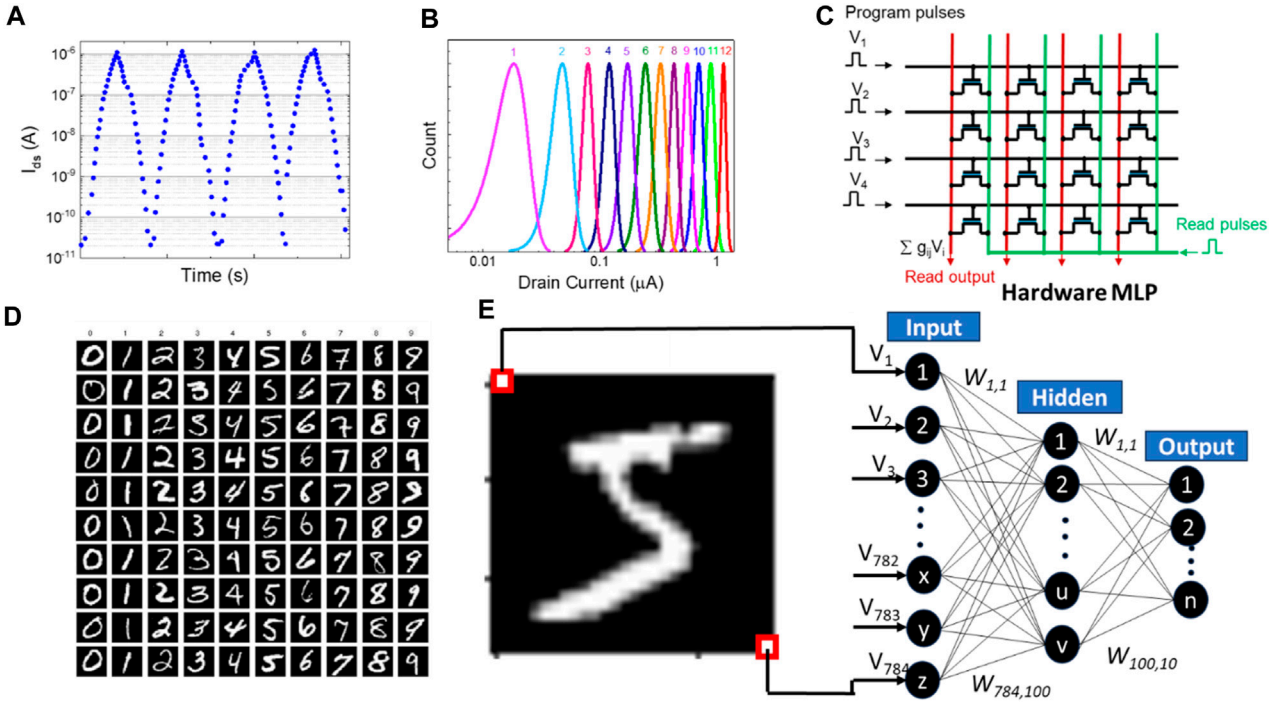

FIGURE 12
(A) Channel currents in analog FeFET device over multiple pulsed switching cycles showing reproducible intermediate state switching. **(B)** Distribution of the 12 conductance states of the FeFET device over multiple cycles of weight update. **(C)** Schematic diagram of the vector matrix multiplication (VMM) architecture using FeFET based crossbar arrays where programming voltage pulses are used as input to the rows connecting the gate terminals and current outputs are extracted from the columns connecting the drain current terminals. The synaptic weight is indicated by the conductance of each FeFET (g_{ij}). The current output from the crossbar is the product of the input voltage (V_i) and FeFET channel conductance (g_{ij}). (**D–E**) Schematic illustration of MNIST handwritten dataset **(D)** and its classification operation in a multi-layer perceptron based deep neural network.

TABLE 1 Sample numbers, deposition parameters and approximate thicknesses (from Majumdar, 2012a).

Sample	Temperature(°C)	No.of pulses	Frequency(Hz)	Approximate thickness(nm)
S1	780	10,000	5	400
S2	780	5,000	5	200
S3	780	10,000	10	400
S4	780	15,000	10	500
S5	700	5,000	10	200

Spin-torque Nano-oscillators (STNO): While the previously discussed MRAM cells can serve excellently as electronic synapses due to their memory properties arising from FM domain structures, other spintronic structures can provide biological neuron-like functionalities (Torrejon, 2017). Spin-torque nanoscale oscillators (STNO) are junctions like spin-valves or MTJs that combine STT and GMR or TMR effects (schematics shown in Figure 3D) to produce oscillating outputs. An injected dc current through the MTJ stack, turns the output current into spin polarized current, that generates the magnetic excitation modes of the free FM layer due to STT. This magnetization dynamics is converted into voltage oscillations utilizing GMR or TMR effect, thus producing an oscillatory electrical signal. The electrical signals are directly linked to the dynamics of the magnetization of the free FM layer and to the MR properties of the junction stack. Magnetization precision frequencies may vary from hundreds of megahertz to several tens of gigahertz resulting in radio-frequency oscillations of up to tens of millivolts, that can be detected by measuring the voltage across the junction. STNOs are ultra-small footprint devices where the lateral size can be scaled down to 10 nm limiting the power consumption to 1 μW (Sato, 2014). As additional advantage, STNOs are tunable with a rate depending on the magnetic mode (considered from 10 MHz/mA up to 1 GHz/mA) and agile (from 1 ms down to 1 ns relaxation time), CMOS compatible and radiation hard. These specificities make them promising candidates for integration in future radio frequency and space electronic systems. Like the frequency of biological neurons, STNO frequencies are highly sensitive to the magnetization dynamics of neighboring oscillators that are coupled to them (Slavin, 2009; Housang, 2016). Finally, the fabrication process for STNO technologies is identical to the STT-MRAMs, making it possible to fabricate the neurons and synaptic devices in same process steps (Grimaldi, 2014), which is of vital importance for reducing fabrication complexity and cost.

Physics of ferromagnetic materials for cryogenic analog memory and neuromorphic computing

The field of spintronics witnessed many fascinating materials and device architectures exhibiting novel physics that lead to miniaturization of computer memories to an unprecedented level. Introduction of semiconductors in the field of spintronics has also substantially contributed to versatile multifunctional spin devices for future memory and logic operations. In this section, we discuss the sensitive and complex world of magnetic domains in thin FM thin films that need to be properly understood and controlled in order to implement them in memory and neuromorphic devices, particularly when they are used in more demanding applications where maintaining data integrity is essential.

Magnetic domain and domain dynamics: All the synaptic and neuronal functionalities like linearly programmable synaptic plasticity, long and short-term potentiation and depression (LTP, STP, LTD, STD, respectively), LIF neuron firing and recovery etc. depend strongly on the magnetic and magneto-transport properties of the FM material. To have an in-depth understanding of MR effects, we have to focus on the spin structures at the nanoscale, which includes domain walls, vortices, skyrmions etc. (Malik, 2020). These complex spin structures arise due to the competition between different energy contributions such as magneto-crystalline anisotropy, magnetoelastic coupling, shape-induced anisotropy or dipole interactions in magnetic materials. Magnetic domain structures and their dynamics is of vital importance for controlling analog memory programming and data retention in spintronic memories. Based on magnetic thin film properties, such as strain, microstructures, grain and phase boundaries etc., magnetic domain structures can vary greatly opening a vast design space for proper control of domain dynamics for their application in memory and neuromorphic hardware. As an example, we focus on half-metallic manganite thin films of $La_{0.67}Sr_{0.33}MnO_3$ (LSMO) (Majumdar, 2013) and evaluate the role of different fabrication parameters, such as substrate-induced strain, temperature, growth rate etc. on the magnetic domain structures and their proper control.

Magnetic domain configuration of a FM thin film depends strongly the balance of the anisotropy energies, as mentioned above. Strain on the crystal lattice is one the most critical factors in determining domain configuration. Magnetoelastic effects associated with substrate induced compressive strain results in perpendicular magnetic anisotropy in FM thin films (Wang, 2014; Wang, 2018). From the measured magnetization vs magnetic field (*M-H*) curves and magnetic force microscope (MFM) imaging, magnetization reversal at 4 K in LSMO nanowires was shown-by Malik et al. and the effective magnetic anisotropy constant (K_{eff}) was calculated (Endo, 2010). With decreasing temperature, K_{eff} increases indicating the enhancement of the magnetoelastic energy at low temperature. Magnetic domains of LSMO thin films are found mobile at 300 K, that eventually settles into a labyrinthine-like pattern. However, at 4 K, they enter a randomly distributed state, that is attributed to the larger saturation magnetization (M_S) and K_{eff} at low temperature. Domain imaging showed how domain reversal at different

magnetic fields occur at low temperatures. For the external magnetic fields exceeding 0.7 T, the LSMO was fully saturated, exhibiting a mono-domain state. At 0.5 T, domains with downwards magnetization started to nucleate. As the field further decreases, the down domain size expanded further, and the volume ratio of up domains shrank. In the absence of external magnetic field, almost equally populated up and down domains were formed, confirming the demagnetization state. In a $La_{0.5}Sr_{0.5}MnO_3$ thin film, at the boundary of ferro- and antiferromagnetic phases, Majumdar et al. (Majumdar, 2024) measured magnetization reversal using photoemission electron microscopy (PEEM), with magnetic contrast from x-ray magnetic circular dichroism (XMCD), known as XMCD-PEEM. These data provided an in-depth understanding of the magnetic domain structures and their reversal at cryogenic temperatures. As shown in Figure 4, due to sweeping magnetic field, XMCD-PEEM image revealed how the magnetic domain rotation happens in $La_{0.5}Sr_{0.5}MnO_3$ thin film at 40 K. The full red or blue states represent magnetic saturation in up or down direction i.e., all electronic spin states being aligned parallel to the external magnetic field direction. Upon withdrawing the field, the saturated state continued in these films, representing the non-volatility of the "1" and "0" states. Application of fields of a few mT resulted in mixed domain phase, showing how the intermediate states appear in the film and their evolution happens due to increasing field strength. The dynamics of the up and down polarized magnetic domains were studied by sweeping the magnetic fields from positive to negative value and back. The red part in the image (A), representing the fully up-polarized domains, remained in their programmed state when the magnetic field in withdrawn (B). Upon field reversal, white parts started to appear (C-D) showing the mixtures of orientations leading to nearly depolarized states in some local areas while the appearance of the blue parts represented existence of some down-polarized domains in the predominant up-polarized matrix. Upon increasing the reverse field strength, the blue area started increasing, eventually consuming the entire area (E-I). The stability of these domains was checked by imaging the domains over extended period after withdrawing the magnetic field and interestingly it was found that some domains are more pinned and can retain their orientation for hours after removing the field. All the intermediate states were found reproducible. However, the magnetic history of these samples was important in exactly determining their mixed polarization states.

In order to address the finite retention of mixed polarization phase, domain reversal dynamics and their stabilization needs more in-depth study and analysis. Clarification of domain pinning mechanism through naturally occurring or artificially engineered pinning sites is an important subject that needs discussion in this direction. Lecoeur et al. (Lecoeur, 1997) studied the effect of epitaxial and polycrystalline films on the magnetic domain reversal and MR effects of FM thin films and their results demonstrate that the presence of microcracks can effectively manipulate the domain structure in LSMO films. In the polycrystalline thin films, formation of domain structures is largely influenced by the grain structure. The average coercive field *Hc* was found to be more than twice as large as that of a single crystal film.

A Kerr-microscope study of the magnetic thin films showed that in polycrystalline films the grains switch mostly independently; each in a narrow range of fields but the distribution of switching fields becomes quite large while considering macroscopic area leading to a higher coercivity of the film. In the smaller grains, *M* is mostly uniform, however, in larger grains, domain walls were found to be involved in the reversal process. Effects of grain-boundaries on the magnetoresistance properties of perovskite manganite films was also studied by Gupta et al. (Gupta, 1996), that showed large MR over a wide temperature range down to 5 K can be obtained in polycrystalline films, which can be explained in terms of switching of magnetic domains in the grains and disorder-induced canting of Mn spins in the grain-boundary region. However, in epitaxial LSMO films, magnetization occurs by rotation and domain-wall movement over large areas unlike in the polycrystalline samples. A domain wall can cross a grain-boundary and its motion can get impeded by surface defects such as scratches. Large low-field MR in polycrystalline films is a result of tunneling of electrons through grain boundary.

Fabrication process control for reliable analog operation

Magnetic domain structures, their motion and stability can be engineered through control of nanofabrication process parameters. For instance, in LSMO films, prepared by pulsed laser deposition technique, substrate-induced strain and different deposition parameters can modify the high and low angle grain-boundaries (Figure 5) affecting the magnetization reversal dynamics and analog response (Majumdar, 2012a). For instance, films grown on single crystal MgO substrates contained higher number of structural defects compared to those on $SrTiO_3$ (STO) and $NdGaO_3$ (NGO) substrates leading to higher polycrystallinity in the films. Also, lower deposition rate and thicker films resulted in more polycrystallinity and grain boundaries that caused broader magnetic transition (Figure 5), deposition parameters are shown in Table 1. This was attributed to large lattice mismatch (9%) between the substrate and the LSMO film. The LSMO films deposited on STO and NGO showed sharper magnetic transition due to lower effect of substrate induced strain. The MR effect measured up to 300 mT field, clearly showed two contributions, one due to grain boundary tunneling and the other due to colossal MR effect. In addition to the substrates, lower pulsed laser frequency, higher deposition temperature and increasing film thickness led to more structural defects in the films, causing broader magnetic transition.

Hawley et al. (Hawley, 2000) studied the stability of the magnetic domain structures in LSMO films grown at 750°C and 800°C. Scanning tunneling and magnetic force microscopy was used to image the film microstructure and domain structures as a function of in-plane magnetic field strength. With increasing field strength, the maze-like domain structures in the film were found to become striped domains with reduced out-of-plane magnetization and decreased wall spacing that confirm parallel alignment of in-plane spin polarization. After removal of the field, the stripe domains remained, however, the wall spacing, and z-component of polarization was found to return to the original value. It was found that magnetic structure of the film with a thin insulating cap layer was reversible, suggesting pinning of the domain walls by the capping layer.

Spintronic synapses: Utilizing this magnetic domain formation and their reversal dynamics in ultrathin FM films, spintronic components with analog and multiple bit storage elements and synaptic weight elements can be fabricated. Previous studies reported that magnetic devices can have promising performance as memristors by storing analog information in their magnetic domains and textures (Sharad, 2012). A spintronic memristor was shown by Wang et al. (Wang, 2009) based on magnetic domain wall displacement of a (Yamaguchi, 2004) in a spin-valve. Also, domain wall motion based memristors has been experimentally demonstrated in MTJs (Chanthboula, 2011; Lequeux, 2016). Position of the domain walls in these spintronic memristors determine the lower or higher resistance states (Grollier, 2003). SOT switching in an antiferromagnet–ferromagnet bilayer has also demonstrated memristive behavior (Miron, 2011; Liu, 2012; Fukami, 2016a; Fukami, 2016b). The variation in switching currents among the magnetic domains with varying exchange-bias magnitudes and directions at the antiferromagnet–ferromagnet interface results in memristive behavior in these structures (Kurenkov, 2017). Thus by harnessing the materials physics, one can design programmable domain features and dynamics. (Marcovic 2020).

Spintronic neurons: In addition to the MTJ-based technology, other types of neurons, based on domain-walls and skyrmion-based neurons have also been reported in literature. Sharad et al. proposed magnetic solitons (Sharad, 2012), that can be manipulated and moved over large distances with spin torques and spin–orbit torques (Yamanouchi, 2004; Thomas, 2010; Woo, 2016). These devices take advantage of the fundamentally stochastic nature of the domain wall motion, their depinning and magnetic nanotextures (Hayashi, 2006; Hayward, 2015; Zázvorka, 2019). Simulations show that cumulative nature of domain wall motion or skyrmion accumulation (Li, 2017; Pinna, 2018; Zázvorka, 2019) and switching can give rise to LIF kind of neuronal activity.

In a recent work, Yang et al. (Yang, 2021) studied a complete spin-based integrated neural network by electrically connecting spin synapses (named, spin-S) and spin neurons (named, spin-N) and evaluated their performance for a pattern classification task, as shown in Figure 6. A stack structure of MgO/CoFeB/W was used in the experiments and the Hall resistance of the device was determined by the position of the current-driven DW motion. A very linear and symmetric weight update in these spin-S devices were attributed to the uniform shifts of the DW due to application of the pulse train of ±12 V of 50 ms duration with a y-axis magnetic field of −80 Oe. It was further observed that a precise weight can be achieved by means of the stripe domains, where domain width can be controlled by material parameter engineering, including perpendicular magnetic anisotropy, dipole energy, Dzyaloshinskii–Moriya interaction, and pinning densities. A high classification accuracy of over 93% was achieved only using the optimization of spin-S and spin-N components without further support of additional software or circuit optimization, proving in terms of synaptic weight update linearity, symmetry, and stability, spintronic components can achieve quite promising performance.

Böhnert et al. (Böhnert, 2023) have demonstrated weighted spin torque nano oscillator (WSTNO) as a programmable building block for neuromorphic computing. The WSTNO circuit used two types of spintronic devices, MTJs as synapses and non-linear STNOs acting as a neuron. The nonlinear output based on the weighted sum of the inputs is demonstrated using three MTJs. The STNO shows an output power more than 3 μW and frequencies of 240 MHz. Both types of MTJs are fabricated using single fabrication process, compatible with monolithic CMOS integration, paving ways for complex neuromorphic computing systems.

Physics of ferroelectric devices for neuromorphic computing

Most of the materials and device physics related to domain formation and reversal for ferromagnetic components can be almost directly applied to ferroelectric components, except for the fact that ferroelectric devices being charge based devices, does not possess infinite endurance, especially in scaled ultrathin capacitor-based structures. However, ferroelectric devices bring the advantage of compatibility with existing CMOS fabrication facilities, especially high-k oxides like hafnia-based systems and large On/Off resistive switching, making their control over analog states more robust and reproducible. Additionally, the rich physics of FE polarization switching, polarization retention and relaxation in FTJ and FeFET architectures opens an avenue for designing dense, low-power, analog spiking neurons and synapses, similar to their biological counterparts with minimum number of components.

FeRAM, FTJs and FeFETs:

Figure 7 shows schematics of different ferroelectric device architectures and their working principles. Traditional FeRAMs consist of a FE capacitor in series with a MOS transistor that stores the memory in terms of FE polarization charge with the MOS transistor acting as a switch. Although a matured technology due to its robust operation, high operating voltage, destructive readout and large footprint of FeRAMs pose challenges for their integration in dense memory arrays.

Ferroelectric tunnel junctions (FTJ): In an FTJ, analogous to an MTJ, two different metal or semiconducting electrodes are separated by an ultrathin layer (1–5 nm) of FE film. However, in an FTJ, the barrier plays the major role as the FE barrier is the active component unlike the passive barrier in an MTJ. In a sweeping electric field, the FE polarization direction in the barrier switches between up or down directions depending on the electric field polarity. Metallic electrodes in FTJs provide the mobile charge carriers to screen the FE bound polarization charges providing the stabilization of FE polarization. Based on the direction of FE polarization in the tunnel barrier, charge carriers are either accumulated or depleted from the FE-electrode interface. Junctions with different metal electrodes on either side of the FE causes an asymmetric screening effect, producing an asymmetric barrier potential in the FTJ. Thus, polarization switching induced modification in the mean tunnel barrier height causes the electrical resistance of FTJs to switch between high and low states. This results in device Off and On states, respectively and this phenomenon is known as the tunneling electroresistance (TER) effect (Kohlstedt, 2005; Tsymbal, 2006; Gruverman, 2009). TER is defined as,

$$TER = \frac{R_{high} - R_{low}}{R_{low}} \tag{5}$$

Where R_{high} and R_{low} are the junction resistance in device Off and On states, respectively. In earlier reports, FTJs with two metal

electrodes are mainly reported. However, studies found that one semiconducting electrode at one end of the FE is capable of leading to larger resistive switching effect due to the Schottky barrier formation at the FE/semiconductor interface (Majumdar, 2018b; Majumdar, 2019a). When the polarization direction moves away from the semiconductor interface, the formed Schottky barrier adds to the effective barrier width, in addition to change in barrier height of the FTJs, causing a larger *TER* effect.

Besides the crucial role of electrodes in determination of barrier height asymmetry (Maksymovych, 2009), charge screening at the electrode-FE interface also affects the long-term stability of FE polarization that determines the non-volatile and volatile data retention of the FTJs. For an electronic synapse, stability of FE polarization can affect the long or short-term potentiation (LTP, STP) and depression (LTD, STD) characteristics. Similar to MTJs, FTJs were mostly used as a bistable resistive switching memory. However, Chanthboula et al. (Chanthboula, 2011) first demonstrated that FTJs not only work as a binary memory, but programmable control of partial switching of FE domains can lead to multiple intermediate resistance states. In large area devices, multiple FE domains are formed to maintain an energetically stable configuration. Control of a mixed domain phase in these devices with coexisting up and down domains is therefore comparatively straight forward. However, with device scaling down, number of FE domains involved approach from multiple to a few-domain limit and a precise control over intermediate states becomes a challenge. For devices with ultrathin FE films, another important consideration is the interface quality of the FE films with its electrodes. In oxide FE based FTJs, in addition to the FE polarization reversal induced resistive switching, multiple other conduction phenomenon can be observed such as electric-field-enhanced reversible migration of oxygen vacancies (Garcia, 2014; Qin, 2016), filamentary conduction and so on. Defects inside the FE film and at the interface cause charge trapping sites, which, over multiple field cycling builds up significantly, causing the device to operate with less On/Off ratio and eventually to fail due to breakdown. In neural network applications, especially for DNN training operation, this is a challenge where 10^9 cycles of on-off cycles are expected from the synaptic weight elements. Therefore, while designing large-scale networks with nanoscale FE memories, control of interface quality and FE domain dynamics, needs to be considered carefully. Also, for synaptic weight elements, switching and relaxation timescales, are of vital importance. A proper design of material stack and device configuration can create an extremely energy efficient and versatile hardware neural network based on FE devices.

Ferroelectric field effect transistors (FeFETs): A FeFET is analogous to a metal-oxide-semiconductor field effect transistor (MOSFET), where the gate dielectric layer of the MOSFET is replaced by a FE material. In a FeFET, an applied gate bias polarizes the FE layer, and the net FE polarization pointing towards or away from the MOSFET channel. With the polarization direction pointing toward the channel, electrons accumulate at the semiconductor-FE interface in *n*-type semiconductors, causing in increased conductivity in the channel, that leads to the device On state. On the other hand, when the polarization direction points away from the channel, a depletion of electrons at the FE-semiconductor interface causes the drain-source current to decrease and leading to device Off state. For a FeFET with *p*-type semiconductor channel, a reverse voltage polarity and therefore FE polarization determines the On and Off states.

In order to operate the FeFET with full polarization switching and thus having the full memory window (MW) available, a gate bias higher than 5 V magnitude is generally needed. However, in a CMOS-integrated circuit, one critical consideration is to keep the access transistors small that poses limitation on the maximum available programming voltage. This opens the design space with novel materials, electrodes, designed interfaces and device architecture for maximizing the memory performance within low operating voltage limit. For analog memories, a large number of stable intermediate states are needed using a relatively lower programming gate bias that causes partial polarization rotation of the FE and leaving a mixture of up and down polarized domains in the gate stack. This mixed polarization phase can neither fully accumulate nor deplete the semiconductor channel, causing intermediate conductance levels. One observed challenge for the partially polarized states is their instability in comparison to the fully polarized states. Additionally, there exists a history dependence of the intermediate states that requires different programming and erasing protocols while designing analog memory circuits with the FeFETs.

Physics of ferroelectric materials for cryogenic analog memory and neuromorphic computing

As the most researched CMOS back-end-of-line (BEOL) compatible ferroelectric in the recent times, we discuss the physics of FE Zr-doped HfO_2 (HZO) system. However, we also discuss other single and polycrystalline FE material due to lack of enough experimental data on Hafnia-based systems. The origin of ferroelectricity in HZO have been discussed in detail in literature (Kim 2019; Onaya 2019). Here, we focus our discussion mainly on the polarization switching and FE domain dynamics, together with the polarization relaxation mechanism. The transient switching dynamics of FE components decides the synaptic and neuronal functionalities of these devices and therefore it is of vital importance to understand and master their proper control.

Ferroelectric materials belong to the broad class of dielectric materials where a net electric polarization arises due to a broken centrosymmetric phase of the crystal lattice and the net polarization can be switched using an external electric field. The net polarization in a FE material changes non-linearly under an electric field. When an external electric field exceeds a certain field, the net polarization of the FE suddenly increases reaching a saturation polarization (P_S) eventually. Upon withdrawal of the electric field, the net polarization is maintained at a non-zero value, called the remnant polarization (P_r). On reversing the polarity of the applied field, the polarization direction rotates to the opposite direction, reaches a zero value at the coercive field (E_C) and eventually reaches the negative P_s value. P_r, P_s and E_C are the critical parameters for FE materials. When the electric field is high enough to saturate the FE polarization, the *P-E* hysteresis loop is wider, and the loop is called a FE major

loop. However, when the applied field is not enough to reach *Ps*, the P-E hysteresis loop narrows, leading to a FE minor loop. The trajectories and dynamics of the major and minor loops are vital parameters for designing stable analog operation of the memories. It is found that long-term retention can readily be obtained for a device reaching its FE major loop (Majumdar 2019a). Therefore, depending on the applied programming voltage, pulsing scheme etc., a non-volatile or a volatile memory performance can be achieved.

In FE devices, there are multiple mechanisms in addition to polarization switching that leads to performance degradation. One such effect is imprint, and another is fatigue. When the switching of one polarization direction is more favored compared to the other and the hysteresis loop is asymmetric along the electric field axis, i.e., the $+E_C$ and $-E_C$ values are different for polarization switching, the FE components are known to have an imprint effect. This is analogous to magnetic exchange-bias effect in FM films. FE-electrode interface and structural defects in the FE play a major role in imprint effect. Fatigue in FE components appear due to repeated switching cycles causing charge trapping, leakage currents or structural degradation in the FE due to bias stress especially arising from high current due to oxygen vacancy movement inside the film. Fatigue results in loss of P_S and P_r values. Device endurance properties strongly depend on the fatigue properties. However, devices can sometimes recover from fatigue states upon withdrawal of the field.

Ferroelectric domain dynamics

In polycrystalline ferroelectric thin films, polarization switching is generally inhomogeneous. The switching mechanism can be explained by nucleation-limited-switching (NLS) model (Tagantsev, 2002) where polarization reversal takes place through independent switching kinetics of different areas in the film. The normalized area of reversed polarization, *S* can be approximated as a function of time *t* and voltage *V* as,

$$S_{\pm}(t, V) = \frac{1}{2} \mp \arctan \frac{\log(t_{mean}(V)) - \log(t)}{\Gamma(V)} \quad (6)$$

assuming a Lorentzian distribution of the logarithm of mean nucleation times (t_{mean}) for each applied voltage pulse *V* with width $\Gamma(V)$ and centred at $\log(t_{mean}(V))$. When considering a one-to-one correspondence between the ferroelectric domain configuration and the FTJ resistance *R*, the fraction of domains with upward polarization (*S*) and with downward polarization (1−*S*) can be expressed using a parallel circuit model,

$$\frac{1}{R} = \frac{1-S}{R_{On}} + \frac{S}{R_{Off}} \quad (7)$$

where the lowest resistance R_{On} and the highest resistance R_{Off} represent fully downward ($S = 0$) and fully upward ($S = 1$) ferroelectric states. (Boyn, 2017; Ma, 2020) From the experimental Resistance–Voltage hysteresis loops (Figure 8), the normalized switched area as a function of programming pulse duration can be calculated at different pulse amplitudes by plotting *R* as a function of pulse duration and by fitting with the NLS model. From the fitted t_{mean} values, it was found in different FE systems (Boyn, 2017; Majumdar, 2021) that the switching time depends exponentially on the electric field as described by the Merz law. (Merz, 1954) Depending on the polycrystalline film morphology (Figure 8), the switching dynamics and mean switching time can be modified and with a proper electric field, the switching time can be as fast as sub-nanosecond, leading to possibility of ultrafast write time in FE memory components. A few reports showed (Park, 2016; Wei, 2022) a 2-stage switching dynamics in ferroelectric HZO, the reason for which was ascribed to either mixture of phases, positively charged oxygen vacancies compensating for the polarization charges or imprint field. This 2-stage switching leads to two different mean switching fields and based on applied field strength or pulse duration, a certain timescale for switching operation can be chosen. In a recent work, Dahlberg et al. (Dahlberg, 2023) showed higher switching speed can be obtained in Zr-rich HZO showing higher anti-ferroelectric phase ensures faster switching speed, however at the cost of lower remanence. As thermal energy assisting domain rotation and oxygen vacancy movements are restricted at lower temperatures, domain dynamics at cryogenic temperatures is expected to be different and need to be investigated in detail for memories and in-memory-computing circuits operating at cryogenic temperatures.

Fabrication process control for reliable analog operation

Analog operation in ferroelectric components results from gradual domain rotation. This feature can be realized using optimized ferroelectric film morphology or FE device design. In polycrystalline thin films, domain rotation is rather gradual where higher number of grain boundaries and structural defects are present. While this was considered an undesirable aspect for digital memory operation, this has proven to be a more effective way to maintain linearity in weight update in synaptic elements. By modifying substrate-induced strain states (Goh, 2020), crystallization temperature and protocol (De, 2021a) and stack ordering (Migita, 2021), it is possible to have control over polarization switching dynamics which can influence the linearity in weight update from FE components. In a recent report, Arabar et al. reported better control of analog states can be achieved using a FE-DE superlattice structure (Arabar, 2022). Similar conclusion was drawn by Majumdar et al. (Majumdar, 2023) where in 2D semiconductor-based synapses linearity of conductance update was obvious. However, this hybrid stack comes at a price of increased depolarization field, leading to quick decay of conductance states. It was shown through simulation that optimization of the stack by using proper thickness and dielectric constant of DE, depolarizing field can be minimized in these structures to achieve long-term retention (Majumdar, 2023).

Ferroelectric synapses

Different kinds of synaptic plasticity functions like long-or short-term potentiation and depression (LTP, STP, LTD and STD respectively) functions have been demonstrated in ferroelectric devices (Boyn, 2017; Majumdar, 2019a) (Figures

9A–C). In FTJ synapses, the applied voltage pulses were found to align the FE domains in a way that the net polarization value of the FE changes resulting in a momentary increase in post-synaptic current (PSC). Withdrawal of the excitation pulses, especially single pulses coming at sufficient intervals lead to a quick decay of the PSC, resulting in STP and STD. STP or STD arises due to finite retention of intermediate polarization states, i.e., when polarization direction is not in a strictly perpendicular orientation, and lead to the recovery of the initial conductance states. Magnitude, width, and frequency of the excitation pulses can modify the relaxation time period and can turn the STP and STD behavior to LTP and LTD behavior (Wang, 2021). In oxide perovskite FTJs, different STDP learning curves based on designed voltage pulses have been demonstrated through controlled ferroelectric domain dynamics by Boyn et al. (Boyn, 2017) In $Hf_{0.5}Zr_{0.5}O_2$ based FTJs, synapse potentiation and depression and STDP were also demonstrated (Yoong, 2018), suggesting a viable path of fabricating FTJs with good CMOS compatibility.

It has often been seen that linearity and symmetry of synaptic conductance has a clear trade-off with the dynamic conductance range. Within a limited conductance range (Majumdar, 2021; Majumdar, 2022b), it is possible to achieve better linearity in weight update compared to when using a larger dynamic range. This can be due to use of programming pulses of certain magnitude or width. In FE devices, large dynamic range is generally associated with higher amplitude or longer duration pulses that lead to more drastic rotation of polarization initially followed by saturation which inhibits the possibility of linear weight update. However, in a FeFET, control over channel conductance for larger dynamic range and linearity is more probable compared to FTJs due to the additional advantage of large On/Off switching of MOSFETs. In such systems even, linearity is mostly limited to application of continuously increasing pulse amplitude that makes the driving circuit complicated.

A single FeFET synapse, based on ferroelectric hafnia and integrated in a 28 nm HKMG technology was shown by Mueller et al. (Mueller, 2012), where a non-volatile, gradual switching of the FE layer was used to continuously tune the conductivity of the transistor channel. This continuous change in conductivity led to the possibility of synaptic weight update over multiple switching pulses leading to synaptic potentiation and depression. Lederer et al. (Lederer, 2021) demonstrated that hafnia based FeFETs are extremely promising as synaptic weight elements that can find application for hardware acceleration of neural networks. Utilization of increasing magnitude or increasing pulse width pulse schemes in Si- or Zr-doped HfO_2 based FeFETs could achieve a linear weight update in devices as small as $100 \times 100\ nm^2$. From the design point of view, smaller grain sizes were found suitable for further device scaling and therefore, microstructure engineering by varying grain size and crystallographic orientation will be of major importance for scaled ferroelectric synaptic devices. For analog operation, devices with larger channel lengths and widths are generally suitable as they involve a large number of FE domains where a mixed polarization phase is easier to achieve. In FeFETs, voltage pulses are applied either at the gate and/or source-drain terminals that switch the polarization of the FE layer in a non-volatile manner, tuning the channel conductivity gradually. Progressively increasing gate pulse amplitude leads to gradual switching of FE layer in the gate stack in the multi-domain devices, turning an initially high-V_{th} state into a low-V_{th} state. STDP was also exhibited by FeFETs (Mulaosmanovic, 2017). A multilayer perceptron based deep neural network accelerator with FeFETs as the analog synapses were demonstrated by Jerry, et al. (Jerry, 2017) A 5-bit symmetric potentiation and depression behavior with a 45x tunability in conductance range was reported using 75 ns pulses. A transient Presiach model predicted the minor loop trajectories and P_r values for arbitrary pulse width, amplitude, and device history. A benchmarking done on on-chip learning accuracy for an affordable area, latency and energy overhead showed a FeFET based synaptic core could achieve a 10^3 to 10^6 times acceleration in online learning latency over multi-state RRAM based analog synapses. Hybrid FeFETs using composite dielectric (DE)-FE gate stack has shown superior performance in achieving multiple intermediate conductance states with high reproducibility due to depolarizing field induced division of larger domains into smaller domains and voltage division across the DE-FE gate stack (Arabar, 2022; Majumdar, 2023). De et al. (De, 2021a) has shown effect of device-to-device (D2D) and cycle-to-cycle(C2C) variation on neural network performance based on the Fe-FinFET platform. The results show that stochastic D2D variation gets compensated during online training and shows almost no effect on the training accuracy, however, a substantial drop in inference accuracy can occur due to systematic degradation of device retention in analog neural networks. Quaternary and binary neural networks with FefinFETs as synaptic devices however demonstrated excellent tolerance toward the stochastic and systematic D2D variations arising from coexisting paraelectric and FE phases due to incomplete crystallization of HZO (De, 2021b).

For large-scale circuit integration of ferroelectric memories, compact modelling of the device performance is of major importance. While several analytical models for the polarization switching in FE materials exist, their parameters are either experimentally challenging to extract, or lacks physics-based definitions, or are computationally very demanding. A few recent works (Lederer, 2023; Paasio, 2023), have shown Spice and Verilog-A compatible Jiles-Atherton model can be implemented for modelling FE capacitors that provides highly computationally efficient prediction of intermediate states by transient switching.

Recently, nearly ideal linear weight update from HZO based devices have been shown at cryogenic temperatures (Bohuslavskyi, 2024). It is shown that temperature is an additional parameter controlling the FE domain dynamics and below 100 K, a significant improvement in potentiation and depression linearity can be obtained, especially at higher operating frequencies. Lack of thermal energy and frozen charge defects at cryogenic temperatures can lead to improved control over FE domain dynamics, leading to the possibility of high accuracy in-memory-computing below 100 K.

Ferroelectric neurons

Polarization switching in FE thin films is accumulative in nature, especially when excited with pulses of amplitude smaller than coercive voltages, and this feature is a promising way to design area and resource efficient LIF neuronal components. A threshold

switching behavior has been introduced in FTJs and FeFETs to mimic neuronal firing activities (Figures 9D–F). In nanoscale FeFETs with Si-doped HfO_2 as the gate material, two key neuronal dynamics such as integration of action potentials and the subsequent firing have been demonstrated. Firing was optimized in these devices by designing specific electrical excitations that can induce a particular NLS kinetics in the FE layer. Depolarizing field (E_{dep}) determine the relaxation of polarization charges in a FE film and therefore E_{dep} could be engineered to tune the firing frequency, arbitrary refractory period and the leaky effect of the neurons. Due to the stochastic nature of switching of single domains, an inherently stochastic nature of switching can be obtained in scaled FeFETs and therefore it is easy to design FeFET-based single cell LIF neurons. One such report is from FeFETs with 30 nm channel length and 80 nm width (Mulaosmanovic, 2018) highlighted the possibility of advanced downscaling of neuron circuits that can significantly reduce the complexity of fabrication and cost of neuromorphic architectures.

In FTJs, LIF neuronal functionalities have been reported by Majumdar et al. (Majumdar, 2019b) by modifying depolarization field strength of the junction. High depolarization field, arising from incomplete screening of polarization charges, results in quick relaxation of polarization leading to volatile switching property. Therefore, when a junction is excited with subthreshold pulses, few domains start to rotate polarization and the number of switched domains keep on accumulating until the net polarization switches, mimicking threshold switching of membrane potential of biological neurons leading to integrate-and-fire function and eventually getting back to its rest condition mimicking reset behavior due to quick relaxation of polarized domains. Engineered depolarizing field in these FTJs by varying charge-carrier densities in the bottom semiconducting electrode, a switch-over from NVM to volatile switching was obtained (Majumdar, 2019b) leading to the possibilities of fabrication of synapses and neurons with same process steps, minimizing the fabrication complexity and cost. By modifying pulse amplitude, frequency and width, it is possible to tune the accumulation and firing frequency and also the leaky behavior. Inherent stochasticity in domain switching helps in replicating the stochastic firing behavior of biological neurons.

Cryogenic memory based on ferroic ordering

Most of the cryogenic characterizations from FE devices are reported from perovskite FE based FTJs like $BaTiO_3$, $PbTiO_3$, $Pb_{1-x}Zr_xTiO_3$ (PZT) etc. (Garcia, 2014; Qin, 2016; Tan, 2019) that shows FTJ performance stability is greatly improved at low temperatures with large On/Off ratio, stable data retention and low leakage currents. However, the switching voltage increases due to cool down that was considered as a drawback. For HZO, most of the available results are from room temperature since developments on HZO are mainly driven from industrial demand side. A few recent reports have studied temperature-dependent studies on Si-doped hafnia (Park, 2018; Wang, 2020b) or HZO capacitors (Wang, 2019) with superconducting NbN electrode (Henry, 2019) and with commonly used TiN electrodes down to 4 K (Hur, 2021). The report by Hur et al. (Hur, 2022), showed excellent endurance performance of the HZO devices at 4 K exceeding 10^{10} cycles with 3.5 V operation. However, analog operation over multiple polarization states in a wide temperature range depending on amplitude and frequency of the applied pulses have not been studied before. In a recent work, Bohuslavskyi et al. (Bohuslavskyi, 2024) reported temperature dependent polarization hysteresis measurements on HZO thin film capacitors. HZO capacitors showed a large open hysteresis with P_r values of 30 μC/cm^2 at room temperature without any wake-up cycles and upon cooling, an increase in P_r value occurred showing a maximum and eventually showing nearly similar P_r at 4 K. The temperature where maximum polarization switching happens is around 75 K, depending on the applied voltage and frequency. At cryogenic temperatures, domain switching becomes more gradual due to the more frozen nature of the domains leading to the possibility for more accurate control of analog states. Another interesting feature is that the leakage current component of the HZO capacitors reduce significantly when measured at 100 K or below, providing a significant improvement in imprint, fatigue and endurance effects, improving the endurance to exceed 10^9 cycles with ±5 V operation, as shown in Figure 10.

Reproducible analog performance remained a challenge

As discussed in the previous sections, different scientific demonstrations so far confirmed that using mixed polarity of ferroic ordering in spintronic and ferroelectric devices, it is possible to have multiple analog conductance states (Mulaosmanovic, 2015). However, reproducibility and retention of these states remained a challenge, mainly in scaled components (Majumdar, 2019a; Covi, 2022). Recent results from indium–tungsten–oxide (Arabar, 2022) and 2D-semiconductor MoS_2 based FeFETs (Majumdar, 2023) demonstrated that with the help of a hybrid FE-dielectric barrier, it is possible to have more controllable analog states. Multiple conductance states obtained from these devices with significantly low read noise and linear and symmetric conductance update under continuously increasing pulse magnitude ensured multi-layer perceptron based deep neural network (DNN) training task can be performed using such FeFETs (Jerry, 2017; Arabar, 2022; Majumdar, 2023). It is found that a significant dispersion in ΔG, the change in synaptic conductance due to subsequent pulses (C2C variation), does not affect training on smaller network (8 × 8 MNIST handwritten dataset) but has detrimental effects with increasing network size. (28 × 28 MNIST handwritten dataset). (Majumdar, 2022b).

Stochasticity in switching is a general feature in nanoscale memristive elements (Tuma, 2016; Mulaosmanovic, 2018). While such stochastic switching is undesirable for precision computing, it can bring certain advantages (McDonnell, 2011; Mass, 2014) for replicating biological computing functions (Faisal, 2008). One such example is probabilistic computing that performs computation upon the probability of a "1" or a "0" state (Li, 2021). Such "1" or "0" can be defined by setting a certain threshold value. For filamentary switching devices, this randomness appears from uncertainty of formation and rupture of filaments while in phase-change memories, such stochasticity results in controlling the phase ratio between the amorphous and crystalline phases (Tuma, 2016). In ferroic components, such uncertainties are due

to switching probabilities of FM or FE domains (Atkinson, 2003; Deng, 2020). Generally, a programming voltage of magnitude larger than coercive field value or a pulse width of millisecond or hundreds of microsecond range leads to higher probability of switching compared to sub-threshold pulse amplitude and width. In micron-scale devices, cumulative effect switching from multiple domains makes the randomness in switching much less pronounced compared to ultra-scaled devices where presence of only a few domains makes the switching more probabilistic than deterministic (Mulaosmanovic, 2018). Stochastic switching of nanodevices can be used both in synaptic devices and nano-scale neurons where the randomness in device switching can lead to probabilistic weight distribution in synapses or stochastically firing neurons, mimicking biology more realistically. Current advancement in neuroscience shows that noise, including stochastic resonance, has beneficial effects in specific cases of sensory data processing that forces the neural networks to be more robust and explore more states. The biological neural noise (Faisal, 2008]) is found beneficial to information processing especially in nonlinear systems (McDonnell, 2011) and is essential for computation and learning in cortical microcircuits (Maass, 2014). It is shown that a network built of probabilistic stochastic resonance model of (SRM) neurons under a simple STDP learning rule could be seen as Bayesian computation (Nessler, 2013). Such neural networks can perform probabilistic sampling, inference, and learning algorithms (Buesing, 2011; Pecevski, 2011; Kappel, 2014) and serve as building blocks for biologically plausible implementations of Boltzmann machines (Pedroni, 2013)] and deep belief networks (OConnor, 2013). It has been discussed in different works that nanoscale memristor based probabilistic spiking neurons (Tuma, 2016; Mehonic, 2020; Woo, 2022) can provide potential advantages over their conventional deterministic counterparts, like leaky integrate-and-fire, in implementing flexible learning rules. One such example being the 2D material based memristive Bayesian learning where generalization is done by sampling over a parameter space which provides a certain quantification over the uncertainty, allowing the neural networks to be more robust and explore more states that can be beneficial in specific cases of sensory data processing (Sebastian, 2022).

To conclude, it is important to mention that stochasticity that arises due to inherent abruptness of physical mechanisms in nanoscale devices, like cycle-to-cycle (C2C) and device to device (D2D) variation can be quantified by physics-based modelling (Deng, 2020), and such stochasticity could be already predicted and the circuit and system designers can take appropriate measures to handle those uncertainties. However, batch to batch variation arising from nanotechnology side, i.e., change in device properties due to unintentionally modified fabrication process parameters, for instance, non-uniform metal line edges, any unpredicted contamination issues leading to non-uniform properties and trap distributions, variation in performance due to non-uniformity of growth, thermal processing of thin semiconductor, metal, dielectric or ferroelectric thin films due to non-uniform thermal profile, plasma flow direction and so on that cannot be predicted and modelled beforehand, could lead to unforeseen challenges that the computing circuit is unable to handle.

Depending on the needs for the system to perform on-line training or inference tasks, requirements from the synaptic weight elements vary. For inference tasks, pretrained weights, optimized in software, are transferred to the hardware based on which the system performs classification task on unknown data. Therefore, long-term retention of the synaptic weights is of vital importance (Majumdar, 2022a). However, for on-line training, devices require to optimize the correct synaptic weights by trial and error, drawing conclusions based on the nearest match and eventually correcting the error after several rounds of adjustments on the weights. This requires devices to adjust continuously to new weight values and therefore to have high endurance and reproducibility. Therefore, based on higher retention or endurance of the synaptic weight elements, different application cases can be achieved.

Large-scale integration of neuromorphic and hybrid CMOS–memristor circuits

For a functional circuit, large scale integration of memristor elements is essential. Especially memristors capable of storing analog synaptic weights could implement very compact models of synapses. Multiple layers of vertical stacking of HZO based FTJs (Chen, 2018) and Fe-diodes (Luo, 2020) has been shown utilizing innovative lithography solutions. HZO based FTJs stacked in 2 vertical layers and HZO diodes stacked in 8 vertical layers provided a promising pathway towards ultra-dense implementation of synaptic weight elements. In a hybrid CMOS-memristor circuit approach for mapping the neural network in hardware, two-terminal memristors are integrated in large and dense crossbar arrays (Cai, 2019; Rao, 2023). CMOS neurons together with the memristor crossbars can perform the vector-matrix-multiplication (VMM) in a parallel way and is able to implement neural network training and inference tasks in a fast and energy-efficient manner (Jerry, 2017). The hybrid CMOS - memristor neuromorphic synapse circuits can obtain dense integration of low-power, programmable synaptic weight storage elements and can emulate detailed synaptic dynamics for implementing relevant computational properties of neural systems. The non-linear activation function and temporal dynamics in such systems are implemented by the CMOS circuits, (as shown in Indiveri, 2013). When a CMOS spiking neuron is operated in linear regime, it can time multiplex the contributions from all spiking inputs, thus requiring one single integrating element, saving circuit complexity and cost. However, one significant challenge identified with the RRAM memristor elements being their high degree of performance variability in terms of switching voltage, On/Off currents, getting stuck at one state etc. compared to CMOS synapses. These unreliable and stochastic features become even more prominent as memristors are scaled down (Mulaosmanovic, 2018) and pose serious limitations for high-precision computing. Computing based on hybrid CMOS-FE systems in hardware have not been demonstrated convincingly yet but recent reports from other memristor technologies (Cai, 2019; Rao, 2023) suggest that taking advantage of matured CMOS transistor performance, many shortcomings of the emerging memristive devices can be complemented.

In a regular MRAM based In-memory-computing (IMC) design scheme, connection between the junctions is realized with the CMOS circuits in a crossbar array configuration (Figure 11).

Computing with spintronic memristors in an artificial neural network with spintronic synapses have been demonstrated by Borders et al. (Borders, 2016) In this circuit an AFM–FM SOT memristors were used to implement the Hopfield model (Hopfield, 1982), doing patterns association and memorizing. Pattern association was demonstrated (Borders, 2016) using three kinds of 3 × 3 block patterns. The Hopfield network consisting of 36 SOT-based memristors used a field-programmable gate array (FPGA) as neurons. that was controlled by a software running on a computer.

The system was initialized by calculating the ideal synaptic weights based on the Hopfield model for the three chosen patterns are then applied to the synaptic devices. Lack of sufficient linearity and uniformity of the spintronic memristors resulted in 20 iterations for the network to remember the given patterns, however, this work demonstrates that learning with spintronic synapses is possible supported by conventional electronics. This work demonstrated that device non-ideality of spintronic synapses can initially lead to lower classification accuracy, however, high endurance could lead to neuromorphic hardware that can provide superior adaptivity through learning. A CMOS–spintronic circuit was demonstrated by Marković et al. (Marković, 2020) that showed a system with 128 inputs and 128 outputs consumes 23 nJ per operation for learning that eventually reduces to 7.4 nJ post-learning. This is a promising improvement over 330 nJ per operation for a low-power spiking CMOS neurons-based system. Hybrid CMOS-spintronics spiking neural network has been demonstrated by Sengupta et al. with on-chip learning capabilities (Sengupta, 2016a).

Other than conventional CMOS-MRAM systems, computation can be done using the device physics. It has been shown that using the domain wall motion, an all-spin ANN system can be designed (Sengupta, 2016b) while using dipolar coupling between nanomagnets, it is possible to directly do computation based on energy minimization that can reduce the CMOS circuit overhead. Physical dipolar interaction between arrays of nanomagnets were used by Bhanja et al. (Bhanja, 2016) to solve a quadratic optimization problem for computer vision applications. A reservoir computing system was demonstrated with dipole-coupled nanomagnets by Nomura et al. (Nomura, 2019) The future of this field is extremely promising with the prospect of utilizing the natural physics of nanomagnets for implementing ultralow-power, scaled ANNs. Also, classification of signals at microwave frequencies was demonstrated by Romera et al. (Romera, 2018) in a small, two-layer neural network by computing with synchronized spin-torque nano-oscillators, providing a promising way for high-frequency signal processing.

For integrating devices into a functional circuit one key consideration is connectivity. In a typical neural network algorithm today, 10 to 1,000 synapses per neuron are used, in comparison to the 10,000 synapses per neuron in the human cerebral cortex. Therefore, the biggest challenge of mimicking biology in neuromorphic hardware is to attain dense interconnection between neurons. Interconnect technology is an extensive research subject that is bringing in improved solutions every day (Wesling, 2020). Spintronic and ferroelectric systems, especially the MTJs and FTJs are made of trilayer systems that can be vertically stacked making it in possible to have dense integration possible in three dimensions. However, while considering such 3D vertical integration, interconnection between layers is a critical consideration. In spintronic nanostructures, vertical and horizontal communication through optical waves or microwave signals emitted by STNOs, could be useful. However, in such cases, an amplifier circuit might be essential to achieve high fan-out. Progress in ferroic materials and device technologies are expected to bring promising possibilities for building complex 3D-integrated computing hardware.

Computing with ferroelectric memristors

As discussed previously, partial rotation of ferroelectric domains results in multiple conductance states in FeFETs and in literature it has been shown that proper control of these intermediate states via gate stack modification (Majumdar, 2023) or a custom-designed programming pulse protocols (Jerry, 2017) can lead to quite linear and symmetric weight update. Efficient DNN training has been demonstrated utilizing the analog synaptic weight update in FeFET-based synapses where proper dynamics of partial polarization switching were induced by the gate voltage-controlled channel conductance (Jerry, 2017; De, 2022; Majumdar, 2023). Figure 12C shows schematically how FeFET based analog crossbar array can perform VMM operation. In the crossbar array, each cross point between row and columns represents one FeFET transistor. This array, surrounded by neuron circuitry, implement the training algorithm i.e., the forward propagation, back propagation, and weight-update operations. In these circuits higher parallelism is achieved using neuron circuit at each row and column that can bypass time-multiplexing. For a compact hardware implementation of such hybrid CMOS-FeFET neural network, FeFETs could be either integrated with CMOS at front end of line (FEOL) or back end of line (BEOL). Co-integration of FeFETs into standard high-k metal gate (HKMG) CMOS platforms were demonstrated by Beyer et al. (Beyer, 2020), leading to a cheap, fast, low-power eFLASH replacement for existing eNVM technology nodes. The FeFETs showed a reversible switching between a low-V_T (LVT) and a high-V_T (HVT) state with a MW of 1.5 V and a good uniformity. A linear increase in programming or erasing voltage led to an exponential increase in the switching speed and found to be independent of the device size, i.e., also observable for ultra-scaled FeFETs (Mulaosmanovic, 2018). The switching time vs V_G curves were found highly sensitive to fabrication process variations and found to shift with respect to the V_G axis or change the slope, leading to short- and long-term retention trends (Mulaosmanovic, 2017). From a system level perspective, Berdan et al. demonstrated FTJ crossbars can scale analogue VMM-intensive applications, like neural inference engines leading towards energy efficiencies above 100 tera-operations per second per watt (Berdan, 2020). while utilizing both volatile and nonvolatile retention of ferroelectric diodes, Chen et al. showed all-ferroelectric reservoir computing systems can be achieved that can operate as a reliable and low-power neuromorphic hardware for temporal information processing (Chen, 2023).

Integration technologies–features and challenges

All non-volatile memory and synaptic or neuronal devices need to be eventually integrated into a complete system, and therefore

combining the memory and synaptic circuits with CMOS-based technologies, are essential. This brings about a whole set of integration challenges. There have been efforts to integrate different components using standard techniques (Heterogeneous integration Roadmap, 2023 edition, Emerging Research Devices), such as 2D, 2.5D and 3D integration of devices with silicon transistors either in the same plane or vertically stacked on top of each other.

2D planar and 2.5D integration are comparatively matured technologies (Sheikh, 2021). In 2D techniques, simple in-plane interconnects are used while 2.5D integration uses silicon interposer techniques, where a chip with lithographically defined interconnections and through-silicon via's (TSV) communicate between different functional units (Gambino, 2015). Although matured, efforts are still needed to reduce the pitch, incorporating large numbers of connections for routing signals between different functional components and loss through interconnects for large-scale integration of neuromorphic circuits. Optimization of materials, etching chemistry and layouts are therefore of vital importance (Rofeh, 2015). In 3D monolithic integration, memory components are grown directly on top of the CMOS wafer and therefore managing the thermal budget is an important issue (Yu, 2021). Although 3D integration can provide highest integration density and low loss interconnects, it imposes material challenges due to the direct growth technique leading to material compatibility issues.

Depending on the application, therefore it is important to choose the correct integration technology. Systems where thermally evaporated magnetic metals or low thermal budget ferroelectric materials can serve the purpose, can use 3D technologies while applications demanding more exotic functionalities need to depend on heterogeneous 2D or 2.5 D integration. Need for high memory bandwidth, less operational heat dissipation, better mechanical stability, and affordable cost would define the technology for building the next-generation neuromorphic systems. In the following section, we discuss a few implemented integration methodologies and their advantages and challenges.

Heterogeneous integration: Heterogeneous integration, where systems on chip and in package can be realized by combining spintronics–CMOS or ferroelectric–CMOS and other components developed on different substrates, makes it possible to integrate exotic material properties of complex oxide material classes. For spintronic systems, complex-oxide materials exhibit a wide range of exotic, functional properties (Majumdar, 2013). However, due to their demanding and non-CMOS compatible fab conditions and requirements for special substrates make them unsuitable for direct integration with CMOS logic and other functional circuits. In such cases, heterogeneous integration and application of strain through heteroepitaxy provide an attractive choice, that can make integration of complex oxides possible with mature semiconductor technologies. Kum et al. demonstrated a universal mechanical exfoliation method (Kum, 2020) that can produce freestanding single-crystalline membranes of complex-oxide materials including perovskite, spinel and garnet crystal structures that can be stacked directly with CMOS electronics, similar to two-dimensional material-based heterostructures, and an integrated logic-memory or neuron synaptic architectures can be realized.

3D Monolithic integration: As mentioned previously, advantages of 3D integration include i) reduced interconnect wire length resulting in lower delay and power, ii) lower parasitic effects, iii) higher packaging density and lower footprint. However, 3D monolithic integration comes at a cost of limited design space for materials and process parameters. Since, devices and circuits are formed in the back-end-of-line of CMOS circuits, no process fabrication steps can exceed a temperature of 500°C and long-term thermal exposure or exposure to chemicals that can affect the passivation layers. In terms of ferromagnetic and ferroelectric materials, this limits the material choice to either evaporated or sputtered transition metals like Fe, Co, Ni and alloys for spintronics and mainly ALD-grown hafnia-based systems for ferroelectric devices. Since 3D monolithic integration technology is a rather recent trend in semiconductor industry, not too much study has been done on 3D integrated spintronic and ferroelectric systems and therefore fabrication and performance limitations are not yet so well understood. Small-scale integrations have been reported for ferroelectric hafnia-based capacitors and FETs (Francois, 2019; Dutta 2020; De, 2022), mainly showing moderate sized memory arrays or mainly CMOS compatible process for FeFETs and SOT-MRAMs respectively (Garello, 2018; Falcone, 2022). Future studies need to advance the knowledge of performance reliability and limitations in such systems and needs for custom materials designs to improve functionalities in such systems.

Application in neuromorphic computing tasks

Deep-Learning Accelerators: High complexity AI tasks, such as image classifications or natural language processing require running of large DNN models with multiple hidden layers. Hardware implementation of such DNN models would benefit massively from high-degree of parallelism obtained by In-memory computing taking place in large crossbar arrays of memristors that map the weight metrices. In IMC primitive, higher prediction accuracy for the AI algorithm model parameters demands higher bit resolution of synaptic weights compared to the highest possible bits per cell in synaptic devices (Jerry, 2017; Luo, 2022). To address such challenges, one possible way is to map the input vectors and weight matrices into multiple crossbar arrays or columns (Wang, 2021). However, determining the system-level efficiency would require considerations from peripheral circuit components, handling the data from to and from the crossbars as well. For instance, in a hardware neural network, the bits of input vector are converted to voltages, and streamed to the synaptic array. Timing of the streaming depends on the bit-precision of the digital-analog converters (DAC). After the voltage pulses pass through the synapses, the dot product of the input voltage vector and conductance matrix is accumulated as current from the columns of crossbar. The output currents are processed in combination with results from multiple time steps or multiple arrays in bit streaming or bit slicing scheme to perform multi-bit VMM operations. The output currents from one or multiple crossbars pass through analog-digital converters (ADC) to get the final output. Multi-level synaptic devices help mapping the synaptic weights onto the crossbar more efficiently, however it increases requirement for bit precision of the ADC making it most power and area consuming element in the circuit. While devices with multiple levels can decrease the number

of synaptic weight elements or number of crossbar arrays in the circuit, higher power and area consumption of ADCs need to be considered while estimating the circuit implementation. Fewer bits per cell synapses, on the other hand, need multiple cross bars to implement the weight mapping. However, the lower bit precision requirement in the ADCs makes the power an area footprint lower for the ADCs. Based on the application, a correct trade off, therefore, needs to be found out and design optimization needs to be done. So far, most of the reported results on IMC hardware predicted the system-level performance based on individual device measurements extrapolated to system level simulation. (Dutta 2020; Bégon-Lours, 2021). However, in these cases, device to device variation, effect of parasitics, size of the crossbar, number of failed or stuck devices have not been taken into account. In future works, full hardware implementation of the crossbar-based computation needs to be done and systematic co-optimization at the material, device, circuit and systems level performed to achieve best results. Some recent works on large-scale integration of CMOS-RRAM systems (Cai, 2019) or CMOS-STT-MRAM systems (Lee, 2019) can provide roadmap in this direction.

Spiking-Neural Network: In comparison to the DNNs, SNNs are more versatile in handling the spatio-temporally varying signal encoding and processing. In SNNs, neurons communicate with each other using binary signals or spikes and timing of the spikes encodes the data. Accumulative and threshold switching behaviour of ferroic devices can make them extremely efficient for hardware implementation of SNNs, both as synaptic weight elements and as leaky-integrate and fire neurons. Utilizing memristive synapses as weight elements, both supervised training and unsupervised training and adaptation has been demonstrated. The unsupervised learning, where the synaptic weights are modified in an unsupervised manner according to the biologically inspired STDP rule (Poo 1998), is rather straightforward to implement in hardware. The STDP rule implements the experimental observation that when a synapse is subjected to a pre-pulse before a post-pulse, the effective synaptic strength increases, and if the pulse ordering reverses, it results in an effective decrease in synaptic strength. Shape and duration of the input pulses can impact the change of synaptic conductance (Majumdar, 2019a). Utilizing hybrid CMOS-Memristor circuits IBM researchers demonstrated an integrated neuromorphic core with 256 × 256PCM synapses fabricated together with CMOS neurons that is capable of on-chip learning based on a simplified STDP rule and can perform auto-associative pattern learning tasks (Kim, 2015). Fang et al. demonstrated that certain optimization problems could be solved efficiently utilizing the coupled dynamics of FeFET-based spiking neurons. It was shown that coupled neurons, with 1T-FeFET structures showing both excitory and inhibitory inputs, communicate and modulate each other's action potentials through event-driven spikes and synchronize their dynamics around the states of optimal solutions (Fang, 2019).

In comparison to the unsupervised learning, implementing a supervised learning in SNN is a more demanding task due to the inherent difficulty in applying gradient descent methods for spiking neuron models with infinite discontinuities at the instants of spikes (Mehonic, 2020). Although, there has been some demonstrations (Nandakumar 2017), there is still urgent needs for development of robust and event-driven learning algorithms for SNNs.

Considering the randomness of the memristive synaptic devices, Bayesian inference and learning could be one potentially important strategy for memristive neural networks in general. Unlike the conventional approach where a single set of parameter vector is used during learning, the Bayesian principle utilises the inference over a probability distribution of the synaptic weights. In presence of sufficient data this distribution focuses on the optimal weight configuration, however, when data are limited, the synaptic weight distribution provides a so-called credibility profile in the parameter space, enabling most probable solutions during inference and exploration during learning.

For applications down to deep cryogenic temperatures, specific features and limitations of both memristive and cryo-CMOS components need to be studied and modelled carefully.

Challenges and future perspectives

The discussion so far highlighted many aspects of ferroic devices that can bring substantial advantages in achieving neuromorphic computing hardware, especially suitable for operation down to cryogenic temperatures. Briefly summarizing, the biggest advantages of devices with ferroic ordering being, 1) **non-volatility**, i.e., spintronic and ferroelectric analog memories can possess long term data retention making them suitable for applications where data persistence is crucial, such as in embedded systems and IoT devices and for AI-inference tasks. 2) **Low Power Consumption** in comparison to traditional memory technologies like DRAM or flash, spintronic and ferroelectric analog memories can offer lower power consumption making them attractive for battery-powered devices and energy-efficient computing. 3) **High Speed:** Spintronic and ferroelectric polarization switching being extremely fast, the ferroic devices can operate at high speeds, making them suitable for applications that require rapid data access and processing, such as real-time signal processing and machine learning accelerators. 4) **Endurance:** Spintronic and ferroelectric memories often have excellent endurance, with the potential for a high number of write and erase cycles without significant degradation or fatigue effects. This endurance is advantageous for applications that require frequent data updates like synaptic devices where online training operation is needed in a neural network accelerator. 5) **Integration with CMOS:** Spintronic and ferroelectric devices can be integrated with CMOS technology, allowing for the development of hybrid memory and logic circuits on a single chip. This integration can lead to more compact and efficient systems. 6) **Resistance to Radiation:** Spintronic and ferroelectric devices are inherently less susceptible to radiation-induced errors compared to some other memory technologies, making them suitable for space and high-radiation environments.

However, some material, fabrication and performance challenges still exist that require substantial research efforts in this direction. 1) **Material Complexity:** Spintronic and ferroelectric memories rely on specialized materials, electrodes and design principles to operate efficiently as analog memories. The fabrication of these materials and devices can be complex and costly. 2) **Write Currents:** Writing data in spintronic memories typically involves passing a significant current through the MTJs, which can lead to high power consumption and heat generation. Developing low power write schemes is a challenge in spintronic

components while in FTJs, the challenge is opposite. In scaled FTJs, the read current is often too low to avoid read noise and successfully read the programmed states. 3) **Retention and Data Stability:** The stability of stored data in spintronic and ferroelectric memories, especially in high-temperature environments and for multiple analog states, is a concern. Ensuring long-term data retention without degradation is essential for non-volatile retention purpose. However, for synaptic weight elements, non-volatile retention time scale can be different and might not pose challenges. 4) **Manufacturability and Yield:** Scaling up the production of spintronic and ferroelectric memories and achieving >95% yields can be challenging due to the intricacies of material deposition and device fabrication. 5) **Variability:** Variability in material properties and manufacturing processes can lead to significant performance variations between individual devices. Achieving uniformity and reliability is crucial for mass adoption of these technologies. 6) **Cost:** The cost of manufacturing spintronic memories, particularly in comparison to established memory technologies like NAND flash or DRAM, can be a barrier to widespread adoption. Reducing production costs is a significant challenge. 6) **Compatibility:** Integrating spintronic memories with existing electronics and semiconductor processes may require adaptations and standards. Compatibility with current computing architectures and interfaces is important for adoption. 7) **Error Correction:** Like other memory technologies, spintronic memories may require advanced error correction techniques to maintain data integrity, particularly as they are used in more demanding applications.

To summarize, spintronic and ferroelectric analog memories offer a range of advantages, including non-volatility, low power consumption, almost infinite endurance, and high speed. However, they face challenges related to materials, manufacturability, variability affecting analog data stability, and cost. Researchers and engineers are actively working to overcome these challenges and unlock the full potential of spintronic and ferroelectric memories in various applications, including embedded systems, IoT, and high-performance computing. Merged logic-memory systems or neuromorphic architectures require a holistic design approach where different cross-layer design, optimization and implementation is needed to create a scalable, high-performance, and energy-efficient chip that is based on materials physics and critical nanotechnology. When successfully scaled, these proposed computation platforms will be able to provide 1,000× improvement in computing performance in terms of energy-latency product. This will be particularly efficient for memory-intensive computing tasks like real-time recognition of images and videos, on-line learning, big-data analytics, secure computing etc. Future research from hardware side should focus on large-scale integration of on-chip memory with energy-efficient computation circuits. Innovations around monolithic 3D integration technologies will be able to provide ultra-high connectivity improving the system level performance while reducing power loss, delay and cost. From circuit, systems and applications side, innovations are needed for computing architectures that embrace sparsity, stochasticity, and nanodevice variability, mimicking human brain. While today's artificial neural networks are supporting large-scale machine learning applications on the cloud, computing hardware supporting these cognitive systems suffer from long and power intensive training times, large training datasets, lack of flexibility and dynamic adaptation, and real-time autonomous decision-making. By leveraging innovations in novel materials and device technologies to create merged logic-memory fabrics, it is possible to accelerate development of real time operating cognitive and secure computing systems.

Different computational models like compute-in-memory, reinforcement learning, hyper-dimensional computing, approximate computing, spike-based computing and so on are used to demonstrate the cognitive ability of the hardware. Utilizing the physics of the novel devices it is possible to overcome the current limitations and achieve dynamic adaptation and parallel on-line learning. Innovations in integration technologies will ensure large-scale systems, capable of handling real world complex problems enabling ubiquitous intelligent systems under energy constrained situations.

Finally, we envision that the development of neuromorphic hardware would require extensive efforts and cross-disciplinary knowledge from different communities, from neuroscience to physics, materials science, nanotechnology, electrical and computer engineering and collaborative efforts could lead to successful development of achievement of the next-generation of energy-efficient, secure and cognitive integrated microsystems. Photo-induced magnetoresistance (Elovaara, 2015) or ferroelectric effects (Tan, 2022) can pave the way for photonic memory and neuromorphic circuits based on ferroic devices. The current review provided an outlook on the designing of energy-efficient, analog memories, synaptic weight and neuronal elements utilizing the physics of ferromagnetic or ferroelectric materials, that could provide multiple benefits for large range of applications with special focus on cryogenic applications for quantum computing and space technologies.

Author contributions

SM: Conceptualization, Funding acquisition, Project administration, Writing–original draft, Writing–review and editing.

Funding

The author(s) declare that no financial support was received for the research, authorship, and/or publication of this article.

Acknowledgments

The author acknowledges financial support from Research Council of Finland through projects AI4AI (no. 350667) and FerrARI (no. 359047) and Business Finland and European Commission through project ArCTIC (no. 101139908).

Conflict of interest

The author declares that the research was conducted in the absence of any commercial or financial relationships that could be construed as a potential conflict of interest.

Publisher's note

References

Aabrar, K. A., Kirtania, S. G., Liang, F.-X., Gomez, J., Jose, M. S., Luo, Y., et al. (2022). BEOL-compatible superlattice FEFET analog synapse with improved linearity and symmetry of weight update. *IEEE Trans. Electron Devices* 69, 2094–2100. doi:10.1109/ted.2022.3142239

Angervo, I., Saloaro, M., Palonen, H., Huhtinen, H., Paturi, P., Mäkelä, T., et al. (2022). Giant magnetoresistance response in Sr2FeMoO6 based organic spin valves. *Appl. Surf. Sci.* 589, 152854. doi:10.1016/j.apsusc.2022.152854

Atkinson, D., Allwood, D. A., Xiong, G., Cooke, M. D., Faulkner, C. C., and Cowburn, R. P. (2003). Magnetic domain-wall dynamics in a submicrometre ferromagnetic structure. *Nat. Mater* 2, 85–87. doi:10.1038/nmat803

Bégon-Lours, L., Halter, M., Popoff, Y., and Offrein, B. J. (2021). Special issue: emerging fluorite- and wurtzite-type ferroelectrics. *Phys. Stat. Solidi RRL* 15, 2000524. doi:10.1002/pssr.202000524

Berdan, R., Marukame, T., Ota, K., Yamaguchi, M., Saitoh, M., Fujii, S., et al. (2020). Low-power linear computation using nonlinear ferroelectric tunnel junction memristors. *Nat. Electron.* 3, 259–266. doi:10.1038/s41928-020-0405-0

Berger, L. (1996). Emission of spin waves by a magnetic multilayer traversed by a current. *Phys. Rev. B* 54, 9353–9358. doi:10.1103/physrevb.54.9353

Beyer, S., Dunkel, S., Trentzsch, M., Muller, J., Hellmich, A., Utess, D., et al. (2020). "FeFET: a versatile CMOS compatible device with game-changing potential," in 2020 IEEE International Memory Workshop (IMW), Dresden, Germany, 17-20 May 2020, 1–4.

Bhanja, S., Karunaratne, D. K., Panchumarthy, R., Rajaram, S., and Sarkar, S. (2016). Non-Boolean computing with nanomagnets for computer vision applications. *Nat. Nanotechnol.* 11, 177–183. doi:10.1038/nnano.2015.245

Böhnert, T., Rezaeiyan, Y., Claro, M. S., Benetti, L., Jenkins, A. S., Farkhani, H., et al. (2023). Weighted spin torque nano-oscillator system for neuromorphic computing. *Commun. Eng.* 2, 65. doi:10.1038/s44172-023-00117-9

Bohuslavskyi, H., Griogoras, K., Ribeiro, M., Prunnila, M., and Majumdar, S. (2024). Ferroelectric Hf0.5Zr0.5O2 for analog memory and in-memory computing applications down to deep cryogenic temperatures. *Adv. Elec. Mater.* doi:10.1002/aelm.202300879

Borders, W. A., Akima, H., Fukami, S., Moriya, S., Kurihara, S., Horio, Y., et al. (2016). Analogue spin–orbit torque device for artificial neural-network-based associative memory operation. *Appl. Phys. Express* 10, 013007. doi:10.7567/apex.10.013007

Boyn, S., Grollier, J., Lecerf, G., Xu, B., Locatelli, N., Fusil, S., et al. (2017). Learning through ferroelectric domain dynamics in solid-state synapses. *Nat. Commun.* 8, 14736. doi:10.1038/ncomms14736

Buesing, L., Bill, J., Nessler, B., and Maass, W. (2011). Neural dynamics as sampling: a model for stochastic computation in recurrent networks of spiking neurons. *PLoS Comput. Biol.* 7 (11), e1002211. doi:10.1371/journal.pcbi.1002211

Cai, F., Correll, J. M., Lee, S. H., Lim, Y., Bothra, V., Zhang, Z., et al. (2019). A fully integrated reprogrammable memristor–CMOS system for efficient multiply–accumulate operations. *Nat. Electron.* 2 (7), 290–299. doi:10.1038/s41928-019-0270-x

Chanthbouala, A., Matsumoto, R., Grollier, J., Cros, V., Anane, A., Fert, A., et al. (2011). Vertical-current-induced domain-wall motion in MgO-based magnetic tunnel junctions with low current densities. *Nat. Phys.* 7, 626–630. doi:10.1038/nphys1968

Chen, A. (2022). Beyond-CMOS roadmap—from Boolean logic to neuro-inspired computing. *Jpn. J. Appl. Phys.* 61, SM1003. doi:10.35848/1347-4065/ac5d86

Chen, L., Wang, T. Y., Dai, Y. W., Cha, M. Y., Zhu, H., Sun, Q. Q., et al. (2018). Ultra-low power Hf0.5Zr0.5O2 based ferroelectric tunnel junction synapses for hardware neural network applications. *Nanoscale* 10, 15826–15833. doi:10.1039/c8nr04734k

Chen, Z., Li, W., Fan, Z., Dong, S., Chen, Y., Qin, M., et al. (2023). All-ferroelectric implementation of reservoir computing. *Nat. Commun.* 14, 3585. doi:10.1038/s41467-023-39371-y

Covi, E., Mulaosmanovic, H., Max, B., Slesazeck, S., and Mikolajick, T. (2022). Ferroelectric-based synapses and neurons for neuromorphic computing. *Neuromorph. Comput. Eng.* 2, 012002. doi:10.1088/2634-4386/ac4918

Dahlberg, H., and Wernersson, L.-E. (2023). "Dynamics of polarization switching in mixed phase ferroelectric-antiferroelectric HZO thin films," in ESSDERC 2023 - IEEE 53rd European Solid-State Device Research Conference (ESSDERC), Lisbon, Portugal, 11-14 September 2023, 33–36.

De, S., Le, H. H., Qiu, B. H., Baig, M. A., Sung, P. J., Su, C. J., et al. (2021a). Robust binary neural network operation from 233 K to 398 K via gate stack and bias optimization of ferroelectric FinFET synapses. *IEEE Electron Device Lett.* 42 (8), 1144–1147. doi:10.1109/LED.2021.3089621

De, S., Muller, F., Laleni, N., Lederer, M., Raffel, Y., Mojumder, S., et al. (2022). Demonstration of multiply-accumulate operation with 28 nm FeFET crossbar array. *IEEE Electron Device Lett.* 43 (12), 2081–2084. doi:10.1109/led.2022.3216558

De, S., Qiu, B.-H., Bu, W.-X., Baig, Md. A., Sung, P.-J., Su, C.-J., et al. (2021b). Uniform crystal formation and electrical variability reduction in hafnium-oxide-based ferroelectric memory by thermal engineering. *ACS Appl. Electron. Mat.* 3 (2), 619–628. doi:10.1021/acsaelm.0c00610

Deng, S., Yin, G., Chakraborty, W., Dutta, S., Datta, S., Li, X., et al. (2020). "A comprehensive model for ferroelectric FET capturing the key behaviors: scalability, variation, stochasticity, and accumulation," in 2020 IEEE Symposium on VLSI Technology, Honolulu, HI, USA, 16-19 June 2020, 1–2.

Elovaara, T., Majumdar, S., Huhtinen, H., and Paturi, P. (2015). Photoinduced colossal magnetoresistance under substantially reduced magnetic field. *Adv. Funct. Mater.* 25, 5030–5037. doi:10.1002/adfm.201502233

Endo, M., Kanai, S., Ikeda, S., Matsukura, F., and Ohno, H. (2010). Electric-field effects on thickness dependent magnetic anisotropy of sputtered MgO/Co40Fe40B20/Ta structures. *Appl. Phys. Lett.* 96, 212503. doi:10.1063/1.3429592

Faisal, A. A., Selen, L. P., and Wolpert, D. M. (2008). Noise in the nervous system. *Nat. Rev. Neurosci.* 9 (4), 292–303. doi:10.1038/nrn2258

Falcone, F., Halter, M., Bégon-Lours, L., and Offrein, B. J. (2022). Back-end, CMOS-compatible ferroelectric FinFET for synaptic weights. *Front. Electron. Mater, Sec. Semicond. Mater. Devices* 2, 849879. doi:10.3389/femat.2022.849879

Fang, Y., Wang, Z., Gomez, J., Datta, S., Khan, A. I., and Raychowdhury, A. (2019). A swarm optimization solver based on ferroelectric spiking neural networks. *Front. Neurosci.* 13, 855. doi:10.3389/fnins.2019.00855

Fernández-Pacheco, A., Streubel, R., Fruchart, O., Hertel, R., Fischer, P., and Cowburn, R. P. (2017). Three-dimensional nanomagnetism. *Nat. Commun.* 8, 15756. doi:10.1038/ncomms15756

ferroelectric memristor, A., Chanthbouala, A., Garcia, V., Cherifi, R. O., Bouzehouane, K., Fusil, S., et al. (2012). A ferroelectric memristor. *Nat. Mater.* 11, 860–864. doi:10.1038/nmat3415

Finocchio, G., Ventra, M. D., Camsari, K. Y., Everschor-Sitte, K., Amiri, P. K., and Zeng, Z. (2021). The promise of spintronics for unconventional computing. *J. Magn. Magn. Mat.* 521 (1), 167506. doi:10.1016/j.jmmm.2020.167506

Francois, T., Grenouillet, L., Coignus, J., Blaise, P., Carabasse, C., Vaxelaire, N., et al. (2019). "IEDM 2019 welcome," in IEEE International Electron Devices Meeting (IEDM), San Francisco, United States, 7-11 December 2019.

Fukami, S., Anekawa, T., Zhang, C., and Ohno, H. (2016a). A spin–orbit torque switching scheme with collinear magnetic easy axis and current configuration. *Nat. Nanotechnol.* 11, 621–625. doi:10.1038/nnano.2016.29

Fukami, S., Zhang, C., Dutta Gupta, S., Kurenkov, A., and Ohno, H. (2016b). Magnetization switching by spin-orbit torque in an antiferromagnet-ferromagnet bilayer system. *Nat. Mat.* 15, 535–541. doi:10.1038/nmat4566

Gambino, J. P., Adderly, S. A., and Knickerbocker, J. U. (2015). An overview of through-silicon-via technology and manufacturing challenges. *Microelectron. Eng.* 135, 73–106. doi:10.1016/j.mee.2014.10.019

Garcia, V., and Bibes, M. (2014). Ferroelectric tunnel junctions for information storage and processing. *Nat. Commun.* 5, 4289. doi:10.1038/ncomms5289

Garcia, V., Bibes, M., Barthelemy, A., Bowen, M., Jacquet, E., Contour, J.-P., et al. (2004). Temperature dependence of the interfacial spin polarization of La2/3Sr1/3MnO3. *Phys. Rev.* B69, 052403. doi:10.1103/PhysRevB.69.052403

Garello, K., Yasin, F., Couet, S., Souriau, L., Swerts, J., Rao, S., et al. (2018). "SOT-MRAM 300MM integration for low power and ultrafast embedded memories," in 2018 IEEE Symposium on VLSI Circuits, Honolulu, HI, USA, 18-22 June 2018, 81–82.

Goh, Y., Cho, S. H., Park, S.-H. K., and Jeon, S. (2020). Crystalline phase-controlled high-quality hafnia ferroelectric with RuO_2 electrode. *IEEE Trans. Electron Devices* 67, 3431–3434. doi:10.1109/ted.2020.2998444

Grimaldi, A., Selcuk, K., Aadit, N. A., Kobayashi, K., Cao, Q., Chowdhury, S., et al. (2022). "Experimental evaluation of simulated quantum annealing with MTJ-augmented p-bits," in 2022 International Electron Devices Meeting (IEDM), San Francisco, CA, USA, December 3-7, 2022, 22.4.1–22.4.4.

Grimaldi, E., Lebrun, R., Jenkins, A., Dussaux, A., Grollier, J., Cros, V., et al. (2014). "Spintronic nano-oscillators: towards nanoscale and tunable frequency devices," in 2014 IEEE International Frequency Control Symposium (FCS), Taipei, Taiwan, 19-22 May 2014, 1–6.

Grollier, J., Boulenc, P., Cros, V., Hamzić, A., Vaurès, A., Fert, A., et al. (2003). Switching a spin valve back and forth by current-induced domain wall motion. *Appl. Phys. Lett.* 83, 509–511. doi:10.1063/1.1594841

Grollier, J., Querlioz, D., Camsari, K. Y., Everschor-Sitte, K., Fukami, S., and Stiles, M. D. (2020). Neuromorphic spintronics. *Nat. Electron.* 3, 360–370. doi:10.1038/s41928-019-0360-9

Gruverman, A., Wu, D., Lu, H., Wang, Y., Jang, H. W., Folkman, C. M., et al. (2009). Tunneling electroresistance effect in ferroelectric tunnel junctions at the nanoscale. *Nano Lett.* 9, 3539–3543. doi:10.1021/nl901754t

Gupta, A., Gong, G. Q., Xiao, G., Duncombe, P. R., Lecoeur, P., Trouilloud, P., et al. (1996). Grain-boundary effects on the magnetoresistance properties of perovskite manganite films. *Phys. Rev. B* 54, R15629(R)–R15632. doi:10.1103/physrevb.54.r15629

Hawley, M. E., Brown, G. W., Yashar, P. C., and Kwon, C. (2000). H-dependent magnetic domain structures in La0.67Sr0.33MnO3 thin films. *J. Cryst. Growth* 211 (1–4), 86–92. doi:10.1016/s0022-0248(99)00849-0

Hayashi, M., Thomas, L., Rettner, C., Moriya, R., Jiang, X., and Parkin, S. S. P. (2006). Dependence of current and field driven depinning of domain walls on their structure and chirality in permalloy nanowires. *Phys. Rev. Lett.* 97, 207205. doi:10.1103/physrevlett.97.207205

Hayward, T. J. (2015). Intrinsic nature of stochastic domain wall pinning phenomena in magnetic nanowire devices. *Sci. Rep.* 5, 13279. doi:10.1038/srep13279

Henry, M. D., Smith, S. W., Lewis, R. M., and Ihlefeld, J. F. (2019). Stabilization of ferroelectric phase of Hf0.58Zr0.42O2 on NbN at 4 K. *Appl. Phys. Lett.* 114, 092903. doi:10.1063/1.5052435

Heterogeneous integration roadmap (2023) *Heterogeneous integration roadmap edition*. Available at: https://eps.ieee.org/technology/heterogeneous-integration-roadmap/2023-edition.html.

Hopfield, J. J. (1982). Neural networks and physical systems with emergent collective computational abilities. *Proc. Natl. Acad. Sci. U. S. A.* 79, 2554–2558. doi:10.1073/pnas.79.8.2554

Houshang, A., Iacocca, E., Dürrenfeld, P., Sani, S. R., Åkerman, J., and Dumas, R. K. (2016). Spin-wave-beam driven synchronization of nanocontact spin-torque oscillators. *Nat. Nanotechnol.* 11, 280–286. doi:10.1038/nnano.2015.280

Hur, J., Luo, Y. C., Wang, Z., Lombardo, S., Khan, A. I., and Yu, S. (2021). Characterizing ferroelectric properties of Hf0.5Zr0.5O2 from deep-cryogenic temperature (4 K) to 400 K. *IEEE J. Explor. Solid-State Comput. Devices Circuits* 7, 168–174. doi:10.1109/jxcdc.2021.3130783

Hur, J., Park, C., Choe, G., Ravindran, P. V., Khan, A. I., and Yu, S. (2022). Characterizing HfO2-based ferroelectric tunnel junction in cryogenic temperature. *IEEE Trans. Electron Devices* 69 (10), 5948–5951. doi:10.1109/ted.2022.3200919

Ielmini, D., and Ambrogio, S. (2020). Emerging neuromorphic devices. *Nanotechnology* 31, 092001. doi:10.1088/1361-6528/ab554b

Ikegawa, S., Mancoff, F. B., Janesky, J., and Aggarwal, S. (2020). Magnetoresistive random access memory: present and future. *IEEE Trans. Electron Devices* 67 (4), 1407–1419. doi:10.1109/ted.2020.2965403

Indiveri, G., Linares-Barranco, B., Legenstein, R., Deligeorgis, G., and Prodromakis, T. (2013). Integration of nanoscale memristor synapses in neuromorphic computing architectures. *Nanotechnology* 24 (38), 384010. doi:10.1088/0957-4484/24/38/384010

Jerry, M., Chen, P.-Y., Zhang, J., Sharma, P., Ni, K., Yu, S., et al. (2017). "Ferroelectric FET analog synapse for acceleration of deep neural network training," in 2017 IEEE International Electron Devices Meeting (IEDM), San Francisco, CA, 02-06 December 2017, 6–2.

Julliere, M. (1975). Tunneling between ferromagnetic films. *Phys. Lett.* 54A, 225–226. doi:10.1016/0375-9601(75)90174-7

Kappel, D., Nessler, B., and Maass, W. (2014). STDP installs in winner-take-all circuits an online approximation to hidden Markov model learning. *PLoS Comput. Biol.* 10 (3), e1003511. doi:10.1371/journal.pcbi.1003511

Katine, J. A., Albert, F. J., Buhrman, R. A., Myers, E. B., and Ralph, D. C. (2000). Current-driven magnetization reversal and spin-wave excitations in Co/Cu/Co pillars. *Phys. Rev. Lett.* 84, 3149–3152. doi:10.1103/physrevlett.84.3149

Kawahara, T., Ito, K., Takemura, R., and Ohno, H. (2012). Spin-transfer torque RAM technology: review and prospect. *Microelectron. Reliab.* 52, 613–627. doi:10.1016/j.microrel.2011.09.028

Khan, A. I., Keshavarzi, A., and Datta, S. (2020). The future of ferroelectric field-effect transistor technology. *Nat. Electron.* 3, 588–597. doi:10.1038/s41928-020-00492-7

Kim, S., Ishii, M., Lewis, S., Perri, T., BrightSky, M., Kim, W., et al. (2015). "NVM neuromorphic core with 64k-cell (256-by-256) phase change memory synaptic array with on-chip neuron circuits for continuous *in-situ* learning," in 2015 IEEE International Electron Devices Meeting (IEDM), Washington, DC, USA, 7-9 December 2015, 17.1.1–17.1.4.

Kim, S. J., Mohan, J., Summerfelt, S. R., and Kim, J. (2019). Ferroelectric Hf0.5Zr0.5O2 thin films: a review of recent advances. *JOM J. Min. Mater. Mat. Soc.* 71, 246–255. doi:10.1007/s11837-018-3140-5

Kohlstedt, H., Pertsev, N., Rodríguez Contreras, J., and Waser, R. (2005). Theoretical current-voltage characteristics of ferroelectric tunnel junctions. *Phys. Rev. B* 72, 125341. doi:10.1103/physrevb.72.125341

Kum, H. S., Lee, H., Kim, S., Lindemann, S., Kong, W., Qiao, K., et al. (2020). Heterogeneous integration of single-crystalline complex-oxide membranes. *Nature* 578, 75–81. doi:10.1038/s41586-020-1939-z

Kurenkov, A., Zhang, C., DuttaGupta, S., Fukami, S., and Ohno, H. (2017). Device-size dependence of field-free spin-orbit torque induced magnetization switching in antiferromagnet/ferromagnet structures. *Appl. Phys. Lett.* 110, 092410. doi:10.1063/1.4977838

Lecoeur, P., Trouilloud, P. L., Xiao, G., Gupta, A., Gong, G. Q., and Li, X. W. (1997). Magnetic domain structures of La0.67Sr0.33MnO3 thin films with different morphologies. *J. Appl. Phys.* 82 (8), 3934–3939. doi:10.1063/1.365700

Lederer, M., Kämpfe, T., Ali, T., Müller, F., Olivo, R., Hoffmann, R., et al. (2021). Ferroelectric field effect transistors as a synapse for neuromorphic application. *IEEE Trans. Electron Devices* 68 (5), 2295–2300. doi:10.1109/TED.2021.3068716

Lederer, M., Olivo, R., Yadav, N., De, S., Seidel, K., Eng, L. M., et al. (2023). SPICE compatible semi empirical compact model for ferroelectric hysteresis. *Solid-State Electron.* 199 (1), 108501. doi:10.1016/j.sse.2022.108501

Lee, K., Kim, W. J., Lee, J. H., Bae, B. J., Park, J. H., Kim, I. H., et al. (2019). "1Gbit high density embedded STT-MRAM in 28nm FDSOI technology," in 2019 IEEE International Electron Devices Meeting (IEDM), San Francisco, CA, USA, 07-11 December 2019, 2.2.1–2.2.4.

Lequeux, S., Sampaio, J., Cros, V., Yakushiji, K., Fukushima, A., Matsumoto, R., et al. (2016). A magnetic synapse: multilevel spin-torque memristor with perpendicular anisotropy. *Sci. Rep.* 6, 31510. doi:10.1038/srep31510

Li, S., Kang, W., Huang, Y., Zhang, X., Zhou, Y., and Zhao, W. (2017). Magnetic skyrmion-based artificial neuron device. *Nanotechnology* 28, 31LT01. doi:10.1088/1361-6528/aa7af5

Li, Z.-x., Geng, X.-y., Wang, J., and Zhuge, F. (2021). Emerging artificial neuron devices for probabilistic computing. *Front. Neurosci. Sec. Neural Technol.* 15, 717947. doi:10.3389/fnins.2021.717947

Likharev, K. K. (2011). CrossNets: neuromorphic hybrid CMOS/nanoelectronic networks. *Sci. Adv. Mat.* 3, 322–331. doi:10.1166/sam.2011.1177

Liu, L., Pai, C. F., Li, Y., Tseng, H. W., Ralph, D. C., and Buhrman, R. A. (2012). Spin-torque switching with the giant spin Hall effect of tantalum. *Science* 336, 555–558. doi:10.1126/science.1218197

Luo, Q., Cheng, Y., Yang, J., Cao, R., Ma, H., Yang, Y., et al. (2020). A highly CMOS compatible hafnia-based ferroelectric diode. *Nat. Commun.* 11, 1391. doi:10.1038/s41467-020-15159-2

Luo, Z., Wang, Z., Guan, Z., Ma, C., Zhao, L., Liu, C., et al. (2022). High-precision and linear weight updates by subnanosecond pulses in ferroelectric tunnel junction for neuro-inspired computing. *Nat. Commun.* 13, 699. doi:10.1038/s41467-022-28303-x

Ma, C., Luo, Z., Huang, W., Zhao, L., Chen, Q., Lin, Y., et al. (2020). Sub-nanosecond memristor based on ferroelectric tunnel junction. *Nat. Comm.* 11, 1439. doi:10.1038/s41467-020-15249-1

Maass, W. (2014). Noise as a resource for computation and learning in networks of spiking neurons. *Proc. IEEE* 102 (5), 860–880. doi:10.1109/jproc.2014.2310593

Majumdar, H. T., Pande, I., and van Dijken, S. (2019b). Crossover from synaptic to neuronal functionalities through carrier concentration control in Nb-doped SrTiO3-based organic ferroelectric tunnel junctions. *Apl. Mater.* 7, 091114. doi:10.1063/1.5111291

Majumdar, S. (2021). Ultrafast switching and linear conductance modulation in ferroelectric tunnel junctions via P (VDF-TrFE) morphology control. *Nanoscale* 13, 11270–11278. doi:10.1039/d1nr01722e

Majumdar, S. (2022a). Back-end CMOS compatible and flexible ferroelectric memories for neuromorphic computing and adaptive sensing. *Adv. Intell. Syst.* 4, 2100175. doi:10.1002/aisy.202100175

Majumdar, S. (2022b). An efficient deep neural network accelerator using controlled ferroelectric domain dynamics. *Neuromorphic Comput. Eng.* 2 (4), 041001. doi:10.1088/2634-4386/ac974d

Majumdar, S. (2017). Organic spintronics: the first decade and beyond contemporary topics in semiconductor spintronics. *World Sci.*, 199–240. doi:10.1142/9789813149823_0008

Majumdar, S., Avramov, P., and Sakai, S. (2018a). Manipulating spins at molecular level: an insight into the ferromagnet-organic interface. *World Sci. Reference Spin Organics* 2, 1–61. doi:10.1142/9789813230187_0001

Majumdar, S., Chen, B., Qin, Q. H., Majumdar, H. S., and van Dijken, S. (2018b). Electrode dependence of tunneling electroresistance and switching stability in organic ferroelectric P (VDF-TrFE)-Based tunnel junctions. *Adv. Funct. Mater.* 28, 1703273. doi:10.1002/adfm.201703273

Majumdar, S., Huhtinen, H., Majumdar, H. S., Laiho, R., and Österbacka, R. (2008). Effect of La0.67Sr0.33MnO3 electrodes on organic spin valves. *J. Appl. Phys.* 104, 033910. doi:10.1063/1.2963814

Majumdar, S., Huhtinen, H., Majumdar, H. S., and Paturi, P. (2012a). Stress and defect induced enhanced low field magnetoresistance and dielectric constant in La0.7Sr0.3MnO3 thin films. *J. Alloys Compd.* 512 (1), 332–339. doi:10.1016/j.jallcom.2011.09.093

Majumdar, S., Laiho, R., Laukkanen, P., Vayrynen, I. J., Majumdar, H. S., and Österbacka, R. (2006). Application of regioregular polythiophene in spintronic devices: effect of interface. *Appl. Phys. Lett.* 89 (12), 122114. doi:10.1063/1.2356463

Majumdar, S., and Majumdar, H. (2012). On the origin of decay of spin current with temperature in organic spintronic devices. *Org. Electron.* 13, 2653–2658. doi:10.1016/j.orgel.2012.07.042

Majumdar, S., Majumdar, H. S., Österbacka, R., and Spintronics, O. (2011) *Comprehensive nanoscience and technology (oxford: academic) vol 1*, 109.

Majumdar, S., Tan, H., Qin, Q., and van Dijken, S. (2019a). Energy-efficient organic ferroelectric tunnel junction memristors for neuromorphic computing. *Adv. Electron. Mater.* 5, 1800795. doi:10.1002/aelm.201800795

Majumdar, S., and van Dijken, S. (2013). Pulsed laser deposition of $La_{1-x}Sr_xMnO_3$: thin-film properties and spintronic applications. *J. Phys. D Appl. Phys.* 47 (3), 034010. doi:10.1088/0022-3727/47/3/034010

Majumdar, S., and Zeimpekis, I. (2023). "Back-end and flexible substrate compatible analog ferroelectric field effect transistors for accurate online training," in *Deep neural network accelerators advanced intelligent systems*.

Majumdar, S., Zhou, Y., Huhtinen, H., Mawass, M.-A., and Cronast, F. (2024) *Controlled domain rotation in La1-xSrxMnO3 (x = 0.5) thin films near ferro-antiferromagnetic phase boundary resulting in multistate analog memory, (Manuscript in preparation)*.

Maksymovych, P., Jesse, S., YuRamesh, P. R., Baddorf, A., and Kalinin, S. V. (2009). Polarization control of electron tunneling into ferroelectric surfaces. *Science* 324, 1421–1425. doi:10.1126/science.1171200

Malik, I. A., Huang, H., Wang, Y., Wang, X., Xiao, C., Sun, Y., et al. (2020). Inhomogeneous-strain-induced magnetic vortex cluster in one-dimensional manganite wire. *Sci. Bull.* 65, 201–207. doi:10.1016/j.scib.2019.11.025

Manipatruni, S., Nikonov, D. E., and Young, I. A. (2018). Beyond CMOS computing with spin and polarization. *Nat. Phys.* 14, 338–343. doi:10.1038/s41567-018-0101-4

Marković, D., Mizrahi, A., Querlioz, D., and Grollier, J. (2020). Physics for neuromorphic computing. *Nat. Rev. Phys.* 2, 499–510. doi:10.1038/s42254-020-0208-2

McDonnell, M., and Ward, L. (2011). The benefits of noise in neural systems: bridging theory and experiment. *Nat. Rev. Neurosci.* 12 (7), 415–425. doi:10.1038/nrn3061

Mehonic, A., Sebastian, A., Rajendran, B., Simeone, O., Vasilaki, E., and Kenyon, A. J. (2020). Memristors—from in-memory computing, deep learning acceleration, and spiking neural networks to the future of neuromorphic and bio-inspired computing. *Adv. Intell. Syst.* 2, 2000085. doi:10.1002/aisy.202000085

Merz, W. J. (1954). Domain Formation and domain wall motions in ferroelectric BaTiO3 single crystals. *Phys. Rev.* 95, 690–698. doi:10.1103/physrev.95.690

Migita, S., Ota, H., Asanuma, S., Morita, Y., and Toriumi, A. (2021). Accelerated ferroelectric phase transformation in HfO2/ZrO2 nanolaminates. *Appl. Phys. Express* 14, 051006. doi:10.35848/1882-0786/abfa75

Miron, I. M., Garello, K., Gaudin, G., Zermatten, P. J., Costache, M. V., Auffret, S., et al. (2011). Perpendicular switching of a single ferromagnetic layer induced by in-plane current injection. *Nature* 476, 189–193. doi:10.1038/nature10309

Mulaosmanovic, H., Chicca, E., Bertele, M., Mikolajick, T., and Slesazeck, S. (2018). Mimicking biological neurons with a nanoscale ferroelectric transistor. *Nanoscale* 10, 21755–21763. doi:10.1039/c8nr07135g

Mulaosmanovic, H., Ocker, J., Muller, S., Noack, M., Muller, J., Polakowski, P., et al. (2017). "Novel ferroelectric FET based synapse for neuromorphic systems," in 2017 Symposium on VLSI Technology, Kyoto, Japan, 5-8 June 2017, T176–T177.

Mulaosmanovic, H., Slesazeck, S., Ocker, J., Pesic, M., Muller, S., Flachowsky, S., et al. (2015). "Evidence of single domain switching in hafnium oxide based FeFETs: enabler for multi-level FeFET memory cells," in 2015 IEEE International Electron Devices Meeting (IEDM), Washington, DC, USA, 7-9 December 2015, 26.8.1–26.8.3.

Muller, J., Yurchuk, E., Schlosser, T., Paul, J., Hoffmann, R., Muller, S., et al. (2012). "Ferroelectricity in HfO2 enables nonvolatile data storage in 28 nm HKMG," in *Symposium on VLSI technology, ser. VLSI* (Honolulu, HI, USA: IEEE), 25–26. doi:10.1109/VLSIT.2012.6242443

Nandakumar, S. R., Boybat, I., Le Gallo, M., Sebastian, A., Rajendran, B., and Eleftheriou, E. (2017). "Supervised learning in spiking neural networks with MLC PCM synapses," in 2017 75th Annual Device Research Conference (DRC), South Bend, IN, USA, 25-28 June 2017, 1–2.

Nessler, B., Pfeiffer, M., Buesing, L., and Maass, W. (2013). Bayesian computation emerges in generic cortical microcircuits through spike-timing-dependent plasticity. *PLoS Comput. Biol.* 9 (4), e1003037. doi:10.1371/journal.pcbi.1003037

Nomura, H., Furuta, T., Tsujimoto, K., Kuwabiraki, Y., Peper, F., Tamura, E., et al. (2019). Reservoir computing with dipole-coupled nanomagnets. *Jpn. J. Appl. Phys.* 58, 070901. doi:10.7567/1347-4065/ab2406

Oconnor, P., Neil, D., Liu, S.-C., Delbruck, T., and Pfeiffer, M. (2013). Real-time classification and sensor fusion with a spiking deep belief network. *Front. Neurosci.* 7, 178. doi:10.3389/fnins.2013.00178

Onaya, T., Nabatame, T., Sawamoto, N., Ohi, A., Ikeda, N., Nagata, T., et al. (2019). Ferroelectricity of HfxZr1−xO2 thin films fabricated by 300 °C low temperature process with plasma-enhanced atomic layer deposition. *Microelectron. Eng.* 215, 111013. doi:10.1016/j.mee.2019.111013

Paasio, E., Prunnila, M., and Majumdar, S. (2023). "Modelling ferroelectric hysteresis of HZO capacitor with jiles-atherton model for non-volatile memory applications," in 2023 IEEE 12th Non-Volatile Memory Systems and Applications Symposium (NVMSA), Niigata, Japan, August 30 - September 1, 2023, 1–2.

Park, M. H., Chung, C.-C., Schenk, T., Richter, C., Hoffmann, M., Wirth, S., et al. (2018). Origin of temperature-dependent ferroelectricity in Si-doped HfO2. *Adv. Electron. Mat.* 4, 1700489. doi:10.1002/aelm.201700489

Park, M. H., Kim, H. J., Lee, Y. H., Kim, Y. J., Moon, T., Kim, K. D., et al. (2016). Two-step polarization switching mediated by a nonpolar intermediate phase in Hf0.4Zr0.6O2 thin films. *Nanoscale* 8, 13898–13907. doi:10.1039/c5nr08346j

Pecevski, D., Buesing, L., and Maass, W. (2011). Probabilistic inference in general graphical models through sampling in stochastic networks of spiking neurons. *PLoS Comput. Biol.* 7 (12), e1002294. doi:10.1371/journal.pcbi.1002294

Pedroni, B. U., Das, S., Neftci, E., Kreutz-Delgado, K., and Cauwenberghs, G. (2013). Neuromorphic adaptations of restricted Boltzmann machines and deep belief networks. *Proc. Int.l Jt. Conf. IEEE Neural Netw.*, 1–6. doi:10.1109/ijcnn.2013.6707067

Pinna, D., Abreu Araujo, F., Kim, J. V., Cros, V., Querlioz, D., Bessiere, P., et al. (2018). Skyrmion gas manipulation for probabilistic computing. *Phys. Rev. Appl.* 9, 064018. doi:10.1103/physrevapplied.9.064018

Qin, Q. H., Äkäslompolo, L., Tuomisto, N., Yao, L., Majumdar, S., Vijayakumar, J., et al. (2016). Resistive switching in all-oxide ferroelectric tunnel junctions with ionic interfaces. *Adv. Mater.* 28 (32), 6852–6859. doi:10.1002/adma.201504519

Rao, M., Tang, H., Wu, J., Song, W., Zhang, M., Yin, W., et al. (2023). Thousands of conductance levels in memristors integrated on CMOS. *Nature* 615, 823–829. doi:10.1038/s41586-023-05759-5

Rofeh, J., Sodhi, A., Payvand, M., Lastras-Montano, M. A., Ghofrani, A., Madhavan, A., et al. (2015). "Vertical integration of memristors onto foundry CMOS dies using wafer-scale integration," in 2015 IEEE 65th Electronic Components and Technology Conference (ECTC), San Diego, CA, USA, 26-29 May 2015, 957–962.

Romera, M., Talatchian, P., Tsunegi, S., Abreu Araujo, F., Cros, V., Bortolotti, P., et al. (2018). Vowel recognition with four coupled spin-torque nano-oscillators. *Nature* 563, 230–234. doi:10.1038/s41586-018-0632-y

Saha, R., Pundir, Y. P., and Pal, P. K. (2022). Comparative analysis of STT and SOT based MRAMs for last level caches. *J. Magnetism Magnetic Mater.* 551, 169161. doi:10.1016/j.jmmm.2022.169161

Sato, H., Enobio, E. C. I., Yamanouchi, M., Ikeda, S., Fukami, S., Kanai, S., et al. (2014). Properties of magnetic tunnel junctions with a MgO/CoFeB/Ta/CoFeB/MgO recording structure down to junction diameter of 11 nm. *Appl. Phys. Lett.* 105, 062403. doi:10.1063/1.4892924

Sebastian, A., Pendurthi, R., Kozhakhmetov, A., Trainor, N., Robinson, J. A., Redwing, J. M., et al. (2022). Two-dimensional materials-based probabilistic synapses and reconfigurable neurons for measuring inference uncertainty using Bayesian neural networks. *Nat. Commun.* 13, 6139. doi:10.1038/s41467-022-33699-7

Sengupta, A., Banerjee, A., and Roy, K. (2016a). Hybrid spintronic-cmos spiking neural network with on-chip learning: devices, circuits, and systems. *Phys. Rev. Appl.* 6, 064003. doi:10.1103/PhysRevApplied.6.064003

Sengupta, A., Shim, Y., and Roy, K. (2016b). Proposal for an all-spin artificial neural network: emulating neural and synaptic functionalities through domain wall motion in ferromagnets. *IEEE Trans. Biomed. Circ. Syst.* 10, 1152–1160. doi:10.1109/TBCAS.2016.2525823

Sharad, M., Augustine, C., Panagopoulos, G., and Roy, K. (2012). Spin-based neuron model with domain-wall magnets as synapse. *IEEE Trans. Nanotechnol.* 11, 843–853. doi:10.1109/tnano.2012.2202125

Sheikh, F., Nagisetty, R., Karnik, T., and Kehlet, D. (2021). 2.5D and 3D heterogeneous integration: emerging applications. *IEEE Solid-State Circuits Mag. Fall* 13 (4), 77–87. doi:10.1109/MSSC.2021.3111386

Slavin, A., and Tiberkevich, V. (2009). Nonlinear auto-oscillator theory of microwave generation by spin-polarized current. *IEEE Trans. Magn.* 45, 1875–1918. doi:10.1109/tmag.2008.2009935

Slonczewski, J. (1996). Current-driven excitation of magnetic multilayers. *J.Magn. Magn. Mat.* 159, L1–L7. doi:10.1016/0304-8853(96)00062-5

Tagantsev, A. K., Stolichnov, I., Setter, N., Cross, J. S., and Tsukada, M. (2002). Non-Kolmogorov-Avrami switching kinetics in ferroelectric thin films. *Phys. Rev. B* 66, 214109. doi:10.1103/physrevb.66.214109

Tan, H., Castro, G., Lyu, J., Loza-Alvarez, P., Sanchez, F., Foncuberta, J., et al. (2022). Control of up-to-down/down-to-up light-induced ferroelectric polarization reversal. *Mat. Horiz.* 9, 2345–2352. doi:10.1039/d2mh00644h

Tan, H., Majumdar, S., Qin, Q., Lahtinen, J., and van Dijken, S. (2019). Mimicking neurotransmitter release and long-term plasticity by oxygen vacancy migration in a tunnel junction memristor. *Adv. Intell. Syst.* 1 (2), 1900036. doi:10.1002/aisy.201900036

Thomas, L., Moriya, R., Rettner, C., and Parkin, S. S. P. (2010). Dynamics of magnetic domain walls under their own inertia. *Science* 330, 1810–1813. doi:10.1126/science.1197468

Torrejon, J., Riou, M., Araujo, F. A., Tsunegi, S., Khalsa, G., Querlioz, D., et al. (2017). Neuromorphic computing with nanoscale spintronic oscillators. *Nature* 547, 428–431. doi:10.1038/nature23011

Tsymbal, E. Y., and Kohlstedt, H. (2006). Tunneling across a ferroelectric. *Science* 313, 181–183. doi:10.1126/science.1126230

Tuma, T., Pantazi, A., Le Gallo, M., Sebastian, A., and Eleftheriou, E. (2016). Stochastic phase-change neurons. *Nat. Nanotechnol.* 11, 693–699. doi:10.1038/nnano.2016.70

Wang, C., Agrawal, A., Yu, E., and Roy, K. (2021). Multi-level neuromorphic devices built on emerging ferroic materials: a review. *Front. Neurosci.* 15, 661667. doi:10.3389/fnins.2021.661667

Wang, D., Wang, J., Li, Q., He, W., Guo, M., Zhang, A., et al. (2019). Stable ferroelectric properties of Hf0.5Zr0.5O2 thin films within a broad working temperature range. *Jpn. J. Appl. Phys.* 58, 090910. doi:10.7567/1347-4065/ab3844

Wang, J., Wu, S., Ma, J., Xie, L., Wang, C., Malik, I. A., et al. (2018). Nanoscale control of stripe-ordered magnetic domain walls by vertical spin transfer torque in La0.67Sr0.33MnO3 film. *Appl. Phys. Lett.* 112. Article 072408. doi:10.1063/1.5017687

Wang, J., Xie, L., Wang, C., Zhang, H. Z., Shu, L., Bai, J., et al. (2014). Magnetic domain-wall motion twisted by nanoscale probe-induced spin transfer. *Phys. Rev. B* 90, 224407. Article 224407. doi:10.1103/physrevb.90.224407

Wang, P., Peng, X., Chakraborty, W., Khan, A. I., Datta, S., and Yu, S. (2020a). "Cryogenic benchmarks of embedded memory technologies for recurrent neural network based quantum error correction," in IEEE International Electron Devices Meeting (IEDM).

Wang, X., Chen, Y., Xi, H., Li, H., and Dimitrov, D. (2009). Spintronic memristor through spin-torque-induced magnetization motion. *IEEE Electron Device Lett.* 30, 294–297. doi:10.1109/led.2008.2012270

Wang, Z., Ying, H., Chern, W., Yu, S., Mourigal, M., Cressler, J. D., et al. (2020b). Cryogenic characterization of a ferroelectric field-effect-transistor. *Appl. Phys. Lett.* 116, 042902. doi:10.1063/1.5129692

Wesling, P. (2020). "The heterogeneous integration roadmap: enabling technology for systems of the future," in 2020 Pan Pacific Microelectronics Symposium (Pan Pacific), HI, USA, February 10-13, 2020, 1–4.

Woo, K. S., Kim, J., Han, J., Kim, W., Jang, Y. H., and Hwang, C. S. (2022). Probabilistic computing using Cu0.1Te0.9/HfO2/Pt diffusive memristors. *Nat. Commun.* 13, 5762. doi:10.1038/s41467-022-33455-x

Woo, S., Litzius, K., Krüger, B., Im, M. Y., Caretta, L., Richter, K., et al. (2016). Observation of room-temperature magnetic skyrmions and their current-driven dynamics in ultrathin metallic ferromagnets. *Nat. Mat.* 15, 501–506. doi:10.1038/nmat4593

Xia, Q., and Yang, J. J. (2019). Memristive crossbar arrays for brain-inspired computing. *Nat. Mater.* 18, 309–323. doi:10.1038/s41563-019-0291-x

Yamaguchi, A., Nasu, S., Miyake, K., Mibu, K., and Shinjo, T. (2004). Real-space observation of current-driven domain wall motion in submicron magnetic wires. *Phys. Rev. Lett.* 92, 077205. doi:10.1103/physrevlett.92.077205

Yamanouchi, M., Chiba, D., Matsukura, F., and Ohno, H. (2004). Current-induced domain-wall switching in a ferromagnetic semiconductor structure. *Nature* 428, 539–542. doi:10.1038/nature02441

Yang, J. J., Strukov, D. B., and Stewart, D. R. (2013). Memristive devices for computing. *Nat. Nanotechnol.* 8, 13–24. doi:10.1038/nnano.2012.240

Yang, S., Shin, J., Kim, T., Moon, K.-W., Kim, J., Jang, G., et al. (2021). Integrated neuromorphic computing networks by artificial spin synapses and spin neurons. *NPG Asia Mater.* 13, 11. Article number: 11. doi:10.1038/s41427-021-00282-3

Yingfen, W., Vats, G., and Noheda, B. (2022). Synaptic behaviour in ferroelectric epitaxial rhombohedral Hf0.5Zr0.5O2 thin films. *Neuromorph. Comput. Eng.* 2, 044007. doi:10.1088/2634-4386/ac970c

Yoong, H. Y., Wu, H., Zhao, J., Wang, H., Guo, R., Xiao, J., et al. (2018). Epitaxial ferroelectric Hf0. 5Zr0. 5O2 thin films and their implementations in memristors for brain-inspired computing. *Adv. Funct. Mat.* 28, 1806037. doi:10.1002/adfm.201806037

Yu, S., Shim, W., Hur, J., Luo, Y. c., Choe, G., Li, W., et al. (2021). "Compute-in-Memory: from device innovation to 3D system integration," in ESSDERC 2021 – IEEE 51st European Solid-State Device Research Conference (ESSDERC), Grenoble, France, September 13-22, 2021, 21–28.

Zázvorka, J., Jakobs, F., Heinze, D., Keil, N., Kromin, S., Jaiswal, S., et al. (2019). Thermal skyrmion diffusion used in a reshuffler device. *Nat. Nanotechnol.* 14, 658–661. doi:10.1038/s41565-019-0436-8

frontiers | Frontiers in Nanotechnology

TYPE Original Research
PUBLISHED 20 May 2024
DOI 10.3389/fnano.2024.1352287

OPEN ACCESS

EDITED BY
Neha Kaushik,
University of Suwon, Republic of Korea

REVIEWED BY
Satheesh kumar Balu,
Saveetha Dental College And Hospitals, India
Yashika Rustagi,
Dana–Farber Cancer Institute, United States

*CORRESPONDENCE
Elena Alexander,
ei2169@columbia.edu

RECEIVED 07 December 2023
ACCEPTED 26 April 2024
PUBLISHED 20 May 2024

CITATION
Alexander E and Leong KW (2024), Immunomodulatory effects of laser-synthesized nanodiamonds on peripheral blood mononuclear cells: evaluation of unconjugated, PEGylated, and antibody-conjugated formulations.
Front. Nanotechnol. 6:1352287.
doi: 10.3389/fnano.2024.1352287

Immunomodulatory effects of laser-synthesized nanodiamonds on peripheral blood mononuclear cells: evaluation of unconjugated, PEGylated, and antibody-conjugated formulations

Elena Alexander* and Kam W. Leong

Department of Biomedical Engineering, Columbia University, New York City, NY, United States

The application of laser-synthesized nanodiamonds (LNDs) is of great interest to biomedical researchers and drug developers because this emerging method of synthesis yields nanodiamonds of consistent size (<5 nm diameter) and surface chemistry that can be functionalized to perform a staggering range of highly specialized tasks. The present study assessed the threshold at which LNDs in various conjugations and concentrations triggered immune responses and cytotoxicity in peripheral mononuclear blood cells from healthy donors, as assessed by changes in ATP concentrations and induced secretion of the cytokines IFN-γ, IL-6 and TNF-α. Conjugations assessed were raw (unconjugated) NDs, PEGylated (PEG5k-NDs), and antibody conjugated to goat anti-mouse antibodies (IgG-NDs). Concentrations of each conjugation were prepared and tested at 50.0, 10.0, 2.0, 0.4, and 0.08 μg/mL. Results showed that pegylated and raw NDs were well tolerated, with the indicators of inflammation or minimal cytotoxicity emerging only at the highest concentrations tested (50.0 μg/mL). IgG-NDs showed signs of inflammatory responses at the two highest concentrations tested (10.0 and 50.0 μg/mL). There was some evidence that the dilutant vehicle used for ND suspension may have contributed to the immune response. All three ND configurations increased ATP concentration in a dose-dependent manner, up to a concentration of 10.0 μg/mL. At the highest concentration (50.0 μg/mL), the ND solutions showed minimal signs of cytotoxicity. Conclusion from this testing suggest that LNDs are likely to offer substantial utility in biomedical applications because of their capacity to evade the immune response at concentrations at least as high as 2.0 μg/mL and potentially up to 50.0 μg/mL.

KEYWORDS

nanodiamond, biomedical application, immune response, nanomaterials, carbon-based nanomaterials (CBNs)

1 Introduction

Nanodiamonds (NDs) describe a family of carbon-based nanomaterials (i.e., diameter <100 nm) with the same sp^3 lattice structure that gives natural diamonds their exceptional hardness and electrical insulating properties. The outer surface of NDs, however, is composed of unpaired carbon atoms in the sp^2 configuration, which makes this novel material relatively easy to manipulate and customize for a variety of highly specific functions (Gao et al., 2019; Reina et al., 2019; Chang et al., 2022). Interest in NDs for biomedical applications has grown dramatically in the past decade, owing largely to their high biocompatibility and easily customizable surface chemistry. Of all known carbon nanomaterials—e.g., nanotubes and fullerenes—NDs have the highest biocompatibility in addition to excellent stability *in vivo*, making them exciting candidates for nanomedical applications (Sadat et al., 2022).

1.1 Nanodiamonds and immunogenicity

Among the many lines of investigation being pursued for deploying NDs to improve human health is their capacity to modulate the immune system. Studies have demonstrated the capacity of NDs to elicit highly specific immune responses by affixing different antibodies and small molecules to their surface (Suarez-Kelly et al., 2021; Paladhi et al., 2022). A few of the many examples include enhanced proliferation of $CD4^+$ and $CD8^+$ T-cells (Ghoneum et al., 2014), B-lymphocytes (Huang et al., 2017; Suarez-Kelly et al., 2017), macrophages (Pentecost et al., 2019), and neutrophils (Chang et al., 2003).

Conversely, many potential applications of NDs seek to minimize or eliminate the immune response to particles so that the latter can perform a particular function unimpeded. Examples include intravenous injection of functionalized fluorescent NDs for bioimaging (Kaçar and Erden, 2020; Montes et al., 2020; van der Laan et al., 2020; Lin et al., 2022; Sharmin et al., 2022; Li et al., 2023) or accumulation of functionalized NDs around damaged tissues (e.g., cardiac, neural) to induce stem-cell repair (Ansari et al., 2016; Alexander et al., 2019; Taylor et al., 2019; Liu et al., 2021).

At the heart of ND interaction with the immune system are Adenosine Triphosphate (ATP) and cytokines. ATP, beyond its role as the cellular "energy currency," functions as a signaling molecule that influences cellular processes, including metabolism, stress responses, and immune signaling (Zimmermann, 2000; Di Virgilio et al., 2018). High ATP levels might indicate increased metabolic activity or stress responses, while low levels could suggest energy depletion or impaired metabolic function (Shao et al., 2018).

Cytokines, as key signaling molecules, play significant roles in mediating immunity and inflammation. Elevated cytokine levels typically signal an active immune response, possibly due to infection or inflammation, and might also indicate autoimmune processes. Conversely, low cytokine levels can point to immune deficiencies or regulatory dysfunctions, highlighting the balance between pro-inflammatory and anti-inflammatory responses as a critical factor in health and disease (Iwamoto et al., 2014).

The interaction between ATP and cytokines is particularly intriguing, as ATP can act as an extracellular signaling molecule influencing cytokine production. This crosstalk is evident in situations of cellular stress or damage, where ATP is released and can trigger inflammatory responses through cytokine production, demonstrating the interconnectedness of energy metabolism and immune responses (Vultaggio-Poma et al., 2020).

In pathophysiological conditions, such as cancer and autoimmune diseases, the dysregulation of ATP production and cytokine secretion is a common feature. In cancer, altered ATP metabolism supports uncontrolled cell proliferation, while in autoimmune diseases, cytokine imbalances drive inflammation and tissue damage, pointing to the potential of targeting these pathways for therapeutic interventions.

Understanding the intricate relationships between ATP levels, cytokine profiles, and disease states could unveil new therapeutic targets and biomarkers for disease detection and monitoring. This knowledge emphasizes the importance of a comprehensive analysis of ATP and cytokine concentrations for developing innovative therapeutic strategies and improving disease management (Kalyanaraman, 2017).

This study aims to dissect the immunomodulatory effects of LNDs, characterized by their purity and consistent nanoscale dimensions, on peripheral blood mononuclear cells (PBMCs). Through examining changes in ATP concentrations and the secretion of key cytokines (IFN-γ, IL-6, TNF-α), we seek to elucidate the mechanisms through which LNDs interact with cellular metabolism and the immune response, contributing to the broader understanding of NDs in biomedical applications.

1.2 Findings and overview

The present study investigated the immunomodulatory effects of three configurations of laser-synthesized NDs (LNDs, diameter <5 nm) on peripheral blood mononuclear cells (PBMCs) from healthy donors. Specifically, NDs were tested as unconjugated (raw-NDs, in-vehicle only), PEGylated (PEG5k-NDs), and antibody conjugated (IgG-NDs).

As measured by changes in ATP concentrations and induced secretion of the cytokines IFN-γ, IL-6, and TNF-α, the pegylated and raw NDs were well tolerated by PBMCs with no indication of inflammation or cytotoxicity, except at the highest concentrations tested (50 μg/mL). PBMCs incubated with IgG-NDs showed signs of inflammatory responses at ND concentrations of 10 and 50 μg/mL. However, there was some evidence that the dilutant vehicle used for ND suspension may have exacerbated the elevation in IL-6 and TNF-α, in addition to stimulating ATP production and cellular proliferation.

PBMC incubation with all three ND formulations resulted in increased ATP concentration in a dose-dependent manner, up to a concentration of 10 μg/mL. At the next-highest concentration assessed (50 μg/mL), the ND solutions showed signs of non-specific cytotoxicity with increases in ATP.

At ND concentrations of 0.08, 0.4, and 2.0 μg/mL, there were no signs of either cytotoxicity or inflammatory response in PBMCs. Taken together, these findings suggest LNDs—including LNDs conjugated to antibodies—may be able to evade the immune response at concentrations at least as high as 2.0 μg/mL and potentially as high as 10 μg/mL.

TABLE 1 Treatment groups and related readouts.

Condition	Dose	Readouts
Media alone	N/A	ATP Glo assay
Vehicle 1 (dH_2O)	10, 2% and 0.4%	IL-6, TNFα, and IFN-γ quantification: Multiplex
Vehicle 2 (custom conjugate diluent)	10, 2% and 0.4%	
Muronomab (OKT3)	5 μg/mL	
ANC28.1	5 μg/mL	
IgG1	5 μg/mL	
Raw-NDs	50, 10, 2, 0.4, 0.08 μg/mL	
PEG5k-NDs		
IgG-NDs		

dH_2O = sterile, filtered deionized water; N/A = not applicable; ND, nanodiamond; OKT3 = plate-bound anti-CD3, stimulus.
Note: Custom conjugant dilutant consisted of 1*PBS +10% FBS; (see Section 2.2).

2 Materials and methods

2.1 Background on laser-synthesized nanodiamonds

LNDs differ from more common forms of NDs (e.g., detonation NDs [DNDs] or high-temperature high-pressure NDs [HTHP-NDs]) in that they are virtually devoid of impurities and have a smaller diameter that consistently ranges from 4 7 nm when compared with DNDs (4–100 nm) 21 and HTHP-NDs (≥40 nm and irregularly shaped) (Baidakova et al., 2013; Perevedentseva et al., 2015) 22. LNDs were chosen for this study because they offer some advantages for highly sensitive bio-applications: higher purity, better structural and spectroscopic properties, higher paramagnetism, easier control of surface chemistry (due to the absence of metal and graphite impurities), and lower cytotoxicity (Peer et al., 2007; Perevedentseva et al., 2015) 22, 23. Recent improvements in LND synthesis yield NDs with a diameter consistently <5 nm and a high purity—i.e., carbon >94% when compared with DNDs that are generally <86% carbon (Perevedentseva et al., 2015). 22.

2.2 Study design

This study evaluated NDs in three conjugations (raw/unconjugated, PEG5k-NDs, and IgG-NDs) for cytotoxicity and immunogenicity in human PBMCs from healthy donors. Endpoints were measured by relative ATP concentration and induced secretion of the cytokines IFN-γ, IL-6, and TNF-α.

NDs were prepared and tested at final assay concentrations of 50, 10, 2, 0.4, and 0.08 μg/ml. A serial dilution of NDs was prepared in assay media with sterile-filtered deionized water (SFDI) or custom conjugate dilutant, resulting in vehicle concentrations of 10%, 2%, 0.4%, 0.08%, and 0.016%. The custom conjugate dilutant consisted of 10% fetal bovine serum in phosphate-buffered solution (abbreviated as 1*PBS +10% FBS). Vehicle controls were tested at 10%, 2%, and 0.4%.

PBMCs were incubated in the presence of media only (plate-bound anti-CD3 stimulus [OKT3], soluble anti-CD28 stimulus, or antibody isotype control) for 72 h. PBMCs were then incubated with NDs at the five assay concentrations (i.e., 50.0, 10.0, 0.4, and 0.08 μg/mL) for 72 h. Each condition was plated in triplicate. After 72 h, supernatants were collected. Cells were lysed, and ATP quantified as a measure of cell number by CellTiter-Glo assay. IFN-γ, IL-6 and TNF-α cytokine concentrations in supernatant were analyzed by multiplex assay (Luminex®). Table 1 provides an overview of all conjugations, doses, and readouts used in the study.

Table 2 provides an overview of the ND conjugations tested and their relevant parameters.

2.3 Preparation and storage of nanodiamonds

Laser-synthesized ND powder with an average grain size <5 nm was obtained from Ray Techniques Ltd. Stock NDs were suspended by sonication before serial dilution in assay media (RPMI containing 2% HEPES, 2% L-Glutamine, and 10% human AB serum) and then incubated with 200,000 PBMCs. Final concentrations of NDs tested were 50 μg/mL, 10 μg/mL, 2 μg/mL, 0.4 μg/mL, and 0.08 μg/mL of raw NDs, PEG5k-NDs and IgG-NDs and 10%, 2%, and 0.4% of custom conjugate diluent and SFDI. Controls consisted of 1 μg/well of anti-CD3, anti-CD28 or isotype control. Cells were incubated in a humidified chamber at 5% CO_2 for 72 h. With the exception of probe sonication, the nanodiamonds were handled in a laminar flow hood to minimize exposure to contamination.

Raw NDs served as a control to determine what effects the ND themselves may have on the cells being studied. Analysis of this source of ND revealed that carboxylic acid groups served as a ready handle for functionalizing via an amide bond using standard EDC/NHS chemistry. Amino-mPEG5k was conjugated to the ND via the NH_2 end group, forming a stable amide bond. The PEG was methoxy terminated to introduce PEG without any additional functional groups. PEG is often coated onto the ND to improve nanoparticle circulation and shield the nanoparticle from the immune system. The length of the PEG was chosen as an intermediate between smaller and larger commercially available PEG lengths and matched well with

TABLE 2 Overview of ND conjugations used for assay testing.

Description	Number, Mean (nm)	PDI	pH	Zeta (mV)	Std dev Zeta
Raw ND in SFDI	160	0.029	4.8	38	1
ND-PEG5k in SFDI	320	0.38	5.2	36.5	0.7
ND-Ab in buffer	370	0.29	7.7	−28	0.7

Ab, antibody; dev, deviation; ND, nanodiamond; PDI; PEG, pegylated; SFDI, spatial frequency domain imaging.

the size of the ND. Goat anti-mouse antibody was chosen as a model antibody because it easily demonstrated functionality once conjugated to the ND via lateral flow assay (LFA) and was more likely to induce an immune response than the other two ND samples tested.

2.3.1 Preparation of ND suspension

Initial ND suspension was performed by adding 10 mg of ND powder to a sterile scintillation vial then adding 10 g of water. The vial was then sealed and placed in a bath sonicator until all NDs had been wetted (approximately 10 min). The ND suspension was disaggregated using a Sonic Ruptor 250™ from Omni Inc® using an OR-T-156 5/32 probe sonicator set at 40% max power (80% max power for probe size) with 60% pulse in a 0°C bath for 6 h. Raw NDs were NDs that only underwent the above preparation via probe sonication without further modification. The particles were characterized via UV-Vis, dynamic light scattering (DLS), zeta potential, and transmission electron microscope (TEM) (Figure 1).

2.3.2 ND PEGylation

Suspended NDs were then transferred to a 15 mL conical tube, and the pH adjusted by adding 25 µL 0.1 M NaOH. Freshly prepared aliquots of EDC[1] and NHS[2] at a concentration of 10 mg/mL (200 µL and 400 µL, respectively) were added to the NDs. The NDs were then incubated end-over-end on a rotator for 30 min. The sample was transferred to a 100 kDa MWCO[3] spin filter and spun at 1,452 rcf for 5 min. The material was transferred to a new 15 mL conical tube and resuspended in 10 mL of SFDI water + 25 µL 0.1 M NaOH. Then, 20 µL of mPEG5k-NH2 (10 mg/mL) was added to the ND suspension and allowed to incubate end-over-end at room temperature for 90 min. Hydroxylamine (50 µL) was added to quench any remaining activated EDC/NHS sites, allowing the sample to incubate for 10 min. The sample was transferred to a new spin filter and spun at 1,452 rcf for 5 min. The filtrate was removed, and the NDs were washed with an additional 5 mL SFDI two more times. PEGylated NDs were transferred to a new 15 mL tube and resuspended with 8 mL SFDI. PEGylated NDs were characterized via UV-vis, DLS, zeta potential, FTIR[4], and TEM and were stored at 4°C.

2.3.3 Antibody conjugation

ND carboxylate groups were again activated with EDC/NHS, as described above, to a 1 mg/mL suspension of sonicated ND in a 15 mL conical tube. Then, 10 µg purified antibody was added to the activated ND and incubated at room temperature for 1 h, followed by quenching with 50 µL hydroxylamine, with an additional 10-min incubation. Then, 100 µL 10% bovine serum albumin (BSA) was added to the ND, and the reaction mixture was incubated at room temp for an additional 10 min. The NDs were centrifuged at 5,000 rcf for 5 min, and the supernatant was removed. The NDs were resuspended in reaction buffer (5 mM sodium phosphate, 0.55 PEG20k, pH 7.4) and incubated on a rotator for 10 min, then centrifuged again at 5,000 rcf for 5 min. The NDs were resuspended in 8 mL of conjugate diluent (0.5× phosphate buffered saline, 0.5% casein, 0.5% BSA, 1% Tween 20™).

Goat-anti-mouse antibody-conjugated NDs (IgG-NDs) were characterized via UV-vis, DLS, zeta potential, and LFA. For LFA to test for the presence of functional Ab conjugated to ND, test strips were used with a negative control line of donkey-anti rabbit located 6 mm below the test line of mouse IgG. Only the test line was visible after running LFA with IgG-NDs. IgG-NDs were stored at 4°C.

2.4 Compunds and reagents tested

SFDI was used and additionally filtered through a 0.22 µm sterile filter. mPEG-5k-Amine was purchased from LyasanBio. EDC (1-ethyl-3-(3-dimethylaminopropyl) carbodiimide), sulfo-NHS (N-hydroxysulfosuccinimide), and hydroxylamine (50% in water) were purchased from Sigma-Aldrich. Goat anti-mouse antibodies (IgG Fc) were purchased from Lampire Biological Laboratories®. Reagents were used as received unless otherwise indicated.

2.5 Samples and assays used for testing

2.5.1 Blood sample collection

50–60 mL of whole blood was collected from healthy donors in sodium heparin vacutainer tubes. PBMCs were isolated from whole blood via density gradient centrifugation. Whole blood was diluted 1:1 in Ca^{2+}/Mg^{2+}-free HHBSS[5] before layering onto Histopaque® 1119. Blood was centrifuged, and contaminating red blood cells were removed with ammonium chloride potassium (ACK) lysis buffer.

1 EDC=(1-ethyl-3-(3-dimethylaminopropyl)carbodiimide hydrochloride).

2 NHS = N-hydroxysuccinimide.

3 MWCO = molecular weight cutoff.

4 FTIR = Fourier transform infrared spectroscopy.

5 HHBSS = HEPES-buffered Hanks balanced salt solution; HEPES = N-2-hydroxyethylpiperazine-N′-2-ethanesulfonic acid.

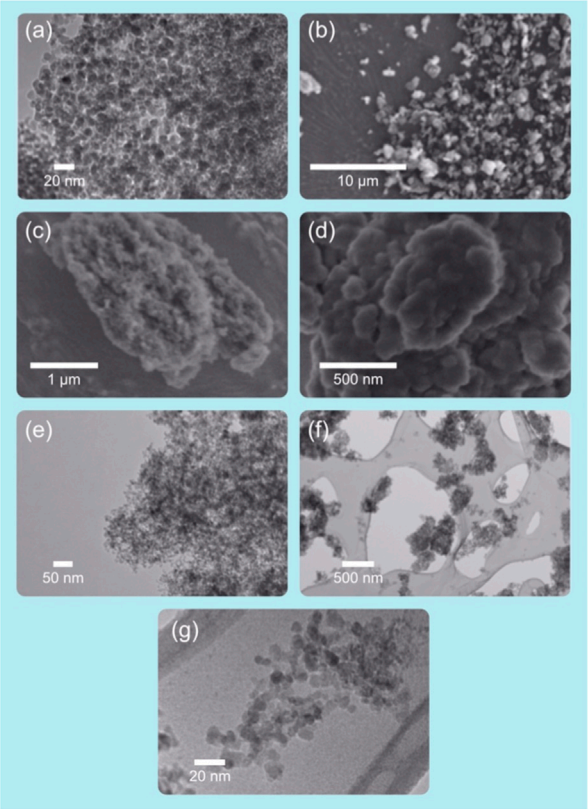

FIGURE 1
Images of NDs at various resolutions as they appear when captured with scanning-electron and transmission-electron microscopes. Laser synthesized nanodiamonds. Images **(A,E,F,G)** TEM. Images **(B–D)** SEM. Original illustration and images.

After isolation, viable PBMCs were counted using acridine orange/propidium iodide (AO/PI) viability stain and a Luna™ cell counter.

2.5.2 ATP Assay

Following a 72-h incubation, the plates were centrifuged, and supernatants were collected and frozen for Luminex analysis. The cells were mixed thoroughly before lysis with 100 µL of Promega Cell Titer Glo 2.0™ reagent. Luminescence was read on a luminometer to measure ATP concentration.

2.5.3 Luminex Assay

Concentrations of IFN-γ, IL-6, and TNF-α in cell culture supernatants were measured using a Bio-plex Luminex platform (BioRad), according to manufacturer's protocol.

2.6 Imaging tools

Nanodiamond grain and cluster sizes were imaged using a JEOL 1010 transmission electron microscope (TEM) equipped with a CCD camera for image capture. Dispersions of nanodiamonds were dried onto carbon-coated TEM grids prior to imaging. Dynamic light scattering (DLS) and zeta potential measurements were obtained from nanodiamond dispersions using a Malvern® Zetasizer Nano ZS™. UV-visible optical spectroscopy was obtained from nanodiamond solutions using an Agilent® 8453 spectrometer. Fourier transform infrared (FTIR) spectra were obtained from dried powder samples in attenuated-total reflectance mode and measured on a PerkinElmer® Spectrum 100™ UATR-FTIR.

3 Results

3.1 ATP levels in peripheral blood mononuclear cells

Incubation for 72 h with anti-CD3 treatment of PBMCs from all donors resulted in increased ATP concentration compared with media controls, which was indicative of increased cell proliferation (Figure 2; left panel). Furthermore, a slight increase in ATP concentration with anti-CD28 treatment but not with isotype control was detected. This suggests that the PBMCs from all donors were suitably plated for this experiment and were capable of proliferating with the control stimulation.

Of the vehicle controls tested, dH_2O had no effect on ATP at concentrations of 0.4%, 2%, or 10% and did not differ notably from the media control. The custom conjugate diluent appeared to reduce ATP concentration when tested at 10% (equivalent to 50 µg/mL). At 2% concentration, the custom conjugate diluent appeared to slightly increase the cell number, while there was no effect at 0.4%. ATP concentrations after 72-h incubation with any of the three ND formulations were very similar (Figure 2; right panel). Cells incubated with all three NDs appeared to show a modest, but concentration-dependent increase in ATP concentration between 80 ng/mL and 10 µg/mL. At 50 µg/mL, there was a negligible difference in ATP concentration when cells were treated with any of the three NDs or with media alone. Mean ATP concentrations are presented below. ATP concentrations from individual donors are presented in Section 6.1 in Supplementary Data.

This figure depicts the mean adenosine triphosphate (ATP) levels in PBMCs from three healthy donors, treated with different concentrations of nanodiamond (ND) formulations. The left panel shows control conditions, while the right panel displays responses to various ND conjugations. Data illustrate a dose-dependent increase in ATP concentration, indicating cell viability across the tested ND concentrations. Error bars represent standard error of the mean (SEM). Abbreviations: dH2O = sterile, filtered deionized water; h = hour; ND = nanodiamond; PBMC = peripheral blood mononuclear cells; SEM = standard error of the mean.

3.2 Cytokine concentrations in cell culture supranatants

PBMCs from all donors showed strong secretion of IFN-γ following anti-CD3 stimulation (Figure 3; top-left panel). There was no detectable induction of IFN-γ when cells were treated with anti-CD28, IgG1 isotype, or media alone. This suggests there was little background activation in the CD3-expressing cells when they were not activated by a specific stimulus.

Similar to IFN-γ, IL-6 was undetectable in media only-treated cells or with isotype control (Figure 3; top-center panel). When cells

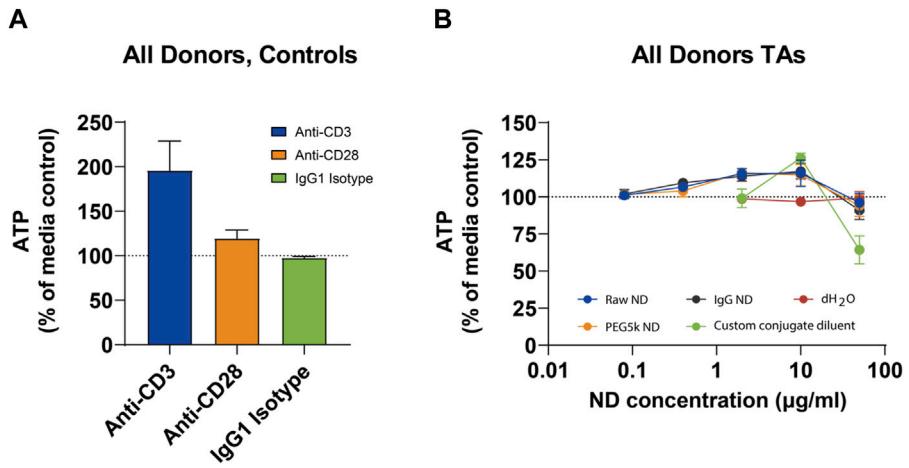

FIGURE 2
Mean ATP Levels in Peripheral Blood Mononuclear Cells in Controls **(A)** and Nanodiamond Conjugations **(B)**.

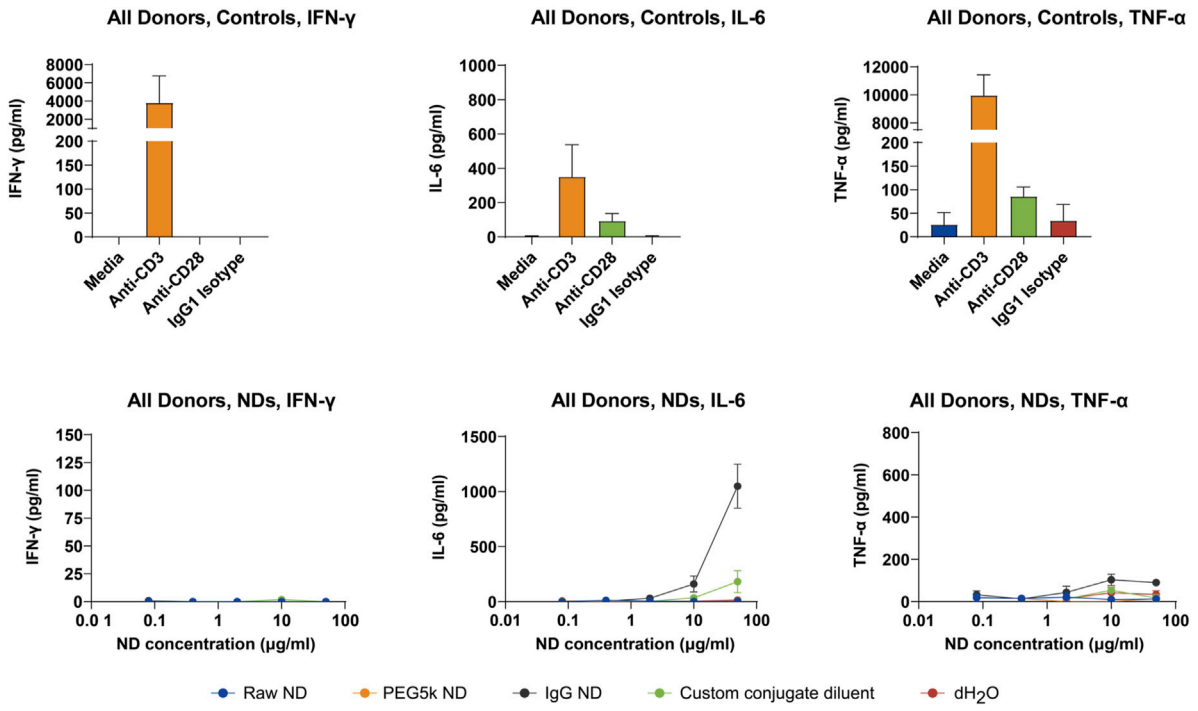

FIGURE 3
Cytokine responses in PBMC culture supernatants.

were treated with anti-CD3 stimulation, there was a consistent increase in IL-6 secretion. IL-6 secretion was also induced, albeit to a much lesser degree, in cells treated with anti-CD28 stimulation. TNF-α was detectable at very low concentrations in supernatants from PBMCs from donors treated with media alone or isotype control (Figure 3; top-right panel). When cells were treated with anti-CD3 stimulation, there was a strong induction of TNF-α secretion in all three donors. Anti-CD28 stimulation trended towards an increase in TNF-α secretion, although at a factor approximately 10-fold lower than anti-CD3.

When PBMCs were incubated with NDs or vehicle, there was no detectable induction of IFN-γ under any condition (Figure 3; bottom-left panel). This suggests there was no specific activation of T or B cells in the PBMCs when tested under these conditions. There was an increase in IL-6 secretion in cells treated with the two highest doses of IgG-NDs (Figure 3; bottom-center panel). This was also apparent in the vehicle at the same concentrations, although to a lesser extent. This result, combined with the ATP data, suggests there may have been cell activation associated with non-specific cytotoxicity when the custom conjugate diluent was tested at 10%, as

well as when the IgG-NDs were tested at 50 μg/mL. This was also evidenced by the modest increase in TNF-α secretion at the highest concentrations of the IgG-NDs (Figure 3; bottom-right panel). Mean cytokine concentrations are presented below. Cytokine concentrations from individual donors are presented in Supplementary Data.

Displayed are the cytokine concentrations (IFN-γ, IL-6, and TNF-α) measured in supernatants from PBMC cultures of three healthy donors. The top panels represent controls, and the bottom panels show results following incubation with different ND formulations. Results highlight the selective cytokine secretion patterns in response to specific ND treatments, pointing towards their immunomodulatory potential. Each point is the mean of triplicate measures, with error bars indicating SEM. Custom conjugant dilutant consisted of 1*PBS +10% FBS; (see Section 2.2). Abbreviations: dH2O = sterile, filtered deionized water; h = hour; ND = nanodiamond; PBMC = peripheral blood mononuclear cells; SEM = standard error of the mean.

4 Discussion

4.1 Interpretation of results

Taken together, these data suggest the experiment yielded valid results, with findings for the controls falling within expected ranges and performing more favorably than detonation NDs (DNDs) (Mytych et al., 2015). Using ATP levels and cytokine concentrations as surrogates for cytotoxicity and immunogenicity, respectively, NDs conjugated to IgG induced inflammation at concentrations of 10 and 50 μg/mL. There was no induction of inflammation in PBMCs from the three healthy donors when incubated with raw-NDs, PEG5k-NDs, or IgG-NDs at 0.08, 0.4 or 2 μg/mL. Additionally, raw-NDs and PEG5k-NDs were well tolerated at concentrations up to 10 μg/mL.

The dose-dependent increase in ATP concentration up to 10 μg/mL across all LND formulations suggests an enhancement in cellular metabolic activity without inducing cytotoxic effects, indicative of the high biocompatibility of LNDs (Pentecost et al., 2017). However, the minimal changes in ATP levels at the highest concentration tested (50 μg/mL) hint at a cytotoxic threshold, aligning with ATP's dual role as both an energy source and a signaling molecule for cellular distress (Zimmermann, 2000; Vultaggio-Poma et al., 2020). The design of this study made it impossible to determine whether the effects observed at 50 μg/mL were caused by the IgG-NDs or exacerbated by the custom conjugate diluent. The results do suggest the custom conjugate diluent is well tolerated at concentrations of ≤0.4% but may have a deleterious effect on cell viability at concentrations of ≥2%. These effects might be caused by non-specific cytotoxicity, which is common in several vehicles tested at this concentration (Park et al., 2010; Sun et al., 2011; Kim et al., 2012; Qu et al., 2012; Crisponi et al., 2017; Lategan et al., 2018; Medici et al., 2021; Abuzreda and Yousif, 2023).

Differential cytokine responses to LND formulations, particularly the elevated secretion of IL-6 and TNF-α at higher concentrations of IgG-NDs, point to immune activation that could be influenced by surface chemistry and conjugation. The more pronounced responses in the presence of IgG-NDs suggest antibody conjugation could potentiate LND immunogenicity, possibly through specific targeting of immune cell receptors or enhanced nanoparticle uptake (Mochalin et al., 2012). This finding underscores the importance of surface modifications in designing nanodiamonds for biomedical applications, as these modifications can significantly influence immunological interactions (Kaur and Badea, 2013)

The strong IFN-γ and TNF-α response to anti-CD3 suggests the cell populations present, most likely T-cells, were sensitive to specific activation. Conversely, the low concentrations of IL-6 following anti-CD3 stimulation suggest controls had no appreciable effect on monocytes. This is further evidenced by the PBMCs' modest cytokine responses to anti-CD28 stimulation alone, which reinforces the conclusion there was no significant cellular activation under these conditions.

Whether PBMCs were incubated with NDs or vehicle, there was no detectable induction of IFN-γ under any condition, suggesting there was no specific activation of T- or B-cells in the PBMCs. Notably, the absence of a significant IFN-γ response across all conditions highlights the specificity of immune modulation induced by LNDs. IFN-γ is a key mediator of adaptive immunity, and its lack of induction suggests that LNDs may primarily influence innate immune mechanisms, offering potential pathways for enhancing anti-tumor immunity or mitigating autoimmune reactions without widespread activation of adaptive immune cells (Yuan et al., 2010)

However, incubation with IgG-NDs led to an increase in IL-6 secretion at higher doses (i.e., 10 and 50 μg/mL). The increase in IL-6 secretion at the highest concentrations tested suggests a pro-inflammatory response, warranting further investigation into the role of nanoparticle size, surface charge, and coating in modulating immune responses, as well as the potential contributory effects of certain diluents (Fadeel and Garcia-Bennett, 2010; Tsai et al., 2016). These observations are crucial for understanding how LNDs might be harnessed to modulate immune responses in therapeutic settingsWhile some of this increase may be attributable to the vehicle, the increases were larger in the IgG-ND group than in the vehicle controls. When considered within the context of the ATP data, it is reasonable to conclude there may have been cell activation associated with non-specific cytotoxicity when the custom conjugate diluent was tested at 10%, as well as when the IgG NDs were tested at 50 μg/mL. This was also evidenced by the modest increase in TNF-α secretion at the highest concentrations of the IgG-NDs.

A very strong positive correlation was observed between ATP production and IFN-γ levels (Pearson correlation coefficient = 0.979), with a statistically significant p-value of 0.021. This indicates that treatments leading to increased ATP production also tend to increase IFN-γ levels, suggesting a link between cellular metabolic activity and the immune response mediated by IFN-γ. Similarly, a very strong positive correlation was found between ATP production and TNF-α levels (Pearson correlation coefficient = 0.992), with a p-value of 0.008, indicating statistical significance. This result suggests that higher ATP production is associated with elevated TNF-α levels, further supporting the relationship between cellular energy levels and immune function, particularly the inflammatory response.

4.2 Comparison with existing literature

Comparatively, existing literature on nanodiamond applications in biomedicine has predominantly focused on detonation nanodiamonds (DNDs) and high-pressure high-temperature (HPHT) nanodiamonds. However, the synthesis methods for DNDs and HPHT NDs often result in a broader size distribution and potential for impurities (Baidakova et al., 2013; Tsai et al., 2016), which can influence their biocompatibility and immune interactions. Our study's emphasis on LNDs, with their consistent size (<5 nm) and high purity, underscores their potential to offer more controlled interactions with biological systems, thereby minimizing unintended immune responses.

Furthermore, previous studies, such as those by Mytych et al., 2015; Lategan et al., 2018, have underscored the critical influence of nanoparticle surface chemistry on their immunogenicity and cytotoxicity (Mytych et al., 2015; Lategan et al., 2018). Our observations that IgG-conjugated LNDs induce pro-inflammatory responses at higher concentrations further emphasize the delicate balance between nanoparticle functionalization and their immune compatibility, an aspect crucial for their application in targeted therapy.

This study also contributes to the ongoing discussion on nanodiamond biocompatibility and functionalization for biomedical applications. By focusing on LNDs, we elucidate how synthesis methods and surface conjugations impact their immunological interactions, providing a comparative analysis that enriches the existing literature on nanodiamonds' therapeutic potential in biomedicine (Sadat et al., 2022).

4.3 Enhanced biomedical applications of LNDs

Our study underscores the remarkable potential of laser-synthesized nanodiamonds (LNDs) in biomedical applications, highlighted by their high tolerance in peripheral blood mononuclear cells (PBMCs) without significant induction of inflammation or cytotoxicity. PEGylated LNDs stand out for drug delivery, offering improved biocompatibility and reduced immune response, which could enhance the delivery and efficacy of therapeutic agents (Turcheniuk and Mochalin, 2017; Gao et al., 2019). Additionally, antibody-conjugated LNDs highlight the precision medicine potential, targeting specific cells or tissues for therapeutic action while minimizing side effects (Suarez-Kelly et al., 2021; Paladhi et al., 2022). Their inherent fluorescence and biocompatibility also position LNDs as advantageous for bioimaging, facilitating the non-invasive monitoring of disease processes and therapeutic response (Perevedentseva et al., 2013).

4.4 Suggestions for future research

Exploring the role of nanoparticle surface chemistry in immune responses and the effects of LNDs on various components of the immune system will be vital for characterizing their immunomodulatory potential. Further studies should delineate the mechanisms underlying LNDs' dose-dependent effects on cellular metabolism and immune activation, optimizing LND design for specific biomedical applications (Stone et al., 2009; Mochalin et al., 2012).

In conclusion, this study contributes valuable insights into the immunomodulatory effects of LNDs on PBMCs, laying the groundwork for future investigations into the therapeutic potential of these nanomaterials. As we continue to unravel the complex interactions between nanodiamonds and the immune system, the promise of nanodiamond-based therapeutics in modulating immune responses for disease treatment and prevention becomes increasingly tangible.

Data availability statement

The original contributions presented in the study are included in the article/Supplementary Material, further inquiries can be directed to the corresponding author.

Ethics statement

Ethical approval was not required for the studies on humans in accordance with the local legislation and institutional requirements because only commercially available established cell lines were used.

Author contributions

EA: Writing–original draft, Writing–review and editing. KL: Writing–review and editing.

Funding

The author(s) declare that no financial support was received for the research, authorship, and/or publication of this article.

Conflict of interest

The authors declare that the research was conducted in the absence of any commercial or financial relationships that could be construed as a potential conflict of interest.

Publisher's note

All claims expressed in this article are solely those of the authors and do not necessarily represent those of their affiliated organizations, or those of the publisher, the editors and the reviewers. Any product that may be evaluated in this article, or claim that may be made by its manufacturer, is not guaranteed or endorsed by the publisher.

Supplementary material

The Supplementary Material for this article can be found online at: https://www.frontiersin.org/articles/10.3389/fnano.2024.1352287/full#supplementary-material

References

Abuzreda, A., and Yousif, A. (2023). *toxicity-of-iron-oxide-nanoparticles-on–antioxidant-enzymes-and-free-radicals-in-male-rats* 7, 140. doi:10.35841/aamsn-7.2.140

Alexander, A., Saraf, S., Saraf, S., Agrawal, M., Patel, R. J., Agrawal, P., et al. (2019). Amalgamation of stem cells with Nanotechnology: a unique therapeutic approach. *Curr. Stem Cell Res. Ther.* 14 (2), 83–92. doi:10.2174/1574888x13666180703143219

Ansari, S. A., Satar, R., Jafri, M. A., Rasool, M., Ahmad, W., and Kashif Zaidi, S. (2016). Role of nanodiamonds in drug delivery and stem cell therapy. *Iran. J. Biotechnol.* 14 (3), 130–141. doi:10.15171/ijb.1320

Baidakova, M. V., Kukushkina, Y. A., Sitnikova, A. A., Yagovkina, M. A., Kirilenko, D. A., Sokolov, V. V., et al. (2013). Structure of nanodiamonds prepared by laser synthesis. *Phys. Solid State* 55 (8), 1747–1753. doi:10.1134/s1063783413080027

Chang, S., Popowich, Y., Greco, R. S., and Haimovich, B. (2003). Neutrophil survival on biomaterials is determined by surface topography. *J. Vasc. Surg.* 37 (5), 1082–1090. doi:10.1067/mva.2003.160

Chang, S. L. Y., Reineck, P., Krueger, A., and Mochalin, V. N. (2022). Ultrasmall nanodiamonds: perspectives and questions. *ACS Nano* 16 (6), 8513–8524. doi:10.1021/acsnano.2c00197

Crisponi, G., Nurchi, V., Lachowicz, J., Peana, M., Medici, S., and Zoroddu, M. (2017). "Chapter 18 - toxicity of nanoparticles: etiology and mechanisms," in *Antimicrobial nanoarchitectonics*. Editor A. M. Grumezescu (Amsterdam, Netherlands: Elsevier), 511–546.

Di Virgilio, F., Sarti, A. C., and Grassi, F. (2018). Modulation of innate and adaptive immunity by P2X ion channels. *Curr. Opin. Immunol.* 52, 51–59. doi:10.1016/j.coi.2018.03.026

Fadeel, B., and Garcia-Bennett, A. E. (2010). Better safe than sorry: understanding the toxicological properties of inorganic nanoparticles manufactured for biomedical applications. *Adv. Drug Deliv. Rev.* 62 (3), 362–374. doi:10.1016/j.addr.2009.11.008

Gao, G., Guo, Q., and Zhi, J. (2019). Nanodiamond-based theranostic platform for drug delivery and bioimaging. *Small* 15 (48), e1902238. doi:10.1002/smll.201902238

Ghoneum, M. H., Pan, D., and Katano, H. (2014). *Enhancement of human T lymphocyte proliferation by nanodiamond and nanoplatinum in liquid. DPV576.*

Huang, K. J., Lee, C., Lin, Y., Lin, C., Perevedentseva, E., Hung, S., et al. (2017). Phagocytosis and immune response studies of Macrophage-Nanodiamond Interactions *in vitro* and *in vivo*. *J. Biophot.* 10 (10), 1315–1326. doi:10.1002/jbio.201600202

Iwamoto, T., Sugimoto, A., Kitamura, T., Akazawa, Y., and Hasegawa, T. (2014). The role of extracellular ATP-mediated purinergic signaling in bone, cartilage, and tooth tissue. *J. Oral Biosci.* 56 (4), 131–135. doi:10.1016/j.job.2014.07.003

Kaçar, C., and Erden, P. E. (2020). An amperometric biosensor based on poly(L-aspartic acid), nanodiamond particles, carbon nanofiber, and ascorbate oxidase-modified glassy carbon electrode for the determination of L-ascorbic acid. *Anal. Bioanal. Chem.* 412 (22), 5315–5327. doi:10.1007/s00216-020-02747-w

Kalyanaraman, B. (2017). Teaching the basics of cancer metabolism: developing antitumor strategies by exploiting the differences between normal and cancer cell metabolism. *Redox Biol.* 12, 833–842. doi:10.1016/j.redox.2017.04.018

Kaur, R., and Badea, I. (2013). Nanodiamonds as novel nanomaterials for biomedical applications: drug delivery and imaging systems. *Int. J. Nanomedicine* 8, 203–220. doi:10.2147/ijn.s37348

Kim, T. H., Kim, M., Park, H., Shin, U. S., Gong, M., and Kim, H. (2012). Size-dependent cellular toxicity of silver nanoparticles. *J. Biomed. Mater Res. A* 100 (4), 1033–1043. doi:10.1002/jbm.a.34053

Lategan, K., Alghadi, H., Bayati, M., de Cortalezzi, M., and Pool, E. (2018). Effects of graphene oxide nanoparticles on the immune system biomarkers produced by RAW 264.7 and human whole blood cell cultures. *Nanomater. (Basel)* 8 (2), 125. doi:10.3390/nano8020125

Li, C., Luo, S. X. L., Kim, D. M., Wang, G., and Cappellaro, P. (2023). Ion sensors with crown ether-functionalized nanodiamonds. Available at: https://arxiv.org/abs/2301.03143.

Lin, Y. W., Su, H. C., Raj, E. N., Liu, K. K., Chang, C. J., Hsu, T. C., et al. (2022). Targeting EGFR and monitoring tumorigenesis of human lung cancer cells *in vitro* and *in vivo* using nanodiamond-conjugated specific EGFR antibody. *Pharmaceutics* 15 (1), 111. doi:10.3390/pharmaceutics15010111

Liu, C. Y., Lee, M. C., Lin, H. F., Lin, Y. Y., Lai, W. Y., Chien, Y., et al. (2021). Nanodiamond-based microRNA delivery system promotes pluripotent stem cells toward myocardiogenic reprogramming. *J. Chin. Med. Assoc.* 84 (2), 177–182. doi:10.1097/jcma.0000000000000441

Medici, S., Peana, M., Pelucelli, A., and Zoroddu, M. A. (2021). An updated overview on metal nanoparticles toxicity. *Seminars Cancer Biol.* 76, 17–26. doi:10.1016/j.semcancer.2021.06.020

Mochalin, V. N., Shenderova, O., Ho, D., and Gogotsi, Y. (2012). The properties and applications of nanodiamonds. *Nat. Nanotechnol.* 7 (1), 11–23. doi:10.1038/nnano.2011.209

Montes, R., Sánchez, G., Zhao, J., Palet, C., Baeza, M., and Bastos-Arrieta, J. (2020). Customized *in situ* functionalization of nanodiamonds with nanoparticles for composite carbon-paste electrodes. *Nanomaterials* 10 (6), 1179. doi:10.3390/nano10061179

Mytych, J., Lewinska, A., Zebrowski, J., and Wnuk, M. (2015). Nanodiamond-induced increase in ROS and RNS levels activates NF-κB and augments thiol pools in human hepatocytes. *Diam. Relat. Mater.* 55, 95–101. doi:10.1016/j.diamond.2015.03.014

Paladhi, A., Rej, A., Sarkar, D., Singh, R., Bhattacharyya, S., Sarkar, P. K., et al. (2022). Nanoscale diamond-based formulation as an immunomodulator and potential therapeutic for lymphoma. *Front. Pharmacol.* 13, 852065. doi:10.3389/fphar.2022.852065

Park, E. J., Kim, H., Kim, Y., Yi, J., Choi, K., and Park, K. (2010). Carbon fullerenes (C60s) can induce inflammatory responses in the lung of mice. *Toxicol. Appl. Pharmacol.* 244 (2), 226–233. doi:10.1016/j.taap.2009.12.036

Peer, D., Zhu, P., Carman, C. V., Lieberman, J., and Shimaoka, M. (2007). Selective gene silencing in activated leukocytes by targeting siRNAs to the integrin lymphocyte function-associated antigen-1. *Proc. Natl. Acad. Sci. U. S. A.* 104 (10), 4095–4100. doi:10.1073/pnas.0608491104

Pentecost, A., Kim, M. J., Jeon, S., Ko, Y. J., Kwon, I. C., Gogotsi, Y., et al. (2019). Immunomodulatory nanodiamond aggregate-based platform for the treatment of rheumatoid arthritis. *Regen. Biomater.* 6 (3), 163–174. doi:10.1093/rb/rbz012

Pentecost, A. E., Witherel, C. E., Gogotsi, Y., and Spiller, K. L. (2017). Anti-inflammatory effects of octadecylamine-functionalized nanodiamond on primary human macrophages. *Biomaterials Sci.* 5 (10), 2131–2143. doi:10.1039/c7bm00294g

Perevedentseva, E., Lin, Y. C., Jani, M., and Cheng, C. L. (2013). Biomedical applications of nanodiamonds in imaging and therapy. *Nanomedicine* 8 (12), 2041–2060. doi:10.2217/nnm.13.183

Perevedentseva, E., Peer, D., Uvarov, V., Zousman, B., and Levinson, O. (2015). Nanodiamonds of laser synthesis for biomedical applications. *J. Nanosci. Nanotechnol.* 15 (2), 1045–1052. doi:10.1166/jnn.2015.9747

Qu, C., Wang, L., He, J., Tan, J., Liu, W., Zhang, S., et al. (2012). Carbon nanotubes provoke inflammation by inducing the pro-inflammatory genes IL-1β and IL-6. *Gene* 493 (1), 9–12. doi:10.1016/j.gene.2011.11.046

Reina, G., Zhao, L., Bianco, A., and Komatsu, N. (2019). Chemical functionalization of nanodiamonds: opportunities and challenges ahead. *Angew. Chem. Int. Ed.* 58 (50), 17918–17929. doi:10.1002/anie.201905997

Sadat, Z., Farrokhi-Hajiabad, F., Lalebeigi, F., Naderi, N., Ghafori Gorab, M., Ahangari Cohan, R., et al. (2022). A comprehensive review on the applications of carbon-based nanostructures in wound healing: from antibacterial aspects to cell growth stimulation. *Biomater. Sci.* 10 (24), 6911–6938. doi:10.1039/d2bm01308h

Shao, D., Li, M., Wang, Z., Zheng, X., Lao, Y., Chang, Z., et al. (2018). Bioinspired diselenide-bridged mesoporous silica nanoparticles for dual-responsive protein delivery. *Adv. Mater.* 30 (29), 1801198. doi:10.1002/adma.201801198

Sharmin, R., Nusantara, A. C., Nie, L., Wu, K., Elias Llumbet, A., Woudstra, W., et al. (2022). Intracellular quantum sensing of free-radical generation induced by acetaminophen (APAP) in the cytosol, in mitochondria and the nucleus of macrophages. *ACS Sensors* 7 (11), 3326–3334. doi:10.1021/acssensors.2c01272

Stone, V., Johnston, H., and Schins, R. P. (2009). Development of *in vitro* systems for nanotoxicology: methodological considerations. *Crit. Rev. Toxicol.* 39 (7), 613–626. doi:10.1080/10408440903120975

Suarez-Kelly, L. P., Campbell, A. R., Rampersaud, I. V., Bumb, A., Wang, M. S., Butchar, J. P., et al. (2017). Fluorescent nanodiamonds engage innate immune effector cells: a potential vehicle for targeted anti-tumor immunotherapy. *Nanomedicine Nanotechnol. Biol. Med.* 13 (3), 909–920. doi:10.1016/j.nano.2016.12.005

Suarez-Kelly, L. P., Sun, S. H., Ren, C., Rampersaud, I. V., Albertson, D., Duggan, M. C., et al. (2021). Antibody conjugation of fluorescent nanodiamonds for targeted innate immune cell activation. *ACS Appl. Nano Mater* 4 (3), 3122–3139. doi:10.1021/acsanm.1c00256

Sun, Z., Liu, Z., Meng, J., Meng, J., Duan, J., Xie, S., et al. (2011). Carbon nanotubes enhance cytotoxicity mediated by human lymphocytes *in vitro*. *PLoS One* 6 (6), e21073. doi:10.1371/journal.pone.0021073

Taylor, A. C., González, C. H., Ferretti, P., and Jackman, R. B. (2019). Spontaneous differentiation of human neural stem cells on nanodiamonds. *Adv. Biosyst.* 3 (4), e1800299. doi:10.1002/adbi.201800299

Tsai, L. W., Lin, Y. C., Perevedentseva, E., Lugovtsov, A., Priezzhev, A., and Cheng, C. L. (2016). Nanodiamonds for medical applications: interaction with blood *in vitro* and *in vivo*. *Int. J. Mol. Sci.* 17 (7), 1111. doi:10.3390/ijms17071111

Turcheniuk, K., and Mochalin, V. N. (2017). Biomedical applications of nanodiamond (Review). *Nanotechnology* 28 (25), 252001. doi:10.1088/1361-6528/aa6ae4

van der Laan, K. J., Morita, A., Perona-Martinez, F. P., and Schirhagl, R. (2020). Evaluation of the oxidative stress response of aging yeast cells in response to internalization of fluorescent nanodiamond biosensors. *Nanomater. (Basel)* 10 (2), 372. doi:10.3390/nano10020372

Vultaggio-Poma, V., Sarti, A. C., and Di Virgilio, F. (2020). Extracellular ATP: a feasible target for cancer therapy. *Cells* 9 (11), 2496. doi:10.3390/cells9112496

Yuan, Y., Wang, X., Jia, G., Liu, J. H., Wang, T., Gu, Y., et al. (2010). Pulmonary toxicity and translocation of nanodiamonds in mice. *Diam. Relat. Mater.* 19 (4), 291–299. doi:10.1016/j.diamond.2009.11.022

Zimmermann, H. (2000). Extracellular metabolism of ATP and other nucleotides. *Naunyn Schmiedeb. Arch. Pharmacol.* 362 (4-5), 299–309. doi:10.1007/s002100000309

Frontiers in Nanotechnology

Explores nanoscale science and engineering of materials, devices and tools

An interdisciplinary journal across nanoscience and nanotechnology, at the interface of chemistry, physics, materials science and engineering. It focuses on new nanofabrication methods and their applications.

Discover the latest Research Topics

See more →

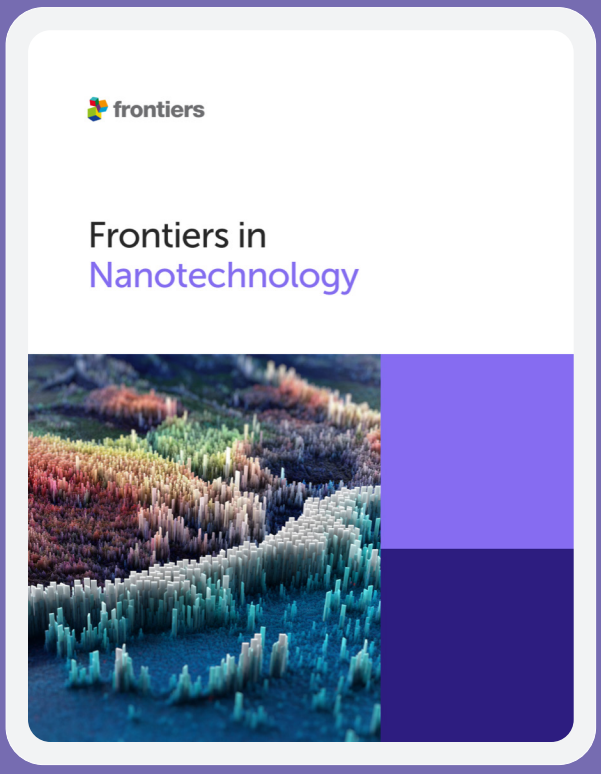

Frontiers

Avenue du Tribunal-Fédéral 34
1005 Lausanne, Switzerland
frontiersin.org

Contact us

+41 (0)21 510 17 00
frontiersin.org/about/contact